Doctoral Dissertation.
Doctoral Program in Civil and Environmental Engineering (38th Cycle)

High-fidelity multiscale modelling for the seismic assessment of infilled RC frames

Marilisa Di Benedetto

Supervisor(s):
Prof. G. C. Marano, Supervisor
Prof. F. Di Trapani, Co-Supervisor
Prof. G. Camata, Co-Supervisor

Doctoral Examination Committee:
Prof. G. Quaranta, Referee, Sapienza University of Rome
Prof. F. De Luca, Referee, University of Bristol
Prof. G. Bertagnoli, Member, Politecnico di Torino

Politecnico di Torino
2026

This doctoral thesis has been developed within the Ph.D. program funded by the National Recovery and Resilience Plan (PNRR), Mission 4, Component 1, “Enhancement of the education and research offer from early childhood to university” - Investment 4.1 “Extension of the number of Ph.D. programs and innovative Ph.D.s for public administration and cultural heritage”, under Ministerial Decree No. 351 of 9 April 2022.

I hereby declare that the contents and organisation of this dissertation constitute my own original work and does not compromise in any way the rights of third parties, including those relating to the security of personal data.

Marilisa Di Benedetto Turin, May 2026

Wherever you are, you're living in our memories.

To you.

Acknowledgments

"Knowing where you are by knowing where you've been."
Moana – Disney

This thesis is not only the result of a research project, but also the outcome of a path that has been academic and, above all, deeply human. A Ph.D. does not only shape the way one thinks as a researcher; it also changes the way one looks at oneself, at growth, and at the people and places that become part of the journey.

This path has not always been linear. It has been made of progress, questions, changes of direction, moments of uncertainty, and the perseverance needed to continue even when the way forward was not immediately clear. In this journey, the environments we live in, the places we call home, the people we meet, those who walk beside us, and even those who leave, all become part of what we become. Every exchange, every shared word, every moment of closeness and confrontation leaves something behind. In different ways, these traces have shaped not only the work presented in this thesis, but also the person who completed it.

Among the people who have left a meaningful trace on this journey, I would first like to thank Professor Fabio Di Trapani. I am deeply grateful to him for introducing me to the world of research and for transmitting to me his passion for this field. Working with him allowed me to understand what research means in practice: asking the right questions, dealing with complexity, and learning to turn doubts into scientific work. The many exchanges we shared over these years have shaped my way of thinking and contributed to my growth, helping me face this journey with greater awareness and maturity.

I would like to sincerely thank Professor Guido Camata for his trust and for the opportunities he gave me throughout these years. Without his support, and without the co-funding of my doctoral scholarship through ASDEA – Advanced Structural Design & Analysis, this path would not have been possible. I am also grateful to

him for introducing me to nonlinear numerical analyses and to the use of STKO, which has become a fundamental tool in my research work. His confidence in me gave me the possibility to grow, to work with a certain degree of independence, and to build an important part of the skills on which this thesis is based.

In this regard, I would also like to thank Dr. Massimo Petracca for his technical support, and for the many things I learned from his webinars on OpenSees and STKO. His clarity, expertise, and ability to make complex numerical issues understandable have been extremely valuable throughout this work. In many moments of numerical uncertainty, he has been my favourite oracle.

I would also like to thank Professor G.C. Marano for his support throughout these years and for introducing me to a broader academic network.

A heartfelt thank you goes to Professor Raffaele De Risi for his guidance during my period at the University of Bristol. I met him at one of the most demanding stages of this journey, and at that moment his support was a light. His knowledge, passion, and genuine enthusiasm for research became a profound source of inspiration for me. The trust he showed in my abilities helped me regain motivation and confidence in myself. I will never forget the positive environment I found in Bristol, nor Raffaele's calm and thoughtful way of approaching problems. He taught me that, even when things appear complex, there is always a way to move forward. Thanks to him, to my colleagues there, and to the environment I experienced in Bristol, I was able to reconnect with an important part of myself. Bristol and what it represented to me will always remain in my heart.

I would also like to thank all the people I had the chance to work with during these years. Research is rarely built in isolation. It takes shape through shared ideas, informal conversations, doubts discussed and clarified, and the quiet support that comes from being surrounded by people who understand this path. To all those who contributed to this work, directly or indirectly, I am sincerely grateful.

A special thanks goes to those colleagues who became much more than colleagues. With them I shared deadlines, long days, small victories, and the kind of everyday moments that often remain outside a thesis, but make the journey possible. Some of them became friends, and their presence made these years lighter, more human, and much more meaningful.

To my friends, old and new, thank you for being part of my life during these years. Thank you for the conversations, the laughter, the patience, and for staying close even when I was distant, tired, or absorbed by this work. Each of you, in your own way, reminded me that there was a world outside the Ph.D., and that I was part of it too.

I would also like to dedicate a special thought to Corso Racconigi, the place I called home for eight years. It was much more than a house: it was a shelter, a meeting point, and a silent witness to changes, friendships, difficult days, and beautiful memories. A part of who I am today will always belong there.

Finally, my deepest gratitude goes to my family and to the people I love. Thank you for your constant presence throughout this journey. Thank you for believing in me when I needed it most, for staying close, and for making me feel at home even in the most uncertain moments. In your eyes and in your hugs, I have always found the safest place in the world.

Summary

Infilled Reinforced Concrete (RC) frame structures represent a large portion of the existing building heritage, worldwide. Although infills significantly influence the overall stiffness and strength, they have traditionally been considered as non-structural components and are often neglected in design procedures or modelled through simplified approaches. However, post-earthquake reconnaissance and various experimental and numerical studies have demonstrated their crucial influence on seismic performance, showing that their presence cannot be neglected in structural modelling, either at the design stage or during safety verification. By interacting with the surrounding RC frame, infills significantly alter both global and local structural behaviour. At the global level, irregular distributions in plan or elevation can generate torsional effects or soft-storey mechanisms. At the local level, instead, the stress transfer from the infill panel to adjacent members induces additional shear forces at column ends and beam-column joints, often responsible for brittle failures in non-ductile RC elements. Existing seismic codes recognise the structural relevance of infills but still rely on simplified modelling approaches, like the equivalent diagonal strut macro-models, that may not capture local interaction effects. Therefore, no validated and widely applicable approach is yet available to assess both global and local effects, leaving a gap between observed behaviour, refined numerical simulations, and practical tools for engineering practitioners.

To address this gap, this thesis develops a high-fidelity multiscale modelling framework for the seismic assessment of infilled RC frames. The main idea is to integrate advanced numerical simulations with simplified predictive tools, thus providing a consistent methodology capable of capturing both global and local effects. The research was framed into complementary studies, each addressing a specific objective:

i. validation of refined modelling strategies against global response and observed damage from experimental tests;
ii. investigation of local infill-frame interaction, extracting internal force distributions not accessible from experimental tests;

iii. development and improvement of simplified macro-modelling strategies able to reproduce both global and local responses, connecting refined simulation results and tools suitable for engineering practice.

To this end, existing modelling approaches for masonry-infilled RC frames under in-plane (IP) loading were first reviewed and discussed. Refined micro-modelling strategies were then implemented in the STKO/OpenSees environment. The first study involved the investigation of global and local effects on single-bay infilled RC frame structures. Calibrated micro-models were used to investigate the variation of global response and stress-transfer mechanisms between the infill and the surrounding frame under monotonic IP loading. By means of *section-cut* techniques, internal forces in RC frame members were analysed, providing insight into phenomena not directly measurable in experimental programmes. The results confirmed the amplification of shear demand induced by infill-frame interaction, which are consistent with post-earthquake reconnaissance and previous research, and established a solid reference for the development of simplified models.

Building on this foundation, the study proceeded to the validation of the micro-modelling strategy under cyclic IP-loading tests. The study involved the reproduction of full-scale single-bay specimens tested within the ERIES-ENFRAG project at the EUCENTRE laboratory. The experimental programme, which involved cyclic displacement-controlled IP loading at different drift and input energy levels, provided a robust benchmark for model validation. The calibrated numerical models accurately reproduced the global response and the evolution of damage, confirming the reliability of the adopted modelling approach.

The third phase of the research focused on connecting high fidelity modelling results with simplified macro-modelling, with particular emphasis on local effects. Two strategies were developed. The first consists of an analytical correction model for the single-strut macro-model, formulated to estimate the additional shear demand as a function of geometrical parameters and the axial force in the equivalent strut. The correction model was calibrated and validated against refined numerical replica of single-bay frames under monotonic IP simulations. This formulation preserves the simplicity and efficiency of conventional single-strut macro-model while improving its predictive accuracy for local interaction effects. The second introduces an equivalent three-strut macro-model, also calibrated and validated on micro-models' results. A genetic algorithm (GA) was employed to optimise the configuration, improving the balance between global and local response. These developments demonstrated that the proposed models can be conveniently applied in the seismic assessment of existing RC structures.

Finally, one of the two proposed strategies, namely the analytical correction model for single-struts, was validated under nonlinear dynamic conditions by numerically reproducing a shake-table test on a three-storey infilled RC building previously tested at the EUCENTRE laboratory within the ISAAC project. The refined model was rigorously calibrated through sensitivity analyses (SA) and GA-based optimisation of vibration frequencies in both elastic and non-linear phases. Once validated, this reference model served as a benchmark for testing the simplified solutions under dynamic excitation. Comparisons with refined simulations confirmed that the proposed model captured peak shear demands even under dynamic conditions, demonstrating their robustness and suitability for safety assessment as well as for large-scale or computationally demanding analyses, without neglecting infill-frame interaction effects.

Overall, the thesis offers a comprehensive framework for evaluating the seismic performance of infilled RC frames. The proposed methodology combines advanced numerical simulations, extensive experimental validation and simplified formulations to address both global and local effects. These outcomes bridge the gap between high-fidelity modelling, simplified modelling, and predictive tools, facilitating improved code provisions and enhancing the seismic safety of existing RC structures with masonry infills.

Contents

List of Figures

List of Tables

Acronyms

BF	Bare Frame
EDP	Engineering Demand Parameter
EMA	Experimental Modal Analysis
ESM	Equivalent Strut Model
FEM	Finite Element Method
FRF	Frequency Response Function
GA	Genetic Algorithm
GM	Ground Motion
GP	Genetic Programming
IDR	Interstorey Drift Ratio
IF	Infilled Frame
IM	Intensity Measure
IP	In-Plane
LS	Limit State
MAC	Modal Assurance Criterion
MaM	Macro-Model
MeM	Meso-Model
MM	Micro-Model
MSM	Multi-Strut Model
NRMSE	Normalized Root Mean Square Error
OOP	Out-of-Plane
PFA	Peak Floor Acceleration
PGA	Peak Ground Acceleration
PSD	Power Spectral Density
RC	Reinforced Concrete
RMSE	Root Mean Square Error
URM	Unreinforced Masonry

Chapter 1

Introduction: The role of infill-frame interaction on the seismic response of infilled RC frames

1.1 Constructional background and post-earthquake reconnaissance

Masonry infilled RC frames, called also infilled frames (IFs), are one of the most widespread building typologies in regions of moderate-to-high seismic hazard. Although unreinforced masonry (URM) buildings were common, the introduction of reinforced concrete (RC) structures encouraged a growing use of masonry infilled frames. Their diffusion since the mid-twentieth century arose from a combination of structural performance and functional reasons, as well as low cost and fast construction (**Kaushik et al., 2006**).

During the early transition from load-bearing masonry to infilled RC frame structures, masonry panels were mostly used for enclosure and environmental comfort. Figure 1.1 shows the transition over the twentieth century from exclusively URM buildings to the advent of IFs, marking the shift from structural to non-structural masonry. After World War II, cities in Europe, South Asia, and Latin America grew quickly. This led to the use of RC frames with brick/block infills as

the standard way to build residential and public buildings, driven by standardisation, material availability, and architectural flexibility.

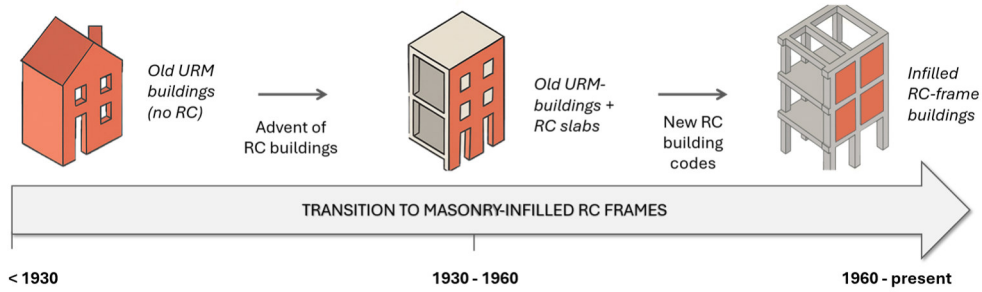

Figure 1.1: Evolution of masonry in buildings: from URM buildings to IFs.

Full-height masonry infills were commonly placed between reinforced concrete columns and beams with a mortar layer at the interface, which activated frictional mechanisms and enabled stress transfer between the two components. Although, infill panels have been traditionally classified as non-structural elements, their interaction with the surrounding frame significantly alters stiffness, strength, vibration periods, and internal force paths under lateral loads (**Fardis and Panagiotakos, 1997; Dolšek and Fajfar, 2008**). Nevertheless, structural analysis continued to rely on bare-frame idealisations, neglecting the presence of infills in both design phase and safety assessment phase. It was only after several decades that their structural contribution was gradually recognised.

Masonry infills can significantly influence the seismic response of RC buildings, causing both positive and negative effects. Their complex behaviour, governed by the interaction with the surrounding frame, requires detailed investigation. As highlighted by several post-earthquake reconnaissance studies, infills contribute to both global and local response modification (e.g. **Sezen et al., 2000; Çelebi et al., 2010; De Luca et al., 2014; Nafeh and O'Reilly, 2024**). **Furtado et al. (2021)** categorised major earthquakes damage observations in RC buildings in practical groups, confirming the complex role of structural and non-structural components. The first groups (Types 1-5) mainly refer to structural deficiencies such as poor detailing of transverse and longitudinal reinforcement, lack of confinement, and inadequate shear or flexural strength, often resulting in brittle failures of columns and beam-column joints (Figure 1.2). Damage Type 6 corresponds to the short-column mechanism, typically caused by partial infills or openings that increase shear demand in adjacent members (Figure 1.3).

Figure 1.2: Example of damage due to structural deficiencies: (a) Poor detailing and design of the beam-column joints (**Furtado et al., 2021**); (b) Shear failure of column due to insufficient transverse reinforcement; (c) Shear failure of beam-column joint due to insufficient transverse reinforcement.

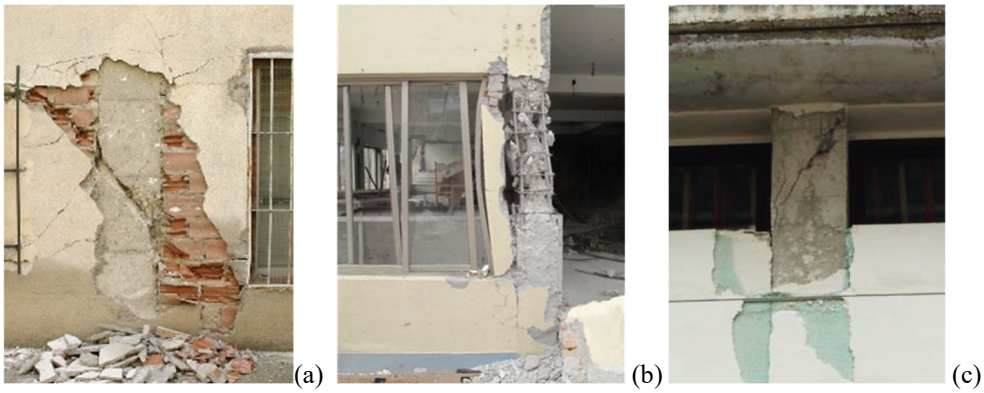

Figure 1.3: Example of short-column mechanisms (**Sezen et al., 2000; Furtado et al., 2021**): (a) Short column shear failure; (b) Short column double plastic hinge mechanism; (c) Short column shear failure due to openings.

Structural irregularities (Type 7) in plan or elevation were among the most unfavourable features, leading to torsional responses or soft-storey mechanisms, particularly in buildings with open ground storeys (Figure 1.4). Further damage mechanisms include pounding between adjacent buildings (Type 8) and failures of secondary elements such as balconies, stairs, and parapets (Type 9). The last identified category (Type 10) involves the infill panels themselves, which frequently experienced diagonal cracking, sliding along mortar joints, corner crushing, and out-of-plane collapses.

Figure 1.4: Example of soft-storey mechanisms.

The combined in-plane (IP) and out-of-plane (OOP) interaction has been recognized as one of the most critical issues, since in-plane cracking and degradation substantially reduce the out-of-plane strength and stability of infill panels. Numerous post-earthquake observations (e.g. **Hermanns et al., 2014; Celano et al., 2016; De Luca et al., 2018; Mazza and Donnici, 2021**) have reported the overturning of slender panels and the collapse of partially infilled façades, particularly in intermediate storeys, posing severe risks to life safety. A more detailed discussion of in-plane mechanisms is presented in the next section; out-of-plane collapse modes are not addressed, as this thesis focuses exclusively on the global and local IP response.

Overall, these findings confirm that masonry infills cannot be simply considered as non-structural elements: their presence modifies the seismic demand and the load paths within the structure, leading to complex coupled behaviours that must be explicitly addressed in both design and assessment frameworks.

1.2 Seismic response of IFs under IP loading

1.2.1 General aspects and global effects

The seismic response of RC frame buildings is strongly influenced by the presence of masonry infill panels, which often play an influential role in the global

and local behaviour of the structure. Alongside the load-bearing members (beams, columns, slabs), non-structural elements, such as infill panels, contribute to the overall performance of the building. According to **NTC (2018, §7.2.3)**, non-structural elements are those that, despite not ensuring the stability of the structure, may significantly influence its dynamic response or pose risks to safety if inadequately designed. They inevitably interact with the frame under horizontal actions, especially during earthquakes, altering structure's lateral stiffness, strength distribution, energy dissipation capacity, vibration periods and failure modes (**Dolšek and Fajfar, 2008; Fiore et al., 2012; Cavaleri et al., 2017**).

Research from the 1960s (e.g. **Polyakov, 1960; Holmes, 1961; Smith, 1966; Paulay and Priestley, 1992**) revealed that the behaviour of infilled frames differs substantially from that of bare frames. When subjected to IP loading, the response can be schematically described in two stages:

- Stage A (full contact): before interface detachment, the frame and the panel deform compatibly, and the system behaves monolithically, with the infill contributing to stiffness and strength (Figure 1.5a).
- Stage B (partial contact): once local sliding and separation occur along the frame-infill interfaces, the infill starts acting as a strut along its diagonal (**Polyakov, 1960**), while tensile stresses along the opposite diagonal led to cracking and separation at the corners (Figure 1.5b).

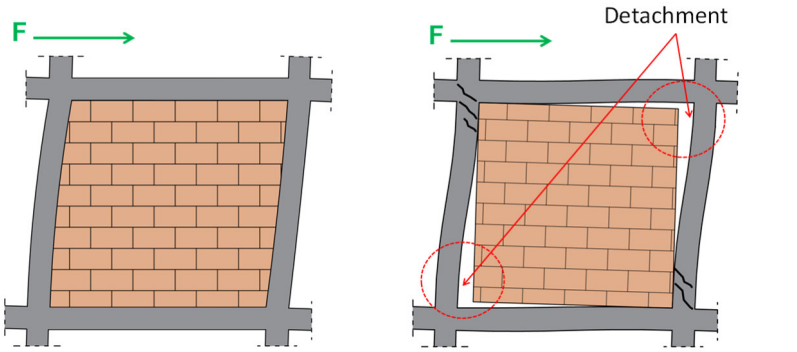

Figure 1.5: IFs subjected to IP loading (a) Before infill detachment; (b) After infill detachment.

This interaction mechanism induces a diagonal compression field in the panel and a truss-like behaviour of the overall system, which generally increases the initial stiffness and reduces the lateral drift capacity (**Paulay and Priestley, 1992**).

However, as the drift demand grows, progressive detachment and cracking lead to degradation of stiffness and strength, and load redistribution within the RC frame.

1.2.2 Typical in-plane failure mechanisms

The inclusion of infills may significantly alter the expected failure mechanisms. The in-plane behaviour of infill panels is governed by the evolution of cracking, sliding, and crushing phenomena under cyclic lateral loading. In general, failure initiates in the weakest component of the system, typically the mortar layers, and progressively involves the masonry units and frame members as deformation increases. Based on prior experimental campaigns and numerical studies, many researchers in the past, identified several damage mechanisms (e.g. **Stafford Smith and Carter, 1969; Mehrabi et al., 1996; Stavridis and Shing, 2010**). For instance, **Mehrabi et al. (1996)** recognized five recurrent infill failures depending on the strength and stiffness of the bounding frame compared to the infill:

- Flexural (A): It is a rare collapse mechanism that develops only when the infill is rigidly connected to the surrounding frame. In this case, the infilled frame behaves as a single cantilevered unit, and failure occurs when the tensile and compressive stresses at the base exceed the strength of both the masonry and the concrete.
- Mid-height crack (B): typically observed in panels built with weak mortars or horizontally perforated units, this mechanism involves the formation of horizontal cracks, often near mid-height, along the bed joints. It leads to separation of masonry portions, causing a marked reduction in lateral strength and a significant increase in overall deformability.
- Diagonal shear (C): shear cracking propagates diagonally across the infill panel. This damage may extend into the surrounding frame, potentially initiating shear failure in columns or beam-column joints. Alternatively, when sliding of masonry units develops near the panel corners, plastic hinges can form at the ends of the columns, leading to localized inelastic rotations.
- Horizontal sliding (D): It originates from the low strength of the mortar or from inadequate bonding between the mortar and the masonry units, which leads to relative sliding of the blocks along horizontal and vertical joints.

- Corner crushing (E): localized compressive damage occurring at the loaded corners of the panel, where the diagonal strut transfers concentrated compressive forces to the surrounding frame.

These mechanisms often develop sequentially, and their combination determines the global hysteretic response of the infilled frame. A scheme of the possible combined infill mechanisms is reported in Figure 1.6.

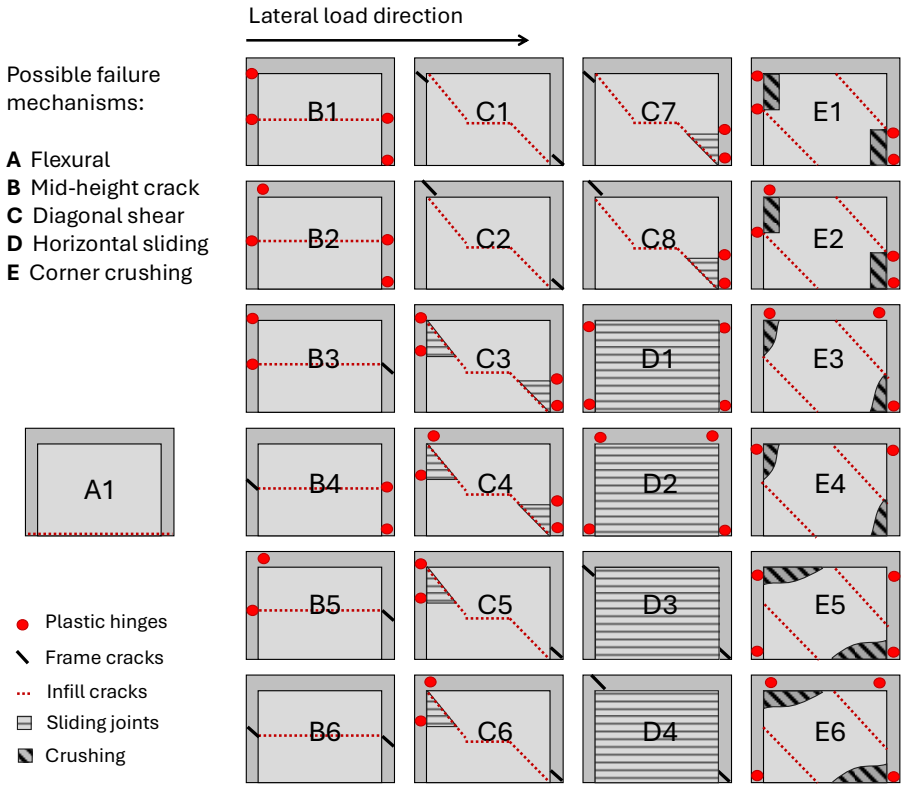

Figure 1.6: IP failure mechanisms of infill frames identified by **Mehrabi et al. (1996)**.

These mixed failure modes where also confirmed from a recent study by **Huang and Burton (2019)**, who collected a database of 114 RC infilled frame specimens from previous experimental campaigns and, through six different machine learning algorithms, classified four failure modes:

- Infill sliding and column flexural hinging (SF)
- Infill sliding and column shear failure (SS)
- Infill crushing and column flexural hinging (CF)
- Infill crushing and column shear failure (CS)

1.2.3 Infill-frame local interaction effects

At the local level, the mechanical interaction between masonry infills and RC frames significantly alters the internal stress distribution within the structural members. As the infill panel starts contributing to the lateral load resistance, diagonal compression struts are progressively mobilised within the masonry, while shear transfer along the contact interfaces with the surrounding concrete frame causes a considerable amplification of shear forces at beam-column joints and column ends. When transverse reinforcement or seismic detailing is insufficient, these localised stress concentrations can cause brittle shear failures (**Uva et al., 2012; Celarec and Dolšek, 2013; Cavaleri et al., 2017; Blasi et al., 2018**), as frequently observed in experimental investigations (e.g. **Mehrabi et al., 1996; Stavridis et al., 2012; Cavaleri and Di Trapani, 2014**).

The internal forces variations have been investigated in previous studies (e.g. **Saneinejad and Hobbs, 1995; Buonopane and White, 1999**). For example, **Saneinejad and Hobbs (1995)** derived a *shear decomposition rule* that separates the total shear demand at column ends into two components: the portion associated with the frame deformation and an additional contribution directly induced by infill-frame contact actions.

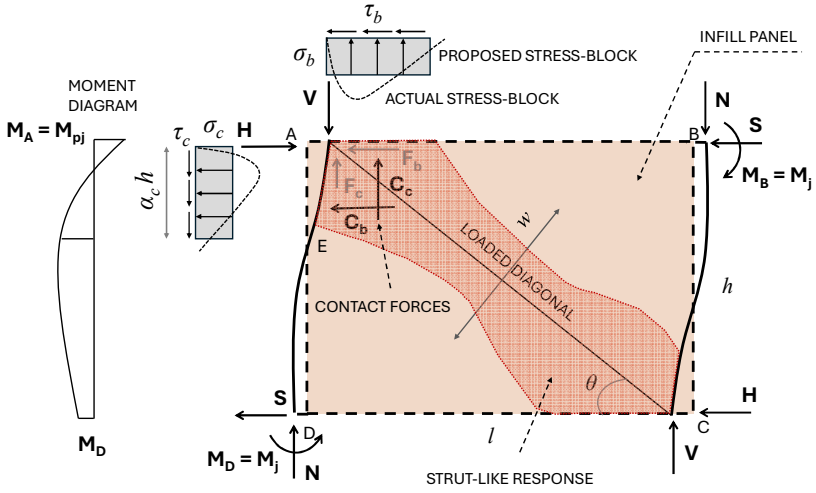

Figure 1.7: Infilled-frame force distribution due to interaction effects (**Saneinejad and Hobbs, 1995**).

The diagonal compressive strut mechanism within the infill generates concentrated axial forces transmitted to the frame at the corners, where vertical and horizontal components of the contact stresses combine to amplify shear and

moment demands (Figure 1.7). As interstorey drift increases, the effective contact length ($\alpha_c \cdot h$) progressively reduces, altering the equilibrium of internal forces and increasing shear concentrations at the column ends. The vertical stress field along the column-infill interface was shown to follow a bell-shaped distribution, while the tangential (frictional) stresses, governed by Coulomb's law, lead to additional shear forces proportional to the normal contact stress and the friction coefficient. Accordingly, **Saneinejad and Hobbs (1995)** proposed a formulation for estimating contact lengths, derived from force equilibrium considerations. In their expression, the contact lengths are expressed as a function of the plastic moments at the RC frame members, as defined below:

$$\alpha_c h = \sqrt{\frac{2M_{pj} + 2\beta_c M_{pc}}{\sigma_c t}} \tag{1}$$

where M_{pc} is the plastic moment of the column, $\beta_c = 0.2$ is an appropriate calibrated reduction factor, σ_c the normal stresses, t the infill thickness, and M_{pj} the bending moment at the loaded corner.

In other studies, the contact length calculation was defined in a more simplified manner, as a function of the macro-model geometry. For instance, **Mainstone (1971)** proposed a contact length based on the vertical component of the equivalent strut width w (Equation 1), while in other studies (**Bertoldi et al., 1993; Paulay and Priestley, 1992**) is defined considering the equivalent strut width equally divided in two portions, one in contact with the column and one with the beam (Equation 2). These discrepancies highlight the degree of uncertainty on the predicted force transferred from the infill to the frame.

$$l_c = \frac{w}{cos\theta} \tag{2}$$

$$l_c = \frac{w}{2 \cdot cos\theta} \tag{3}$$

In summary, the local infill-frame interaction governs the stress redistribution and brittle failures that occur at column ends or beam-column joints, playing a decisive role in defining the overall seismic vulnerability of infilled RC frames. A

reliable assessment of such effects requires analytical or numerical formulations capable of capturing the progressive evolution of the contact forces, automatically related to the contact lengths, and the resulting amplification of shear demand at RC frame members.

1.2.4 Code and standards provisions

The seismic performance of building structures is governed, in major international codes, by ensuring adequate safety levels and limiting non-structural damage. The way national and international standards handle the interaction between RC frames and masonry infills, especially the local effects induced by the presence of infill panels on RC members, varies considerably, reflecting both the complexity of the phenomena and modelling uncertainties.

1.2.4.1 Global performance requirements

In Europe, performance requirements are regulated by **Eurocode 8 (CEN, 2004a)**, which defines limit states, design criteria and verification rules for structural and non-structural components, including masonry infill panels.

Eurocode 8 (CEN, 2004a) prescribes that structures located in seismic regions must satisfy two fundamental performance levels:

- Ultimate Limit State (ULS), associated with life-safety and prevention of global or local collapse for seismic actions with a reference return period ($T_{r,\,ULS}$).
- Damage Limitation State (DLS), defined for more frequently occurring actions, characterised by a reference return period ($T_{r,\,DLS}$).

At the ULS, the structure is required to maintain integrity and residual load-bearing capacity, avoiding brittle or unstable collapse mechanisms. At the DLS, the verification is displacement-based and focuses on interstorey drift ratios ($d_{r,\,DLS}/h$) with **Eurocode 8 (CEN, 2004a)** providing drift limits of 0.50% for brittle non-structural elements, 0.75% for ductile ones and 1.00% where no infill-frame interaction is expected.

The second generation of **Eurocode 8 (CEN/TS 2024)** introduces a comprehensive and explicit framework for the seismic design of reinforced concrete frames with masonry infills, formally recognising their interaction with

the primary structure. Masonry infills are first classified as interacting or non-interacting, with interacting infills further distinguished as ductile or non-ductile. Infills in direct contact with the frame, in the absence of separation joints, are systematically classified as interacting. Ductile interacting infills and non-interacting infills are required to accommodate frame deformations up to the Significant Damage (SD) limit state, amplified by a drift amplification factor γ_{drift}, accounting for modelling uncertainties. Interstorey drift limits are explicitly prescribed at Operational (OP), Damage Limitation (DL) and SD limit states and depend on masonry typology. For unreinforced masonry infills with clay units in Groups 1-3, drift limits range approximately from 0.15-0.20% at OP, 0.30-0.45% at DL and up to 0.80-1.10% at SD, whereas more restrictive limits apply to Group 4 units. Ductile masonry infills are allowed larger deformation capacities, provided that their performance is demonstrated experimentally. Drift limits are reduced in the presence of openings or combined in-plane and out-of-plane actions. The code explicitly requires consideration of both global and local effects of infill-frame interaction, including stiffness irregularities in plan and elevation and additional shear demand in columns. Regarding the analysis for designing, a hierarchy of approaches is provided, ranging from bare-frame models for regular configurations to linear and nonlinear analyses explicitly modelling the infill-frame interaction. While concentric struts are deemed adequate for global response, local effects such as column shear amplification must be verified through dedicated procedures, marking a decisive shift toward a fully understanding of the importance of masonry infills in structural performance.

Other internation codes, such as **FEMA 356 (2000)** acknowledges that masonry infills can substantially modify the in-plane seismic response of RC frames. According to the code, infills may be modelled through eccentric equivalent struts or using concentric braced frame models. **FEMA 356 (2000)** provides clear qualitative descriptions of the expected damage to unreinforced masonry infill panels at different structural performance levels. At Immediate Occupancy (IO), the infill remains essentially intact, with only minor hairline cracking, typically less than 1/8 inch, and negligible permanent deformation; any spalling is limited to a few isolated corners or openings. As the performance level transitions to Life Safety (LS), the extent of cracking increases and localized crushing may develop, although the wall generally remains in place without loss of units. Panels may experience more pronounced spalling, particularly around stress concentrations, but the integrity is still largely maintained. At the Collapse Prevention (CP) level, the infill

undergoes extensive cracking and crushing with high detachment portions. These qualitative descriptions align with the associated drift limits specified by the standard, which progressively increase from approximately 0.1% at IO to 0.5-0.6% at LS and CP, reflecting the increasing severity of damage and degradation of the panel's load bearing and deformation capacity.

1.2.4.2 Local shear verifications

At the local level, the total shear demand at column ends should be verified against the column shear capacity. The issue is to define the shear demand due to the infill. To this end, **Eurocode 8 (CEN, 2004a)** addresses infill-frame interaction effects by requiring the verification of the shear transfer from the masonry infill to the adjacent frame members over an effective contact length l_c. The additional shear demand induced by the presence of the infill at the critical section of the column, denoted as $V_{d,inf}$, is defined as the lower value between two different terms. The first corresponds to the horizontal component of the resistance of the infill panel ($V^S_{d,inf}$), whereas the second is associated with the development of a flexural plastic mechanism in the column over the contact region ($V^f_{d,inf}$), as follows:

$$V_{d,\mathrm{inf}} = \min\left(V^{s}_{d,\mathrm{inf}}; V^{f}_{d,\mathrm{inf}}\right) \tag{4}$$

Specifically, $V^S_{d,inf}$ is evaluated based on the shear strength of the masonry bed joints f_{v0} acting on the horizontal cross-sectional area of the infill panel, while $V^f_{d,inf}$ is computed by considering the shear corresponding to a double plastic hinge mechanism developing over the contact length l_c which is typically estimated as the vertical projection of the equivalent diagonal strut width w.

Regarding the definition of the contact length, **Eurocode 8 (CEN, 2004a)** prescribes that l_c may be taken equal to the full clear height of the column at ground-floor levels when the infill is in contact with the frame on one side only. In other configurations, alternative formulations are permitted. Accordingly, the classical expression proposed by **Mainstone (1971)**, based on the vertical projection of the equivalent strut width, is also adopted within the code framework.

Similarly, **ASCE/SEI 41-13 (2014)** defines $V^S_{d,inf}$ as an upper bound for the horizontal component of the resistance associated with the equivalent diagonal strut. In this framework, the strut resistance is commonly evaluated based on the

compressive strength of the masonry infill. Consequently, both approaches are primarily aimed at estimating the maximum additional shear demand induced by infill-frame interaction, which can then be conservatively adopted as a design action for the verification of reinforced concrete columns.

On th other hand, when masonry infills are explicitly represented within the structural model, **FEMA 356 (2000)** allows for the a preliminary estimation of the shear demand by applying the forces transmitted by the struts directly to the adjacent frame members. Within this interpretation, the total shear demand acting on a column, $V_{d,tot}$ is obtained by adding to the drift-related shear demand $V_{d,frame}$, an additional contribution arising from the horizontal component of the equivalent strut force. The latter depends on the current axial force developed in the strut N, and on its inclination angle θ.

$$V_{d,tot} = V_{d,frame} + N\cos\theta \tag{5}$$

To facilitate comparison among different approaches, Table 1 summarizes how selected standards account for the local shear demand induced by masonry infills.

Table 1: Standard provisions for the estimation of the additional shear demand $V_{d,inf}$.

Standard	Modelling of the infill	Infill-frame additional shear demand
Eurocode 8 (CEN, 2004a)	Equivalent single-strut macro-model	$V_{d,\text{inf}} = \min\left(V^{s}_{d,\text{inf}}; V^{f}_{d,\text{inf}}\right)^{*}$ $V^{s}_{d,\text{inf}} = A_w f_{v0}$ $V^{f}_{d,\text{inf}}$ shear due to double plastic hinge mechanism for the contact length (l_c) $l_c = \frac{w}{cos\theta}$ or $l_c = \frac{w}{2\cdot cos\theta}$
Eurocode 8 (CEN/TS 2024)	Refined model or Simplified macro-model	Explicit modelled or *
ASCE/SEI 41-13 (2014)	Equivalent single-strut macro-model	$V^{s}_{d,\text{inf}} = A_w f_{v0}$
FEMA 356 (2000)	Equivalent single-strut macro-model	$V_{d,\text{inf}} = N\cos\theta$

1.3 Research motivation and thesis structure

Despite decades of research on masonry-infilled RC frames, a modelling strategy that is both practically applicable and capable of capturing global and local interaction effects is still lacking. Current design codes attempt to condense decades of experimental and numerical evidence into simplified provisions, yet these rules are largely grounded in modelling approaches validated only at the global level. Consequently, they remain unreliable when it comes to predicting local force-transfer mechanisms, especially the additional shear demand induced at column ends. Moreover, existing prescriptions often rely on analytical formulations or experimental observations that assume a fixed contact length, typically evaluated at peak response; this assumption prevents any assessment of how the contact evolution changes with increasing drift and limits the ability to reproduce the progressive activation of strut mechanisms. High-fidelity numerical strategies, such as micro-modelling calibrated against experimental benchmarks, offer a powerful means to overcome these limitations. They can accurately reproduce the global behaviour of infilled frames and provide detailed insight into the evolving stress-transfer mechanisms along the concrete frame, enabling direct evaluation of the internal force distribution. These refined models are computationally demanding and impractical for engineering practice or large-scale analyses; here, they are therefore used as experiment-informed benchmarks. In engineering practice, infills are commonly idealised through simplified equivalent-strut representations, which reproduce initial stiffness but fail to capture the localisation of stresses and the actual mechanics of frame-infill interaction. This mismatch between the accuracy obtainable from high-fidelity models and the simplicity required in engineering practice creates a significant research gap, one that currently limits the development of reliable, codifiable procedures for both global assessment and local demand prediction in masonry-infilled RC frames.

This thesis addresses this gap through a multiscale modelling framework that links refined numerical simulations, physical insights, and simplified predictive models into a coherent methodology, as illustrated in Figure 1.8. The research progresses from detailed micro-model characterisation toward simplified, engineering-oriented tools capable of reproducing both global behaviour and local shear-transfer mechanisms with increased reliability and reduced computational cost. This integrated strategy aims to enable more accurate seismic assessment

procedures and to inform the development of improved code provisions for masonry-infilled RC frames.

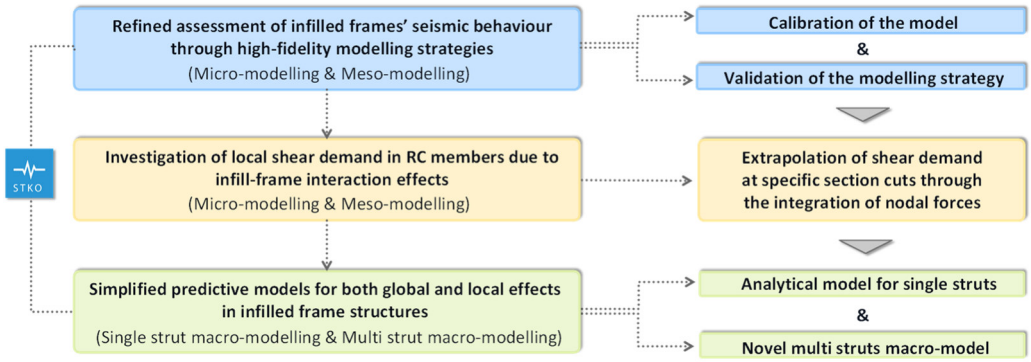

Figure 1.8: Research framework.

The thesis follows a structured progression consistent with this conceptual framework. The reader should not view this as a collection of individual studies, but rather the result of this PhD research on the topic.

Chapter 2 establishes the background for this research through a critical literature review. It examines the global and local effects of infill-frame interaction, the evolution of modelling strategies proposed in the literature, and the main limitations that continue to hinder reliable seismic assessment of infilled RC frames. The chapter highlights unsolved issues, particularly the inadequate representation of local interaction mechanisms, that motivate the adoption of a multiscale modelling approach.

Chapter 3 introduces the high-fidelity micro-modelling framework developed in STKO/OpenSees to simulate the seismic behaviour of masonry-infilled RC frames. The chapter describes the modelling assumptions, constitutive laws and calibration procedures used to replicate benchmark experiments. Calibration is not pursued solely for accuracy, but to enable the extraction of physically meaningful response-parameters that cannot be obtained experimentally. These experiment-informed digital replicas, indeed, form the methodological foundation of the thesis, enabling the investigation of both global response and local interaction mechanisms. Particular attention is dedicated to the extraction of internal shear forces through *section-cut* analyses, which provide quantitative evidence of shear amplification at column ends.

Chapter 4 extends the refined modelling framework to cyclic in-plane loading. The micro-models are validated against full-scale experimental specimens tested within the ERIES-ENFRAG project at EUCENTRE. The simulations accurately reproduce the global response and damage evolution observed experimentally, allowing the identification of representative damage states.

Chapter 5 marks the transition from refined numerical analysis to simplified predictive modelling. This chapter introduces the first simplified predictive tool developed in this research: an analytical correction model that enhances the reliability of the conventional single-strut macro-model on the local response. The proposed formulation estimates the additional shear demand at column ends as a function of geometric parameters and the axial force in the equivalent strut. The model represents a practical strategy for incorporating local interaction effects in simplified models.

Chapter 6 presents a second simplified modelling approach: a novel multi-strut macro-model. Its configuration is optimised through a genetic algorithm to achieve an improved balance between accurate global response prediction and reliable simulation of local force transfer. Both simplified models are calibrated and validated against the results of the refined micro-models, demonstrating their effectiveness in capturing essential interaction mechanisms with significantly reduced computational effort.

Chapter 7 evaluates the performance of the simplified models under nonlinear dynamic conditions. A three-storey infilled RC building previously tested on a shake table at EUCENTRE within the ISAAC project is numerically reproduced. Following extensive calibration, including sensitivity analyses and GA-based optimisation, the refined model serves as a benchmark for assessing the accuracy of simplified strategies under realistic seismic excitation. The results confirm the ability of both simplified models to predict peak shear demands and key response features even under dynamic loading.

In the Conclusions, the key findings are summarised, with a focus on the significant advancements offered by this multiscale approach. Future research developments are also discussed, providing guidance for further investigation and progression in this field of study.

Chapter 2

Modelling strategies for the In-Plane behaviour of infilled frames: State of the Art

A wide range of modelling strategies is available for masonry infilled RC frames subjected to in-plane seismic actions, and their adoption largely depends on the specific objectives of the study as well as on the associated computational cost. Additionally, the complex infill-frame interaction remains an open issue in the existing literature. While the global response of infilled frames is often governed by the stiffness and strength contributions provided by the masonry panels, local interaction phenomena play a crucial role in determining the internal forces transferred from the infill to the surrounding RC columns, which is particularly relevant for the seismic assessment and safety verification of existing structures. Capturing both aspects within a modelling approach represents a central challenge in the numerical analysis of infilled structures.

The modelling approaches proposed in the literature range from highly detailed micro-models to simplified equivalent macro-models, differing in their assumptions, level of discretisation, and target response quantities. Micro-modelling strategies explicitly represent the micro-mechanical interactions between the infill and the surrounding frame, allowing an accurate reproduction of complex local phenomena (**Karavelić et al., 2019; Sinaie et al., 2018**). However, common practice or computationally demanding simulations cannot incur the high computational costs associated with such an approach. For this reason, macro-modelling strategies are more commonly adopted, particularly when the primary interest lies in capturing the global structural response (**Vamvatsikos and Fragiadakis, 2010; De Risi et al., 2017**). Despite their efficiency, these models generally lack a robust formulation to account for local interaction effects, such as the amplification of internal forces in RC frame members induced by infill-frame

interaction. Consequently, the predictive capability strongly depends on the adopted modelling assumptions. Models calibrated to reproduce global force-displacement behaviour may fail to capture local demand concentrations, whereas formulations capable of representing both global and local effects are typically too refined to be feasible for large-scale analyses.

Within this background, the purpose of this chapter is to review the modelling strategies developed for the in-plane behaviour of masonry infilled RC frames, providing a structured overview of existing approaches across different levels of modelling detail. The review encompasses micro-, meso-, and macro-modelling strategies, which are examined with respect to their assumptions and predictive capabilities. Micro- and meso-modelling approaches are first discussed. Subsequently, macro-modelling strategies are analysed in detail, with particular attention to equivalent strut formulations, constitutive model, and multi-strut configurations. Additionally, this chapter includes the open issue of representing local infill-frame interaction effects within simplified modelling approaches. Therefore, the critical analysis presented herein aims at identifying the main limitations of existing strategies and presenting the research gaps that motivate the modelling approaches developed in this thesis.

2.1 Review methodology

Masonry-infilled RC frames have been extensively investigated over the past six decades. Nevertheless, the existing body of literature remains fragmented and does not yet provide a fully conclusive framework. Therefore, this chapter presents a methodology-oriented state of the art on modelling strategies for the in-plane behaviour of masonry-infilled RC frames. Rather than aiming at a systematic literature review, the purpose of this study is to identify and organise the main modelling approaches adopted in the literature, highlighting their level of detail, principle implementations, and capability to reproduce both global and local response.

To this end, a targeted and selective review of the literature was carried out, with the objective of capturing the most representative and influential contributions within the field. The literature survey was conducted primarily using Scopus as the main bibliographic database. The search activity was guided by a set of keywords closely related to the scope of the chapter, including combinations of terms such as *“masonry infilled frames”*, *“in-plane behaviour”*, *“micro-modelling”*, *“meso-modelling”*, *“macro-modelling”*, *“equivalent strut”*, and *“infill-frame*

interaction", along with their common variants. The search was restricted to the engineering domain to exclude contributions not directly relevant to the structural modelling of infilled frames.

The collected literature was subsequently screened and interpreted, focusing on relevant studies proposing modelling frameworks, numerical implementations, or validation against experimental evidence. Contributions dealing exclusively with out-of-plane response were not considered, as this aspect lies outside the scope of the thesis.

Overall, this review provides a focused state of the art and supports a comparative interpretation of the different approaches, with particular attention to their ability to capture local infill-frame interaction effects within simplified models.

2.2 Classification of Modelling Strategies for the In-Plane Response of Masonry-Infilled RC Frames

The analysis of the selected literature highlights that, despite the large variety of formulations proposed over the last six decades, the modelling strategies for the in-plane response of masonry-infilled reinforced concrete (RC) frames can be consistently grouped into a limited number of conceptual categories. These categories mainly differ in terms of modelling resolution, computational demand, physical hypotheses, and capability to capture global and local interaction mechanisms between the frame and the infill.

At the highest level of refinement, two-dimensional (2D) or three-dimensional (3D) finite element (FE) modelling strategies explicitly represent both the reinforced concrete (RC) frame and the masonry infill as continuum elements. Depending on the degree of discretisation adopted for the masonry panel, these approaches are commonly classified into meso-modelling and micro-modelling strategies.
In meso-modelling approaches, masonry is treated as an equivalent homogenised continuum, and such models are employed either within a linear elastic framework or through fully nonlinear constitutive formulations (**D'Ayala et al., 2009; Fiore et al., 2012; Riccardo R Milanesi et al., 2018**). These strategies allow an efficient representation of the global in-plane response while retaining a simplified description of masonry damage mechanisms. Micro-modelling strategies, on the other hand, explicitly reproduce the heterogeneous nature of masonry and are

generally regarded as benchmark solutions (**Lotfi and Shing, 1994; Mehrabi and Shing, 1997; Al-Chaar et al., 2008; Stavridis and Shing, 2010; Koutromanos et al., 2011; Nasiri and Liu, 2017; Di Trapani et al., 2018**). Although these approaches provide a highly accurate description of both global behaviour and local infill-frame interaction mechanisms, their application is typically limited by the substantial computational cost and modelling effort required.

A second category comprises hybrid modelling approaches, in which the masonry infill is discretised using two-dimensional elements, while the surrounding RC frame is represented by one-dimensional beam-column elements (**Doudoumis, 2007; Cavaleri and Di Trapani, 2015**). This strategy, employing elastic or nonlinear models, aim to achieve a compromise between accuracy and computational efficiency, enabling a refined simulation of infill behaviour and damage evolution while preserving a simplified representation of the frame response.

Other modelling strategies fall within the domain of macro-modelling approaches, which represent the infill panel through equivalent strut systems. Single-strut models, elastic or nonlinear, idealise the infill contribution by means of a single diagonal element and are primarily intended to reproduce the global stiffness and strength increase induced by the presence of masonry. Within this group, different formulations can be distinguished depending on the adopted constitutive law for the equivalent strut, including mono-mechanism, multi-mechanism, and data-driven calibrated models (**Fardis and Panagiotakos, 1997; Dolšek and Fajfar, 2008; Cavaleri and Di Trapani, 2014; De Risi et al., 2018; Di Trapani et al., 2018; Liberatore et al., 2018**). Conversely, multi-strut models (elastic or nonlinear) employ a system of diagonal and off-diagonal struts to represent the infill panel, allowing a more realistic simulation of load transfer mechanisms and, in some cases, an improved estimation of local interaction effects, such as shear demand amplification at column ends (**Chrysostomou et al., 2002; El-Dakhakhni et al., 2003; Crisafulli and Carr, 2007; Roosta and Liu, 2022**).

The proposed classification, schematically illustrated in Figure 2.1, provides a method for interpreting the wide spectrum of modelling approaches available in the literature. It also clarifies the positioning of the modelling strategies adopted and developed in this thesis, which are discussed in detail in the subsequent chapters.

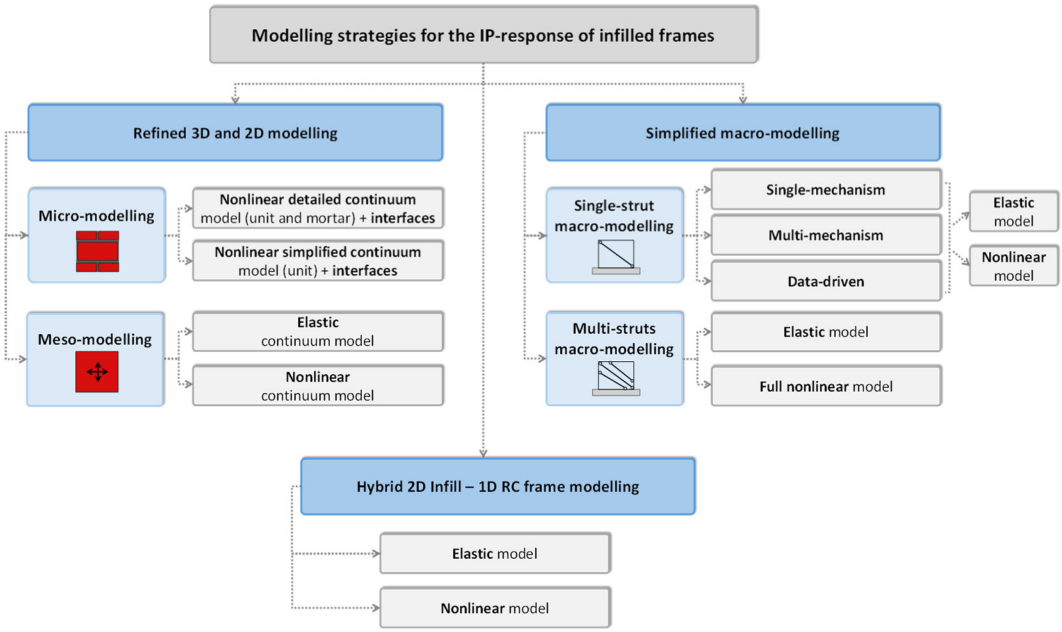

Figure 2.1: Classification of the main modelling strategies for masonry infilled RC frames under IP loading.

2.3 Micro- and meso- modelling strategies

Micro- and meso-modelling strategies represent advanced numerical approaches developed to investigate the seismic behaviour of masonry-infilled RC frames with a high level of detail. Due to their intrinsic modelling complexity and significant computational demand, these approaches are generally unsuitable for engineering applications. Nevertheless, they play a fundamental role in research-oriented studies as complementary tools to experimental testing, providing detailed insight into internal mechanisms and response quantities that are difficult or impossible to directly measure in laboratory experiments (**Campione et al., 2015**). Moreover, the increasing availability of parallel computing resources has recently fostered a wider adoption of micro- and meso-modelling techniques.

Depending on the level of discretisation adopted, micro-modelling strategies can be subdivided into detailed micro-modelling and simplified micro-modelling, which mainly differ in the representation of masonry components. In detailed micro-modelling, masonry is described as an assemblage of units and mortar layers, both discretised as continuum elements and interacting through contact interfaces. On the other hand, in simplified micro-modelling strategies, masonry units are generally modelled as expanded continuum elements, while mortar joints are replaced by zero-thickness interface elements.

Meso-modelling strategies represent a further conceptual and computational simplification with respect to micro-modelling approaches. In this case, the discrete nature of masonry is no longer explicitly represented. Instead, the brick-mortar assemblage is idealised as an equivalent homogeneous continuum, governed by constitutive laws calibrated to reproduce the average mechanical behaviour of masonry panels. The main objective of meso-modelling is to preserve the essential features of infill behaviour, such as stiffness contribution, strength, cracking, and crushing, while avoiding the complexity associated with the explicit modelling of individual units, joints, and interfaces. A schematic comparison between detailed micro-modelling, simplified micro-modelling, and meso-modelling strategies is illustrated in Figure 2.2.

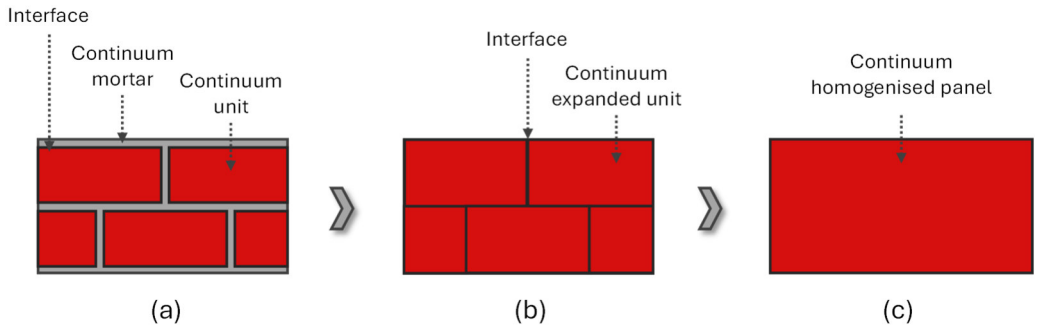

Figure 2.2: Schematic representation of masonry modelling strategies: (a) Detailed micro-model; (b) Simplified micro-model; (c) Meso-model.

Within this framework, the following sections review the main micro- and meso-modelling approaches proposed in the literature, outlining their fundamental assumptions, modelling techniques, and most relevant outcomes.

2.3.1 Detailed and simplified micro-modelling strategies

Early developments in micro-modelling of masonry-infilled RC frames were driven by the need to understand the complex infill-frame interaction mechanism. A decisive step in the implementation of micro-modelling strategies was provided by **Lotfi and Shing (1994)**, who proposed a mechanically grounded formulation in which masonry units were represented by continuum elements, while mortar joints were explicitly modelled through interface elements. A plasticity-based constitutive model for dilatant interfaces was developed by the authors, capable of reproducing mixed tension-shear and compression-shear fracture, joint dilatancy, and progressive strength degradation. The interface formulation, based on a hyperbolic yield surface smoothly transitioning between Mohr-Coulomb and tension cut-off

criteria, incorporated non-associated flow rules and softening laws governed by fracture energy (Figure 2.3). This formulation provided a physically consistent representation of mortar joint behaviour, including shear dilatation and frictional degradation, and was successfully validated against experimental results.

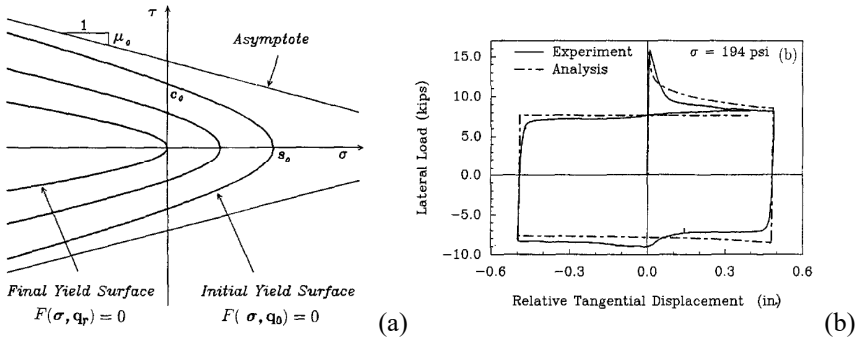

Figure 2.3: Mortar interfaces modelling according to **Lofti and Shing (1994)** (a) Hyperbolic yield criterion; (b) Comparison between experimental and numerical direct shear test on brick-bed joints.

In addition, the interface formulation was coupled with a smeared crack approach to account for tensile cracking and compressive damage in masonry units. The pre-cracking response of masonry units was described by a von Mises plasticity model with associated flow rule and isotropic hardening/softening, while crack onset was detected through a Rankine tensile cut-off criterion. After cracking, the material response was governed by a rotating smeared crack model, ensuring a consistent representation of tensile and compressive behaviour (Figure 2.4).

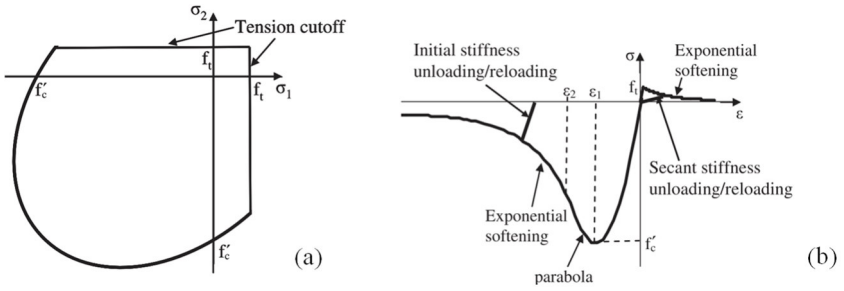

Figure 2.4: Constitutive model adopted for masonry unit implemented by **Lofti and Shing (1991)**: (a) Yield criterion; (b) Uniaxial response in both tension and compression.
(Source for figure: **Koutromanos et al. 2011**).

The results showed that the proposed modelling strategy was able to satisfactorily reproduce the initial stiffness, peak strength, and damage patterns of

the system, while it was not capable of capturing the post-peak softening behaviour. Following the development of interface plasticity models for masonry joints, subsequent work focused on integrating these formulations into numerical representations. In this context, **Mehrabi and Shing (1997)** proposed a comprehensive FE model in which both the RC members and the masonry units were described through smeared-crack continuum elements, whereas mortar joints and frame-infill contacts were explicitly represented by interface elements governed by an improved dilatant constitutive law. They introduced specific refinements to capture cyclic interface phenomena (e.g., compressive hardening, reversibility of dilatancy and normal contraction under sliding) and investigated the role of steel-concrete bond-slip on stiffness degradation and failure mechanisms. The numerical simulations showed good agreement with full-scale experimental tests in terms of peak strength and dominant failure mechanisms, while bond-slip formulations do not affect the overall response of infilled RC frames (Figure 2.5).

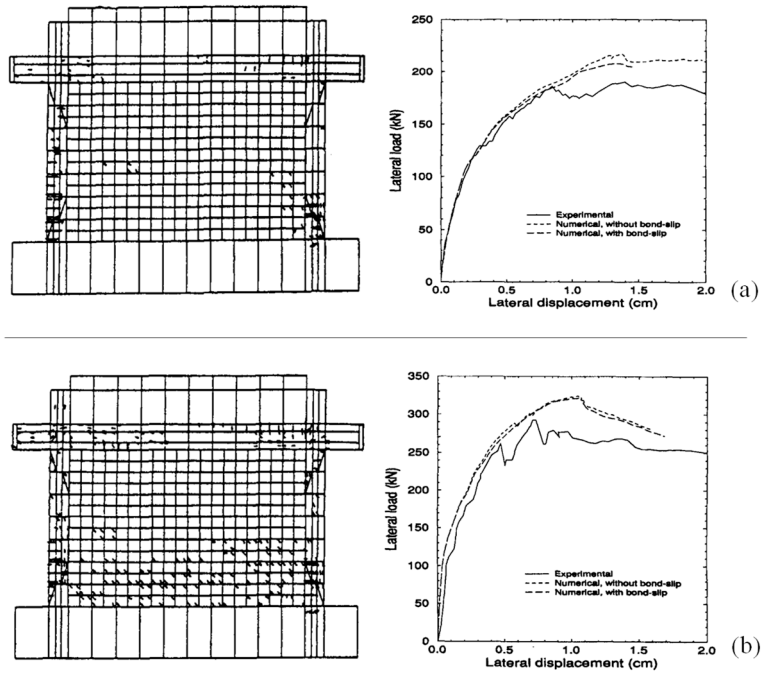

Figure 2.5: Results from **Mehrabi and Shing (1997)** in terms of crack pattern and force-displacement curves: (a) Specimen S8; (b) Specimen S9.

Subsequently, the growing availability of commercial finite element software enabled the broader application of micro-modelling approaches. In this context, **Al-Chaar et al. (2008)** developed a micro-model combining rotating smeared crack continuum elements for masonry and concrete with interface formulations,

implemented within the FE code DIANA and validated against experimental evidence. The model was first calibrated using masonry prism tests and a weak-infill frame, characterised by joint shear and sliding failure, and then applied to a strong-infill configuration. Although the proposed strategy was able to satisfactorily reproduce strength and failure mechanisms, it showed limitations in capturing shear failure in RC columns when relying solely on smeared crack approach, which led the authors to introduce interface elements at critical regions to reproduce shear cracking and overall capacity more accurately. In this regard, a significant methodological advance was introduced by **Stavridis and Shing (2010)**, who proposed a combined smeared-discrete crack modelling framework aimed at overcoming the stress-locking deficiencies of traditional smeared crack approaches. Reinforced concrete members were discretised using triangular smeared crack elements interconnected by zero-thickness interface elements, allowing discrete shear and flexural cracks to develop (Figure 2.6a). Masonry infill panels were modelled using continuum elements for units and cohesive interface elements for mortar joints, enabling the simulation of sliding, diagonal cracking and compressive crushing (Figure 2.6b). The constitutive formulation adopted for the smeared continuum elements was based on the model proposed by **Lotfi and Shing (1991)**.

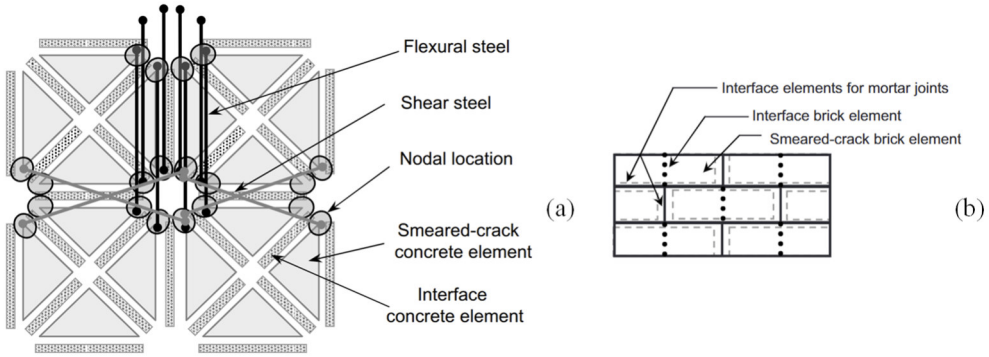

Figure 2.6: Modelling assumptions for the infilled RC frame according to **Stavridis et al. (2010)**: (a) Column FE discretisation; (b) Masonry panel FE discretisation.

With such a methodology, the authors were able to successfully reproduce experimental load-displacement responses, crack patterns and failure mechanisms, as shown in Figure 2.7.

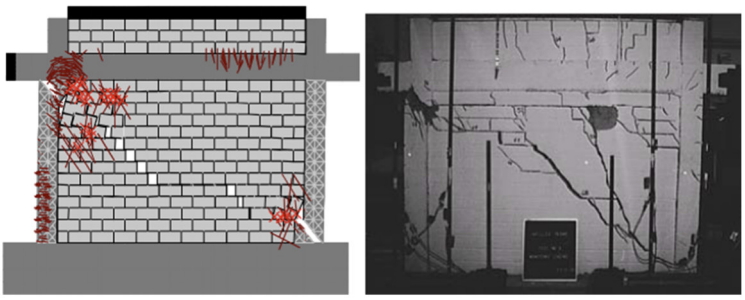

Figure 2.7: Comparison between experimental and numerical crack pattern (**Stavridis et al., 2010**).

This scheme was further extended by **Koutromanos et al. (2011)**, who demonstrated its capabilities with respect to cyclic loading. By coupling discrete cohesive interfaces with smeared crack continuum elements, the proposed approach achieved accurate simulation of cyclic response, including strength degradation and hysteretic behaviour, in both quasi-static and dynamic analyses. Applications to shake-table tests confirmed the capability of the model to capture cumulative damage effects, failure mechanisms and overall response quantities, although with substantial computational effort (Figure 2.8).

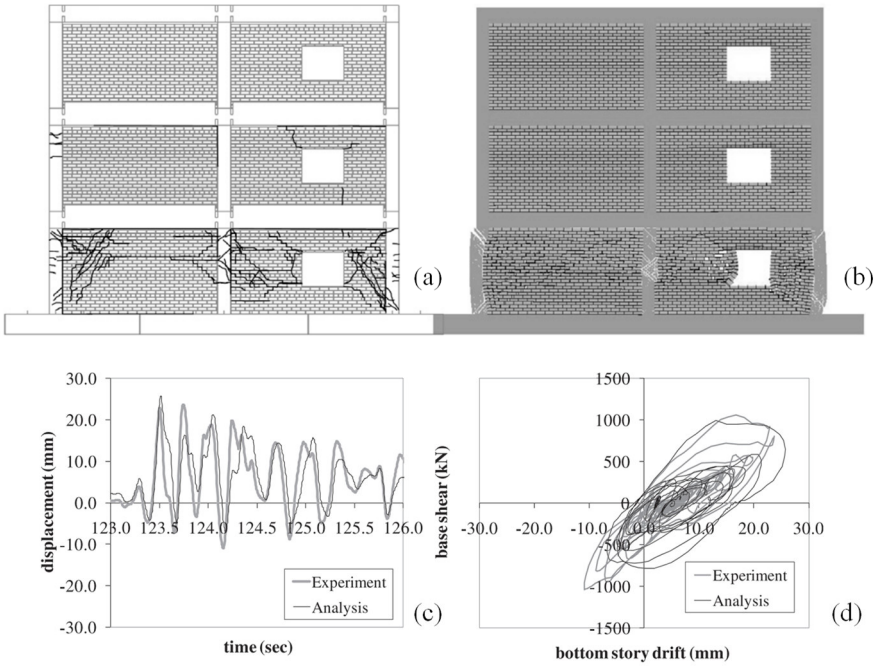

Figure 2.8: Comparison between experimental and numerical response (**Koutromanos et al., 2010**): (a) Experimental cracks; (b) Numerical cracks; (c) Bottom storey drift time-history; (d) Base shear-bottom storey drift hysteretic curves.

Despite the high accuracy achieved by combined smeared-discrete crack formulations, their substantial computational burden has limited their applicability to extensive parametric studies and 3D analyses. Within this context, an alternative class of micro-modelling strategies has emerged based on damage-plasticity formulations for masonry units and concrete frame, most notably the Concrete Damage Plasticity (CDP) model implemented in commercial finite element software such as ABAQUS and ATENA. In this model, the nonlinear behaviour of concrete and masonry units is described through a unified continuum formulation in which plasticity and damage are coupled. The total strain is decomposed into elastic and plastic components, while stiffness degradation is governed by isotropic damage variables acting on the elastic stiffness tensor. Two independent scalar damage variables are introduced to distinguish tensile cracking and compressive crushing, allowing different degradation paths in tension and compression. Plasticity is defined in the effective stress space through a pressure-dependent Drucker-Prager yield surface (Figure 2.9a), with isotropic hardening variables controlling the evolution of strength in tension and compression (Figure 2.9b). A non-associated flow rule is adopted, enabling independent control of volumetric dilatancy. In this framework, cracking and crushing are treated as progressive damage processes, resulting in a continuous degradation of stiffness and strength.

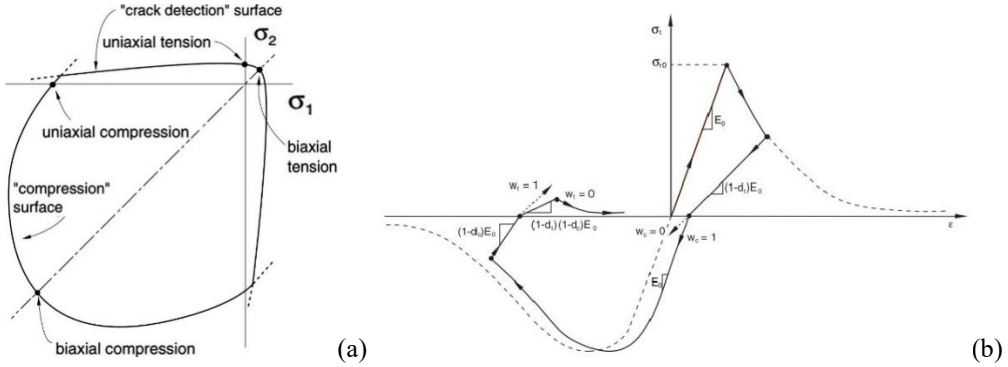

Figure 2.9: Concrete Damage Plasticity model (CDP) adopted for masonry unit and RC frame: (a) Drucker-Prager yield criterion; (b) Uniaxial response in both tension and compression. (Source for figure: **Nasiri et al. 2017**)

In this background, an application of such model is given by **Nasiri and Liu, (2017)**, who employed a simplified micro-modelling strategy in which both masonry units and reinforced concrete members were represented by solid continuum elements governed by the CDP model, while mortar joints were replaced by zero-thickness interface elements. The study demonstrated that the CDP formulation is capable of capturing the in-plane response of masonry-infilled RC

frames with satisfactory accuracy (Figure 2.10). Moreover, a sensitivity analysis was carried out on the interface element parameters governing strength, energy dissipation, and dilatancy. The results highlighted that the characteristics of the failure surface and the dilatation angle play a dominant role in controlling stiffness, peak resistance, and both pre- and post-peak response.

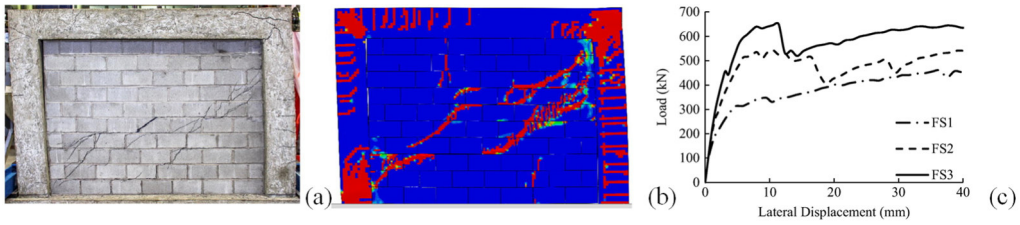

Figure 2.10: Comparison between experimental and numerical response (**Nasiri et al., 2017**): (a) Experimental cracks; (b) Numerical cracks; (c) Influence of the variation of the interface failure surfaces parameters on the specimen global response.

A similar approach guided the study of **Di Trapani et al. (2018)**, who employed refined finite element models based on damage-plasticity formulations as numerical benchmarks to derive stress-strain relationships for equivalent macro-models. Their analyses showed a close correspondence between numerical crack patterns and experimental observations (Figure 2.11), supporting the use of CDP-based micro-models as reliable tools for parametric studies and calibration of simplified modelling strategies.

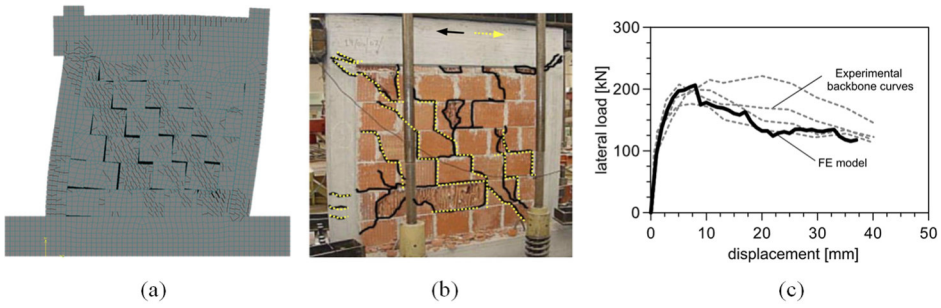

Figure 2.11: Comparison between experimental and numerical response (**Di Trapani et al., 2018**): (a) Numerical cracks; (b) Experimental cracks; (c) Numerical and experimental backbone curves comparison.

More recently, and consistently with the aforementioned developments, the availability of high-performance computational resources and parallel computing has significantly fostered the use of micro-modelling techniques. These approaches are increasingly adopted not as stand-alone predictive tools, but rather as complementary instruments to experimental investigations, enabling the analysis of

response quantities that are difficult or impossible to measure directly in laboratory tests. In addition, micro-models are often employed to enrich existing experimental datasets and to explore the influence of modelling or material parameters beyond those investigated experimentally (**Anić et al., 2021; Penava et al., 2016; Wali et al., 2026**). In this context, refined numerical simulations frequently serve as high-fidelity benchmarks for the interpretation of experimental results and for the development and validation of subsequent simplified modelling strategies.

2.3.2 Meso-modelling strategies and investigation on local effects

Meso-modelling strategies were introduced to reduce the computational cost of refined micro-models while still retaining an explicit representation of the infill-frame interaction mechanisms. In these approaches, the masonry panel is typically described as an equivalent homogenised continuum, whereas the interaction with the RC members is governed through contact/interface formulations that allow progressive detachment, re-contact and frictional sliding.

Beyond reproducing the global lateral response, meso-models have often been employed to investigate local effects induced by the activation of the diagonal compression field, such as the amplification of shear forces and bending moments in critical frame sections (beam and column ends), and the evolution of the effective contact length along the panel perimeter. Within this perspective, **D'Ayala et al. (2009)**, **Fiore et al. (2012)**, and **Milanesi et al. (2018)** adopted conceptually similar numerical frameworks: the RC frame and the infill were discretised with two-dimensional continuum (shell/plate or plane-stress) elements, while the frame-infill interface was represented by unilateral contact components, implemented either as contact elements or as compression-only truss/interface elements, capable of transferring compression and shear through friction and allowing separation when tensile stresses develop. The main differences among these studies concern the chosen constitutive description for the continuum (from simplified smeared laws to rotating crack/total strain crack models) and the level of refinement used for the interface (e.g., explicit frictional laws and tensile cut-off), rather than the overall modelling philosophy. The numerical results consistently indicate that meso-level representations are able to satisfactorily reproduce the global response and the progression of damage when diagonal shear mechanisms dominate the infill behaviour. In these conditions, the homogenised description of the masonry panel is adequate, as the structural response is governed by the formation and evolution of a diagonal compression field. Conversely, failure modes involving significant sliding along unit-mortar interfaces cannot be explicitly captured within a meso-

modelling framework; in such cases, meso-models may lead to inaccurate predictions of both global response and local force demands. In the studies reviewed herein, the expected and experimentally observed failure mode was diagonal shear cracking of the infill, for which the numerical models showed good agreement with test results (Figure 2.12).

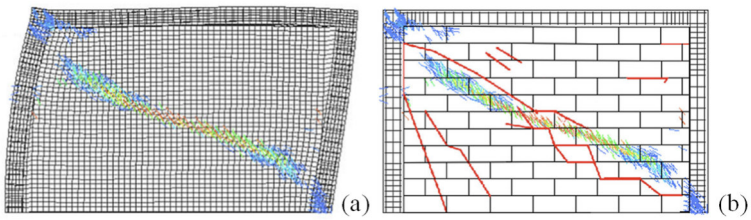

Figure 2.12: Comparison between experimental and numerical response (**Milanesi et al., 2018**): (a) Experimental cracks; (b) Numerical cracks.

Accordingly, this approach can be regarded as reliable tools for estimating local response quantities, such as concentrated shear and bending demands in frame members, that are difficult or impossible to measure directly in experimental investigations. **D'Ayala et al. (2009)** demonstrated that contact-driven infill-frame interaction can significantly alter the internal force distribution within the reinforced concrete frame. In particular, the activation of compressive contact between the masonry panel and the surrounding members induces pronounced concentrations of shear demand at the ends of the columns, in correspondence with the effective contact length between infill and frame (Figure 2.13).

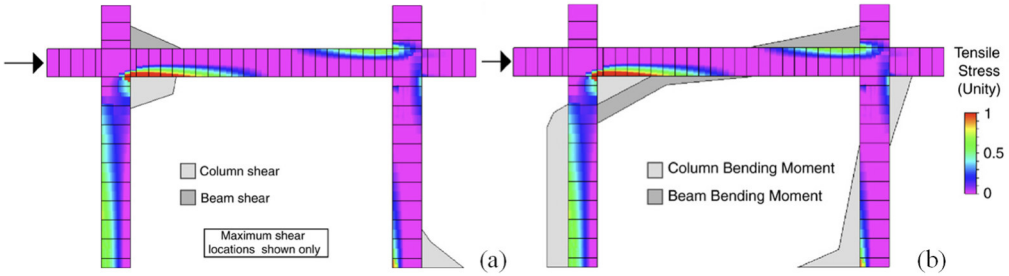

Figure 2.13: Internal forces distribution along the RC frame in infilled frames (**D'Ayala et al., 2009**): (a) Shear diagram; (b) Bending moment diagram.

Fiore et al. (2012) reached a similar conclusion by explicitly tracking the distribution of interface forces: while global displacements were only mildly affected by interface friction, the position and magnitude of the resulting contact forces, especially along the columns, varied markedly, with direct implications for

local shear and moment demands. **Milanesi et al. (2018)**, by combining a plane-stress continuum discretisation with a rotating-crack formulation and frictional interface elements, further confirmed that meso-models can reproduce the characteristic diagonal strut development and provide a reliable approximation of the increased shear actions transferred to the RC members with respect to the bare frame (Figure 2.14), while maintaining a computational effort substantially lower than that of detailed micro-models. These findings provide numerical confirmation of earlier analytical observations by **Saneinejad and Hobbs (1995)**, highlighting the critical role of masonry panels and infill-frame contact conditions in governing local force amplification mechanisms.

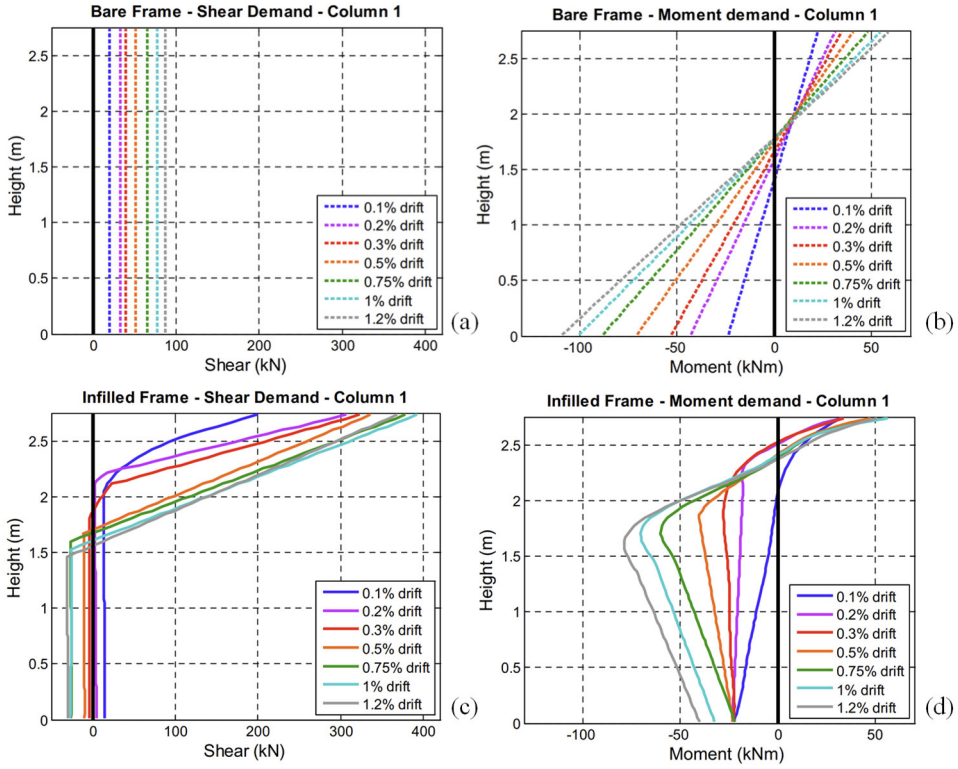

Figure 2.14: Comparison between bare frame and infilled frame internal forces distribution along windward column at different drift levels (**Milanesi et al., 2018**): (a) Bare frame shear demand; (b) Bare frame moment demand; (c) Infilled frame shear demand; (d) Infilled frame moment demand.

2.4 Hybrid FE modelling strategies

Hybrid strategies group together modelling frameworks in which different idealisations are combined within the same numerical model to achieve a

favourable balance between accuracy and computational cost. In this sense, "hybrid" does not identify a single, unique discretisation choice, but rather a broader philosophy: retain refined descriptions only where they are most influential (e.g., for capturing contact, stress concentrations, or stiffness contributions), while adopting simpler elements elsewhere to speed up the analysis. A representative example of this family is the 1D+2D hybrid FE approach, where the RC frame is modelled with 1D beam-column elements and the infill panel is represented through 2D continuum/shell (or plane-stress) elements, with an infill-frame interface formulation to allow separation, re-contact, and (when included) frictional transfer.

Within this hybrid perspective, **Mallick and Severn (1967)** represent one of the earliest attempts to combine different element families in a single model, adopting shell elements for the infill and beam elements for the frame to quantify the stiffening effect provided by masonry in one-storey, one-bay frames. A different hybrid strategy was proposed by **Papia (1988)** through a coupled FEM-BEM procedure, in which the frame is discretised with finite elements whereas the infill is represented via boundary elements (Figure 2.15).

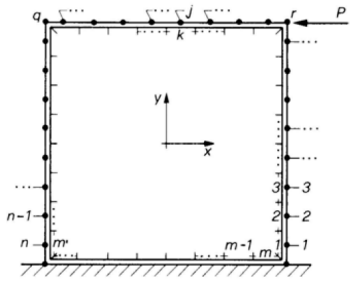

Figure 2.15: Infilled RC frame FEM-BEM model according to **Papia (1988)**.

In this case, the interaction between the two substructures is transferred through distributed boundary stresses for the panel and equivalent nodal forces for the frame, enabling an iterative simulation of partial separation when tensile interface stresses would otherwise occur. The author also extended the procedure to infills with openings, providing estimates of stiffness reduction as a function of opening size. Subsequent hybrid developments emphasised the need for a more explicit and mechanically consistent representation of the infill-frame interface. **Doudoumis (2007)** addressed the interface problem by enforcing unilateral contact combined with Coulomb friction law, modelling the interaction through frictional gap/contact-link elements placed along the frame-infill boundary. The study showed that the assumed interface law can strongly influence both global stiffness

and stress concentrations, highlighting the limitations of excessively simplified fixed-support interface assumptions.

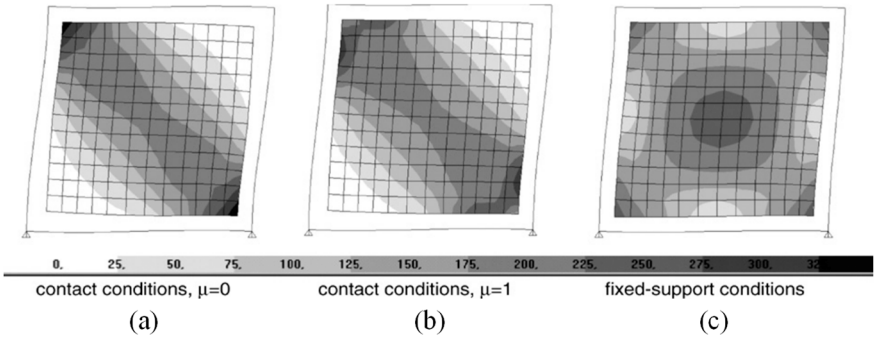

Figure 2.16: Von Mises stress distribution for different interface conditions (**Doudoumis, 2007**).

More recently, **Cavaleri and Di Trapani (2015)** employed a 1D+2D hybrid FE model as a tool to evaluate local response measures that are not accessible with equivalent-strut macro-models alone. In their model, the infill is discretised using (orthotropic) shell elements, connected to the beam-column frame through compression-only interface links that can reproduce detachment and transfer of normal forces (Figure 2.17).

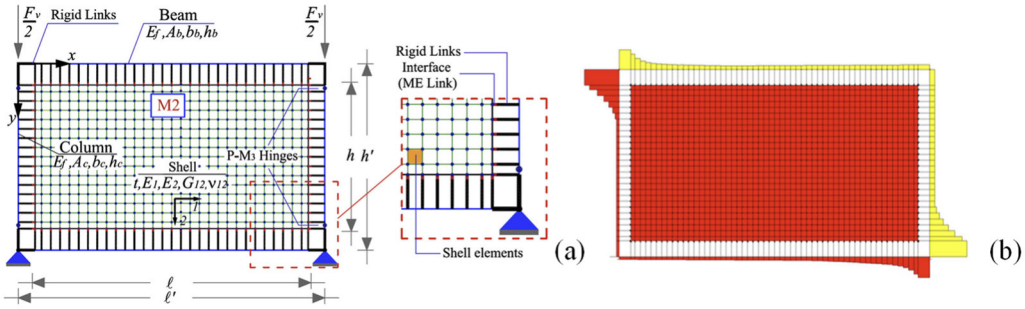

Figure 2.17: Infilled RC frame modelling proposed by **Cavaleri and Di Trapani (2015)**: (a) Modelling assumptions; (b) Shear diagram along the RC frame.

2.5 Macro-modelling strategies

Despite the availability of high-performance computing and the proven effectiveness of micro- and meso-modelling approaches, simplified modelling strategies remain the favoured choice for engineering applications and large-scale structural analyses. These approaches aim to reproduce the contribution of masonry infills to the structural response by preserving their overall stiffness and strength through one or more equivalent diagonal struts (single- or multi-struts). The main

idea is the idealisation of the masonry infill panel through one or more equivalent strut, replicating the compression mechanism developed in the infill panels when subjected to lateral loading. Although the apparent simplicity of this idealisation, macro-models encompass a wide range of formulations that differ in terms of geometric assumptions, constitutive descriptions, and ability to represent stiffness and cyclic degradation. To this end, this section provide an overview of the main macro-modelling strategies developed in the literature for the in-plane response of masonry-infilled RC frames, considering both single- and multi-strut macro-model configurations.

2.5.1 Single strut macro-model

Single-strut macro-modelling constitutes the most established strategy for representing the in-plane contribution of masonry infill panels in reinforced concrete frames. Within this framework, the definition of the equivalent diagonal strut requires addressing a limited number of key modelling aspects, such as the evaluation of its effective width (w), the formulation of a nonlinear backbone curve, and the definition of constitutive laws capable of reproducing the cyclic response under seismic loading. A general scheme of the single-strut macro-model idealisation is provided in Figure 2.18.

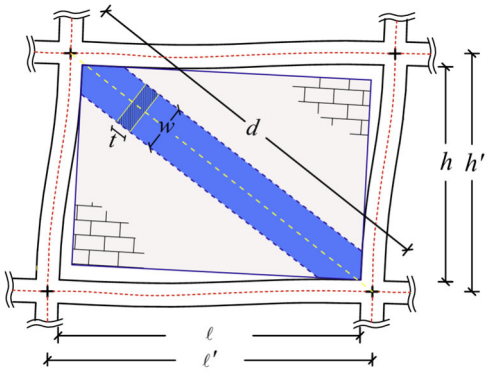

Figure 2.18: Geometrical definition of a single-strut macro-model.

2.5.1.1 Effective width of the equivalent diagonal strut

Within the single-strut macro-modelling framework, the definition of the effective width of the equivalent diagonal strut represents a central modelling issue, as it directly governs the axial stiffness assigned to the infill contribution and, consequently, the in-plane response of the infilled frame. The earliest formulations proposed in the literature define the strut width as a constant portion of the infill

diagonal length, derived from experimental observations on infilled frames subjected to lateral loading. A well-known example is the empirical rule introduced by **Holmes (1961)**, according to which the effective width w is taken as one third of the diagonal length (d). Similarly, **Moghaddam and Dowling (1988)** proposed to estimate the effective width as one sixth of the diagonal length, while **Paulay and Priestley (1992)** as a one fourth. Later, some researchers have demonstrated that constant-width assumptions are unable to capture the influence of the relative stiffness between the infill panel and the surrounding frame, which plays a key role in the development of contact regions and compression fields within the masonry. On this basis, a second class of formulations relates the effective strut width to a dimensionless parameter ($\lambda h'$) accounting for the relative stiffness of the infill-frame system. This approach was initially introduced by **Smith (1966)** and further developed by **Mainstone, (1971, 1974)**, who proposed empirical relationships linking the ratio between the strut width and the diagonal length to a stiffness parameter incorporating the elastic properties of masonry and concrete as well as the geometric characteristics of the frame. Variants and extensions of this formulation were subsequently proposed to account for different frame geometries and boundary conditions (**Stafford Smith and Carter, 1969**; **Liauw and Kwan, 1984; Decanini and Fantin, 1986; Durrani and Luo, 1994; Turguay et al. 2014**).

More refined stiffness-based formulations were later introduced to incorporate additional aspects of the infill-frame interaction. In particular, **Papia et al. (2003)** proposed a procedure in which the effective width w is obtained by enforcing equivalence between the initial stiffness of a FEM-BEM numerical model and that of the simplified strut representation. This approach explicitly accounts for the elastic properties of masonry along the diagonal direction, leading to a numerically evaluated w/d ratio expressed as an analytical fitting function of the equivalent stiffness parameter (λ^*) introduced by the authors. This approach was further extended by **Asteris et al. (2016)**, who introduced the influence of vertical loads transferred from the frame to the infill on the effective strut stiffness.

For the sake of brevity, some of the most employed expressions proposed in the literature are summarised in a comparative table (Table 2) reporting the reference source, the corresponding formulation for the effective width, and the main parameters involved.

Table 2: Literature formulations for the estimation of the effective width *w*.

(a) Constant width formulations	
Reference	**Effective width *w***
Holmes (1961)	$\frac{w}{d}=\frac{1}{3}$
Moghaddam and Dowling (1988)	$\frac{w}{d}=\frac{1}{6}$
Paulay and Priestley (1992)	$\frac{w}{d}=\frac{1}{4}$
(b) Stiffness-based formulations	
Stafford Smith (1966)	$\frac{w}{d}=f(\lambda h')\qquad \lambda h'=h'\sqrt[4]{\frac{E_i t}{4E_f I_f h}}$
Stafford Smith and Carter (1969)	$\frac{w}{d}=f(\lambda h')\qquad \lambda h'=h'\sqrt[4]{\frac{E_i t\sin(2\theta)}{4E_f I_c h}}$
Liauw and Kwan (1984)	$\frac{w}{d}=\frac{0.95\sin 2\theta}{2\sqrt{\lambda}}\qquad \lambda h'=h'\sqrt[4]{\frac{E_i t\sin(2\theta)}{4E_f I_c h}}$
Decanini and Fantin (1986)	$w=\left(0.01+\frac{0.707}{\lambda}\right)\qquad \lambda h'=h'\sqrt[4]{\frac{E_i t\sin(2\theta)}{4E_f I_c h}}$
Durrani and Luo (1994)	$\frac{w}{d}=0.32\sin^{1.5}(2\theta)\left(\frac{E_i t h'^4}{m E_c I_c h}\right)^{0.1}\qquad m=6\left(1+\frac{6}{\pi}arctg\frac{I_b h'}{I_c \ell'}\right)$
Papia et al. (2003)	$\frac{w}{d}=\frac{c}{z}\frac{1}{(\lambda^*)^\beta}\qquad \lambda^*=\frac{E_d}{E_f}\frac{th'}{A_c}\left(\frac{h'^2}{\ell'^2}+\frac{1}{4}\frac{A_c}{A_b}\frac{\ell'}{h'}\right)$ $c=0,249-0,0116\nu_d+0,567\nu_d^2$ $\beta=0,146-0,0073\nu_d+0,126\nu_d^2$
Turguay et al. (2014)	$\frac{w}{d}=\frac{0.18}{4\sqrt{\lambda}}\qquad \lambda h'=h'\sqrt[4]{\frac{E_i t\sin(2\theta)}{4E_f I_c h}}$
Asteris et al. (2016)	$\frac{w}{d}=\kappa\frac{c}{z}\frac{1}{(\lambda^*)^\beta}\qquad \lambda^*=\frac{E_d}{E_f}\frac{th'}{A_c}\left(\frac{h'^2}{\ell'^2}+\frac{1}{4}\frac{A_c}{A_b}\frac{\ell'}{h'}\right)$ $\kappa=1+(18\lambda^*+200)\varepsilon_v\qquad \varepsilon_v\frac{F_v}{2A_c E_f}$

**Note: the explicit expressions of some formulations are not reported in full due to their complexity or piecewise definition; interested readers are referred to the original sources.*

Parameters involved:
t infill thickness
h infill height
h' frame height
E_i or E_d masonry elastic modulus
E_f concrete elastic modulus
I_f or I_c moment of inertia of the column cross- section
I_b moment of inertia of the beam cross-section
θ strut inclination
A_c cross section area of the column
A_b cross section area of the beam
v_d Poisson coefficient
F_v vertical load on the columns

A comparison of several formulations available in the literature was carried out by **Bouarroudj and Boudaoud (2022)**, who evaluate the effective width formulations in function of the relative stiffness variation, using specimen S9 from the experimental campaign by **Mehrabi et al. (1996)** as a reference case. Their results showed that the different formulations lead to markedly different predictions of the effective width, with discrepancies becoming more pronounced for lower values of relative stiffness, as illustrated in Figure 2.19.

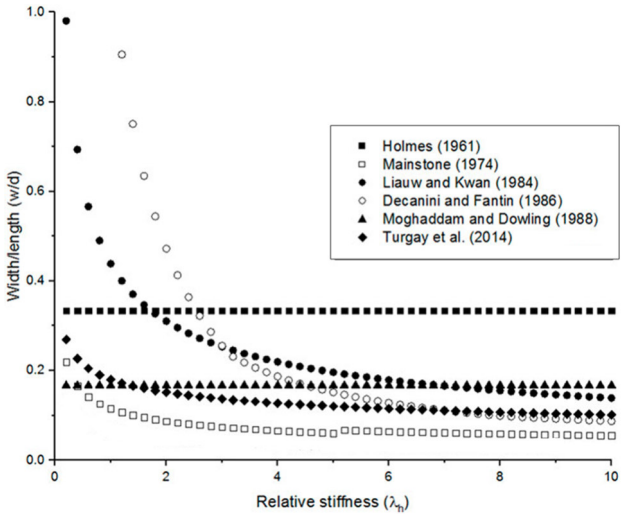

Figure 2.19: Comparison of different equivalent strut width formulations with respect to the relative stiffness variation for the S9 specimen from **Mehrabi et al. (1996)**. Source: **Bouarroudj and Boudaoud (2022)**.

Overall, the wide range of available formulations reflects the absence of a unique and universally accepted expression for the effective strut width. The predicted values of *w* may vary significantly for the same structural configuration, depending on the adopted assumptions.

2.5.1.2 Nonlinear constitutive model for the equivalent strut

The adoption of nonlinear macro-modelling strategies requires the definition of an appropriate constitutive relationship for the equivalent diagonal strut, capable of reproducing the in-plane force-deformation response of the masonry infill under increasing lateral load. Since the equivalent strut represents an idealisation rather than a physical structural member, its nonlinear behaviour cannot be derived directly from material properties, but must instead be inferred from the observed global response of infilled frames subjected to monotonic and cyclic loading (**Klingner and Bertero, 1978; Bertoldi et al., 1993**). In general, nonlinear constitutive models for the equivalent strut are defined through a backbone curve describing the monotonic in-plane response, which is subsequently employed as the envelope for cyclic loading rules. The backbone curve typically includes an initial elastic branch, a peak strength associated with the onset of major damage mechanisms, and a post-peak softening regime that accounts for stiffness and strength degradation. Despite this common structure, significant differences exist among the proposed formulations in terms of the physical assumptions adopted to define the peak strength and the post-peak response.

Based on the modelling philosophy, the backbone curves proposed in the literature for single-strut macro-models can be consistently grouped into three main categories: mono-mechanism models, multi-mechanism models, and empirically or data-driven calibrated models.

Mono-mechanism formulations represent the nonlinear in-plane contribution of masonry infills by assuming that the response of the equivalent diagonal strut is governed by a single prevailing failure mechanism. Within this class of models, the formulation proposed by **Panagiotakos and Fardis (1996)** represents the most established backbone model for masonry infills. In this approach, the in-plane behaviour of the infill is idealised through an equivalent diagonal strut whose nonlinear response is governed by the progressive development of diagonal cracking, assumed to control the global strength and stiffness degradation of the panel. The backbone curve is defined through a linear force-displacement relationship characterised by an initial elastic branch, a yielding point associated

with first cracking of masonry, a peak resistance corresponding to the full activation of the diagonal compression strut, and a descending branch describing post-peak softening. Accordingly, the initial stiffness K_1 is evaluated on the basis of the masonry panel shear modulus G_m, whereas the post-yielding stiffness K_2 is defined as a function of the masonry elastic modulus E_m, as expressed below:

$$K_1 = \frac{G_m t l}{h} \;\; ; \;\; K_2 = \frac{E_m t w}{d} \tag{6}$$

where l and h are the infill length and height, respectively, t is the infill thickness, w is the infill equivalent width, and d is the diagonal length. The stiffness of the softening branch K_3 is assumed within the range $0.005K_1 \leq K_3 \geq 0.1K_1$.

The yielding force S_1 is directly related to the masonry shear strength, according to:

$$S_1 = f_{v0} t l \tag{7}$$

where f_{v0} represents the shear resistance of the infill masonry. The maximum force S_2 is assumed equal to $1.25 \cdot S_1$. The residual force S_3 is assumed to lie within the range $0 \leq S_3 \geq 0.1S_1$.

With reference to the corresponding displacements, the displacement associated with the maximum force S_2 is defined by:

$$\Delta_2 = \Delta_1 + \frac{S_2 - S_1}{K_2} \tag{8}$$

Finally, the displacement corresponding to the residual force Δ_3 is defined according to:

$$\Delta_3 = \Delta_2 + \frac{S_2 - S_3}{K_3} \tag{9}$$

The key limitation of this model lies in the assumption that a single failure mechanism governs the entire nonlinear response. As a consequence, alternative damage modes such as sliding along mortar joints or local crushing at the panel

corners are not explicitly represented. Several subsequent formulations may be interpreted as direct extensions or refinements of the mono-mechanism philosophy introduced by **Panagiotakos and Fardis (1996)**, retaining the assumption of a single governing mechanism while modifying the definition of characteristic points of the backbone curve. The model proposed by **Dolšek and Fajfar (2008)** adopts a trilinear backbone formulation conceptually consistent with the mono-mechanism approach. In this case, the equivalent strut properties are defined with the primary objective of reproducing the influence of masonry infills on the overall capacity and deformation demand of reinforced concrete frames, while the governing failure mode remains implicitly associated with diagonal cracking. Several modifications were implemented. In particular, the maximum force was assumed equal to that proposed by **Žarnić and Gostič (1997)**, the ratio between cracking and maximum forces was revised, the residual strength was neglected, and the displacement parameters were adjusted to improve consistency with experimentally observed structural behaviour.

A further development is represented by the formulation proposed by **De Risi et al. (2018)**.This approach explicitly builds upon the backbone proposed by **Panagiotakos and Fardis (1996)**, but introduces systematic correction factors to the cracking force, peak resistance, and initial stiffness, post-yielding stiffness, and softening stiffness. These corrections are derived from an extensive experimental database and aim to reduce the tendency of the original mono-mechanism formulation to overestimate strength and stiffness under cyclic loading conditions. Although the model preserves the conceptual simplicity of a single governing mechanism, its parameters are empirically adjusted to enhance robustness and predictive accuracy across a wider range of masonry typologies and frame configurations.

Overall, mono-mechanism backbone formulations offer a simple and efficient representation of the nonlinear in-plane behaviour of masonry infills. However, their inherent assumption of a single dominant failure mechanism restricts their ability to capture the variability of damage patterns observed in experimental tests, especially when multiple mechanisms contribute to strength degradation and post-peak response.

Alternatively, multi-mechanism formulations represent an evolution of the single-strut macro-modelling philosophy by explicitly acknowledging that the in-plane response of masonry infills cannot, in general, be attributed to a single governing failure mechanism. Experimental evidence has consistently shown that

different damage modes, such as diagonal compression, sliding along mortar joints, corner crushing, and diagonal shear cracking, may develop either sequentially or concurrently, depending on the relative properties of the infill and the surrounding frame. Multi-mechanism models aim to reflect this complexity by defining the peak resistance of the equivalent strut as the outcome of multiple failure modes. Among this class of models, the formulation proposed by **Bertoldi et al. (1993)** constitutes a representative and widely cited example of a multi-mechanism backbone model for masonry infills. In this approach, the nonlinear response of the equivalent diagonal strut is governed by the minimum resistance associated with a predefined set of possible failure mechanisms, each characterised by a distinct mechanical interpretation. So that the peak axial force of the equivalent strut is determined as:

$$S_2 = (\sigma_w)_{\min} tw \cos\theta \tag{10}$$

Where σ_w is defined as the minimum stress among those associated with diagonal compression crushing, corner crushing, sliding shear, and diagonal shear failure of the masonry panel. Each resistance is expressed as a function of masonry strength parameters and geometric characteristics of the infill, under the assumption of uniform stress distribution along the equivalent strut. The corresponding formulations are summarised below:

- Infill crushing (at the centre)

$$\sigma_{w1} = \frac{1.16\sigma_{m0} \tan\theta}{k_1 + k_2 \lambda h'} \tag{11}$$

- Corner crushing

$$\sigma_{w2} = \frac{1.12\sigma_{m0} \sin\theta \cos\theta}{k_1 (\lambda h')^{-0.12} + k_2 (\lambda h')^{0.88}} \tag{12}$$

- Sliding along mortar joints

$$\sigma_{w3} = \frac{(1.2\sin\theta + 0.45\cos\theta)u + 0.3\sigma_{m0}}{\frac{k_1}{\lambda h'} + k_2} \tag{13}$$

- Diagonal shear failure

$$\sigma_{w4} = \frac{0.6 f_{v0} + 0.3\sigma_0}{\frac{k_1}{\lambda h'} + k_2} \tag{14}$$

where k_1 and k_2 are calibration coefficients dependent on the dimensionless parameter $\lambda h'$, σ_{m0} denotes the compressive strength of the masonry infill, u represents the sliding resistance of the bed joints, and σ_0 is the average normal stress acting on the panel. The stiffness K_{ms} represents another key parameter in the definition of the backbone constitutive model and is evaluated according to the formulation proposed by **Mainstone (1971)**:

$$K_{ms} = \frac{E_m w t}{d} \cos^2 \theta \tag{15}$$

The main strength of this formulation lies in its explicit mechanical interpretation of the peak resistance, which allows different damage scenarios to be represented within a unified modelling framework. At the same time, the need to evaluate several resistances increases the number of required material parameters and introduces additional sources of uncertainty, particularly when reliable experimental data on masonry properties are not available. Subsequently, **Cavaleri and Di Trapani (2014)** proposed an empirically calibrated nonlinear backbone formulation for the equivalent diagonal strut, specifically aimed at enhancing the agreement between the predicted strength of infilled frames and experimental evidence. The proposed model introduces a new formulation for estimating the peak strength, defined as the superposition of two collapse mechanisms, one associated with the infill panel and the other with the reinforced concrete frame, thereby accounting for infill-frame interaction, at least at the global level. To this end, the authors defined a fictitious strut strength (infill + frame), obtained by modifying an initial estimate of the strut resistance through an empirical amplification factor ω_s, which depends on the relative contribution of the infill to the overall lateral resistance. This factor was calibrated on the basis of experimental observations. Another relevant contribution is provided by **Liberatore et al. (2018)**, who developed regression-based relationships for defining the constitutive parameters of the equivalent strut on the basis of an extensive experimental database. Their approach is founded on the assumption of multiple failure mechanisms;

accordingly, the axial strength used to estimate the peak strut resistance is taken as the minimum among those associated with corner crushing, sliding, diagonal shear failure, and compressive failure. Even though the model preserves the assumption of multi-mechanisms failure modes, correction factors were introduced and calibrated against the experimental dataset through regression analysis to mitigate the underestimation inherent in this idealised assumption.

Alternative strategies employed pure data-driven approach, deriving the nonlinear response of the equivalent diagonal strut primarily from experimental and/or numerical evidence. In these approaches, the shape and parameters of the backbone curve are obtained through regression analyses, statistical fitting, or calibration against large experimental datasets, with the objective of reproducing the overall in-plane global behaviour of masonry-infilled frames rather than a specific physical failure mechanism. Unlike mechanically grounded models, the infill response is described through simplified force-displacement or stress-strain relationships whose parameters are calibrated to match observed global behaviour. A well-established model within this category is the macro-model proposed by **Di Trapani et al. (2018)**, which adopts a distributed plasticity approach based on nonlinear fiber-section force-based beam-column elements for the RC frame, coupled with a truss element with fiber section for the equivalent diagonal strut governed by a nonlinear constitutive law. The equivalent strut stress-strain relationship is derived directly from experimental and numerical evidence. According to the authors, the nonlinear axial response of the equivalent strut is characterised by four fundamental stress-strain parameters: the peak compressive stress f_{md0}, the corresponding strain ε_{md0}, the ultimate (post-peak) stress f_{mdu}, and the ultimate strain ε_{mdu}. Through calibration based on extensive experimental data and numerical parametric analyses, four dimensionless correlation parameters were identified as representative of the infill-frame mechanical behaviour, as defined below:

$$\alpha = \frac{\tilde{f}_m^{\,2} \cdot w \cdot t}{\left(f_{vm} + \mu\sigma_n\right)^{0.2} \left(l/h\right) \cdot \lambda^{*0.2}}; \quad \beta = \frac{f_{md0}^{\,0.7} \cdot w \cdot t}{\tilde{E}_m^{\,0.2} d}$$

$$\gamma = \left(\frac{f_{mdu}^{\,2}}{f_{md0}}\right)\left(\frac{E_c}{\tilde{E}_m^{\,1.5}}\right); \quad \delta = \tilde{E}_m^{\,0.20} \cdot \varepsilon_{md0} \tag{16}$$

These parameters depend on both the geometric and mechanical properties of the infilled frame. In particular, they are functions of the conventional masonry compressive strength, defined as the square of the product of the compressive strengths in the two principal directions ($\tilde{f}_m = \sqrt{f_{m1} \cdot f_{m2}}$), the conventional masonry elastic modulus ($\tilde{E}_m = \sqrt{E_{m1} \cdot E_{m2}}$), the concrete elastic modulus E_c, the equivalent stiffness parameter λ^* as defined by **Papia et al. (2003)**, the masonry shear resistance f_{vm}, the friction coefficient μ, and the average compressive stress σ_n. The latter is defined as follows:

$$\sigma_n = \frac{F_v}{A_m}\left(\frac{E_{m2}A_m}{2E_cA_c + E_{m2}A_m}\right) \tag{17}$$

where F_v denotes the vertical load transferred to the infill panel, A_c is the concrete cross-sectional area, and $A_m = t \cdot l$ represents the transverse area of the infill. A constant friction coefficient $\mu = 0.7$ is assumed in the formulation. Regression analyses performed on the combined experimental-numerical dataset reveal a clear correlation between the four dimensionless parameters and the normalized stress-strain quantities. The following empirical relationships were derived through least-squares minimization:

$$\begin{aligned} &\frac{f_{md0}}{\tilde{f}_m} = 26.9\alpha^{-0.287}; \quad \frac{f_{mdu}}{f_{md0}} = 0.043\beta - 0.06 \\ &\frac{\varepsilon_{md0}}{\varepsilon_{m0}} = 3.024 \cdot \gamma^{0.347}; \quad \frac{\varepsilon_{mdu}}{\varepsilon_{md0}} = 0.0184 \cdot \delta^{-1.166} \end{aligned} \tag{18}$$

where ε_{m0} denote the reference compressive strength and strain of masonry in compression.

Similar philosophy inspires the work of **Huang (2020)**, who proposed a fully empirical framework for defining the backbone curve parameters of equivalent diagonal struts representing masonry infills. Using an extensive experimental database, the backbone parameters, initial stiffness, yielding, peak strength, residual strength, characteristic deformations, and post-peak stiffness, are treated as independent response variables and related to geometric and material properties of the infilled frame through multivariate regression analysis.

Subsequently, **Di Trapani et al. (2021)** extends and refines the previous data-driven formulations (**Di Trapani et al., 2018**) by proposing a hybrid empirical framework for the identification of the inelastic force-displacement parameters of equivalent diagonal struts. The authors construct a hybrid dataset combining experimental test results and additional numerical data generated through refined finite element micro-models validated against experiments. For each case, the parameters governing the nonlinear backbone of the strut are calibrated iteratively by minimising the discrepancy between numerical predictions and reference force-displacement responses. The resulting dataset is then analysed to derive empirical correlation laws that directly relate the backbone parameters to a reduced set of geometric and mechanical properties of the infilled frame, accounting for aspect ratio, stiffness ratio, masonry strength and strut properties.

Recent studies, including those by **Van et al. (2022)**, **Adibi et al. (2022)**, and **Guettala et al. (2024)**, primarily focus on numerical implementation and validation of empirically calibrated backbone models within commercial or open-source finite element platforms. These works confirm the suitability of empirical formulations for nonlinear seismic assessment, while highlighting the sensitivity of results to backbone calibration and parameter selection.

Overall, data-driven backbone formulations provide a pragmatic alternative to mechanically based mono- and multi-mechanism models. Their main strength lies in their ability to reproduce observed global behaviour with directly observed influence geometrical and/or mechanical parameters.

For clarity and comparison purposes, the backbone formulations most commonly adopted in the literature and discussed in the previous sections are summarised in Figure 2.20 , highlighting their conceptual differences, characteristic parameters, and typical representation of the in-plane nonlinear response of masonry infills.

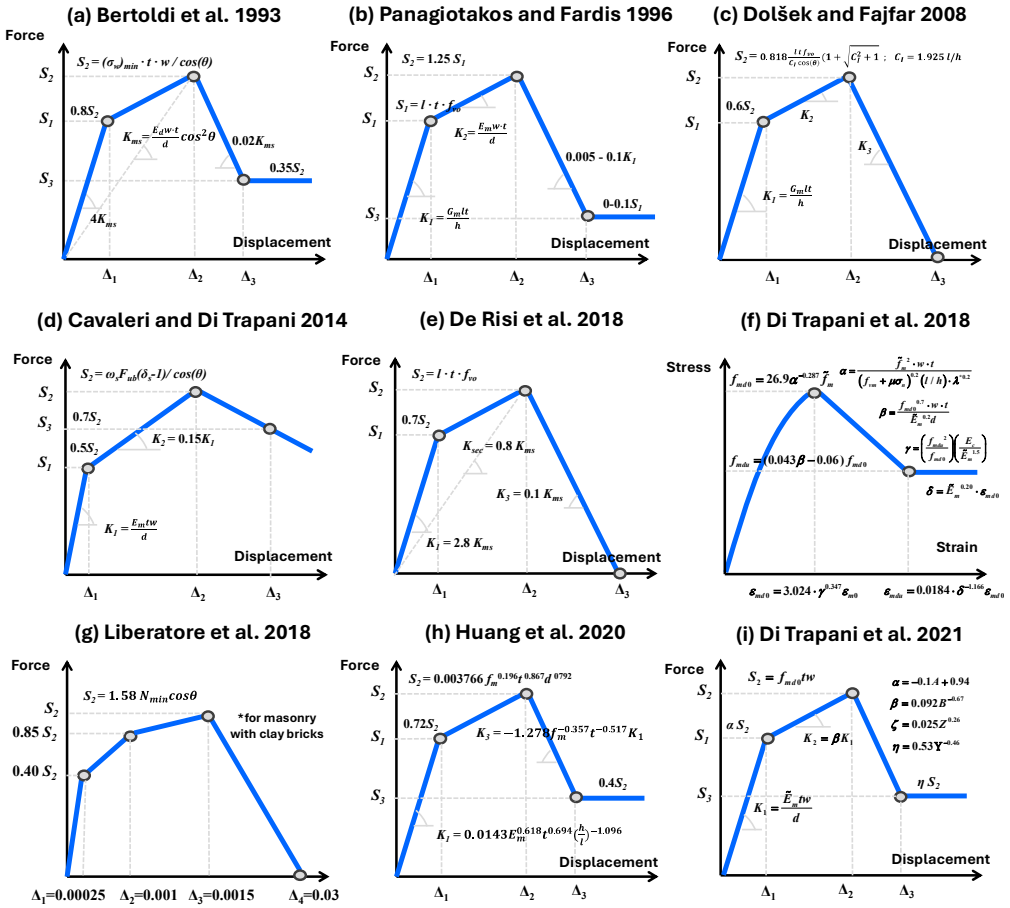

Parameters involved:
S_1, S_2, and S_3 crack, peak, and residual forces
Δ_1, Δ_2, Δ_3 displacements at crack, peak, and residual forces
K_1, K_2, and K_3 tangent stiffness, post-yielding stiffness, and softening stiffness
K_{sec} secant stiffness and K_{ms} stiffness proposed by Mainstone (1971)
l, h, t, length, height, and thickness of the infill panel
w, d, θ effective width, diagonal length and inclination of the equivalent strut
f_m, E_m, G_m, f_{v0} compressive strength, elastic modulus, shear modulus, and shear strength of the masonry panel
δ_s ratio between the ultimate lateral strength of the infilled frame and that of the corresponding bare frame
ω_s correction factor linking the strength contribution of the infill to the global resistance of the bare frame
N_{min} and $(\sigma_w)_{min}$ minimum axial force and minimum compressive stress estimation among the different failure modes

Figure 2.20: Schematic representation of the backbone formulations adopted for the in-plane macro-modelling of masonry-infilled RC frames, including mono-mechanism, multi-mechanism, and data-driven approaches.

A comparative assessment of the predictive reliability of several backbone formulations is provided by **Di Trapani et al. (2021)**, who evaluated the performance of different equivalent strut models against a set of experimental tests. The comparison includes data-driven and mechanics-based formulations, like the formulations proposed by **Di Trapani et al. (2018)**, **Panagiotakos and Fardis**

(1996), **Dolšek and Fajfar (2008)**, and **Bertoldi et al. (1993)**. The results of the comparison are reported in Figure 2.21.

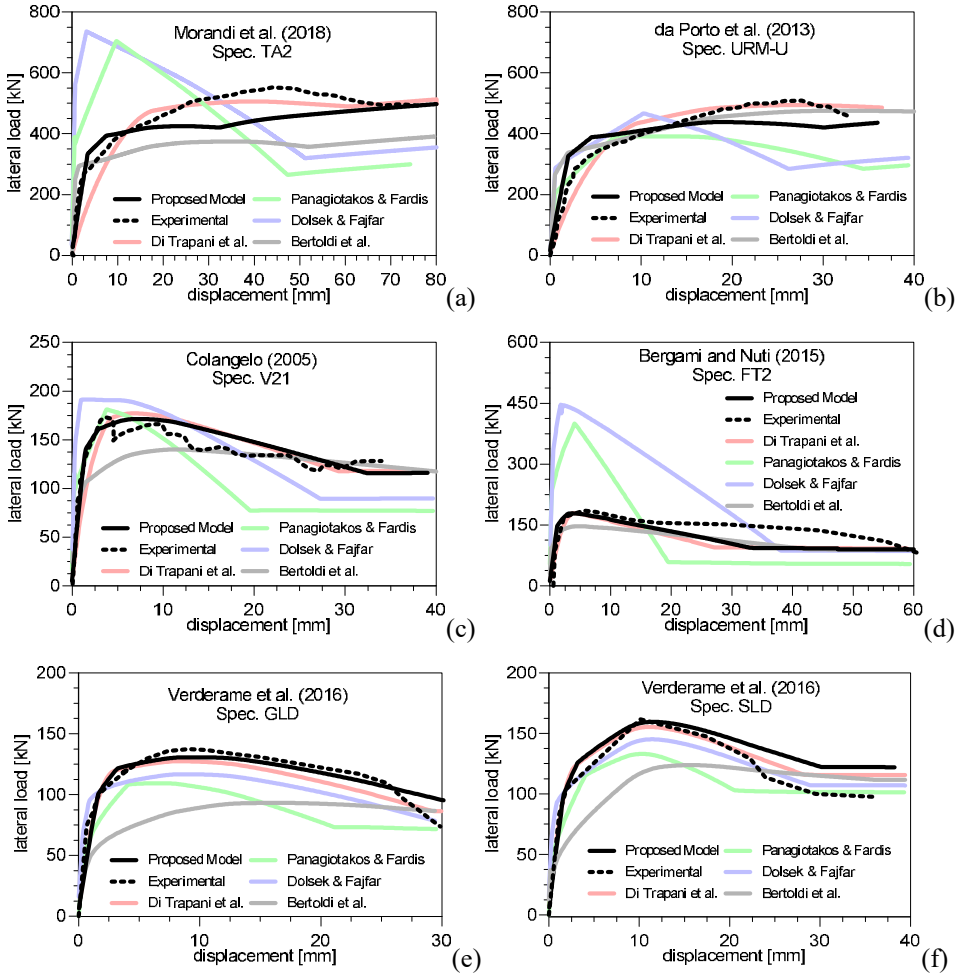

Figure 2.21: Comparison between experimental in-plane responses of masonry-infilled RC frames and numerical predictions obtained using different equivalent diagonal strut backbone formulations (from **Di Trapani et al., 2021**): (a) **Morandi et al. (2018)**; (b) **da Porto et al. (2013)**; (c) **Colangelo et al. (2005)**; (d) **Bergami and Nuti (2015)**; (e) **Verderame et al. (2016a)**; **Verderame et al. (2016b)**.

The outcomes, provided by the author, highlight that the accuracy of each model strongly depends on the test configuration and governing failure mechanism. Data-driven-based models consistently exhibit robust predictive capability across all examined cases, while mono-mechanism formulations based on a single assumed collapse mode tend to overestimate peak strength when alternative mechanisms develop. Multi-mechanism models provide a more reliable estimation of peak resistance, though often at the expense of conservative predictions.

Significant discrepancies are also observed in the post-peak response, with some mechanics-based models amplifying brittle behaviour due to simplified assumptions on ultimate displacement and residual strength.

2.5.1.3 Hysteretic law for the equivalent strut

The models discussed above primarily address the definition of the nonlinear backbone response. Nevertheless, while some of the previously mentioned formulations also provide recommendations for adapting the constitutive law to cyclic loading conditions and have been validated through cyclic analyses, others are limited to the definition of the monotonic envelope calibrated against pushover results only. Given the significant influence of cyclic degradation, pinching, and energy dissipation on the seismic response of infilled frames, an accurate representation of the cyclic behaviour is a crucial aspect that cannot be neglected. Early hysteretic models, such as those originally proposed by **Klingner and Bertero (1978)**, introduced on the basis of experimental outcomes the stiffness degradation which was directly linked to the geometric and mechanical characteristics of the infilled frame. As shown in Figure 2.22, the model represents the equivalent strut as a component with limited strength capacity, however it relied on simplified unloading-reloading rules, typically assuming elastic unloading stiffness and neglecting damage accumulation effects.

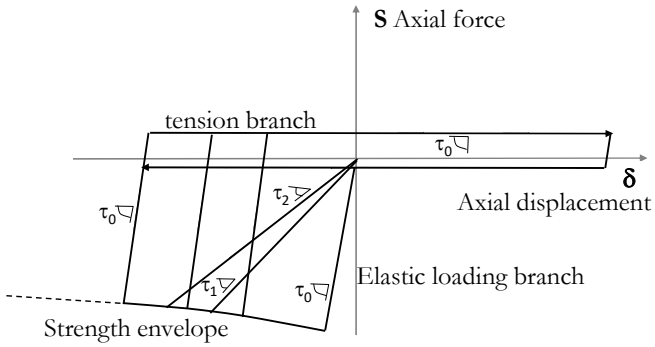

τ_o =angle defining initial stiffness and first branch of unloading curve
τ_i = arctg(S^*/δ^*), reloading angle after peak strength reaching
δ^* = maximum displacement of the cycle;
S^* = strength value on the enveloper curve corresponding to the maximum displacement of the cycle δ^*

Figure 2.22: Cyclic response proposed by **Klingner and Bertero (1978)**.

Subsequent formulations progressively addressed specific shortcomings of the earliest hysteretic models by introducing distinct features. For instance, the model

proposed by **Doudoumis and Mitsopoulou (1986)** focuses on the representation of activation thresholds by assuming that the equivalent strut remains inactive not only in tension but also in compression until a predefined deformation level is reached, as schematically illustrated in Figure 2.23. At the same time, unloading and reloading branches are governed by constant stiffness values and do not explicitly account for cumulative damage effects.

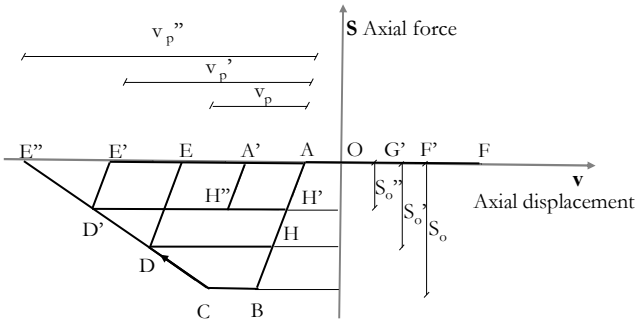

Figure 2.23: Cyclic response proposed by **Doudoumis and Mitsopoulou (1986)**.

The formulation by **Panagiotakos and Fardis (1996)** introduces a cyclic force-displacement constitutive model calibrated on experimental tests of infilled frames, in which stiffness and strength degradation are implicitly embedded in the envelope definition, while reloading paths remain relatively simple and history dependence is limited (Figure 2.24a). A further step is achieved by **Madan et al. (1997)**, who explicitly incorporate strength degradation, stiffness degradation, and pinching effects within a unified hysteretic framework by combining a monotonic envelope with additional constitutive components (Figure 2.24b). In this case, cyclic degradation is explicitly linked to the deformation history, allowing a more realistic reproduction of pinching and energy dissipation at the expense of increased model complexity and parameter calibration effort.

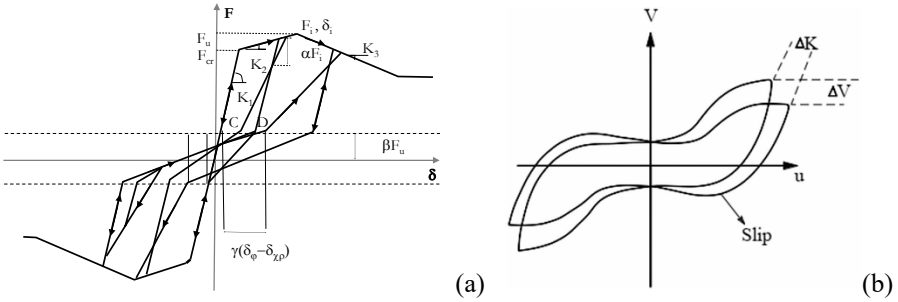

Figure 2.24: Cyclic constitutive model of the equivalent strut: (a) **Panagiotakos and Fardis (1996)**; (b) **Madan et al. (1997)**.

More advanced cyclic formulations were developed by **Crisafulli (1997)**, providing one of the most comprehensive macro-modelling frameworks for masonry-infilled frames. These models explicitly account for multiple failure mechanisms, frictional effects along mortar bed joints, and local contact phenomena between infill and frame through dedicated constitutive components. While this approach offers a physically meaningful representation of the cyclic response, it requires the calibration of a large number of parameters, which may limit its applicability in practical or large-scale analyses. More recently, **Di Trapani et al. (2018)** adopted a simplified yet effective strategy by representing the equivalent diagonal strut through a *fibre section* governed by the *Concrete02* material model in OpenSees, combined with the monotonic envelope curve defined in the previous section. In this formulation, strength degradation is implicitly governed by the envelope, while cyclic stiffness degradation is controlled through the unloading-reloading rules of the material model. In particular, the ratio between loading and unloading stiffness is regulated by the parameter λ, which was calibrated against experimental data. The authors reported good agreement with experimental cyclic responses in terms of global hysteretic behaviour and energy dissipation for a value of $\lambda = 0.08$, demonstrating that a reduced-parameter cyclic model can still capture the essential features of infilled-frame cyclic response.

To sum up, the reviewed cyclic formulations highlight a clear trade-off between physical completeness and modelling efficiency, showing that while highly refined hysteretic models offer an accurate representation of infill-frame seismic response, simplified cyclic laws calibrated on experimental evidence can still provide a reliable description of strength and stiffness degradation and energy dissipation, making them particularly suitable for nonlinear seismic analyses of infilled frames.

2.5.2 Multi struts macro-model

Multi-strut macro-modelling strategies were developed as an evolution of the classical single-strut idealisation, with the specific aim of improving the representation of the in-plane interaction between masonry infills and reinforced concrete frames. While single-strut models are generally adequate for reproducing the global stiffness and strength contribution of infills, they are limited in capturing the local transfer of forces to the surrounding frame members due to the concentric position of the strut. Multi-strut formulations were therefore introduced to overcome these limitations by distributing the infill contribution through multiple equivalent elements, allowing a more realistic representation of internal force demands and frame-infill interaction mechanisms. Despite the diversity of multi-strut approaches proposed in the literature, they share a common modelling philosophy: the infill panel is replaced by a set of axial elements whose number, orientation, and location are chosen to better approximate the actual stress transfer between infill and frame. In practical applications, simplified rules are typically adopted to distribute the overall infill stiffness among the different struts. For instance, in three-strut configurations, it is commonly assumed that approximately 50% of the total infill stiffness is associated with the central strut, while the remaining 50% is equally shared by the two off-diagonal struts. In models employing two diagonal struts, the stiffness is generally divided equally between the two elements, whereas in configurations combining one diagonal and one non-diagonal strut, the diagonal element is often assigned about 75% of the total stiffness.

One of the earliest attempts to move beyond the single-strut idealisation was proposed by **Leuchars and Scrivener (1976)**, who introduced a macro-model combining two diagonal compression struts with a shear spring located at the centre of the infill panel. The shear spring was specifically conceived to reproduce shear-sliding failure along mortar bed joints, thus allowing axial and shear resisting mechanisms of the infill to be represented separately within a simplified framework. This idea of coupling diagonal struts with an explicit shear component influenced several subsequent developments.

A systematic investigation of multi-strut configurations was carried out by **Crisafulli (1997)**, who examined the influence of single-, double-, and triple-strut layouts on the structural response of infilled frames. By comparing macro-model predictions with refined finite element simulations, the study demonstrated that multi-strut schemes provide a significantly improved estimation of bending

moments and shear forces in columns compared to single-strut models. In particular, a triple-strut configuration consisting of one central strut and two off-diagonal struts, with redistributed cross-sectional areas and located at a distance equal to half of the contact length proposed by **Stafford Smith (1966)**, was found to provide the most realistic distribution of internal forces compared to refined FEM models (Figure 2.25).

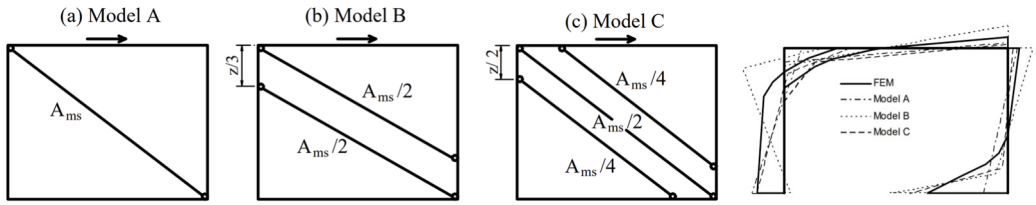

Figure 2.25: Different macro-models together with the associated bending moment diagram compared against refined FE model (**Crisafulli, 1997**).

Building on these findings, **Crisafulli and Carr (2007)** proposed a more advanced multi-strut macro-model designed to balance modelling accuracy and computational efficiency. The authors formulated a four-node panel element in which the masonry infill is represented by two parallel axial struts and a shear spring acting in each loading direction (Figure 2.26c). This configuration allows the compressive and shear responses of the infill panel to be treated separately, while maintaining a clear mechanical interpretation. The shear spring follows a frictional constitutive law, enabling the interaction between vertical compression in the struts and shear resistance along mortar joints to be captured. The spacing of the struts is defined as a function of the infill-frame contact length ($\lambda h'$), originally introduced by **Stafford Smith (1966)**, and the overall stiffness is partitioned between axial and shear components through calibrated coefficients. Although the model remains relatively simple, it represents a substantial improvement in reproducing local interaction effects compared to earlier single-strut approaches.

Alternative multi-strut configurations were proposed with the explicit objective of improving the distribution of internal forces within the surrounding frame. **Chrysostomou et al. (2002)** modelled each infill panel using six compression-only diagonal struts, with three struts activated in each loading direction (Figure 2.26a). This formulation was intended to account for stiffness and strength degradation of the infill while providing a more refined description of local interaction effects. Similarly, **El-Dakhakhni et al. (2003)** proposed a three-strut macro-model consisting of one concentric diagonal strut and two additional off-diagonal struts

positioned at locations corresponding to maximum bending moments in beams and columns (Figure 2.26b).

Further developments pursued to achieve a compromise between modelling refinement and simplicity. **Fiore et al. (2012)**, for instance, proposed a model based on two non-parallel equivalent struts of equal width, whose positions are defined as functions of the infill aspect ratio *l/h* (Figure 2.26d). Validation against refined finite element models demonstrated that an appropriate choice of strut location can significantly enhance the prediction of frame-infill interaction effects without introducing excessive modelling complexity.

More recently, renewed attention has been given to multi-strut macro-models by **Roosta and Liu (2022)**, who developed a multi-struts macro-model explicitly focused on the representation of shear behaviour along mortar bed joints. Their formulation concentrates on three dominant failure mechanisms: frame failure at contact regions, masonry compression failure at the corners or at the panel centre, and shear sliding along mortar joints. The proposed model combines a multi-strut configuration with a dedicated shear spring, retaining the general philosophy of **Crisafulli and Carr (2007)**. However, **Roosta and Liu (2022)** implemented the shear spring in series with the compressive struts, so that the total in-plane displacement of the infill is decomposed into a compressive component along the diagonal struts and a concentrated shear component. In this framework, the infill is represented by six compression-only diagonal struts arranged symmetrically for cyclic loading (Figure 2.26e), with strut areas distributed according to the three-strut principle (**El-Dakhakhni, 2003**). The shear spring is explicitly calibrated from masonry triplet tests under varying levels of pre-compression, enabling bond degradation, frictional sliding, and residual shear resistance to be captured through a tri-linear constitutive law. Implemented in OpenSees, the model demonstrated improved accuracy in reproducing the overall capacity as well as the cyclic response, particularly in cases where shear-sliding failure modes are not negligible compared to other available models, as shown in Figure 2.27.

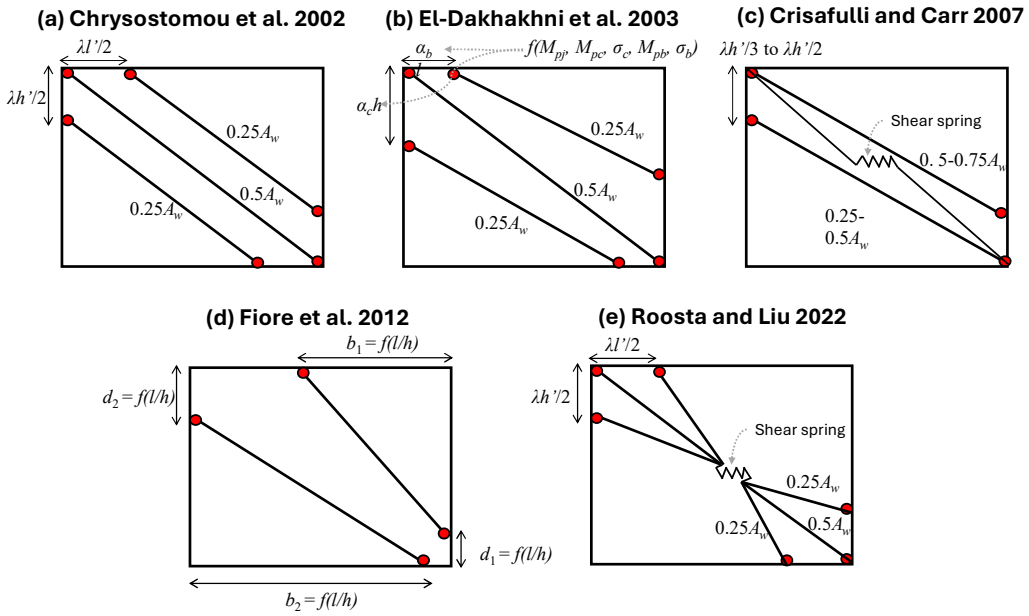

Figure 2.26: Overview of representative multi-strut macro-model configurations for masonry infills, illustrating alternative arrangements of diagonal and off-diagonal struts adopted in the literature.

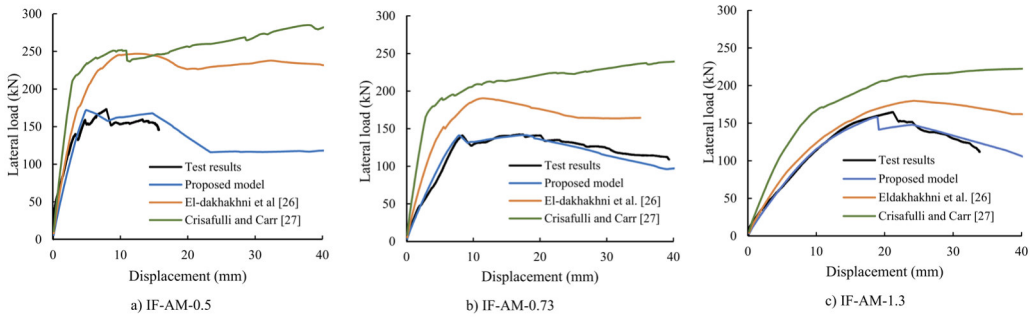

Figure 2.27: Comparison between the global response predicted by available multi-strut macro-models and experimental results for three different specimens (**Roosta and Liu, 2022**): (a) Test 1; (b) Test 2; (c) Test 3.

To conclude, multi-strut macro-models represent a significant improvement over single-strut idealisations in capturing frame-infill interaction. Nevertheless, their validation is often limited to the global structural response, while experimental verification of local shear demands on RC members remains limited or is not provided. Moreover, uncertainties related to strut geometry, positioning, and stiffness distribution persist, so that the choice of a specific formulation still relies largely on modelling objectives and engineering judgement, with no universally accepted approach available.

2.5.3 Local shear-oriented macro-models

As discussed in previous sections, local infill-frame interaction plays a key role in governing the distribution of internal forces in reinforced concrete frames, particularly by inducing significant amplification of the shear demand at column ends. This phenomenon originates from the transfer of compressive forces along the infill-frame contact zones and cannot be adequately reproduced by simplified modelling approaches. Indeed, an accurate quantification of such local effects generally requires refined numerical models, whereas conventional single equivalent strut formulations are inherently unable to capture the complex mechanisms governing frame-infill interaction. This limitation has been recognised in the literature in the last two decades and has motivated the development of several modelling strategies aimed at improving the prediction of local effects while retaining the simplicity of macro-modelling approaches. In this context, some researchers have proposed to preserve the concentric equivalent strut idealisation and explicitly account for local interaction effects through additional corrective terms. Within this framework, **Basha and Kaushik (2018)** suggested combining the traditional concentric strut model with uniform distributed forces (F) applied along the infill-frame contact length (l_c), aimed at reproducing the shear transfer mechanism more realistically. The effective contact length is suggested to be estimated through the **Eurocode 8 (CEN 2004a)** provisions, while force F is assessed by the authors with respects to the crushing strength R_{cr}, thus:

$$R_{cr} = f_m^{'} w \cdot t \tag{19}$$

where $f_m^{'}$ is the masonry compressive strength, w the equivalent width and t the infill thickness. A schematic representation of their approach is illustrated in Figure 2.28.

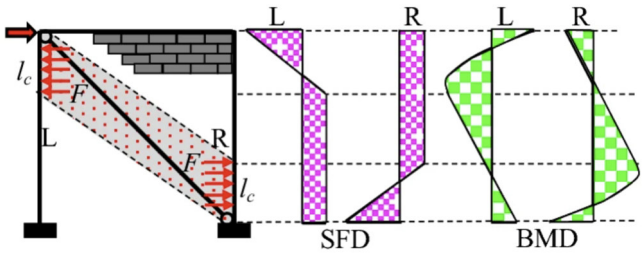

Figure 2.28: Single-strut model for infilled frames proposed by **Basha and Kaushik (2018)** to account for the shear demand amplification together with the shear force diagram (SFD) and the bending moment diagram (BMD).

Similarly, **Wararuksajja et al. (2020)** proposed simplified design equations to estimate the additional shear demand at column ends as a function of the expected infill failure mechanism. This approach considers the formation of a plastic mechanism in the column, which is subjected to a force transferred by the equivalent strut. The actual shear demand acting on the column is estimated based on the governing mechanism, which in turn depends on the relative strength of the column-infill system. Two mechanisms are identified: the first corresponds to a strong column and weak infill configuration (Figure 2.29a), while the second represents a weak column and strong infill configuration (Figure 2.29b).

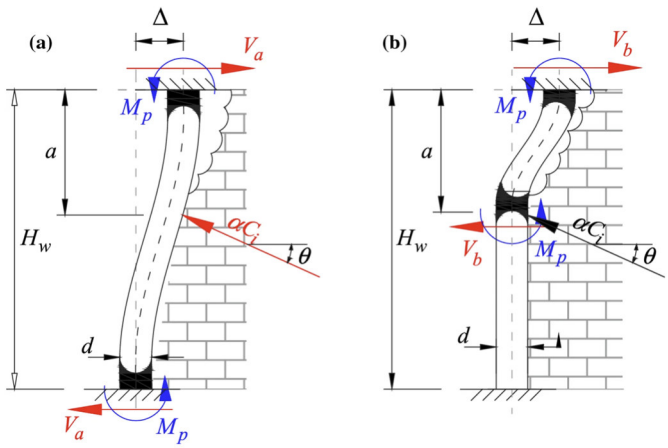

Figure 2.29: Shear demand assessment based on two different failure modes according to **Wararuksajja et al. (2020)**: (a)Strong column-weak infill; (b) Weak column-strong infill.

Accordingly, the additional shear demand is calculated following these two failure modes and the corresponding force-transfer schemes shown in Figure 2.29, thus resulting in two different contribution V_a and V_b, as expressed by the following equations:

$$V_a = \frac{2M_p}{H_w} + \frac{\alpha C_i \cos\theta (H_w - a)}{H_w}$$
$$V_b = \frac{2M_p}{a} \quad (20)$$

here, M_p denotes the plastic moment at the formed plastic hinges, H_w is the column height, C_i represents the compressive force transferred from the infill to the column, α is a reduction factor calibrated by the authors within the range 0.4 - 0.7, a is the distance corresponding to the point of application of the resultant compressive

force, and θ is the inclination of this resultant. The acting shear force is finally taken as the minimum value between the shear demands associated with the two identified mechanisms and is subsequently compared with the shear capacity of the column.

Another approach was proposed by **Cavaleri and Di Trapani (2015)**, who directly formulated the total shear demand at frame members as a function of the axial force acting on the equivalent single strut. In this approach, empirical correlation coefficients α_c are introduced to relate the strut axial force N to the shear demand at both windward and leeward column ends, generally expressed as:

$$V_{d,tot} = \alpha_C N \tag{21}$$

These coefficients are calibrated as a function of the infill aspect ratio and depend on a predictor ψ that incorporates the relative frame-infill stiffness, the beam-to-column flexural strength ratio, and the masonry shear resistance, as follows:

$$\begin{aligned} &\alpha_{CW} = 0.96\psi^{-0.37}; \qquad \alpha_{CL} = 1.03\psi^{-0.35} \quad (\text{if } l/h=1) \\ &\alpha_{CW} = 1.05\psi^{-0.36}; \qquad \alpha_{CL} = 1.08\psi^{-0.30} \quad (\text{if } l/h=2) \end{aligned} \tag{22}$$

The predictor ψ was evaluated as:

$$\psi = \lambda^* \xi^* f_{v0} \tag{23}$$

where ξ^* represents the beam-to-column flexural strength ratio, f_{v0} corresponds to the shear masonry shear strength, and λ^* denotes the infill-frame stiffness. The latter is defined as follows:

$$\lambda^* = \frac{\tilde{E}_m}{E_c}\frac{th'}{A_c}\left(\frac{h'^2}{l'^2} + \frac{1}{4}\frac{A_c}{A_b}\frac{l'}{h'}\right) \tag{24}$$

where A_c, and A_b are the beam and column cross-section areas, E_m is the masonry elastic modulus, E_c is the concrete elastic modulus, t is the infill thickness, and h' and l' represent the dimensions of the frame model.

The predictive capability were assessed through a FE modelling comparison. However, even the formulations proposed by the authors (Equations (21) and (22)) provides a practical tool for estimating local shear amplification, its predictions inherently reflect the assumptions of the reference numerical models adopted for calibration, particularly the neglect of tangential forces at the infill-frame interface.

More recently, **Di Trapani et al. (2018)** proposed a refinement of the **FEMA 356 (2000)** approach by introducing a corrective term to account for the reduction in the infill's lateral force caused by frictional forces between masonry infill and RC beams. In this formulation, the frictional contribution is expressed as a function of the vertical component of the axial force acting on the equivalent strut, assuming a constant friction coefficient μ=0.7. This modification allows a more realistic estimation of the additional shear demand by explicitly considering the role of friction in limiting the force transfer between the infill and the frame.

$$V_{d,tot} = V_{d,frame} + N\cos\theta - \mu N\sin\theta \tag{25}$$

Against this background, **Biondi and Candigliota (2006)** addressed the well-known limitation of the single equivalent strut model in reproducing the internal force distribution in RC members, especially the shear concentration at column ends induced by frame-infill interaction. To retain the simplicity of strut-based macro-modelling while improving the representation of local effects, they proposed an equivalent three-strut scheme composed of one central diagonal strut and two off-diagonal struts. The geometry of the system is not assigned arbitrarily: the mutual widths of the three struts and the position of the lateral struts are derived by enforcing equivalence of the global horizontal stiffness with the corresponding single-strut model, while adopting mechanically consistent assumptions for the location of lateral struts based on the infill-column contact stress distribution (Figure 2.30).

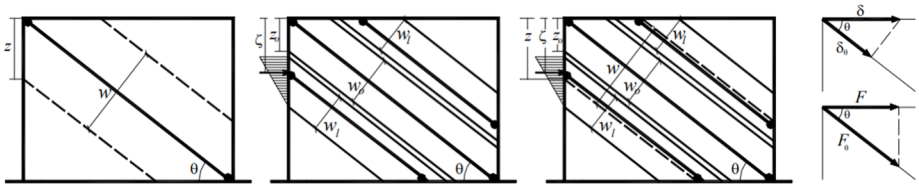

Figure 2.30: Equivalent strut geometry and force-displacement components associated with the lateral strut position (**Biondi and Candigliota, 2006**).

In parallel, the authors calibrated a monotonic nonlinear uniaxial law for the equivalent struts, covering cracking, peak strength, softening and a residual friction-controlled branch, by matching the response of a refined nonlinear FEM model including masonry softening and frictional contact at the interface. Validation through pushover comparisons showed that single- and three-strut models provide similar global force-displacement curves, whereas the three-strut formulation better reproduces the column shear demand distribution predicted by FEM at cracking and peak strength levels, as shown in Figure 2.31.

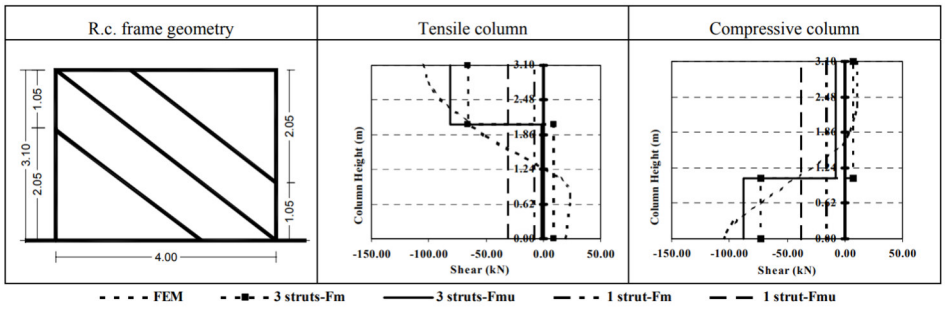

Figure 2.31: Shear forces distribution along the RC columns at peak forces (**Biondi and Candigliota, 2006**).

As emerged from the reviewed literature, no consolidated modelling approach is currently available for reliably estimating the shear demand amplification at column ends induced by infill-frame interaction. Although several simplified formulations based on single equivalent struts have been proposed, they are often derived from analytical assumptions, numerical models, or experimental evidence that have not been sufficiently validated.

Multi-strut macro-models provide a more realistic representation of force transfer mechanisms and generally improve the description of global response. However, they are mostly calibrated to reproduce global stiffness and strength, and a systematic experimental validation of column shear amplification is still lacking. Although some studies, such as **Biondi and Candigliota (2006)**, explicitly address shear distribution, validation against a broad experimental dataset encompassing different failure mechanisms remain unavailable. As a result, the inclusion of the actual local shear demand prediction in simplified macro-models still be regarded as an open research issue.

2.6 Conclusions and future trends

The in-plane behaviour of masonry-infilled RC frames has been the subject of extensive research over the last six decades, owing to its recognised influence on the seismic response of framed structures. A wide spectrum of modelling strategies has been proposed, reflecting the intrinsic complexity of infill-frame interaction and the need to balance accuracy with computational efficiency. This chapter has provided a critical overview of the main modelling approaches available in the literature, with particular emphasis on their capability to reproduce both global structural response and local interaction effects.

Based on the critical review presented in this chapter, the following remarks can be drawn:

- Micro- and meso-modelling approaches represent the closest approximation to the actual mechanics governing infill-frame interaction. They allow a detailed description of stress transfer mechanisms, damage evolution, and local force demands on RC members. However, their practical applicability is limited by high computational burden, modelling complexity, and demanding calibration requirements. Consequently, these approaches are rarely adopted in engineering practice, but they remain essential as benchmark tools for the interpretation of experimental evidence and for the calibration and validation of simplified models.

- Equivalent single-strut macro-modelling constitutes the most practical and widely adopted strategy for representing infill-frame interaction in seismic analyses of RC structures. These models efficiently capture the global stiffness and strength contribution of masonry infills with limited computational effort. Nevertheless, their simplified idealisation generally lacks an explicit and robust representation of local interaction effects, such as the redistribution of internal forces and the amplification of shear demand in RC members.

- The definition of key modelling assumptions in single-strut macro-models, like the effective strut width, the nonlinear backbone curve, or the cyclic constitutive law, remains one of the most debated aspects in the literature. Although several formulations have been proposed and calibrated against experimental data, no unified framework has yet emerged. The predicted response is often highly sensitive to the adopted assumptions, and different models may lead to significantly different estimates even for similar structural configurations.

- Multi-strut macro-models have revealed the potential to overcome single-strut limitation in reproducing the internal force redistribution within the RC frame, particularly in terms of bending moments and shear forces at column ends. However, the definition of strut geometry, positioning, and stiffness distribution is not unique and remains strongly model-dependent. Moreover, most of the available models are validated against global response, while the prediction of shear demand amplification is not yet validated against experimental data.

- Correction formulation for macro-modelling strategies explicitly oriented towards local shear demand estimation have been proposed in recent years. While these approaches represent an important step towards addressing a critical limitation of traditional strut models, they are still largely preliminary. In many cases, they rely on simplified assumptions, and experimental validation remains predominantly focused on global response quantities, whereas systematic verification of local shear demand and force transfer mechanisms to RC members is still limited.

Chapter 3

High-fidelity micro-modelling of infilled frames for the analysis of internal forces in frame members

As highlighted in the previous chapter, frame-infill interaction plays a crucial role in the seismic response of RC buildings, with effects that can be either beneficial or detrimental depending on masonry properties and damage evolution. Infills are also a major source of post-earthquake losses due to their high vulnerability (**De Risi et al., 2019; Del Vecchio et al., 2018**). Their in-plane behaviour is governed by combined global and local mechanisms: the former influence stiffness, strength, ductility and collapse modes **(Dolšek and Fajfar, 2008; Fiore et al., 2012; Cavaleri et al., 2017**); the latter arise when detachment occurs, causing significant shear transfer along the contact interfaces and increased shear forces at column ends, as reported in early analytical and experimental studies (e.g., **Saneinejad and Hobbs, 1995; Buonopane and White, 1999**). These local effects cannot be captured by standard single-strut macro-models due to their concentric position. Although several enhanced macro-models have been proposed, like multi-strut approaches (**Chrysostomou et al., 2002; El-Dakhakhni et al., 2003; Crisafulli and Carr, 2007; Pashaie and Mohammadi, 2019**), distributed-force at contact length strategies (**Basha and Kaushik, 2019**), and failure-based shear demand equation (**Wararuksajja et al., 2020**), their reliability remains sensitive to parameters difficult to quantify experimentally, such as the evolution of contact lengths.

For this reason, high-fidelity micro-modelling provides an essential means for extending the understanding of frame-infill interaction. Building on the research gaps identified in the literature review, this chapter introduces a refined modelling framework developed in STKO/OpenSees (**Petracca et al., 2017a; McKenna et**

al., 2000), in which masonry units, mortar and RC components are represented as continuum elements, and frictional interfaces explicitly reproduce contact conditions between the masonry infill and the RC frame. The models are validated against four experimental tests covering different masonry typologies, ensuring their capability to replicate both global response and local damage mechanisms.

A key feature of this modelling strategy is the possibility to extract physically meaningful internal force distributions in frame members through *section-cuts* integration, information that are otherwise inaccessible from experiments. Using this capability, a parametric study is conducted to investigate how the evolution of contact lengths, damage patterns and masonry mechanical properties govern local shear demand. Emphasis is placed on the role of the strength ratio between masonry units and mortar, which proves to be a key parameter influencing both the failure mechanism and the magnitude of the induced shear forces.

Overall, the chapter provides the validated numerical foundation for the predictive models proposed later in the thesis and offers new insights into how refined micro-modelling can support the interpretation of experimental results and the development of improved infill-aware assessment methods.

The outcomes presented in this chapter have been peer-reviewed and published in:

- Di Trapani, F., *Di Benedetto, M.*, Petracca, M., and Camata, G. (2024). Local infill-frame interaction under seismic loads: Investigation through refined micro-modelling. Engineering Structures, 315, 118088.

3.1 Micro-modelling of masonry-infilled RC frames

In this study, a damage-mechanics-based micro-modelling strategy is adopted to reproduce the inelastic response of mortar, masonry units and reinforced concrete members. Each component is represented by separate continuum elements, enabling the model to localise damage with high accuracy, for example identifying sliding along mortar joints when damage concentrates in the mortar layers, or cracking of the masonry units when it develops within the bricks. The refined 2D continuum models are generated in the STKO environment (**Petracca et al., 2017a**), which provides plastic-damage material models for continuum elements. Figure 3.1 illustrates the overall modelling layout. The following sections describe

in detail the numerical implementation, together with the subsequent calibration and validation processes.

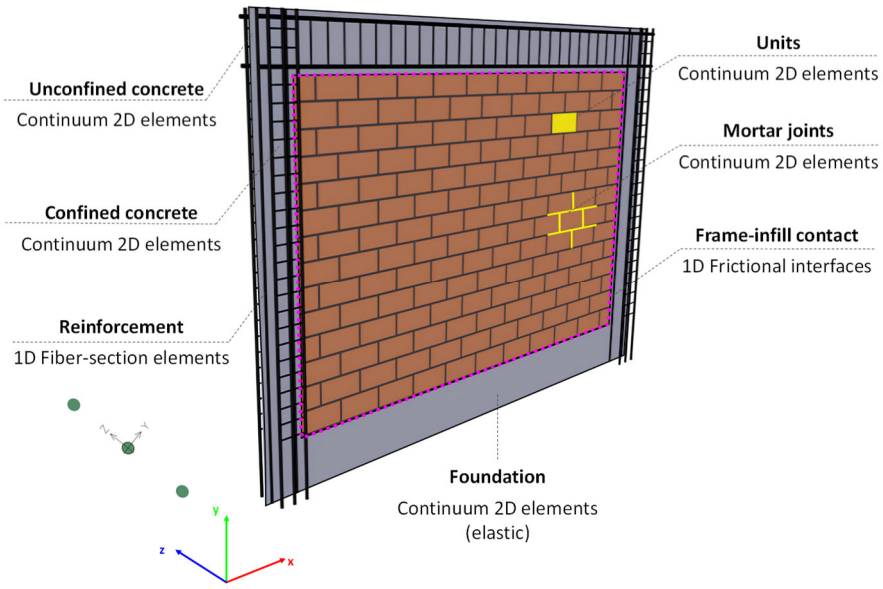

Figure 3.1: High-fidelity 2D micro-model of the masonry infilled RC frame in OpenSees/STKO.

3.1.1 Modelling strategy for RC frames and masonry infills

The RC frames and masonry infills are modelled using 2D nonlinear continuum *quadrilateral* elements, whereas the steel reinforcement is represented through 1D *fiber-section beam-column* elements. The combination of continuum elements for concrete and *fiber-section* elements for rebars enables a distributed-plasticity formulation, since the nonlinear constitutive laws assigned to each fibre allow plastic strains to develop and spread along the member without prescribing plastic hinges a priori. Nonlinear behaviour is integrated along the member length using a *force-based beam-column* formulation (**Spacone et al., 1996**) with Gauss-Lobatto integration points. The latter enforces exact equilibrium between element and section forces, even in the presence of material nonlinearity. Section forces are obtained from the basic element forces through equilibrium-based interpolation, resulting in a constant axial force and a linear bending moment distribution in the absence of distributed loads. Compatibility between section and element deformations is ensured through the Principle of Virtual Forces (PVF).

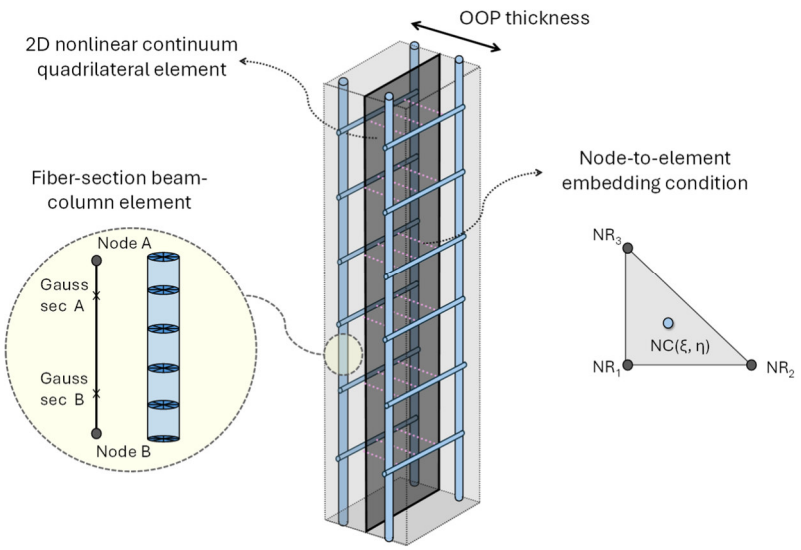

Figure 3.2: Modelling detail of RC frame members.

Steel rebars are embedded within the concrete continuum using the *ASDEmbedding* node-element (**Petracca et al., 2017a**), which implements a node-to-element coupling: steel nodes act as constrained degrees of freedom (*NC*), while the surrounding concrete nodes serve as restrained nodes (NR_i), ensuring full bonding. While this assumption is commonly adopted in nonlinear simulations, it may influence the local response under high shear demand and cyclic loading. In particular, bond-slip mechanisms may lead to stiffness degradation, redistribution of curvature along the RC member, and potential modification of infill-frame contact lengths. Therefore, the results presented in this study should be interpreted considering that possible bond-slip effects are not explicitly captured and further research should be done to investigate its influence. To correctly reproduce the flexural stiffness of the reinforcement, each bar is modelled according to its actual three-dimensional arrangement, preserving its true cross-sectional area (Figure 3.2). The rebars follow an elasto-plastic constitutive law with strain hardening, implemented via the uniaxial *Hysteretic* material model, which also enables the simulation of bar rupture once the ultimate strain is reached.

The masonry infill is represented by modelling masonry units and mortar joints as distinct continuum elements (Figure 3.3).

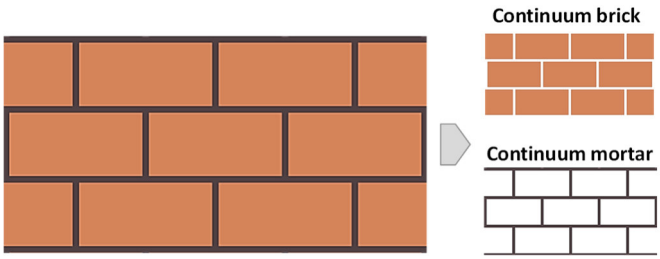

Figure 3.3: Masonry infill continuum micro-modelling.

The nonlinear response of both RC frames and masonry infills is described using the *ASDConcrete3D* constitutive model (**Petracca et al., 2023**), which is based on a continuum plastic-damage mechanics formulation. This new model extends the existing continuum damage framework (**Petracca et al., 2017b**) by introducing plasticity to capture inelastic deformations and improve the description of masonry behaviour under cyclic loading. The latter was introduced by the authors in a simplified way, avoiding internal iterative procedures and preserving the explicit stress-strain update typical of continuum damage models. Additionally, a mixed implicit-explicit integration scheme (**Oliver et al., 2008**) was adopted to increase robustness and numerical stability when dealing with softening behaviour. A detailed description of the constitutive formulation, including the failure surfaces and damage variables, is provided below, as these components represent a fundamental part of the modelling strategy.

In **Petracca et al. (2023)**'s plastic-damage framework, the nominal stress tensor $\boldsymbol{\sigma}$ is described by:

$$\boldsymbol{\sigma} = (1 - d_c^+)\bar{\boldsymbol{\sigma}}^+ + (1 - d_c^-)\bar{\boldsymbol{\sigma}}^- \tag{26}$$

where $\bar{\boldsymbol{\sigma}}^+$ and $\bar{\boldsymbol{\sigma}}^-$ are the positive (tensile) and negative (compressive) parts of the effective stress tensor. The parameters d_c^+ and d_c^- are the tensile and compressive cracking damage indices, which take into consideration stress and stiffness reduction of the effective stress due to crack opening. This formulation allows the model to reproduce the degradation mechanisms associated with cracking in tension and crushing or softening in compression.

The positive and negative parts of the effective stress ($\bar{\boldsymbol{\sigma}} = \bar{\boldsymbol{\sigma}}^+ + \bar{\boldsymbol{\sigma}}^-$) are defined as follows:

$$\bar{\boldsymbol{\sigma}}^{\pm} = (1 - d_{pl}^{\pm})\tilde{\boldsymbol{\sigma}}^{\pm} \tag{27}$$

being $\tilde{\boldsymbol{\sigma}}^{+}$ and $\tilde{\boldsymbol{\sigma}}^{-}$ the tensile and compressive components of the trial effective stress tensor. Additionally, the variables d_{pl}^{+} and d_{pl}^{-} are the tensile and compressive plastic damage indices, respectively, which introduce a decrease of the trial effective stress due to plasticity. A concise form of the trial effective stress evaluation is given below.

The trial effective stress tensor (elastic predictor) is computed incrementally as:

$$\tilde{\boldsymbol{\sigma}} = \bar{\boldsymbol{\sigma}}_{\boldsymbol{n}} + \boldsymbol{C_0} : (\boldsymbol{\varepsilon} - \boldsymbol{\varepsilon_n}) \tag{28}$$

where $\bar{\boldsymbol{\sigma}}_n$ represents the effective stress at the previous step and $\mathbf{C_0}$ the elastic stiffness tensor, which multiplied by ($\boldsymbol{\varepsilon}$ - $\boldsymbol{\varepsilon_n}$) gives the increment of the elastic trial stress. Thus, $\tilde{\boldsymbol{\sigma}}^{+}$ and $\tilde{\boldsymbol{\sigma}}^{-}$ are computed through spectral decomposition:

$$\tilde{\boldsymbol{\sigma}}^{\pm} = \sum_{i=1}^{3} \langle \tilde{\sigma}_i \rangle \boldsymbol{p_i} \otimes \boldsymbol{p_i} \tag{29}$$

being $\tilde{\sigma}_i$ the eigenvalue while $\boldsymbol{p_i}$ the corresponding eigenvector.

The loading, unloading, and reloading phases are described by the compressive and tensile damage surfaces, following the approach of **Lubliner et al. (1989)**, defined as follows:

$$\tilde{\tau}^{+} = H(\tilde{\sigma}_{\max}) \cdot \left[\frac{1}{1-\alpha} \left(\alpha \tilde{I}_1 + \sqrt{3\tilde{J}_2} + \beta \langle \tilde{\sigma}_{max} \rangle \right) \frac{f_t}{f_{cp}} \right] \tag{30}$$

$$\tilde{\tau}^{-} = H(-\tilde{\sigma}_{\min}) \cdot \left[\frac{1}{1-\alpha} \left(\alpha \tilde{I}_1 + \sqrt{3\tilde{J}_2} + k_1 \beta \langle \tilde{\sigma}_{max} \rangle \right) \right] \tag{31}$$

where $\tilde{\tau}^+$ and $\tilde{\tau}^-$ represent the equivalent stresses in tension and compression, respectively (scalar quantities). In Eqs. (30) and (31), $\bar{I}_1$ denotes the first invariant of the trial effective stress tensor, while $\bar{J}_2$ is the second invariant of the trial effective deviatoric stress tensor. The term $\tilde{\sigma}_{max}$ identifies the maximum trial effective principal stress, f_t the tensile strength, and f_{cp} the compressive strength. The coefficients α and β, are given by:

$$\alpha = \frac{k_b - 1}{2k_b - 1}; \beta = \frac{f_{cp}}{f_t}(1-\alpha) - (1+\alpha) \tag{32}$$

In this formulation, the parameter k_b expresses the ratio between the compressive strength under bi-axial loading and that obtained in uniaxial compression. The coefficient k_1, instead, governs how strongly the compressive failure surface influences the dilatancy response of the material. Its value ranges from 0 to 1: setting $k_1 = 0$ makes the model coincide with the Drucker-Prager yield criterion, while choosing $k_1 = 1$ activates the criterion originally proposed by **Lubliner et al. (1989)**, as shown in Figure 3.4.

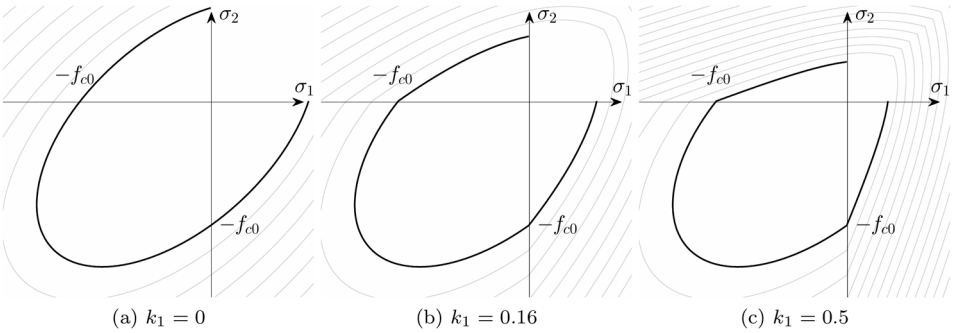

Figure 3.4: Compressive failure surface varying the parameter k_1 (**Petracca et al., 2017b**).

The functions $H(\tilde{\sigma}_{max})$ and $H(-\tilde{\sigma}_{min})$ in Eqs. (30) and (31) represent the Heaviside functions of the maximum and minimum eigenvalues. These ensure that the compressive failure surface is activated only when at least one principal stress is negative, and the tensile surface is activated only when at least one principal stress is positive. This activation is essential because, although tensile and compressive damage variables act only on their respective positive and negative stress components, the corresponding damage surfaces in Eqs. (30) and (31) depend on the full stress tensor.

Additionally, the equivalent stress measures ($\tilde{\tau}^{+}$ and $\tilde{\tau}^{-}$), are modified to maintain consistency with standard continuum-damage models. So that the equivalent stresses are subsequently modified as follows:

$$\tau^{\pm} = \tilde{\tau}^{\pm} + E\lambda_n^{\pm} \tag{33}$$

being E the Young's modulus, and $\lambda_n^{\pm}$ the tensile and compressive equivalent plastic strains carried over from the previous step. This adjustment guarantees that the resulting equivalent stress measures remain consistent with those obtained using a conventional continuum-damage formulation based on total strains.

In **Petracca et al. (2023)**'s model, damage irreversibility is accounted for by the tensile and compressive damage thresholds (scalar quantities), r^{+} and r^{-} and defined in Eqs. (34) and (35). At any time, these variables account for the maximum values ever attained by the equivalent stresses $\tau^{\pm}$.

$$r^{+}(t) = \max\left(\underset{s\in[0,t]}{max}\,\tau^{+}(s); f_t\right) \tag{34}$$

$$r^{-}(t) = \max\left(\underset{s\in[0,t]}{max}\,\tau^{-}(s); f_{c0}\right) \tag{35}$$

being f_t and f_{c0} the tensile and compressive elastic limits. These thresholds behave as if derived from a standard total-strain formulation. Accordingly, their total-strain counterparts and the associated nominal hardening variables can be expressed as:

$$\varepsilon_{tot}^{\pm} = \frac{r^{\pm}}{E} \tag{36}$$

$$q^{\pm} = f^{\pm}(\varepsilon_{tot}^{\pm}) \tag{37}$$

where $f^{\pm}$ are the tensile and compressive hardening laws, illustrated in Figure 3.5.

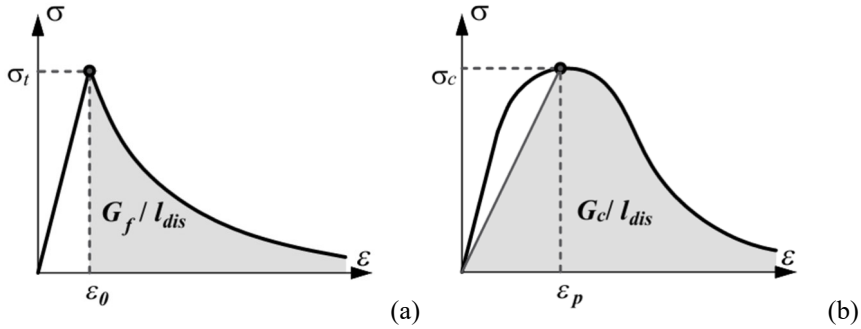

Figure 3.5: *ASDConcrete3D* uniaxial constitutive law: (a) in tension; (b) in compression.

The tensile and compressive plastic-damage quantities are obtained as:

$$d_{pl}^{\pm} = 1 - \frac{q_{pl}^{\pm}}{\tilde{r}^{\pm}} \tag{38}$$

with the auxiliary thresholds and plastic hardening variables:

$$\tilde{r}^{\pm} = E\left(\varepsilon_{tot}^{\pm} - \lambda_{n}^{\pm}\right) \tag{39}$$

$$q_{pl}^{\pm} = q^{\pm} + (1 - \omega^{\pm})(r^{\pm} - q^{\pm}) \tag{40}$$

Here, $\tilde{r}^{\pm}$ are the trial damage thresholds associated with the trial effective stress tensor; $q_{pl}^{\pm}$represent the hardening measures related solely to the plastic component; while $\omega^{\pm}$ are the positive and negative plastic-damage weights, ranging from 0 (full damage) to 1 (full plasticity).

Knowing the plastic hardening quantities, the cracking damage variables follow as:

$$d_{c}^{\pm} = 1 - \frac{q^{\pm}}{q_{pl}^{\pm}} \tag{41}$$

Considering plastic and cracking damage components, the plastic effective stress tensor and the nominal stress tensor can be computed using Eqs. (26) and (27). So that the equivalent plastic strains are finally calculated as:

$$\lambda^{\pm} = \varepsilon_{tot}{}^{\pm} - \frac{q_{pl}{}^{\pm}}{E} \tag{42}$$

A schematic illustration of this procedure under uniaxial loading is reported in Figure 3.6.

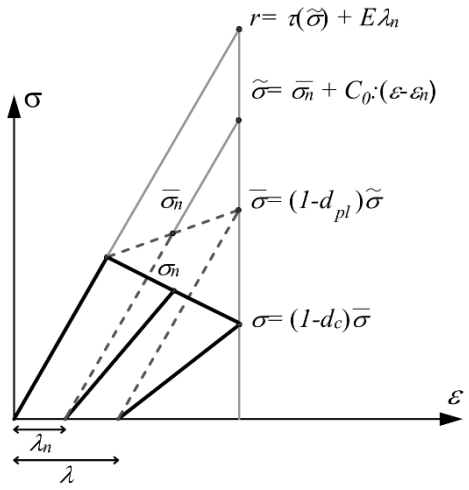

Figure 3.6: Plastic and damage correction applied to the elastic predictor in a uniaxial case.

To mitigate the effects of strain localization, the *ASDConcrete3D* model incorporates an automatic fracture-energy regularization procedure (Figure 3.5) that adapts to the chosen mesh resolution. With this approach, the tensile and compressive fracture energies, G_t and G_c are linked to the size of the damaged region l_{dis}, which is assumed to coincide with the characteristic length of the finite element l_{ch} (**Bažant and Oh, 1983; Oliver, 1989; Petracca et al., 2017b**). This leads to the following relationships:

$$g_f \, l_{dis} = G_f \tag{43}$$

$$g_c \, l_{dis} = G_c \tag{44}$$

where g_f is the specific fracture energy per unit volume.

For further details on the whole plastic-damage framework, the reader may refer to **Petracca et al. (2023)** and **Petracca et al. (2017b)**.

3.1.2 Contact interface material

The adopted micro-modelling strategy also includes an explicit representation of the interface between the masonry infill and the RC frame. This was implemented by first defining a *node-to-node* interaction and then modelling the contact behaviour through the *Zero-Length Implex* contact element (**Petracca et al., 2017a, 2017b**). This element can reproduce both separation and frictional sliding at the interface, which naturally arise from the interaction between the concrete frame and the masonry panel (Figure 3.7).

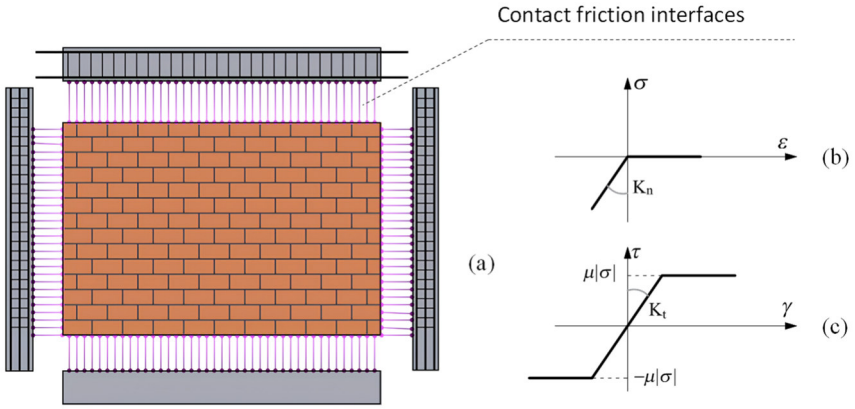

Figure 3.7: Infill-frame interface modelling: (a) Scheme of the interfaces (magnified distances); (b) Contact model; (c) Friction model.

The contact law relies on a continuum-based friction model that links the normal and shear stresses to the corresponding strain components. Through spatial integration, these stress quantities are converted into self-equilibrated interface forces and subsequently into nodal reactions at the contact boundaries (**Oliver et al., 2008**). Contact is enforced using a penalty-based formulation, combined with a Coulomb friction law to account for tangential resistance, expressed as follows:

$$\dot{\boldsymbol{\sigma}} = \boldsymbol{C}^{cf}\,\dot{\boldsymbol{\varepsilon}} \tag{45}$$

where $\dot{\boldsymbol{\sigma}}$ and $\dot{\boldsymbol{\varepsilon}}$ are the increments of the stress and strain vectors, defined as:

$$\boldsymbol{\sigma} = \begin{pmatrix} \sigma \\ \tau \end{pmatrix};\ \boldsymbol{\varepsilon} = \begin{pmatrix} \varepsilon \\ \gamma \end{pmatrix} \tag{46}$$

being C^{cf} the constitutive tangent tensor. This tensor is a function of the parameters K_n, K_t, and μ, which correspond to the normal and tangential penalty stiffnesses for contact and sticking, and to the friction coefficient, respectively (**Oliver et al., 2008**). The contact and frictional formulations are coupled in a unidirectional manner: the normal stress evaluated within the contact law directly influences the slip criterion, as also evident from the constitutive relationships shown in Figure 3.7 (b, c).

3.1.3 Boundary conditions and analysis procedure

The numerical model was constrained against both horizontal and vertical displacements at the foundation nodes. To reproduce the typical in-plane loading sequence used in experimental tests on infilled frames, the analysis was carried out in two successive phases. First, vertical loads were applied at the column tops. Afterwards, the lateral response was simulated by imposing a monotonic horizontal displacement at the top beam. The nonlinear equilibrium equations were solved using the *Krylov-Newton* algorithm. Different integration schemes were adopted for the two stages: *Load Control* for the application of vertical forces, and a *Parallel Displacement Control* algorithm with a prescribed target displacement for the horizontal loading phase. A schematic overview of the boundary conditions and loading configuration for the reference model is provided in Figure 3.8.

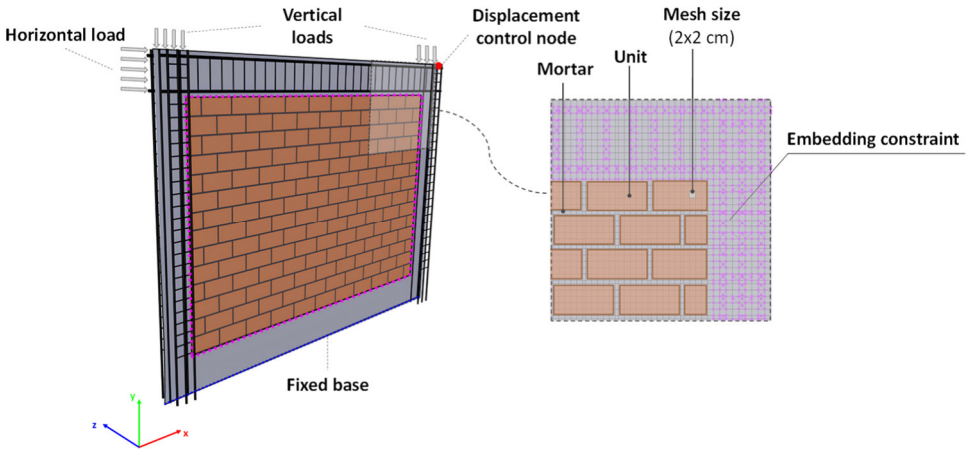

Figure 3.8: Constraint and loading condition for a generic monotonic in-plane test of infilled RC frames and mesh detailing.

The micro-models were discretised using a uniform quadratic mesh, with an element size of 2×2 cm for masonry units and concrete, and 2×1 cm for the mortar joints (Figure 3.8). Preliminary simulations with different mesh discretisation (6

cm, 4 cm and 2 cm) were carried out. These showed consistent trends in terms of global and local response. In particular, no significant variations were observed in the key response quantities used in this study. This suggests that the main conclusions are not significantly affected by the adopted mesh size.

To enhance computational efficiency, the analyses were executed in parallel through the OpenSeesMP solver, which requires splitting the global mesh into as many subdomains as the processors employed. For optimal performance, each processor should handle approximately 5,000 to 7,000 elements. Figure 3.9 provides an example in which the model is divided into five subdomains and shows the corresponding element distribution among processors. The use of parallel computation proved highly effective, reducing the total runtime to approximately 15-20 minutes per analysis.

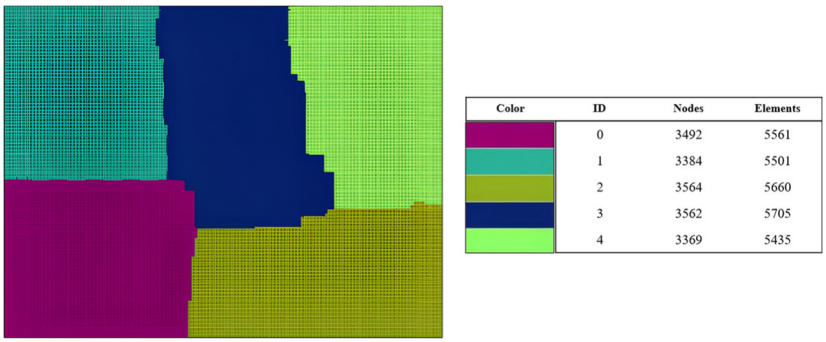

Figure 3.9: Model partitioning for parallel computing with OpenSeesMP.

3.2 Simulation of in-plane experimental response in masonry-infilled RC frames

3.2.1 Reference in-plane tests selection

To assess the overall robustness of the proposed micro-modelling strategy, the reference database was selected to cover a various spectrum of masonry infill typologies. Four in-plane experimental tests on infilled RC frames were therefore considered as benchmarks for validating the numerical framework. These specimens were drawn from the experimental programmes of **Mehrabi et al. (1996)** and **Cavaleri and Di Trapani (2014)**, both of which provide full mechanical characterization of the masonry materials. Specifically, specimens S8 and S9 from **Mehrabi et al. (1996)** were constructed using hollow clay units (S8)

and solid clay bricks (S9). Conversely, the specimens S1A and S1B from **Cavaleri and Di Trapani (2014)** were built with solid calcarenite blocks and hollow clay masonry units, respectively (Table 3). All specimens were first subjected to vertical preloading. Afterwards, lateral loading was applied monotonically for S8 and S9, while S1A and S1B were tested under cyclic in-plane loading. The aspect ratio *l/h* of the infill panels was equal to 1.5 for S8 and S9, and equal to 1.0 for S1A and S1B. The infills in S8 and S9 were assembled using 92×92×194 mm units, either hollow or solid depending on the specimen. For S1A, the masonry consisted of calcarenite blocks measuring 210×160×360 mm, while S1B was built with hollow clay units of dimensions 150×250×300 mm. Mortar bed and head joints were 10 mm thick for S8 and S9, and 12 mm for S1A and S1B. The geometry and reinforcement layouts of the infilled frame specimens are reported in Figure 3.10 and Figure 3.11, whereas the mechanical properties adopted in the models are summarised in Table 2.

Table 3: Specimens' details.

Reference	Specimen ID	Masonry type	Aspect Ratio (*l/h*) (-)	Load on columns (kN)
Mehrabi et al. (1996)	S8	Hollow concrete bricks	1.5	97.9
	S9	Solid concrete bricks	1.5	97.9
(Cavaleri and Di Trapani, 2014)	S1A	Solid calcarenite units	1.0	200
	S1B	Hollow clay units	1.0	200

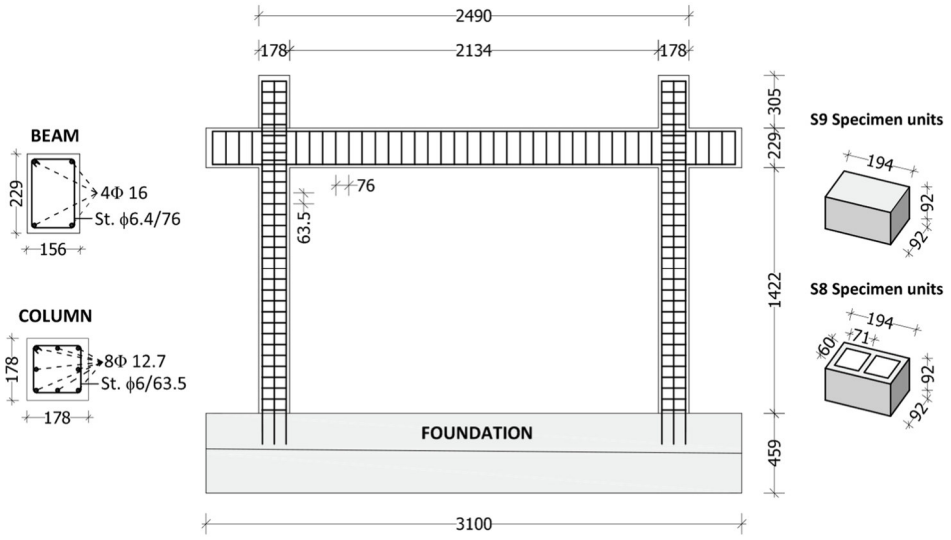

Figure 3.10: **Mehrabi et al. (1996)** S8 and S9 specimens' details (dimensions in mm).

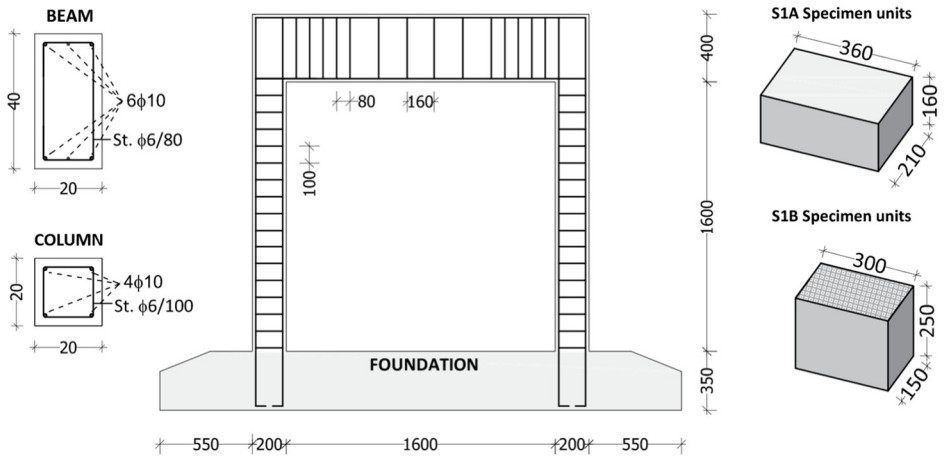

Figure 3.11: **Cavaleri and Di Trapani (2014)** S1A and S1B specimens' detail (dimensions in mm).

Table 4: Mechanical properties of materials for the selected specimens.

Specimen ID	Concrete		Steel	Units		Mortar
	Compressive strength (f_c) (MPa)	Elastic modulus (E_c) (MPa)	Yielding Strength (f_y) (MPa)	Compressive strength (f_{bv}) (MPa)	Compressive strength (f_{bh}) (MPa)	Compressive strength (f_m) (MPa)
S8	26.8	17225	420	16.48	8.51	8.01
S9	26.8	17225	420	15.57	15.57	12.47
S1A	25.0	25500	450	7.06	7.06	3.06
S1B	25.0	25500	450	37.68	2.06	9.16

3.2.2 Mechanical characterization of masonry and concrete materials

The material parameters obtained from the experimental characterization were employed to define the uniaxial constitutive laws for both the masonry units and the mortar. The units are modelled as separate isotropic continuum elements. To account, in a simplified manner, for the distinct mechanical behaviour exhibited in the horizontal and vertical directions due to the presence of holes, an equivalent compressive strength $\tilde{f}_b$ is assigned following the formulation commonly adopted in the literature (**Di Trapani et al., 2018, 2022**). This conventional strength combines the horizontal and vertical compressive strengths (f_{bh} and, f_{bv} respectively) and is expressed as:

$$\tilde{f}_b = \sqrt{f_{bh} \cdot f_{bv}} \tag{47}$$

For solid masonry units, where the horizontal and vertical compressive strengths coincide ($f_{bh} = f_{bv}$), equivalent value reduces to $\tilde{f}_b = f_{bh} = f_{bv}$.

Regarding mortar, the experimentally measured compressive strengths (Table 4) are directly adopted. The remaining mechanical parameters not determined through testing are derived as functions of the compressive strengths of both the masonry units and the mortar. The elastic moduli of the units (E_b) and the mortar (E_m) are then calibrated within the following ranges:

$$\begin{aligned} E_b &\cong (500 \div 600)\tilde{f}_b \\ E_m &\cong (100 \div 300) f_m \end{aligned} \tag{48}$$

The empirical relationships reported in Eq. (10) follow the formulation proposed by (**Kaushik et al., 2007**). In an analogous manner, the tensile strengths of the masonry units (f_{tb}) and the mortar (f_{tm}) are identified within the following ranges:

$$\begin{aligned} f_{tb} &\cong (0.10 \div 0.15)\tilde{f}_b \\ f_{tm} &\cong (0.025 \div 0.060) f_m \end{aligned} \tag{49}$$

The peak strain values are then derived by evaluating the secant elastic modulus corresponding to the peak compressive strengths of the masonry units (E_b^S) and the mortar (E_m^S). Accordingly, the following expressions are used:

$$\varepsilon_b \cong \frac{\tilde{f}_b}{E_b^S}; \qquad \varepsilon_m \cong \frac{f_m}{E_m^S} \tag{50}$$

where E_b^S may be assigned a value of $0.5\,E_b$, while E_m^S can be adjusted within the range $E_m^S = (0.33 \div 0.66)E_m$.

The tensile (G_t) and compressive (G_c) fracture energies of both the masonry units and the mortar were also calibrated. The tensile fracture energies G_t required for the damage-plasticity formulation were initially evaluated following the recommendations of the **Model Code (2010)**, according to:

$$G_t = 0.073 \cdot f_c^{0.18} \tag{51}$$

where, f_c is the material compressive strength.

The compressive fracture energies G_c were derived following an approach analogous to that proposed by (**Nakamura, 2001**), assuming them to be proportional to the corresponding tensile fracture energies. Accordingly:

$$G_c = A \cdot G_t \tag{52}$$

where the coefficient A was taken equal to 250 for concrete, 170 for the masonry units, and 200 for the mortar. Minor adjustments to these values were occasionally introduced to further enhance the agreement between the numerical model and the experimental response.

The final calibrated parameters used for the constitutive models of the masonry units and mortar are summarised in Table 5 and Table 6.

Table 5: Mechanical properties used for masonry units.

Specimen ID	$\tilde{E}_b$ (MPa)	$\tilde{f}_b$ (MPa)	f_{tb} (MPa)	ε_b (MPa)	G_c (N/mm)	G_t (N/mm)
S8	5920	11.84	1.30	0.0033	19.70	0.114
S9	7786	15.57	1.71	0.0033	20.50	0.120
S1A	3530	7.06	0.78	0.0040	17.50	0.104
S1B	5286	8.81	0.79	0.0033	18.50	0.108

Table 6: Mechanical properties used for mortar joints.

Specimen ID	E_m (MPa)	f_m (MPa)	f_{tm} (MPa)	ε_m (MPa)	G_c (N/mm)	G_t (N/mm)
S8	1602	8.01	0.24	0.020	21.23	0.106
S9	3741	12.47	0.70	0.010	22.40	0.120
S1A	306	3.06	0.11	0.020	17.80	0.089
S1B	916	9.16	0.27	0.020	21.75	0.109

For the RC members, confinement effects are incorporated following the formulation of (**Mander et al., 1988**), by differentiating the compressive behaviour of the confined core concrete from that of the unconfined cover. Implementing the concrete constitutive laws therefore requires, as a first step, the evaluation of the confined concrete strength f_{cc}. The tensile strength f_{tc} was obtained as 11% of the unconfined compressive strength f_c. Lastly, the tensile and compressive fracture energies were computed using Eqs. (51) and (52). For confined concrete, the confined compressive strength f_{cc} was employed to determine the corresponding confined compressive fracture energy G_{cc}, whereas the tensile fracture energy was taken to be identical to that of the unconfined material. The mechanical parameters adopted for the concrete material model are summarised in Table 7.

Table 7: Mechanical properties used for concrete.

Specimen ID	E_c (MPa)	f_c (MPa)	f_{cc} (MPa)	f_{tc} (MPa)	G_c (N/mm)	G_{cc} (N/mm)	G_t (N/mm)
S8	17220	26.8	33.50	2.76	33.00	49.50	0.132
S9	17220	26.8	33.50	2.76	33.00	49.50	0.132
S1A	25500	25.0	30.00	2.75	32.58	48.87	0.130
S1B	25500	25.0	30.00	2.75	32.58	48.87	0.130

3.2.3 Determination of contact and friction interface parameters

The calibration of the contact parameters was carried out iteratively by tuning the zero-length contact *ASDImplex* elements adopted at the interface. These elements simulate a frictional interaction between the masonry and concrete nodes, effectively behaving as zero-length springs in both the normal and tangential directions. Initial estimates of the normal and tangential stiffnesses, K_n and K_t, were obtained as follows:

$$K_n = \frac{E_m A_j}{l_j}; \qquad K_t = \frac{G_m A_j}{l_j} \tag{53}$$

where E_m and G_m denote the normal and tangential moduli of the mortar at the interface, and $A_j = t_j \times l_j$ represents the tributary area of the joint associated with each node. Here, t_j is the mortar joint thickness, while l_j corresponds to the tributary length, which depends on the mesh subdivision near the interface. In the absence of specific experimental measurements, G_m may be approximated as 40% of E_m. The

calibrated values of the contact parameters for the interface elements used in the reference tests are reported in Table 8.

Table 8: Parameters governing the contact interface.

Specimen ID	K_n (N/mm)	K_t (N/mm)	μ (-)
S8, S9	$1 \cdot 10^5$	$1 \cdot 10^4$	0.7
S1A, S1B	$1 \cdot 10^5$	$1 \cdot 10^5$	0.7

3.2.4 Comparison between experimental results and numerical simulations

The outcomes of the numerical monotonic analyses were compared with the corresponding experimental responses of the tested specimens. Figure 3.12 reports these comparisons in terms of lateral force versus top lateral displacement. For specimens S1A and S1B (**Cavaleri and Di Trapani, 2014**), which were subjected to cyclic loading, the numerical results were contrasted with both the positive and negative monotonic envelopes extracted from the experimental hysteresis loops. Each of these specimens was tested twice, yielding two experimental envelopes per case (Figure 3.12a, and 3.11b). Conversely, specimens S8 and S9 (**Mehrabi et al., 1996**) were tested under monotonic loading; therefore, a single experimental force-displacement curve was available for each and was used directly for comparison with the numerical simulations (Figure 3.12c, and 3.11d). Overall, the numerical models successfully captured the global behaviour observed in the experiments, reproducing the stiffness, peak load capacity, and the degradation beyond the maximum resistance.

Figure 3.13 and Figure 3.14 compare the experimental damage patterns at the end of the tests with those obtained from the numerical simulations. Overall, the micro-models were able to reproduce the key damage mechanisms observed in the specimens, including brick crushing and mortar-joint sliding in the infill, as well as shear and flexural cracking in the RC members. The specimens tested by **Mehrabi et al. (1996)** showed significantly different failure modes. For specimen S8 (Figure 3.13a), both the experimental evidence and the numerical results revealed widespread sliding along the mortar joints, with limited brick crushing due to the lower mortar compressive strength. The simulations also accurately captured the onset of shear damage at the top of the left column and the base of the right one. In specimen S9 (Figure 3.13b), failure involved a combination of shear damage in the

left column and diagonal cracking across the infill. Two pronounced diagonal cracks crossing both joints and units were recorded experimentally, and the numerical model reproduced this pattern with good consistency.

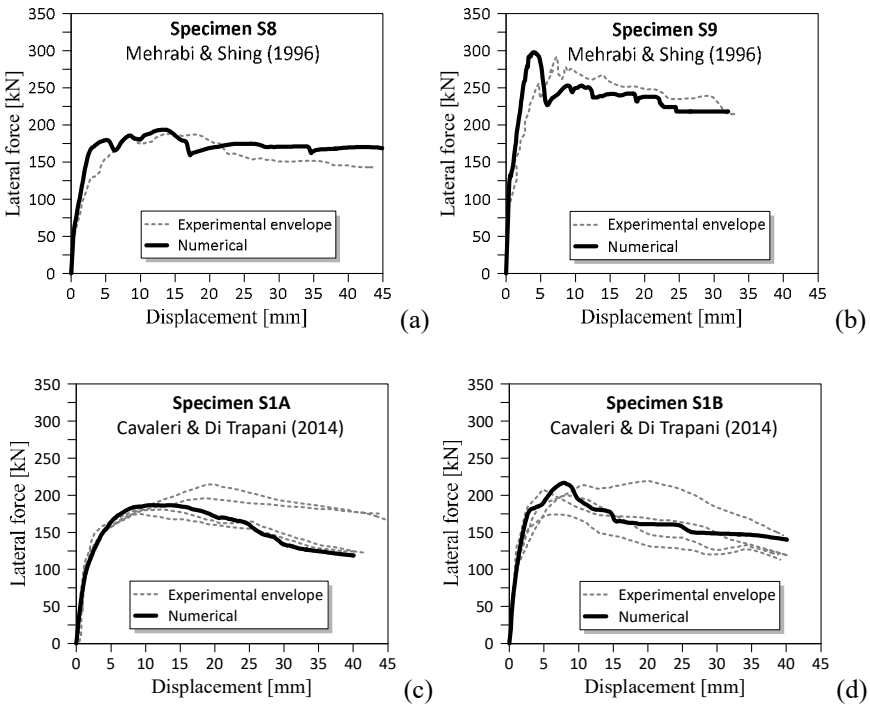

Figure 3.12: Experimental VS numerical monotonic response simulations for specimens: (a) S8; (b) S9; (c) S1A; (d) S1B.

Specimens S1A and S1B from **Cavaleri and Di Trapani (2014)** exhibited substantially different behaviours. In S1A, damage primarily affected the horizontal mortar joints, with only minor degradation of the calcarenite blocks (Figure 3.14a). In contrast, specimen S1B displayed a mixed mechanism involving both unit sliding and unit crushing (Figure 3.14b). The numerical analysis reproduced the sliding along two major diagonals; however, it was less effective in capturing the extensive unit failures observed experimentally, largely because the numerical model represents hollow units as equivalent solid elements. Additionally, both the tests and the simulations displayed minor shear and flexural damage in the RC frame.

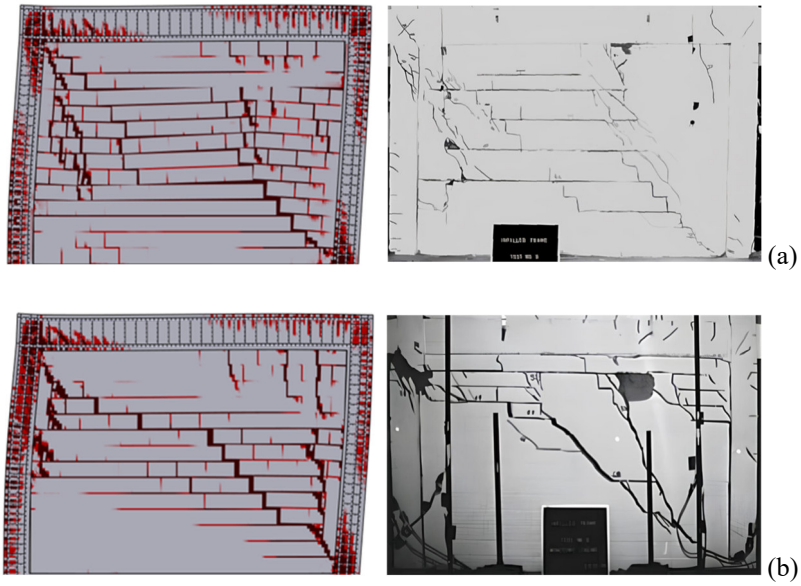

Figure 3.13: Comparison of numerical and experimental damage patterns for **Mehrabi et al. (1996)** specimens: (a) S8; (b) S9.

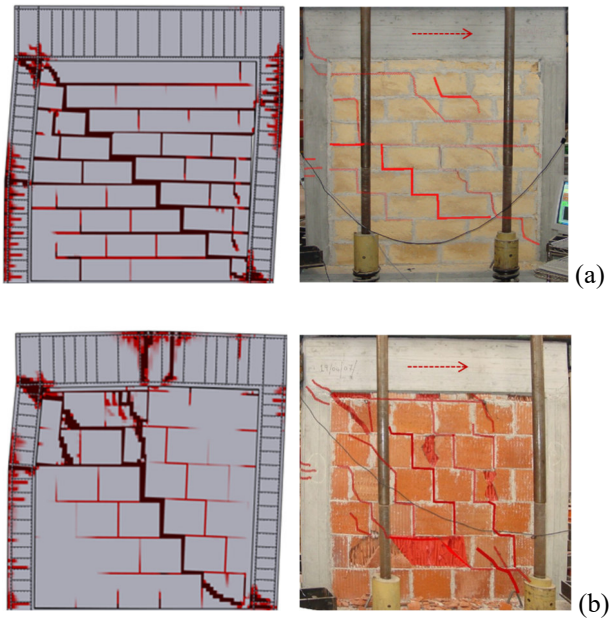

Figure 3.14: Comparison of numerical and experimental damage patterns for **Cavaleri and Di Trapani (2014)** specimens: (a) S1A; (b) S1B. (Experimental cracks are highlighted in red only for the left to right direction).

3.3 Analysis and extrapolation of internal force demand in structural frame members

3.3.1 Internal forces' extrapolation

The determination of internal actions within the RC frame members was carried out using a dedicated Python routine incorporated into the STKO post-processing platform. The script allows the user to define a line of interest, labelled a *section cut*, along which a specific group of nodes is selected. For each of these nodes, the force components are extracted in the local coordinate system associated with the cut. The integration of these nodal quantities along the chosen line yields the respective internal force resultants. When the section cuts are positioned perpendicular to the member's longitudinal axis, they enable the direct computation of axial force, shear, and bending moment, regardless of whether the beams and columns are represented through 2D or 3D continuum elements. This approach makes it possible to reconstruct the internal force diagrams of the frame members in a consistent and mechanically meaningful manner.

Each tested specimen was analysed using multiple section cuts placed at predefined locations. Figure 3.15 illustrates an example of how these cuts were distributed along the structural members of an infilled frame. The symbols n_{sb} and n_{sc} represent the number of cuts assigned to beams and columns, while $s_{b,\mathrm{i}}$ and $s_{c,\mathrm{i}}$ indicate the generic cut along each element. The adopted number of cuts for both beams and columns is reported in Table 9.

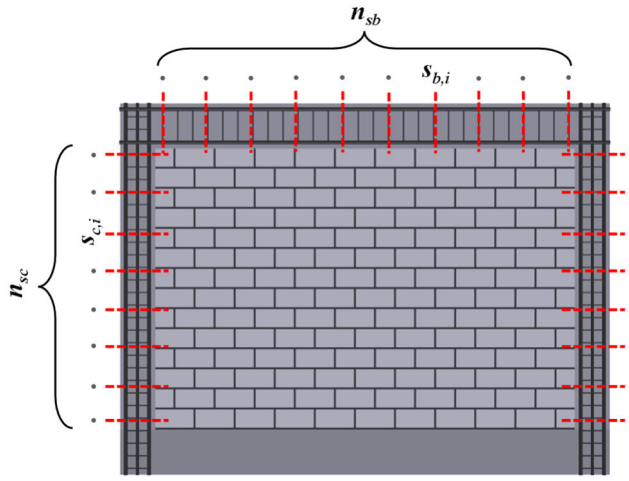

Figure 3.15: Section-cut scheme for the RC frames' internal forces analysis.

Table 9: Selected number of section cuts in RC members.

Specimen ID	Beam n_{sb}	Columns n_{sc}
S8	22	15
S9	22	15
S1A	10	11
S1B	10	13

Internal forces in RC members are tracked incrementally at every analysis step. Figure 3.16 and Figure 3.17 present the evolution of shear and bending moment diagrams for the examined specimens, illustrating their configuration at three key stages: the onset of cracking, the attainment of maximum lateral strength, and the final stage of the analysis.

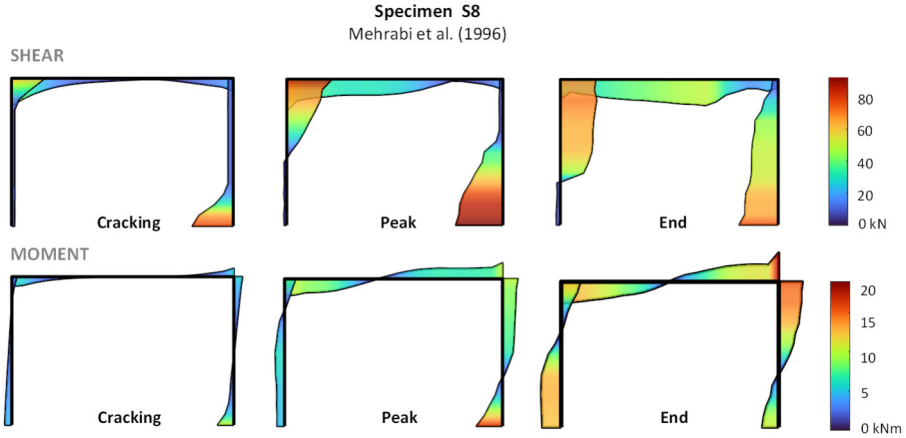

Figure 3.16: Shear and moment distribution in RC frame for specimen S8 (**Mehrabi et al., 1996**).

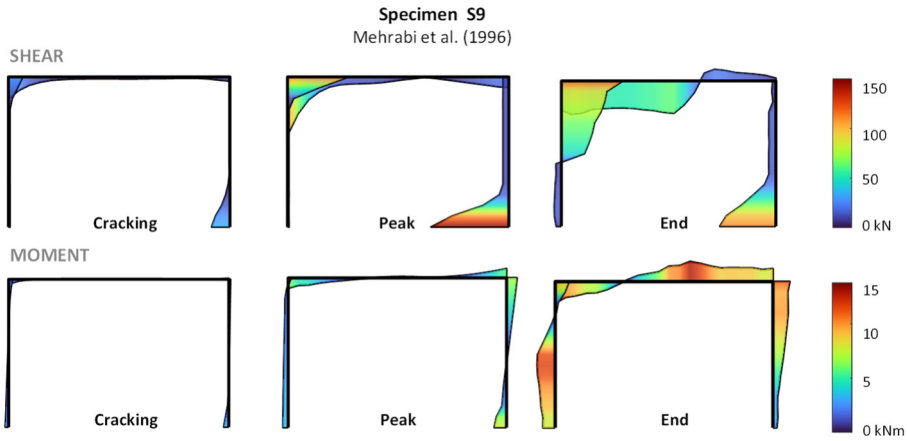

Figure 3.17: Shear and moment distribution in RC frame for specimen S9 (**Mehrabi et al., 1996**).

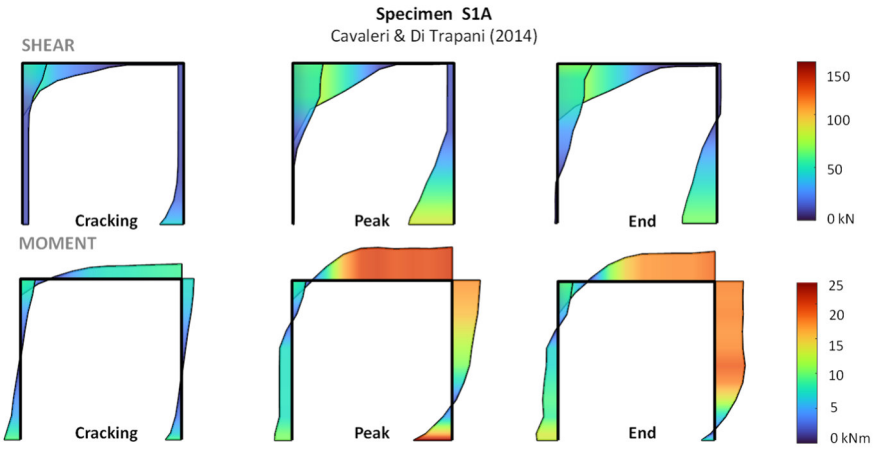

Figure 3.18: Shear and moment distribution in RC frame for specimen S1A (**Cavaleri and Di Trapani, 2014**).

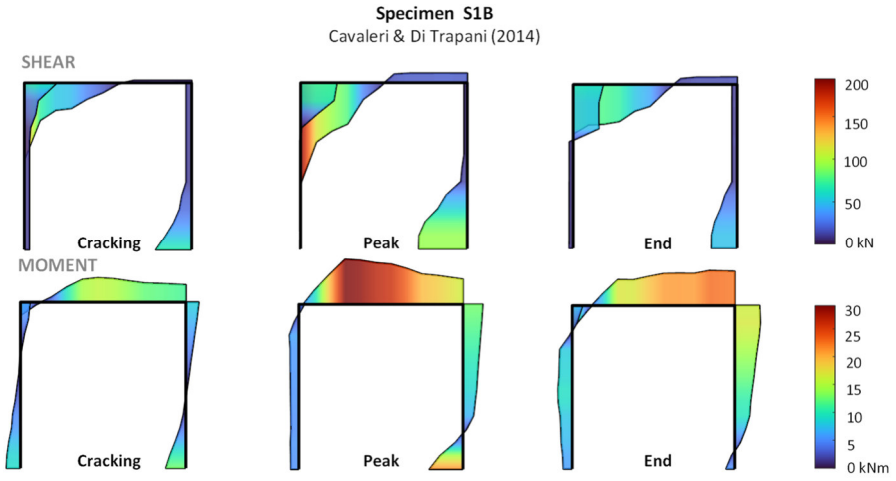

Figure 3.19: Shear and moment distribution in RC frame for specimen S1B (**Cavaleri and Di Trapani, 2014**).

3.3.2 Comparative examination of internal forces' distributions

The internal force diagrams presented in Figure 3.16 through Figure 3.19 exhibit noticeable deviations from those anticipated in the bare frame (BF) configuration. Specifically, while a uniform shear demand is typically expected along the columns in BF scenarios, the presence of infill alters this distribution, shear forces intensify in regions where the frame and infill are in contact and reduce in areas lacking such interaction. Similarly, moment diagrams, which are generally

linear with a zero crossing near midspan in BF cases, now display nonlinear behaviour, with the zero points shifting toward the contact zones.

These phenomena, previously discussed in studies by **Cavaleri and Di Trapani (2015)**, **D'Ayala et al. (2009)**, and **Milanesi et al. (2018)** are further clarified through micro-modelling approaches. By explicitly representing mortar joints instead of relying on homogenised masonry models, the analysis reveals sliding mechanisms that emerge when mortar strength is inferior to that of the masonry units. This behaviour becomes evident when comparing the shear diagram evolution of specimens S8 and S1A to that of S9 and S1B. The former group experiences pronounced sliding, which increases the contact length as lateral drift progresses. This is reflected in Figure 3.16 and Figure 3.19, where the constant shear segments, indicative of non-contact zones, shrink, and shear demand becomes more distributed along the column length. In contrast, specimens S9 and S1B primarily undergo unit cracking with minimal sliding. Their shear diagrams (Figure 3.17 and Figure 3.19) show only a modest increase in contact length as drift intensifies, resulting in a more localized concentration of shear forces. Across all examined cases, the altered internal force distributions also influence beam behaviour. The resulting shear and moment diagrams, shaped by infill interaction, tend to counteract those generated by gravity loads, suggesting a reduced vulnerability under seismic conditions.

The progression of contact lengths is further illustrated in Figure 3.20 to Figure 3.23, which depict the minimum principal stress fields within the infills. These figures also identify contact points, locations where the normal interface registers compressive forces. As lateral displacement increases, the primary compression zones shift away from the diagonal, a consequence of stress redistribution following significant diagonal cracking. This effect is more pronounced in sliding specimens S8 and S1A (Figure 3.20 and Figure 3.22), explaining their greater contact length expansion compared to S9 and S1B (Figure 3.21 and Figure 3.23). Additionally, the deformation patterns differ markedly: S8 and S1A exhibit shear-dominated deformation consistent with sliding, whereas S9 and S1B show prominent bending at the top beam's midspan and the upper section of the left column.

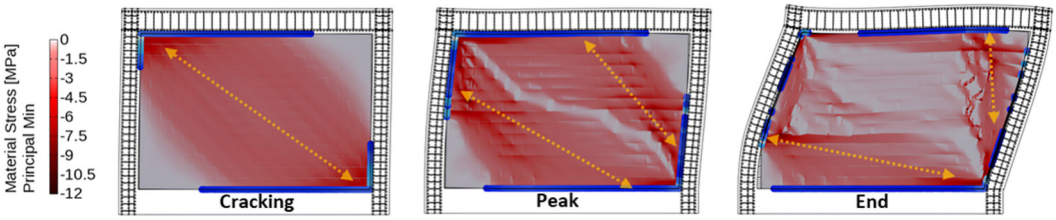

Figure 3.20: Minimum principal stresses on the masonry infill and contact points for Specimen S8 (**Mehrabi et al., 1996**).

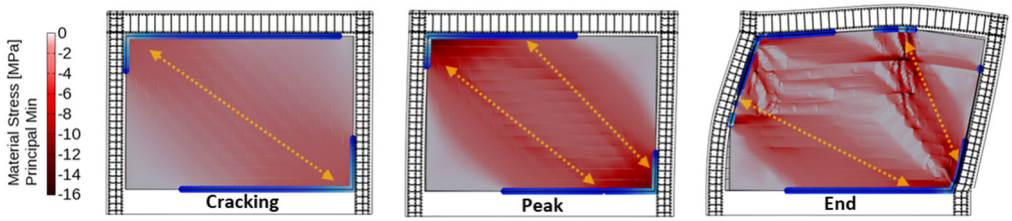

Figure 3.21: Minimum principal stresses on the masonry infill and contact points for Specimen S9 (**Mehrabi et al., 1996**).

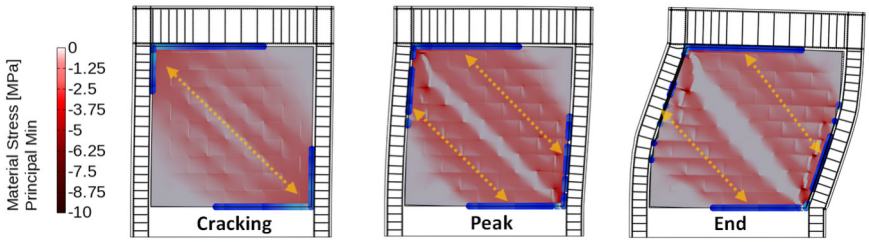

Figure 3.22: Minimum principal stresses on the masonry infill and contact points for Specimen S1A (**Cavaleri and Di Trapani, 2014**).

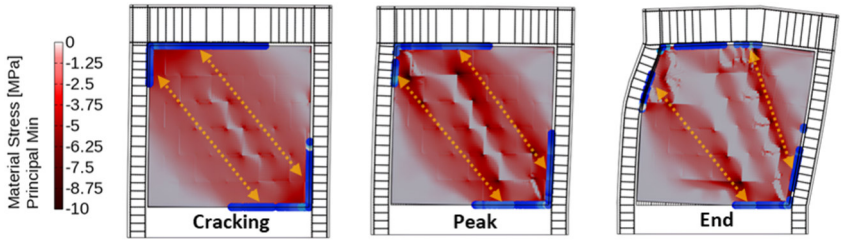

Figure 3.23: Minimum principal stresses on the masonry infill and contact points for Specimen S1B (**Cavaleri and Di Trapani, 2014**).

The internal force profiles of the infilled frames were compared against those derived from pushover simulations of their bare frame counterparts. Specimens S8

and S1B were selected as representative cases, illustrating dominant sliding and crushing failure behaviours, respectively. Figure 3.24 and Figure 3.25 illustrate these comparisons, showing the shear and bending moment demands at key stages, initial cracking, peak strength, and final step, for both left and right columns. These diagrams also include the corresponding internal force demands from bare frames at matching drift levels. The vertical axis in these figures denotes the normalised column height, expressed as h/h_c. From the shear diagrams (Figure 3.24a and b, Figure 3.25a and b), it is evident that the peak shear forces in the contact zones of the infilled specimens were roughly twice those observed in the bare frame configuration. Interestingly, these elevated shear levels were already present at the onset of cracking, although the distribution evolved significantly with increasing lateral displacement. Initially, the shear profiles in contact regions were nearly linear, transitioning to trapezoidal shapes as deformation progressed.

The extent of contact along the column height varied markedly between the two specimens, influenced by the dominant damage mechanism. In specimen S1B, which primarily experienced unit crushing, the contact lengths remained relatively stable, around 30% of the column height on the left and 40% on the right. In contrast, specimen S8, characterized by substantial sliding along mortar joints, exhibited pronounced changes in contact length with increasing drift. These ranged from 20% to 70% of the column height on the left side and from 30% to 90% on the right. Such transformations in shear distribution, from linear to trapezoidal, and the dynamic nature of contact length were not captured in earlier studies (e.g., **D'Ayala et al., 2009; Milanesi et al., 2018**), likely due to the use of homogenised masonry models that overlooked sliding at mortar bed joints level. Regarding moment demand, the interaction between frame and infill did not significantly alter the peak moment values at the column ends. However, the moment distribution along the column length became distinctly nonlinear, with the zero-moment point shifting toward the contact zones. This shift aligns with the formation of plastic hinges at the ends of a reduced length of the columns.

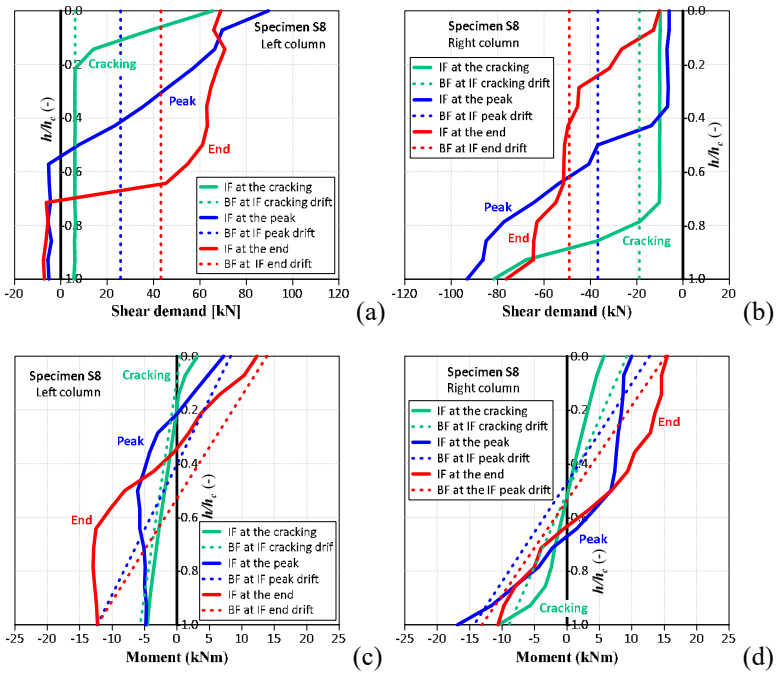

Figure 3.24: Shear and moment demand comparisons at various analysis steps for specimens S8 (**Mehrabi et al., 1996**): (a) shear at left column; (b) shear at right column; (c) moment at left column; (d) moment at right column.

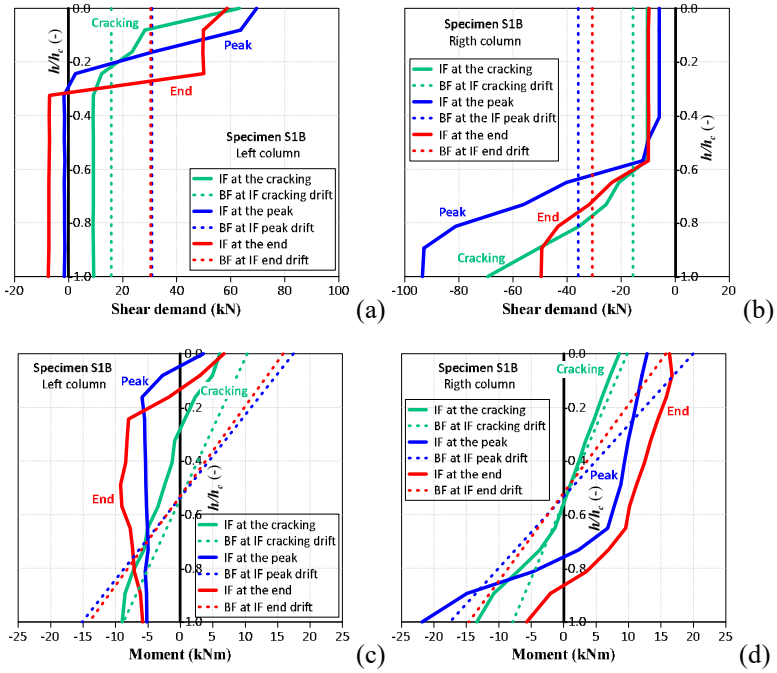

Figure 3.25: Shear and moment demand comparisons at various analysis steps for specimens S1B (**Cavaleri and Di Trapani, 2014**): (a) shear at left column; (b) shear at right column; (c) moment at left column; (d) moment at right column.

3.4 The role of masonry design variables in affecting the internal force distributions and failure modes

To evaluate how masonry design variables influence shear force distribution and failure patterns in infilled frames, a parametric study was conducted. Two specimens, S1A and S1B (**Cavaleri and Di Trapani, 2014**), were chosen due to their markedly different ratios of unit strength to mortar strength, as detailed in Table 10. The investigation involved systematically altering the initial mortar strength (f_{m0}) while keeping the unit strength constant. For specimen S1A, the mortar resistance was increased by scaling f_m/f_{m0} of 1.5, 2.0, and 3.0 relative to f_{m0}. Conversely, for specimen S1B, the mortar strength was reduced using scaling factors of 0.8, 0.6, and 0.4 (see Table 10). Both local and global structural responses were recorded and compared across these variations. Adjusting the mortar strength altered the unit-to-mortar resistance ratio ($\tilde{f}_b / f_m$), resulting in a range of values between 0.77 and 2.40 (Table 10). These changes also influenced associated material properties, such as the modulus of elasticity E_m and tensile strength f_t which were recalculated for each configuration accordingly.

Table 10: Mechanical inputs and strength relationships considered in the parametric analysis of S1A and S1B **(Cavaleri and Di Trapani, 2014)**.

Specimen ID	**Units**	**Mortar**				
	$\tilde{f}_b$ (MPa)	f_m (MPa)	f_m / f_{m0} (-)	$\tilde{f}_b / f_m$ (-)	E_m (MPa)	f_{tm} (MPa)
S1A	**7.06**	**f_{m0}=3.06**	**1.0**	**2.31**	**306**	**0.11**
S1A-1		4.59	1.5	1.54	459	0.16
S1A-2		6.12	2.0	1.15	612	0.21
S1A-3		9.18	3.0	0.77	918	0.32
S1B	**8.81**	**f_{m0}=9.16**	**1.0**	**0.96**	**916**	**0.32**
S1B-1		7.33	0.8	1.20	733	0.26
S1B-2		5.50	0.6	1.60	550	0.19
S1B-3		3.66	0.4	2.40	366	0.13

Figure 3.26 illustrates how changing the mortar strength influences the global structural response of specimens S1A and S1B. For specimen S1A, increasing the mortar strength led to a steady enhancement in peak load capacity, culminating in a gain of approximately 50% when the mortar resistance was tripled (Figure 3.26a). This enhancement, however, was accompanied by a shift in the global response, from an initially ductile behaviour to one characterized by a distinct peak followed by a progressively extreme softening phase. In contrast, specimen S1B, which was

subjected to decreasing levels of mortar strength, exhibited a reduction in peak resistance of up to 28% (Figure 3.26b). Specifically, as the mortar became weaker, the overall structural response transitioned toward a more ductile behaviour, indicating increased energy dissipation capacity despite the lower strength.

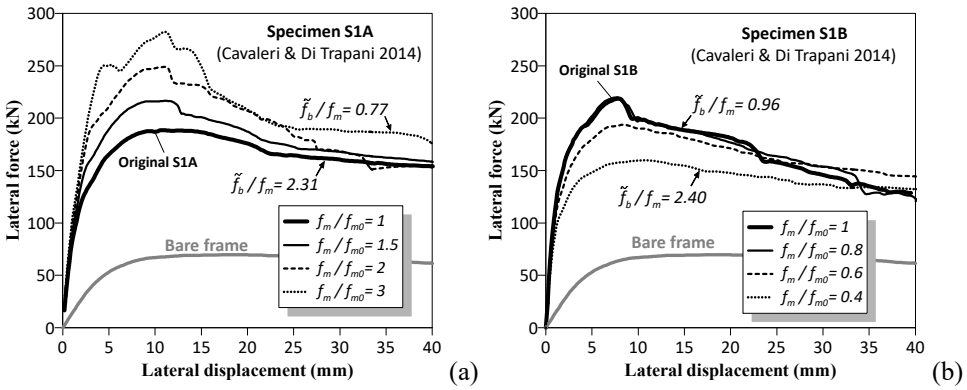

Figure 3.26: Effect of mortar strength variation on the global behaviour of the infilled RC frame for: (a) Specimen S1A; (b) Specimen S1B.

Figure 3.27 provides a visual comparison of the distinct damage mechanisms and the evolution of shear deformation within the mortar joints for specimens S1A and S1B. In specimen S1A (Figure 3.27a), the progression from an initial sliding behaviour to a dominant diagonal compression failure is clearly observable. This transition is not only evident in the overall damage pattern but also in the distribution of shear strain across the mortar joints. For weaker mortar, deformation was spread along the horizontal joints at mid-height, indicating a sliding mechanism. However, as mortar strength increase, the deformation became concentrated along the principal diagonal, marking the onset of diagonal shear failure. Conversely, specimen S1B (Figure 3.27b) exhibited an opposite trend. For the original specimen with higher mortar strength (lower $\tilde{f}_b / f_m$), the specimen showed a diagonal shear failure, accompanied by localized crushing of the bricks and noticeable damage to the surrounding frame elements. However, as the $\tilde{f}_b / f_m$, ratio increase, the failure mode evolved into a predominantly sliding mechanism. In this phase, the mortar joints allowed relative movement between units, reducing the stress concentration and limiting further damage to the frame. The overall deformation became more distributed and less severe, indicating a more ductile response. These contrasting behaviours underscore the critical role of mortar strength and $\tilde{f}_b / f_m$ ratio in governing the failure mode of infilled frames. The

ability of the mortar to either transmit or dissipate shear forces directly influences whether the structure will exhibit brittle or ductile response, with significant implications for seismic performance and energy dissipation.

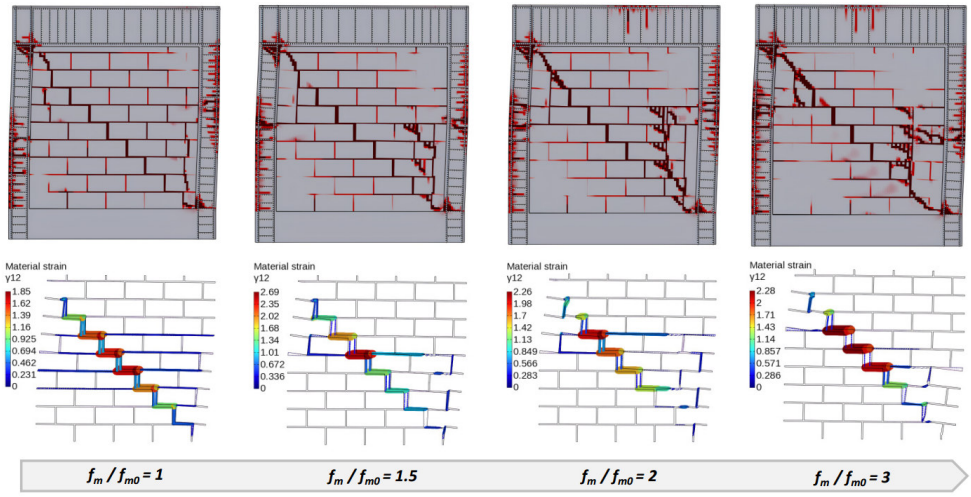

(a)

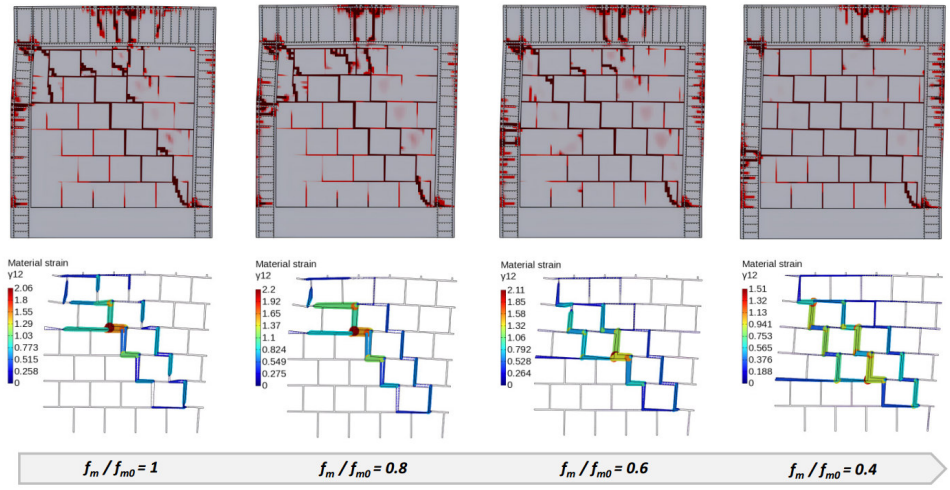

(b)

Figure 3.27: Effect of mortar strength on the evolution of damage and mortar sliding as a function of unit-to-mortar strength ratio: (a) Specimen S1A; (b) Specimen S1B.

The behaviour of the specimens was further examined by evaluating the distribution of shear forces along the surrounding frame. In the case of specimen S1A, increasing the compressive strength of mortar led to a gradual reduction of the contact zones, areas where shear forces due to the infill tend to concentrate (Figure 3.28a). As these zones became more confined, the intensity of the shear

demand within them increased. This shift was also reflected in the shape of the shear diagram along the contact zones, which evolved from a nearly linear profile to a markedly nonlinear one as the decreasing frame-infill contact area reduced the effective load-transfer region, causing the infill-induced shear to concentrate over progressively smaller portions of the columns rather than being almost uniformly distributed. On the other hand, specimen S1B, which was subjected to a reduction in mortar strength, exhibited an opposite response (Figure 3.28b). The contact lengths increased significantly, accompanied by more pronounced sliding behaviour and a noticeable decrease in localized shear demand. This redistribution of forces resulted in a less concentrated shear demand at column ends and a likely-linear profile, highlighting the influence of weaker mortar on the overall structural response.

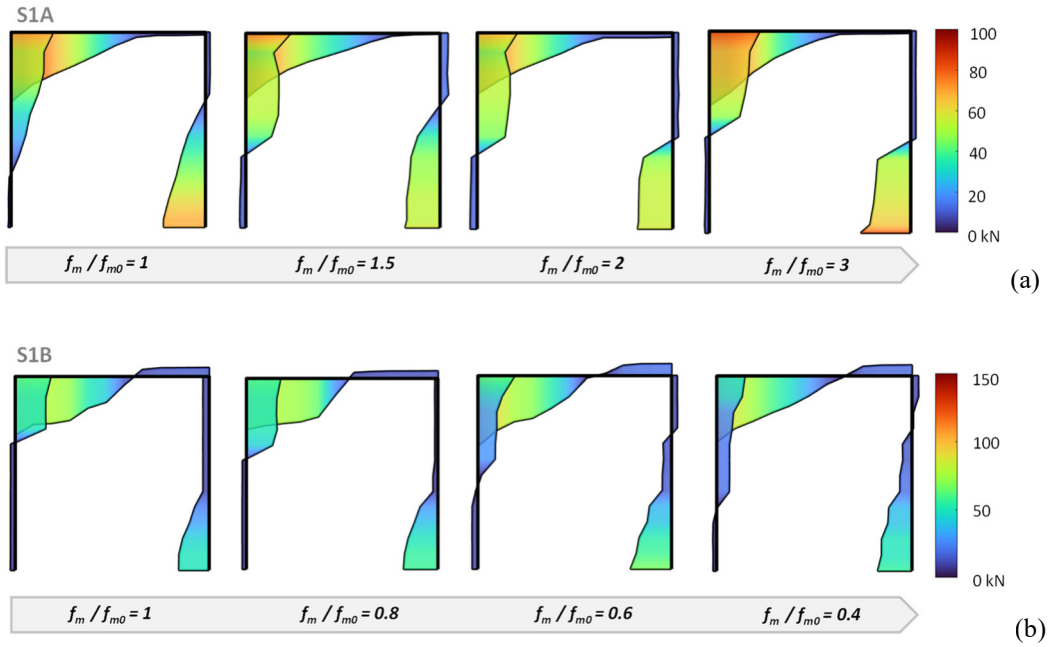

Figure 3.28: Effect of mortar strength variation on the shear demand distribution over the surrounding frame: (a) Specimen S1A; (b) Specimen S1B.

The findings of the current parametric investigation allow for several fundamental observations. A key factor influencing both global and local structural response is the unit-to-mortar strength ratio ($\tilde{f}_b / f_m$). The latter plays a decisive role in influencing the failure mode and overall performance of masonry-infilled RC frames. For both specimens analysed, each representing different masonry configurations, low values of $\tilde{f}_b / f_m$ (e.g. less than one) were associated with failure mechanisms dominated by diagonal shear with units crushing. Although these configurations exhibited higher global capacity, their response was particularly brittle due to the higher concentration of shear demand in a reduced contact zone. In contrast, when $\tilde{f}_b / f_m$ ratio increases, particularly over 2, the failure mode shifted toward a pure sliding mechanism within the infill. This transition resulted in a more ductile global response and less severe damage of column ends due to a reduction of shear demand concentration, even though with a reduction in global capacity. From a structural design and assessment perspective, it is important to highlight that although higher ratios correspond to lower overall strength, the capacity remains substantially greater than that of a bare frame. For example, specimen S1A, with $\tilde{f}_b / f_m = 2.31$, achieved a peak strength 2.7 times that of the bare frame, while specimen S1B, with $\tilde{f}_b / f_m = 2.40$, reached 2.3 times the bare frame's capacity. In both cases, the behaviour was classified as ductile. This ratio also has implications for local shear demand. Figure 3.29 presents the shear forces recorded at the top of the left column and the base of the right column during testing. These are compared against the shear capacity (V_R), calculated using the **Sezen and Moehle, (2004)** formulation, which assumes a reduced shear span equal to one-fifth of the column height, as illustrated in Figure 3.24 and Figure 3.25. Comparable results would be obtained using the **Eurocode 2 (2004)** approach.

As shown in Figure 3.29, modifications in the unit-to-mortar strength ratio can either amplify or reduce local shear demands. In some cases (e.g., Figure 3.29b), the demand even exceeds the calculated column shear strength. This localised increase is attributed to two main factors: the higher force transfer from infills built with stronger mortar, and the reduction of contact zones, which intensifies shear concentration in those regions.

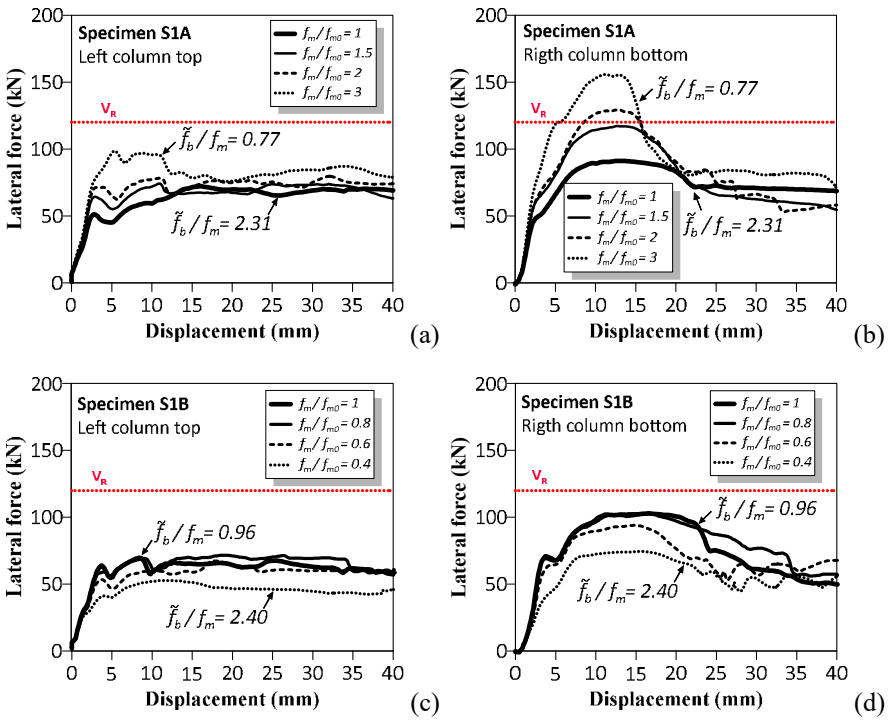

Figure 3.29: Effect of mortar strength on the local shear demand: (a) Specimen S1A left column top; (b) Specimen S1A right column bottom; (c) Specimen S1B left column top; (d) Specimen S1B right column bottom.

Figure 3.30 presents a synthesis of how the $\tilde{f}_b/f_m$ ratio influences local shear demand, expressed as the shear force recorded at the ends of the infilled frame columns ($V_{d,IF}$), normalised against the corresponding values from the bare frame configuration ($V_{d,BF}$). The data reveal that the bottom end of the right column consistently absorbs a greater portion of the shear force compared to the top end of the left column. Furthermore, across all examined scenarios, an increase in the strength ratio correlates with a general reduction in localised shear effects. This trend emphasises the significance of this ratio not only in affecting the mechanical behaviour of the infilled frames, but also as a potentially valuable parameter for both the design of new masonry infills and a possible estimator of local shear demand in case of existing structures.

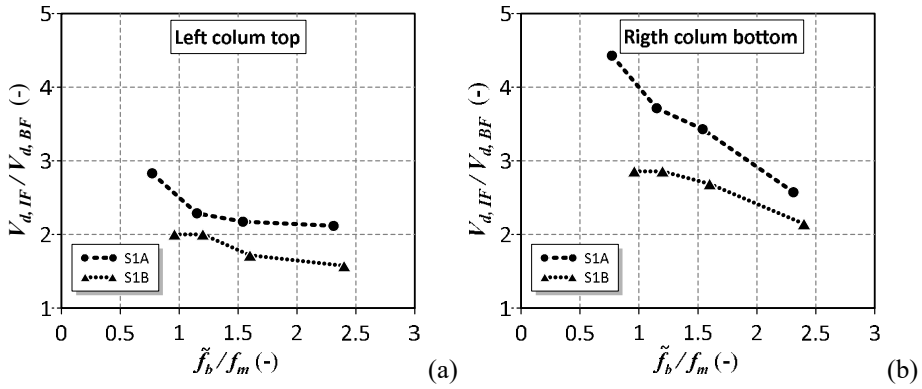

Figure 3.30: Normalised variation of the local shear demand of the infilled frame compared to the bare frame configuration, examined against the $\tilde{f}_b/f_m$ ratio: (a) Specimen S1A and S1B left column top; (b) Specimen S1A and S1B right column bottom.

3.5 Conclusions

This chapter introduced a detailed framework for high-fidelity numerical micro-modelling of RC frames with masonry infills, capable of replicating experimental tests, assessing parameters not available from the experiments, and simulating new configurations. Masonry units, mortar joints, and concrete elements were modelled as separate continuum elements. The micro-modelling strategy was implemented using the STKO interface for OpenSees, leveraging parallel computing for the analyses. Validation was performed through comparison with four experimental tests involving infilled frames realised with different masonry typologies. The calibrated and validated models were then employed to explore how masonry design parameters influence the distribution of internal forces, calculated through numerical integration of nodal forces at various cross-sections, and the resulting failure mechanisms.

Key findings from the study include:

- The proposed micro-modelling approach accurately captured both global and local responses of infilled frames, as well as the associated damage mechanisms. It proved useful for extracting physical and mechanical insights that are difficult to obtain experimentally and for generating numerical specimens to complement experimental datasets.

- Modelling mortar joints explicitly enabled the identification of sliding mechanisms that occur when joint strength is lower than that of the masonry units, addressing limitations in previous studies that used homogenised masonry representations.
- The internal force distribution within frame members was closely linked to the observed damage mechanisms, which influenced the frame-infill contact lengths, zones where shear demand tends to concentrate.
- Specimens exhibiting sliding behaviour showed a progressive increase in contact length as the lateral drift grows, while those experiencing a purer diagonal shear maintained reduced contact zones.
- Shear demand in contact regions significantly exceeded the maximum values expected for bare frames. In contrast, no relevant modification affected the maximum moment expected at the column ends.
- The parametric investigation revealed that the unit-to-mortar strength ratio ($\tilde{f}_b / f_m$) is a critical factor in shaping both global and local structural responses. Ratios above 2 led to pure sliding mechanisms in the infill, resulting in ductile behaviour with reduced overall strength. Ratios below 1 were associated with diagonal shear failure, yielding higher overall capacity but more brittle responses.
- Increasing the $\tilde{f}_b / f_m$ ratio generally led to a reduction in local shear effects. This suggests that the ratio may serve as a useful parameter in the design of masonry infills and as a potential indicator for estimating local shear demand in existing infilled frame structures.

Chapter 4

Cyclic validation of the micro-modelling strategy

This chapter is dedicated to the validation of the refined micro-modelling strategy developed in the previous chapter, with the specific aim of assessing its capability to reproduce the in-plane cyclic response of masonry-infilled reinforced concrete frames. While the modelling framework has already been shown to capture the monotonic response with good accuracy, its reliability under cyclic loading conditions must be carefully verified, given the pronounced stiffness degradation, strength deterioration and damage accumulation typically observed in masonry infills subjected to repeated displacement cycles.

The validation is therefore not limited to the reproduction of global response indicators, such as peak strength or backbone envelopes, but extends to the accurate simulation of the full cyclic behaviour, including loading and unloading branches, strength degradation and the evolution of damage mechanisms. This step is essential to establish the proposed micro-modelling approach as a robust numerical reference, capable of realistically representing the complex infill-frame interaction under cyclic in-plane loading and of supporting subsequent analytical and modelling developments presented in the thesis.

To this end, the present chapter employs refined STKO/OpenSees micro-models calibrated against the ERIES-ENFRAG experimental campaign conducted at the EUCENTRE laboratory. Once calibrated, the numerical model is used to investigate the influence of different quasi-static cyclic loading protocols on the structural response of infilled frames, with particular attention to the effects of drift amplitude, loading history and cycle repetition on the observed damage patterns and overall global response prediction accuracy.

The results presented in this chapter are part of an ongoing research activity carried out within the ERIES-ENFRAG project, coordinated by University College London and Sapienza University of Rome. The reference experimental campaign is mentioned here to provide essential context for the numerical study; its presentation and discussion is outside the scope of this chapter. The experimental outcomes has been submitted for potential publication in *Earthquake Engineering and Structural Dynamics* as one of the ERIES-ENFRAG project results:

- Roberto Gentile, Giulia Angelucci, Jingren Wu, *Marilisa Di Benedetto*, Riccardo Milanesi, Giulio Augusto Tropea, Fabrizio Mollaioli, Fatemeh Jalayer, Fabio Freddi, Fabio Di Trapani, Paolo Morandi, Gerard J. O'Reilly. Characterising earthquake damage using energy-based approaches: an experimental campaign on masonry infills (*Under revision*).

4.1 Reference experimental campaign within the ERIES-ENFRAG project

The experimental campaign was designed to investigate the in-plane cyclic response of masonry-infilled reinforced concrete frames and the associated damage mechanisms induced by different loading histories. To this purpose, the specimens were subjected to quasi-static in-plane cyclic loading protocols characterised by identical peak displacement demands, while varying the imposed energy demand. Although dynamic out-of-plane shake-table tests were performed following the quasi-static in-plane phase, only the in-plane response is relevant to the objectives of this chapter. The following sections provide an overview of the specimen details, test configuration, loading protocols, and the instrumentation adopted for the in-plane loading phase.

4.1.1 Specimens' details

The experimental campaign investigated three full-scale masonry infill specimens (SP1, SP2, SP3), each with dimensions of 3.50 m in length, 2.75 m in height, and 13 cm in thickness, including a 1 cm plaster layer. The infills were installed inside a rectangular steel-concrete composite frame composed of UPN400 S355 steel profiles, filled with high-strength concrete with internal reinforcement. Following the approach of **Morandi et al. (2025)**, this type of frame was chosen because it reproduces the in-plane deformation response of a non-seismically detailed RC frame while remaining essentially linear-elastic, enabling repeated use

and ensuring uniform boundary conditions throughout the tests. As reported in **Morandi et al. (2025)**, preliminary cyclic loading was applied to the bare frames to generate controlled micro-cracking in the composite sections, thereby standardizing stiffness and initial damage before installing the infills. The infill walls were built using 12 cm-thick hollow clay blocks (12×25×25 cm, 65% void ratio) laid with 1 cm mortar joints. A general-purpose M2.5 mortar (nominal compressive strength 2.5 MPa), representative of common Italian construction practices from the 1960s to the 1980s, was employed; head joints were only partially filled to reflect typical workmanship of that era. To ensure proper connection with the surrounding frame, the perimeter joint was filled with mortar. With plaster applied on one face only, the resulting masonry exhibited a volume weight of 8.20 kN/m³, corresponding to an infill self-weight of approximately 10.3 kN. General details of the specimens are shown in Figure 4.1.

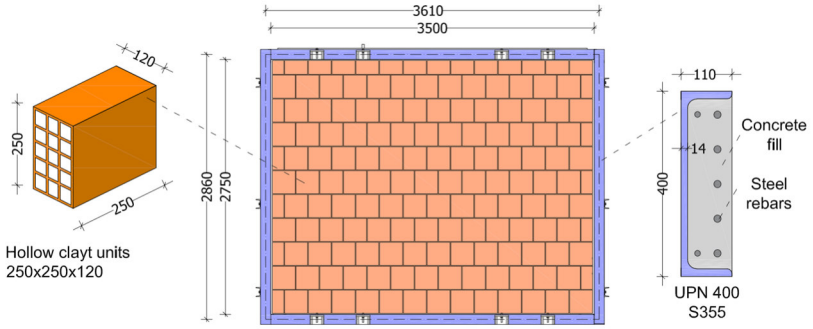

Figure 4.1: Specimens' details.

A comprehensive set of material tests was performed to determine the mechanical properties of the components, with the results summarised in Table 11.

Table 11: Mechanical parameter characterisation of the specimens' materials.

Material	Mechanical property	Symbol	Mean	CoV
Clay units	Vertical compressive strength	f_b	7.20 MPa	14.10%
	Horizontal compressive strength	f'_b	4.04 MPa	14.50%
Mortar	Flexural strength	f_{fl}	0.384 MPa	20.30%
	Compressive strength	f_m	1.553 MPa	13.80%
Masonry	Vertical compressive strength	f_{vert}	1.503 MPa	17.80%
	Vertical elastic modulus	E_{vert}	3811 MPa	17.00%
	Horizontal compressive strength	f_{lat}	2.557 MPa	7.50%
	Horizontal elastic modulus	E_{lat}	2683 MPa	41.50%

4.1.2 Test setup

The experimental setup adopted for the campaign corresponds to that of **Morandi et al. (2025)** and is illustrated in Figure 4.2. As previously stated, the programme involved a quasi-static cyclic IP phase followed by shake-table dynamic OOP tests. However, only the IP configuration is relevant to the scope of this chapter, and the OOP phase is therefore omitted here. During the IP tests, the shaking table was locked and behave as a rigid strong floor. The specimen was installed on a dedicated steel foundation system placed directly on the table, consisting of a welded double-HEB400 beam stiffened with vertical plates and anchored to the platform through thirty-four M30 bars. Fourteen additional bars connected this foundation beam to the composite frame. To ensure sufficient stiffness along the top boundary, a HEA200 beam was bolted to the upper part of the frame using M18 and M27 bolts. Two steel girder boxes at the top corners provided the anchorage points for a diagonal restraint system composed of S355 steel tubular members connected through hinged joints. These diagonals ensured out-of-plane stability throughout the IP loading. In-plane forces were applied by a 500 kN servo-hydraulic actuator positioned between one of the girder boxes and a rigid reaction wall, enabling displacement-controlled loading while the locked table ensured a fixed reaction base. Instrumentation for the IP phase included accelerometers and linear potentiometric transducers, used to record accelerations, displacements, and inter-storey drifts.

Figure 4.2: Test setup for the ERIES-ENFRAG campaign.

The three IP loading protocols are illustrated in Figure 4.3 and summarised in Table 12. Each protocol consisted of displacement-controlled cycles applied at increasing drift amplitudes, corresponding to a sequence of target drift levels $\theta_{max} = [\theta_1, ..., \theta_d]$. For each drift level, a full loading cycle $[0, \theta_{max}, -\theta_{max}, 0]$ was repeated c times.

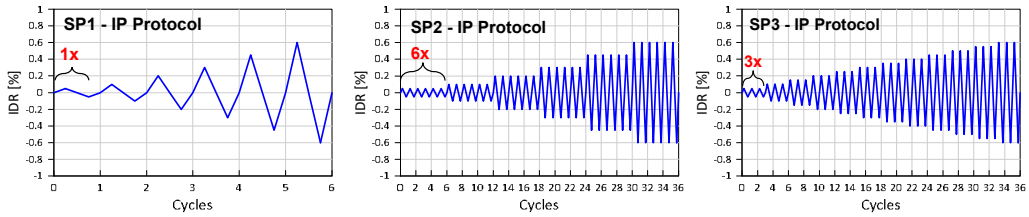

Figure 4.3: IP loading protocols for specimens SP1, SP2, SP3.

All three protocols were defined through a process of calibration defining cyclic displacement histories up to the same nominal maximum in-plane drift of 0.65%, a value selected to induce a moderate level of IP damage. The three loading protocols were differentiated to produce diverse hysteretic energy-drift relationships. For SP1, the protocol was designed to generate a lower energy input by limiting the number of cycles at each drift level (seven drift levels with only one cycle per level). In contrast, SP2 followed a protocol intended to yield a higher energy input, achieved by increasing the number of repetitions per drift level (seven drift levels, six cycles each). SP3 protocol was designed to match the energy-drift trend of SP2 but through a different strategy: the protocol included a larger number of drift levels (twelve in total) combined with a standard repetition count (three cycles per level).

Table 12: Loading IP protocols for the three specimens.

Specimen ID	**Nominal in-plane drift levels (%)**	**c**	**Notes**
SP1	0.10, 0.20, 0.30, 0.40, 0.50, 0.65	1	**Low** $E_h \vert EDP_{IP}$
SP2	0.10, 0.20, 0.30, 0.40, 0.50, 0.65	6	**High** $E_h \vert EDP_{IP}$
SP3	0.10, 0.15, 0.20, 0.25, 0.30, 0.35, 0.40, 0.45, 0.50, 0.55, 0.60, 0.65	3	**High** $E_h \vert EDP_{IP}$

4.2 Micro-modelling of the infilled RC frames

The numerical strategy adopted is an application of the micro-modelling approach presented in the previous chapter and is therefore only summarised here focusing on minor variations due to different project needs. For a complete description of the modelling assumptions, element formulations, and constitutive laws, the reader is referred to Chapter 3.

4.2.1 General features and model assembly

Although the present study focuses on the IP phase, the numerical models were constructed in a full 3D environment within STKO/OpenSees software so that the same setup can be directly employed in future out-of-plane dynamic analyses. An overall scheme of the micro-model is reported in Figure 4.4.

The infilled frame was represented through a continuous micro-model. In this approach, the masonry panel was discretised using layered *ASDShellQ4* elements (**Lu et al., 2015; Petracca et al., 2017a**), which follow the principles of composite-material mechanics. In this formulation (**Lu et al., 2015**), the section is subdivided into multiple layers, each characterised by its own thickness and nonlinear material properties, allowing the model to represent the actual layers within the thickness of the infill (masonry layers and plaster layer). During the analysis, strains and curvatures are first computed at the mid-surface of the shell; the strains in the remaining layers are then obtained by assuming linear variation through the thickness. Stresses are evaluated layer by layer through the assigned constitutive laws, and the internal forces (membrane forces and bending moments) are obtained by numerical integration across the layered section. This approach enables the element to capture the coupled in-plane and out-of-plane deformation, including bending, shear, and bending-shear interaction. The layered-shell formulation is therefore well suited for representing multi-layered materials and is consistent with potential extensions of the model to out-of-plane dynamic simulations.

Material nonlinearity was reproduced through the *ASDConcrete3D* damage-plasticity model (**Petracca et al., 2023**), applied consistently to both masonry and mortar layers. Different compressive and tensile strengths were assigned to mortar joints depending on their structural role: bed joints adopt the experimentally measured material properties, while head joints are reduced to 50% of these values. This strategy indirectly accounts for the different contact conditions observed in

hollow clay masonry: solid-to-solid interfaces (full contact, no reduction) and hollow-to-hollow interfaces (50% reduction).

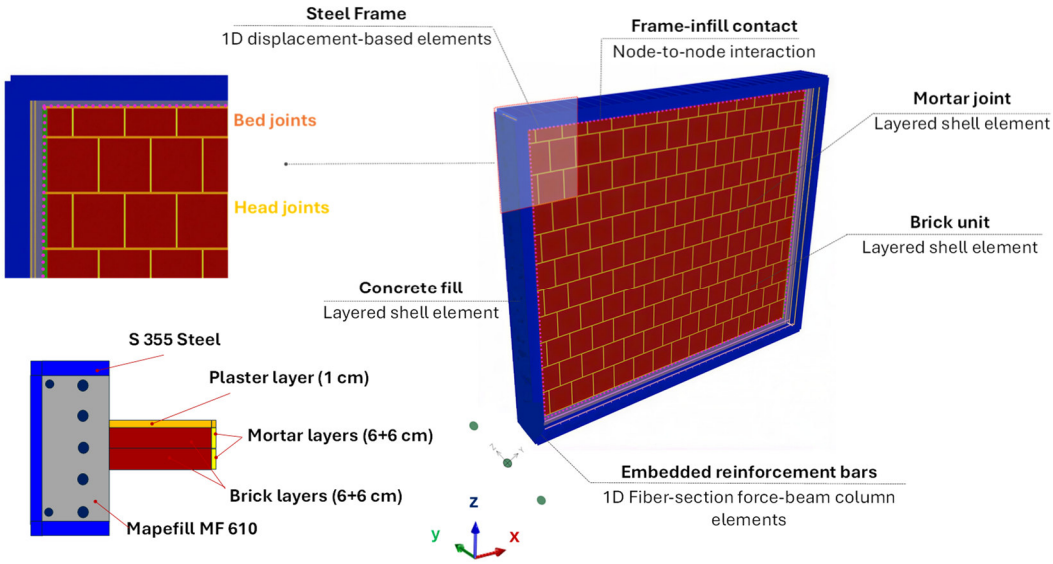

Figure 4.4: Scheme of the micro-modelling strategy adopted for reproducing the experimental tests.

The composite steel-concrete frame was modelled using the same strategy described previously: steel UPN profiles were represented by 1D displacement-based beam-column elements with a distributed-plasticity fiber discretisation and *Steel02* constitutive law, while concrete infill inside the steel profiles was modelled through *ASDShellQ4* layered-shell elements using *ASDConcrete3D*. Reinforcing bars within the concrete matrix were modelled as 1D force beam-column fiber elements (**Petracca et al., 2017a**), embedded into the concrete frame elements via *ASDEmbedded* node-interactions to enforce perfect bond between steel rebars and concrete. The interface between the masonry panel and the frame is described through zero-length *ASDImplex* contact elements (**Oliver et al., 2008; Petracca et al., 2017a**) assigned to node-to-node interactions along the perimeter of the infill.

Boundary conditions replicated those of the experimental setup: the base of the frame was fully restrained, horizontal displacements along the top edge reflect the bracing system used in the laboratory, and self-weights were applied consistently through distributed edge and surface loads. The in-plane loading history was imposed at the top of the frame through an imposed-displacement, following the IP drift records of the experimental tests. The mesh was generated as a structured

quadrilateral discretisation, with an average element size of 20 mm, refined around mortar joints. To efficiently perform nonlinear cyclic analyses, the model was partitioned into 10 subdivisions and run using OpenSeesMP, as already discussed in Chapter 3.

4.2.2 Calibration and validation

A dedicated calibration phase was nonetheless required to ensure that the model could accurately reproduce the overall response corresponding to the IP protocols defined in Section 4.1.2. To this end, the material parameters not directly measurable from the experimental campaign were calibrated following the procedure described in Chapter 3. Slight adjustments were made for fracture energies in tension and compression to ensure consistency with the experimentally observed crack patterns and with the measured lateral force-displacement hysteretic response. The calibration phase was carried out using the specimen tested under the first IP protocol (SP1). Once the material parameters were identified, the same set of properties was adopted for the remaining two specimens (SP2 and SP3) for validation, as the panels were nominally identical and differed only in their loading protocol. The finally adopted material parameters are reported in Table 13.

Table 13: Mechanical properties used for the concrete fill and the masonry panel.

Material	E (MPa)	f_c (MPa)	f_t (MPa)	G_c (N/mm)	G_t (N/mm)
Concrete fill	39000	70	7.00	39.00	0.157
Masonry unit	2878	4.00	0.40	8.00	0.07
Mortar bed joint	840	1.5	0.036	10.00	0.04
Mortar head joint	420	0.75	0.018	6.00	0.02
Plaster	840	1.5	0.036	10.00	0.04

The subsequent validation therefore consisted in comparing the numerical response with the corresponding experimental hysteretic curves, verifying that the model accurately reproduced the observed stiffness degradation, peak strength, pinching behaviour and cumulative hysteretic energy. Figure 4.5 presents the comparison between the numerical and experimental force-displacement responses for the three analysed specimens.

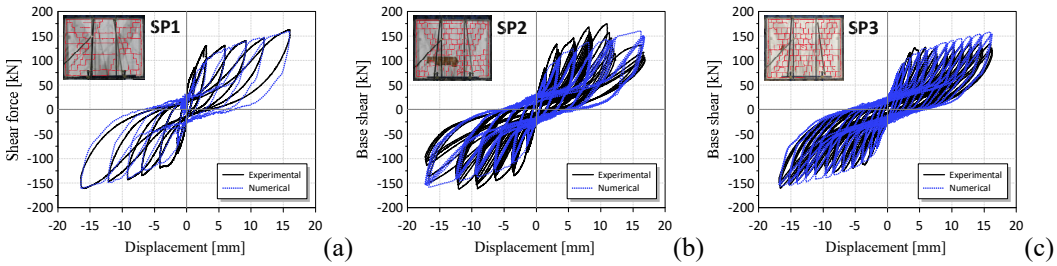

Figure 4.5: Numerical vs. Experimental cyclic response of the three tested specimens: (a) SP1; (b) SP2; (c) SP3.

As expected, the agreement for SP1 is high across all key response indicators, initial stiffness, peak strengths, and pinching, reflecting the fact that this specimen was used for calibration. For SP2 and SP3, which were instead used for validation, the numerical response remains in good agreement with the experimental curves, although some discrepancies appear in the peak strength per cycle. These differences are more pronounced in SP2, where the experiment exhibited a partial expulsion of bricks during the analysis. Such phenomenon cannot be captured by the adopted continuous finite-element micro-model, which represents the masonry as a smeared continuum rather than allowing discrete unit loss. Despite this limitation, the overall cycle shape is well reproduced for both specimens.

The generally good match across all three tests suggests that the model can capture the cumulative degradation mechanisms governing energy dissipation under cyclic loading. A direct comparison of the experimental and numerical hysteretic energies is provided in Figure 4.6 for all three protocols.

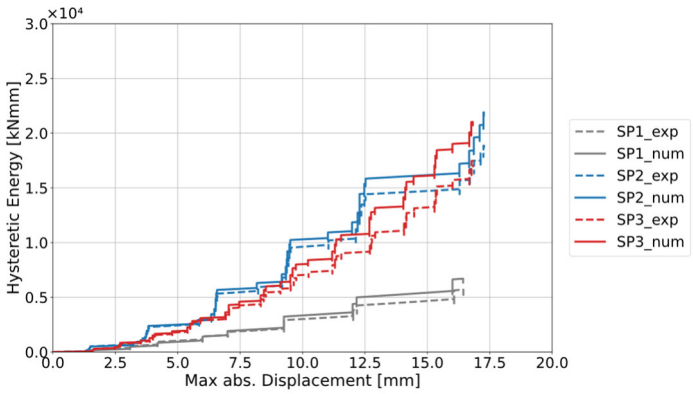

Figure 4.6: Numerical vs. Experimental cumulative hysteretic energy of the three tested specimens (SP1, SP2, SP3).

The comparison of cumulative hysteretic energy (Figure 4.6) further confirms the satisfactory predictive capability of the model. For SP1, the agreement between numerical and experimental energy dissipation is notable. Specimens SP2 and SP3 show a less accurate match, particularly at larger drift levels. Nevertheless, the overall response remains well captured, and the numerical model reproduces the cumulative energy with acceptable accuracy. Taken together, these results indicate that the model provides a sufficient robust representation of the energy dissipation mechanisms across all IP loading protocols.

Additionally, a comparison between the simulated and experimentally observed damage mechanisms is presented to validate the modelling approach. Figure 4.7 illustrates the crack patterns comparison. The micro-model successfully reproduces the key features of the response, like the progressive sliding along mortar joints and shear sliding cracks, and the detachment of infill from the steel-concrete frame at a certain drift level. These mechanisms are consistent with those recorded experimentally. The correspondence between experimental and numerical mechanisms further supports the reliability of the calibrated model and its ability to represent the interaction governing the cyclic behaviour of masonry-infilled frames.

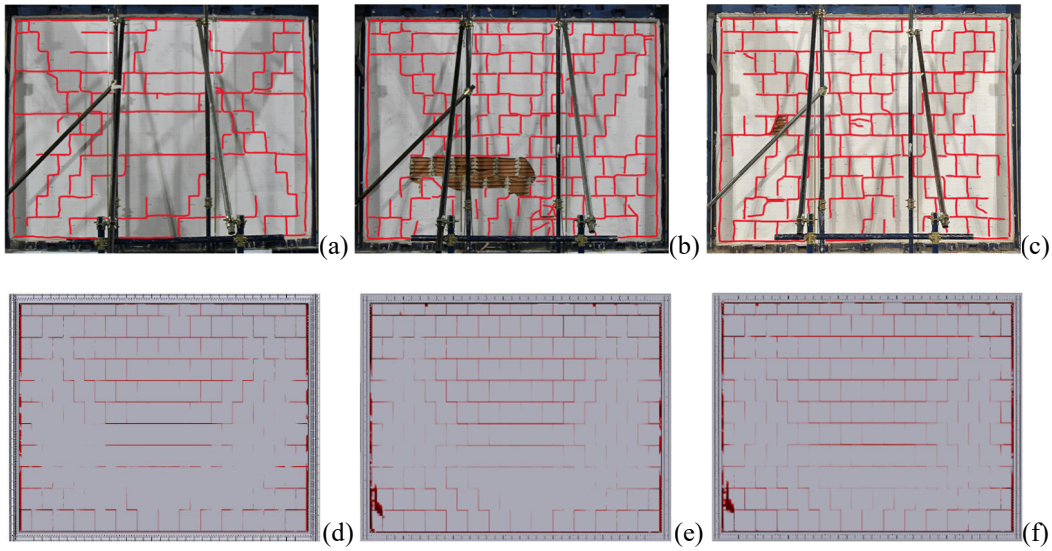

Figure 4.7: Numerical vs. Experimental damage pattern of the three tested specimens: (a) SP1 (exp); (b) SP2 (exp); (c) SP3 (exp); (d) SP1 (num); (e) SP2 (num); (f) SP3 (num).

4.5 Conclusions

This chapter has presented the cyclic validation of the refined micro-modelling strategy developed in this thesis, through comparison with full-scale quasi-static in-plane experimental tests on masonry-infilled reinforced concrete frames. The numerical models, calibrated on a reference experimental test and subsequently validated against different cyclic loading protocols, have demonstrated a satisfactory capability to reproduce both the global response and the key features of the cyclic behaviour observed experimentally.

The comparisons show that the proposed micro-modelling framework accurately captures initial stiffness, peak strength, stiffness degradation, pinching effects and overall hysteretic response across the three investigated loading protocols. Although some discrepancies were observed at higher drift levels, particularly for specimens exhibiting partial expulsion of masonry units during testing, these differences can be attributed to modelling limitations inherent to the adopted continuous smeared representation of the masonry, which does not allow for discrete unit loss. Despite this limitation, the overall shape of the hysteretic loops and the evolution of the cyclic response remain well captured.

The validation was further supported by a qualitative comparison of damage mechanisms. The numerical simulations successfully replicated the experimentally observed cracking patterns, including progressive sliding along mortar joints, shear-related cracking and partial detachment of the infill from the surrounding frame. This correspondence confirms that the adopted modelling approach is able to capture the governing infill-frame interaction mechanisms under cyclic in-plane loading.

Overall, the validated micro-modelling strategy provides a robust and high-fidelity representation of the experimental tests, even under cyclic loading, and can therefore be reliably used to investigate relevant response parameters and to serve as a reference benchmark for the development and assessment of simplified modelling approaches, which are discussed in subsequent chapters.

Chapter 5

Local shear demand analytical correction model for equivalent single strut macro-model

The seismic interaction between masonry infills and reinforced-concrete frames remains a complex and debated issue, especially regarding how to incorporate the additional forces generated by local infill-frame interaction. A comprehensive overview of the available modelling strategies and formulations has already been provided in Chapter 2; here, only the essential references are recalled contextualising the treatment of local interaction in simplified infilled-frame models.

As outlined in Chapter 2, refined homogenised- and micro-modelling approaches can reproduce the local interaction mechanisms, enabling the direct extraction of the resulting shear demand (e.g. **D'Ayala et al., 2009; Cavaleri and Di Trapani, 2015; Milanesi et al., 2018; Di Trapani et al., 2024**). Among these, the micro-modelling strategy, introduced in Chapter 3 offers the most comprehensive representation of local response, as it can capture a wider range of failure scenarios, such as sliding along mortar joints, not accounted for in homogenised-modelling approaches based on homogenised masonry. This makes micro-modelling significantly more reliable for investigating local interaction effects. However, such high-fidelity analyses are rarely used in engineering practice due to their computational cost and modelling complexity. More commonly, practitioners adopt simplified single-strut macro-models (e.g. **Dolšek and Fajfar, 2008; Rodrigues et al., 2010; Di Trapani et al., 2018; Liberatore et al., 2018**), which greatly reduce modelling effort but cannot reproduce local effects because of the concentric position of the strut. So that several authors proposed multi-strut formulations (**Chrysostomou et al., 2002; El-Dakhakhni et al., 2003; Crisafulli**

and Carr, 2007; Fiore et al., 2012; Jeon et al., 2015; Pashaie and Mohammadi, 2019). Although attractive, these models were mostly validated only against global responses, and not for local induced force, due to the lack of experimental measurements of column-end shear. Additionally, limited agreement exists on how to define strut geometry, nonlinear properties, and contact lengths. Given these challenges, several authors have pursued to preserve the simplicity of the concentric single-strut model by incorporating the additional shear demand as an explicit supplementary term.

A few simplified formulations have been proposed in the literature to estimate the additional shear transmitted by infill walls. Since the mathematical expressions and underlying assumptions of these models are extensively discussed in Chapter 2, only their conceptual background is briefly summarised here for the reader's convenience. **Basha and Kaushik (2019)** introduced a distributed force pattern along the contact regions, while **Wararuksajja et al. (2020)** proposed equations linking the extra shear to the expected failure mode. **Eurocode 8 (CEN, 2004a)**, for example, provides an upper-bound estimate of the extra shear that should be considered at column ends for design purposes. **ASCE/SEI 41-13 (2014)** offers a comparable interpretation based on the compressive capacity of the infill strut. **Hak et al. (2013)** introduced a drift-dependent reduction factor to modulate this additional shear at low deformation levels. **FEMA 356 (2000)** proposes either the use of eccentric struts or the application of strut axial forces directly to the columns to recover local shear effects. **Cavaleri and Di Trapani (2015)** derived empirical correlations linking the total shear demand to the axial force in the equivalent strut. Finally, **Di Trapani et al. (2018)** incorporated friction-related reductions to account for sliding at the base of the infill. For additional details, see Chapter 2, Section 2.4.

Overall, the literature presents fragmented and sometimes conflicting recommendations. With this motivation, in this chapter it is offered a practice-oriented analytical model capable of estimating the total shear demand at column ends while retaining the simplicity of concentric strut modelling. As suggested in **Di Trapani et al. (2018)**, the total shear is computed as the sum of the drift-induced shear and an additional shear contribution, updated step-by-step during nonlinear analysis. The proposed formulation differentiates between windward and leeward column ends and relies on semi-empirical estimates of the effective contact lengths between the masonry panel and the surrounding frame. Calibration is carried out using high-fidelity FE simulation internal forces results based on the extrapolation

methodology presented in Chapter 3 (**Di Trapani et al., 2024**). The predictive capability of the model, combined with the equivalent strut approach, is evaluated against a dataset of twenty numerically high-fidelity virtual copies of the experimental tests.

The outcomes presented in this chapter have been peer-reviewed and published in:

- Di Trapani, F., *Di Benedetto, M.*, Sberna, A. P., and Camata, G. (2025). Local Shear Demand Correction Model for the Analysis of Infilled Frames Using Equivalent Struts. Journal of Structural Engineering, 151(12), 04025208.

5.1 Evaluating additional shear demand induced by frame-infill interaction through an analytical approach

This work introduces an analytical formulation aimed at adjusting the shear demand at the ends of columns, employing a single equivalent strut macro-model. The approach assumes that the total shear force acting at a column cross-section in an infilled frame, denoted as $V_{d,tot}$, can be split into two distinct components (see Figure 5.1). The first, $V_{d,frame}$, corresponds to the shear associated with the lateral drift, while the second, $V_{d,inf}$, accounts for the additional shear induced by the interaction between the frame and the infill, specifically due to the horizontal force transmitted through the contact interface. Accordingly, the total shear demand at the column end is expressed analytically as:

$$V_{d,tot} = V_{d,frame} + V_{d,inf} \tag{54}$$

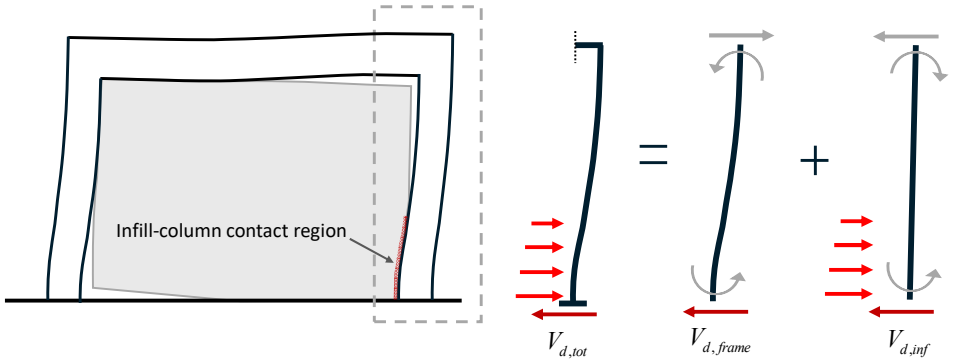

Figure 5.1: Decomposition of column-end shear demand in masonry-infilled RC frames.

This conceptual approach, previously introduced by **Saneinejad and Hobbs (1995)**, is referred to as the "*shear decomposition rule*." By assuming static equivalence between the simplified infilled frame represented through an equivalent strut model (Figure 5.2a) and the actual structural configuration of the infilled frame (Figure 5.2b), it is possible to formulate the global horizontal equilibrium for both systems. For the idealized model shown in Figure 5.2a, the equilibrium condition can be expressed as follows:

$$F = 2V_{d,frame} + N\cos\theta \tag{55}$$

In the idealised strut representation, the external lateral load F is balanced by the concentrated reaction forces at the supports. In this framework (see Eq.(55)), the axial force N acting in the equivalent strut and its inclination θ define the horizontal component contributing to equilibrium. Under this assumption, the shear demand recorded at the base of the right column corresponds solely to the drift-induced contribution ($V_{d,frame}$). Conversely, in the actual infilled-frame system, the horizontal force balance must consider all mechanisms transferring shear within the structure (Figure 5.2b). In particular, the frictional forces T mobilised along the beam-infill contact interface also participate in the equilibrium. As a result, the horizontal equilibrium condition for the real system becomes:

$$F = V_{d,\mathrm{tot}} + V_{d,frame} + T \tag{56}$$

where, the total shear demand $V_{d,tot}$ related to the frame-infill interaction is measured at the right column end.

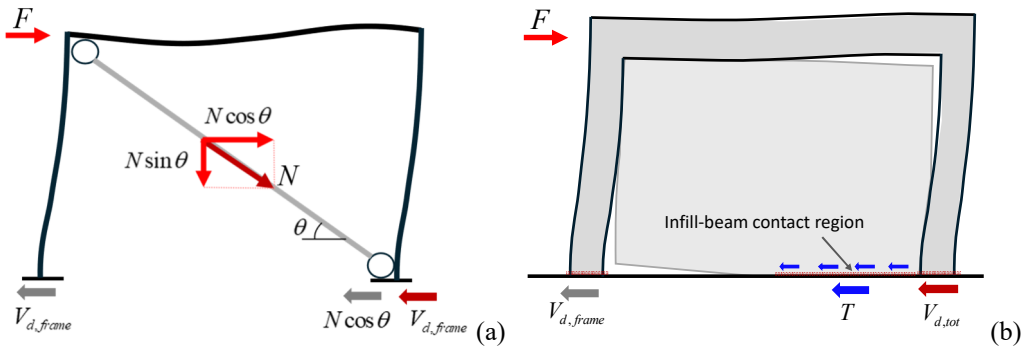

Figure 5.2: Lateral force equilibrium in infilled frames: (a) Equivalent-strut macro-model; (b) Actual frame-infill system.

By substituting the shear-decomposition expression from Eq. (54) into the horizontal equilibrium relation of Eq. (56), the following formulation is obtained:

$$F = 2V_{d,frame} + V_{d,\inf} + T \tag{57}$$

By enforcing global static equivalence between the two systems, by setting Eq. (55) equal to Eq. (57), the resulting expression for the additional shear demand can be derived as follows:

$$V_{d,inf} = N\cos\theta - T \tag{58}$$

Eq. (58) defines the additional shear demand arising from the interaction between the frame and the infill as a function of the axial force currently acting on the equivalent strut. This formulation establishes a direct analytical link between the simplified equivalent strut representation and the actual force transmission occurring within the physical structure. By substituting Eq. (58) into Eq. (54), it becomes possible to compute the total shear demand at the ends of the columns within an infilled frame modelled using the equivalent strut approach. This formulation remains applicable throughout all stages of structural analysis, including both linear and nonlinear regimes.

To apply Eq. (58), it is necessary to estimate the tangential friction force T at the interface between the infill and the frame. This force is associated with the effective contact length between the two components. A simplified evaluation of T can be performed by analysing the equilibrium of the portion of the masonry infill that is in contact with the frame, as illustrated in Figure 5.3a, where the forces involved in Eq. (58) are active. This contact region typically assumes a triangular configuration, with its base referred to as the "*equivalent contact length*." This length can be expressed as αl, where $\alpha \leq 1$, represents the portion of the panel length l in contact with the surrounding frame. The diagonal dimension a, oriented orthogonally to the direction of the equivalent strut, is then defined as $a = \alpha l / \sin\theta$.

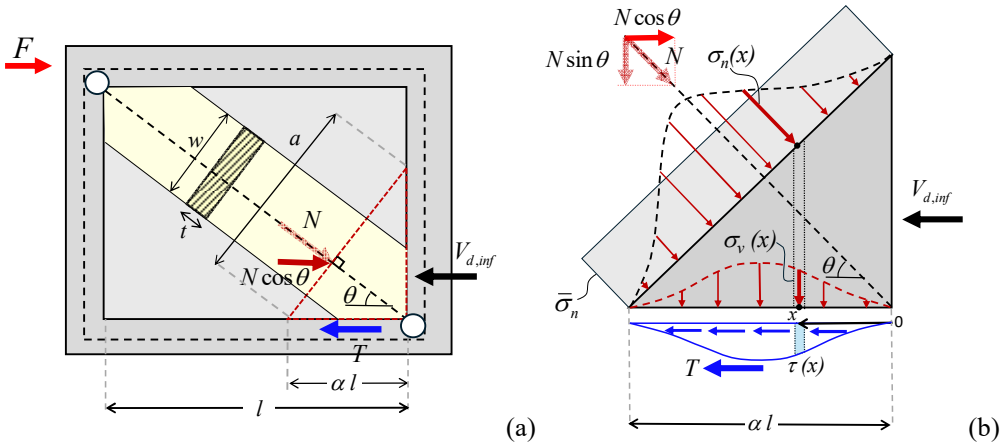

Figure 5.3: Load transfer at the right column end induced by frame-infill interaction: (a) overall configuration; (b) local force equilibrium in the infill corner.

Figure 5.3b provides a closer view of the force transfer taking place in the corner region of the infill. In this area, the tangential friction force T arises from the distribution of shear stresses $\tau(x)$ acting along the contact length αl. This force can be obtained by integrating the shear stress over the corresponding interface segment, as expressed by:

$$T = t \cdot \int_0^{\alpha l} \tau(x) dx \tag{59}$$

being t the thickness of the infill. The shear stress distribution $\tau(x)$ can be related to the normal compressive stresses $\sigma_v(x)$ acting along the interface by adopting a Mohr-Coulomb frictional law, which leads to the following relationship:

$$\tau(x) = \mu \sigma_v(x) \tag{60}$$

where μ is the friction coefficient. The latter can be assumed equal to 0.7, consistently with values commonly reported in the literature for mortar-to-concrete interfaces. In Eq. (60), the cohesion term is omitted, based on the assumption that it rapidly diminishes after the initial loading cycles. The vertical stress distribution $\sigma_v(x)$ can be represented as the projection of the normal stress $\sigma_n(x)$ acting along the diagonal length a. This stress profile typically follows a bell-shaped curve, as

depicted in Figure 5.3b and previously observed by **Saneinejad and Hobbs (1995)**. Accordingly, the resulting expression is:

$$\sigma_v(x) = \sigma_n(x)\sin\theta \tag{61}$$

By substituting the expressions given in Eq. (61) and Eq. (60) into Eq. (59), the following relation is obtained:

$$T = t \cdot \int_0^{\alpha l} \mu\sigma_n(x)\sin\theta dx \tag{62}$$

To make the integral in Eq. (62), more manageable, the variable normal stress $\sigma_n(x)$ is replaced with an equivalent constant value $\overline{\sigma}_n$ (Figure 5.3b). Under this simplification, the tangential force can be approximated as:

$$T \cong \mu\overline{\sigma}_n \sin\theta \cdot t \cdot \alpha l \tag{63}$$

where $\overline{\sigma}_n$ is obtained by dividing the axial force carried by the equivalent strut by its cross-sectional area, namely:

$$\overline{\sigma}_n = N/(w \cdot t) \tag{64}$$

where w denotes the width of the equivalent strut. By substituting the expression Eq. (64) into Eq. (63), and subsequently Eq. (63) into Eq. (58), leads to:

$$V_{d,\inf} = N\cos\theta - \frac{\mu \cdot N\sin\theta \cdot \alpha l}{w} = N\left(\cos\theta - \frac{\mu \cdot \sin\theta \cdot \alpha l}{w}\right) \tag{65}$$

Eq. (65) establishes a direct analytical relationship between the axial force currently acting on the equivalent strut and the corresponding additional shear demand at the ends of the columns. This formulation allows the shear contribution from the infill-frame interaction to be quantified at any stage of the structural

analysis. As introduced In Eq. (62) and then in Eq. (65), the determination of the equivalent contact length αl plays a crucial role in the accuracy of the model.

$$V_{d,tot} = V_{d,frame} + N\left(\cos\theta - \frac{\mu \cdot \sin\theta \cdot \alpha l}{w}\right) \tag{66}$$

This method leverages the simplicity of the equivalent strut macro-modelling approach while retaining the ability to account for the additional shear demand transmitted to the column ends. Eq. (66) is formulated as a correction to the shear demand obtained from structural analysis ($V_{d,frame}$), allowing for incremental capacity-to-demand evaluations at the column ends. Its formulation is particularly well-suited for nonlinear analysis, as it incorporates the axial force in the equivalent strut as a state variable reflecting the infill's response. The calibrated performance of Eq. (65) and (66) is discussed in detail in the subsequent sections.

5.2 Definition of Micro and Macro-scale FE models for infilled RC frames

Eq. (66) links the total shear demand of the real system ($V_{d,tot}$) to the axial force (N) obtained from the simplified equivalent-strut idealisation. To represent the behaviour of the actual infilled frame, a refined micro-model based on continuum FE elements can be employed, providing a high-fidelity numerical replica of the physical system. In parallel, a corresponding equivalent-strut macro-model can also be implemented, enabling a direct comparison between the response parameters predicted by the two modelling strategies. The formulation and implementation of the micro-models were already discussed in Chapter 3 and here briefly summarised, while macro numerical models are presented in the following sections.

5.2.1 Micro-model definition

For completeness, a brief overview of the micro-modelling approach adopted in this study is provided here; the full formulation, constitutive laws and calibration procedures are presented in Chapter 3. The micro-model, developed in STKO software platform for OpenSees, is based on a damage-mechanics framework and explicitly represents all physical components of the infilled frame. Masonry units, mortar joints and RC members are modelled as separate 2D continuum *quadrilateral* elements, allowing the numerical model to localise deformation and

capture distinct failure mechanisms, such as sliding along bed joints or cracking within the units. Nonlinear behaviour is reproduced through advanced damage-plasticity constitutive laws (*ASDConcrete3D* for both masonry units, mortar joints and RC frame) implemented in STKO/OpenSees, while reinforcing bars are modelled using embedded 1D *fiber-section* force *beam-column* elements, with *Hysteretic* material model, embedded in the concrete matrix with *ASDEmbedded* interaction to ensure full bond. The interaction between the masonry panel and the surrounding frame is described through *zero-length* contact elements with frictional behaviour, reproducing separation, contact and sliding along the interface. Boundary conditions, loading protocols and mesh refinement follow the same strategy discussed in Chapter 3.

5.2.2 Macro-model definition

The equivalent strut micro-models adopted in this study are developed within the OpenSees/STKO framework, following the fiber-section methodology introduced by **Di Trapani et al. (2018)**. The modelling scheme, illustrated in Figure 5.4a and Figure 5.4b, represents the strut as a no-tension, pinned element characterised by a concrete-like stress-strain behaviour. This constitutive law is defined by four key parameters: f_{md0} (peak strength), ε_{md0} (peak strain), f_{mdu} (ultimate strength) and ε_{mdu} (ultimate strain). These parameters are determined through specific empirical relationships, detailed in the following expressions.

$$f_{md0} = 26.9 \cdot \alpha^{-0.287} \cdot \tilde{f}_m \tag{67}$$

$$f_{mdu} = \left(0.043\beta - 0.06\right) f_{md0} \tag{68}$$

$$\varepsilon_{md0} = 3.024 \cdot \gamma^{0.347} \cdot \varepsilon_{m0} \tag{69}$$

$$\varepsilon_{mdu} = 0.0184 \cdot \delta^{-1.166} \cdot \varepsilon_{md0} \tag{70}$$

The parameters α, β, γ, and δ used in the empirical correlations are predictor variables introduced by **Di Trapani et al. (2018)** and reported in Chapter 2. The conventional compressive strength of the masonry, denoted as $\tilde{f}_m$, is defined as $\tilde{f}_m = \sqrt{f_{m1} \cdot f_{m2}}$, where f_{m1} and f_{m2} are the vertical and horizontal average

compressive strengths of the masonry, and $\varepsilon_{m0} = 0.0015$. The stress-strain behaviour of the equivalent strut is implemented in OpenSees using the Kent-Scott-Park *Concrete02* material model. Geometrically, the strut is modelled with a rectangular cross-section, where the thickness t corresponds to that of the infill wall, and the width w is determined following the procedure proposed by **Asteris et al. (2016)** outlined in Chapter 2. It is worth noting that alternative formulations may be adopted to define the compressive response of the equivalent strut. However, as indicated by Eq. (66), any uncertainty in the capacity model directly affects the accuracy of the estimated shear demand.

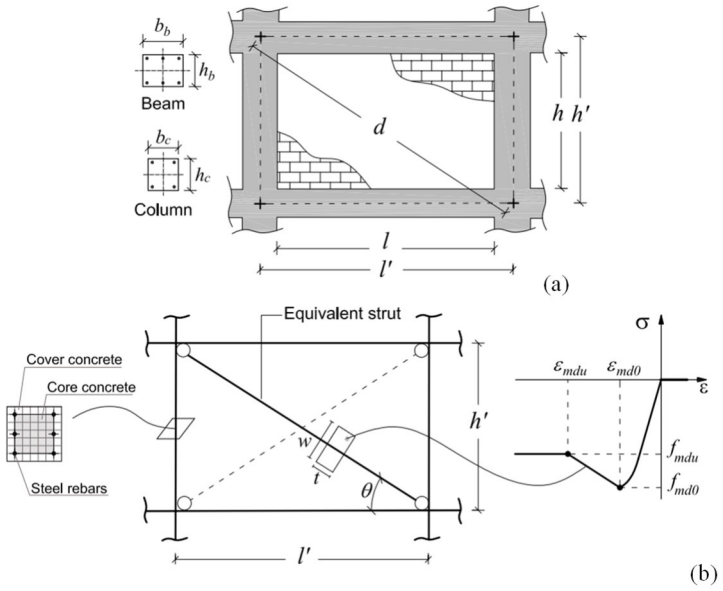

Figure 5.4: Macro-model representation of the infilled frame following **Di Trapani et al. (2018)**: (a) geometric layout of the physical system; (b) corresponding FE model.

The frame elements are represented using 1D force-based *beam-column* elements. Their fiber-sections incorporate different stress-strain behaviours for confined and unconfined concrete under compression. To account for fracture energy and ensure mesh-independent results, the uniaxial *ASDConcrete1D* material model is adopted for the concrete, which includes automatic regularization features. The overall modelling configuration, illustrated in Figure 5.4b, is pinned at the base nodes when replicating single-storey, single-bay experimental tests on infilled frame specimens. Consistent with the micro-modelling approach, the macro-model is initially subjected to vertical loading, followed by a displacement-controlled lateral pushover analysis.

5.3 Framework for defining the semi-empirical αl model to be used in Eq. (65) and Eq. (66) to predict additional and total shear demand

Eq. (65) and Eq. (66) rely on the definition of the equivalent contact length αl, where α denotes the fraction of the total infill length engaged in force transfer. To estimate this coefficient, a dedicated semi-empirical model is developed here, supported by an experimentally derived dataset. A key observation is that, according to the shear-decomposition concept expressed in Eq. (66), the coefficient α, and thus the corresponding contact length αl, can be evaluated by comparing the responses predicted by refined micro-models and simplified macro-models for the same infilled frame configuration. This becomes evident when Eq. (66) is rewritten in its simplified symbolic form:

$$V_{d,tot} = V_{d,frame} + V_{d,inf}\left(\alpha l\right) \tag{71}$$

In the proposed formulation, the only unknown quantity is the additional shear demand $V_{d,inf}\left(\alpha l\right)$, whereas both the total shear demand $V_{d,tot}$ and the drift-related component $V_{d,frame}$ can be directly obtained from the micro-model and macro-model, respectively. This allows the equivalent contact length αl to be determined at any step of the analysis by satisfying Eq. (71). To define a single representative value of αl for estimating the total shear demand, it is assumed that this parameter is evaluated at the point where the total shear demand reaches its maximum. Accordingly, the following condition is imposed on Eq. (71):

$$\max\left\{V_{d,tot}\right\} = \max\left\{V_{d,frame} + V_{d,inf}\left(\alpha l\right)\right\} \rightarrow \alpha l \tag{72}$$

Within this framework, the validation of the shear decomposition model introduced in Eq. (66) and applied under the condition defined in Eq. (72), is initially performed using a representative set of experimental tests on infilled frames. Subsequently, an empirical formulation for the parameter α is developed with the aim of minimizing the discrepancy between the maximum shear demand at the column ends obtained from the refined numerical model and that predicted by the proposed analytical model (Eq. (66)).

The overall procedure is structured as follows:

1. Define a dataset of experimental tests on infilled frames with complete material characterisation.

2. Model each specimen using both micro-modelling and macro-modelling approaches and calibrate lateral pushover analyses against the corresponding experimental backbone curves.

3. Extract the total shear demand ($V_{d,tot}$) and the drift-related shear component ($V_{d,frame}$) from the micro and macro models, respectively.

4. Apply and validate the shear decomposition model (Eq. (66)) for estimating the total shear demand, using the condition expressed in Eq. (72).

5. Develop an empirical analytical expression for α, based on geometric and mechanical parameters of the infilled frame.

6. Validate the predictive model using both training and independent validation specimens.

A schematic representation of this framework is provided in Figure 5.5.

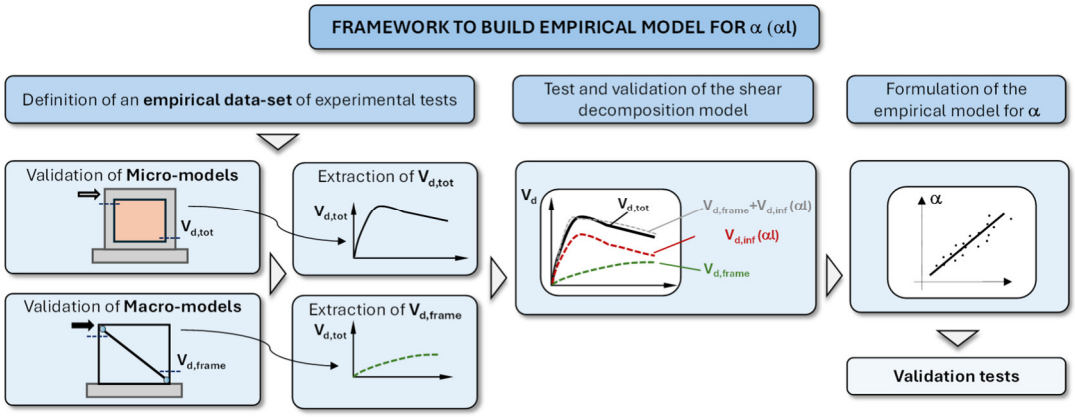

Figure 5.5: Framework for the semi-empirical model of α (αl).

5.4 Experimental dataset definition and validation of the numerical models

5.4.1 Reference experimental dataset

A wide range of in-plane experimental investigations on infilled reinforced concrete frames can be found in the literature (**Huang and Burton, 2019; Blasi et al., 2021**). However, only a limited number of these studies provide a complete characterisation of the materials involved. For the purposes of the current study, a heterogeneous selection of tests was made to cover different masonry typologies, aspect ratios, and failure mechanisms. The choice of these specific experimental programs was primarily motivated by their level of completeness, particularly the availability of detailed material data. In fact, the presence of results from associate tests on masonry prisms, both in compression along the principal directions and in shear, the compression tests on masonry units and mortar prisms were considered essential for the reliable definition and calibration of numerical models.

On this basis, fifteen in-plane tests on infilled frames were selected to form the training dataset, complemented by additional five tests used for validation. These specimens were drawn from the experimental campaigns conducted by **Mehrabi et al. (1996)**, **Colangelo (2005)**, **Blackard et al. (2009)**, **Cavaleri and Di Trapani (2014)**, **Bergami and Nuti (2015)**, **Ricci et al. (2018)**, **Morandi et al. (2018)**, and **Di Trapani et al. (2024)**. In all cases, the frames were first subjected to vertical loading and subsequently tested under cyclic or monotonic lateral actions. The aspect ratio of the infill panels (l/h) varied between 1.0 and 2.07, while the masonry typologies included solid and hollow clay bricks, hollow clay and concrete blocks, as well as solid calcarenite units. The geometric characteristics of the specimens are summarised in Table 14, together with the principal strength parameters of the masonry in compression (f_{m1} and f_{m2}) and in shear (f_{vm}). Additional mechanical properties obtained from the experimental programs are discussed in the following paragraph. By combining such a diverse set of experimental results, the study ensures that the proposed analytical and numerical framework is validated against a wide spectrum of structural behaviours. This approach not only strengthens the reliability of the model but also enhances its potential for application in practical design and assessment scenarios.

Table 14: Training and validation datasets: Typological, geometric, and mechanical details of the specimens.

	Reference	Spec. ID	Type of masonry	l (mm)	h (mm)	t (mm)	b_c (mm)	h_c (mm)	b_b (mm)	h_b (mm)	f_{vm} (MPa)	f_{m1} (MPa)	f_{m2} (MPa)
Training	Mehrabi et al. (**1996**)	S3	Solid concrete	2108	1422	92	178	178	152	228.6	1.15	14.19	14.19
		S5	Solid concrete	2108	1422	92	178	178	152	228.6	1.15	13.84	13.84
		S6	Hollow concrete	2108	1422	92	203	203	152	228.6	0.70	5.30	10.10
		S8	Hollow concrete	2108	1422	92	178	178	152	228.6	0.85	2.54	4.91
		S9	Solid concrete	2108	1422	92	178	178	152	228.6	1.00	14.19	14.19
		S11	Solid concrete	2948	1422	92	178	178	152	228.6	1.03	11.44	11.44
	Colangelo (**2005**)	C1	Hollow clay	1700	1300	120	200	200	200	250	0.87	3.39	5.10
		L2	Hollow clay	2300	1300	120	200	200	200	250	0.87	3.39	5.10
		N1	Hollow clay	2300	1300	160	200	200	200	250	0.58	2.74	3.90
	Cavaleri and Di Trapani (**2014**)	S1A	Solid calcarenite	1600	1600	200	200	200	200	400	0.73	3.08	2.67
		S1B	Hollow clay	1600	1600	150	200	200	200	400	1.07	4.18	8.70
		S1C	Solid concrete	1600	1600	300	300	300	300	400	0.29	0.30	1.70
	Blackard et al. (**2009**)	S	Solid clay	3378	1867	192	279	279	279	368	1.20	19.10	19.10
	Morandi et al. (**2018**)	TA2	Hollow clay	4220	2950	350	350	350	350	350	0.36	1.08	4.64
	Di Trapani et al. (**2024c**)	FIF	Hollow clay	2200	2100	230	250	250	250	350	0.36	2.52	3.36
Validation	Mehrabi et al. (**1996**)	S7	Solid concrete	2108	1422	92	203	203	152	228	0.93	13.60	13.60
		S12	Solid concrete	2946	1422	92	178	178	152	228	1.07	13.60	13.60
	Colangelo (**2005**)	V21	Hollow clay	2300	1300	160	200	200	200	250	0.35	2.56	2.24
	Ricci et al. (**2018**)	R1	Hollow clay	2350	1830	80	270	200	270	200	0.20	2.50	1.80
	Bergami and Nuti (**2015**)	FT2	Hollow clay	2300	1300	120	200	200	200	250	1.26	2.90	6.20

5.4.2 Micro- and Macro-models calibration and validation

To obtain reliable values of αl from Eq. (66), consistency between micro- and macro-model responses must be ensured, so that the equilibrium condition expressed in Eqs. (57) and (58) is satisfied. For this purpose, the experimental tests listed in Table **14** were reproduced according to the modelling procedures described earlier. Following the approach outlined in Chapter 3, all unknown mechanical properties were derived from the available experimental data. The mechanical properties of the materials, both experimental and calculated, including compressive strengths (f_c, f_b, and f_m), tensile strengths (f_{ct}, f_{bt}, and f_{mt}), elastic moduli (E_c, E_b, and E_m), and fracture energies, are reported in Table 14 and Table 15.

Table 15: Experimental and calculated material parameters for concrete and steel.

	Spec. ID	Concrete					Steel
		f_c (MPa)	f_{ct} (MPa)	E_c (MPa)	G_c (N/mm)	G_t (N/mm)	f_y (MPa)
Training	S3	30.87	3.29	21910	33.75	0.135	420
	S5	20.88	1.81	18052	32.50	0.130	420
	S6	25.84	3.13	19843	32.75	0.131	420
	S8	26.80	2.76	17220	33.00	0.132	420
	S9	26.80	2.76	17220	33.00	0.132	420
	S11	25.70	3.09	18120	32.75	0.131	420
	C1	43.70	3.20	34200	36.00	0.144	530
	L2	48.90	3.30	35417	37.00	0.145	530
	N1	44.50	3.20	34429	36.00	0.144	530
	S1A	25.00	2.75	25500	32.58	0.130	450
	S1B	25.00	2.75	25500	32.58	0.130	450
	S1C	25.00	2.75	25500	32.58	0.130	450
	S	30.50	3.00	30500	33.75	0.135	450
	TA2	27.05	2.70	27045	33.04	0.132	520
	FIF	11.23	0.70	16000	28.20	0.113	440
Validat.	S7	33.42	2.26	18603	34.32	0.137	420
	S12	26.87	2.98	20119	33.00	0.132	420
	V21	42.50	3.18	34000	35.80	0.143	550
	R1	36.00	2.77	32308	34.80	0.139	550
	FT2	24.90	1.90	30000	32.60	0.130	550

Table 16: Experimental and calculated material parameters for masonry units and mortar joints.

	Spec. ID	Masonry unit								Mortar		
		f_{bh} (MPa)	f_{bv} (MPa)	$\tilde{f}_b$ (MPa)	f_{bt} (MPa)	$\tilde{E}_b$ (MPa)	G_c (N/mm)	G_t (N/mm)	f_m (MPa)	f_{mt} (MPa)	E_m (MPa)	G_c (N/mm)	G_t (N/mm)
Training	S3	15.57	15.57	15.57	1.71	7786	20.50	0.120	15.98	0.80	4795	22.00	0.110
	S5	15.57	15.57	15.57	1.56	9343	20.50	0.120	17.57	0.50	3514	24.00	0.120
	S6	8.51	16.48	11.84	1.30	5920	19.70	0.114	8.65	0.22	865	21.50	0.108
	S8	8.51	16.48	11.84	1.30	5920	19.70	0.114	8.01	0.24	1602	21.23	0.106
	S9	15.57	15.57	15.57	1.71	7786	20.50	0.120	12.47	0.70	3741	22.40	0.120
	S11	15.57	15.57	15.57	1.71	7786	20.50	0.120	13.02	0.46	1302	23.17	0.116
	C1	2.19	18.70	6.40	0.58	2560	16.30	0.102	15.50	0.39	1550	23.90	0.120
	L2	2.19	18.70	6.40	0.58	2560	16.30	0.102	15.50	0.39	1550	23.90	0.120
	N1	2.19	16.40	5.99	0.48	2397	16.00	0.100	10.40	0.21	1040	22.00	0.090
	S1A	7.06	7.06	7.06	0.78	3530	17.50	0.104	3.06	0.11	306	17.80	0.089
	S1B	2.06	37.68	8.81	0.79	5286	18.50	0.108	9.16	0.27	916	21.75	0.109
	S1C	3.15	4.07	3.58	0.39	1790	15.37	0.092	9.57	0.24	765	21.90	0.110
	S	33.37	33.37	33.37	3.14	20022	27.45	0.130	8.00	0.80	2400	21.23	0.106
	TA2	3.15	9.81	5.56	0.51	2224	16.10	0.099	7.68	0.15	768	21.10	0.105
	FIF	2.89	11.54	5.77	0.21	3213	15.80	0.099	2.70	0.08	1080	16.40	0.087
Validat.	S7	15.57	15.57	15.57	1.71	9344	23.93	0.120	15.50	1.09	7751	23.91	0.120
	S12	15.57	15.57	15.57	1.71	7786	23.93	0.120	17.85	0.54	1785	24.53	0.120
	V21	4.68	1.79	2.89	0.32	1737	17.70	0.088	2.50	0.13	1000	17.22	0.086
	R1	5.00	2.00	2.53	0.28	1265	17.30	0.086	8.29	0.17	829	21.36	0.107
	FT2	2.74	18.70	7.16	0.72	4295	20.80	0.104	11.72	0.29	1172	22.74	0.114

The macro-models of the same specimens were developed following the procedure proposed by **Di Trapani et al. (2018)**. This approach required the definition of the strut width (w) in the equivalent strut representation, together with the stress-strain parameters f_{md0}, ε_{md0}, f_{mdu}, and ε_{mdu}. These parameters were initially derived using Eq.s (67) to (70) and subsequently refined through minor adjustments

to achieve close agreement with the experimental results. The final calibrated values adopted for the training dataset are reported in Table 17.

Table 17: Geometrical and mechanical parameters of the equivalent struts for the selected specimens.

	Spec. ID	w (mm)	$\tilde{f}_m$ (MPa)	f_{md0} (MPa)	f_{mdu} (MPa)	ε_{md0} (-)	ε_{mdu} (-)
Training	S3	541.20	14.19	5.50	1.65	0.0010	0.0090
	S5	552.20	13.84	5.20	1.60	0.0010	0.0090
	S6	628.40	7.34	2.71	0.94	0.0014	0.0084
	S8	620.20	3.53	3.40	1.20	0.0019	0.0100
	S9	560.10	14.19	6.00	1.90	0.0010	0.0100
	S11	740.90	11.44	4.10	1.19	0.0008	0.0071
	C1	618.50	4.15	2.02	0.90	0.0018	0.0085
	L2	657.30	4.15	2.00	0.98	0.0017	0.0085
	N1	670.50	3.24	1.20	0.76	0.0020	0.0088
	S1A	636.20	2.86	1.52	1.00	0.0012	0.0090
	S1B	663.90	6.03	2.28	1.20	0.0015	0.0080
	S1C	736.30	0.72	1.20	0.65	0.0015	0.0100
	S	628.60	19.10	5.40	1.60	0.0009	0.0063
	TA2	1246.70	2.24	1.00	0.70	0.0015	0.0090
	FIF	828.80	2.91	1.00	0.62	0.0014	0.0080
Validat.	S7	539.51	13.60	9.00	1.70	0.0015	0.0090
	S12	559.03	13.60	6.80	1.12	0.0012	0.0074
	V21	630.24	2.39	1.20	0.75	0.0015	0.0085
	R1	968.09	2.11	1.40	0.28	0.0012	0.0100
	FT2	551.05	4.24	2.45	1.10	0.0015	0.0110

Figure 5.6 presents a comparison between the numerical simulations obtained from the micro- and macro-models for the training dataset, alongside the experimental backbone curves expressed as lateral force versus top displacement. The comparison highlights that both numerical strategies successfully capture the global response of the specimens over the displacement history. In particular, the initial elastic stiffness and the peak strength are predicted with good accuracy, confirming the capability of both approaches. Furthermore, the post-peak degradation branch follows the experimental trend, suggesting that the models are able to approximate the softening behaviour associated with extensive cracking and progressive loss of infill-frame interaction. In addition, Figure 5.7 provides a direct comparison between the experimentally observed crack patterns and those simulated by the micro-model. The agreement between the two is notable: the onset and progression of diagonal cracking, the localisation of damage within the masonry units or mortar joints, and the detachment regions along the frame-infill interface are all well reproduced considering the reference experimental damage patterns which are not reported here for the sake of conciseness. This correspondence demonstrates the capacity of the micro-modelling strategy to replicate not only the force-displacement curves but also the underlying physical mechanisms governing damage evolution. Overall, these results confirm the

robustness of the adopted micro-model and its suitability as a reference for calibrating and validating the proposed shear decomposition model.

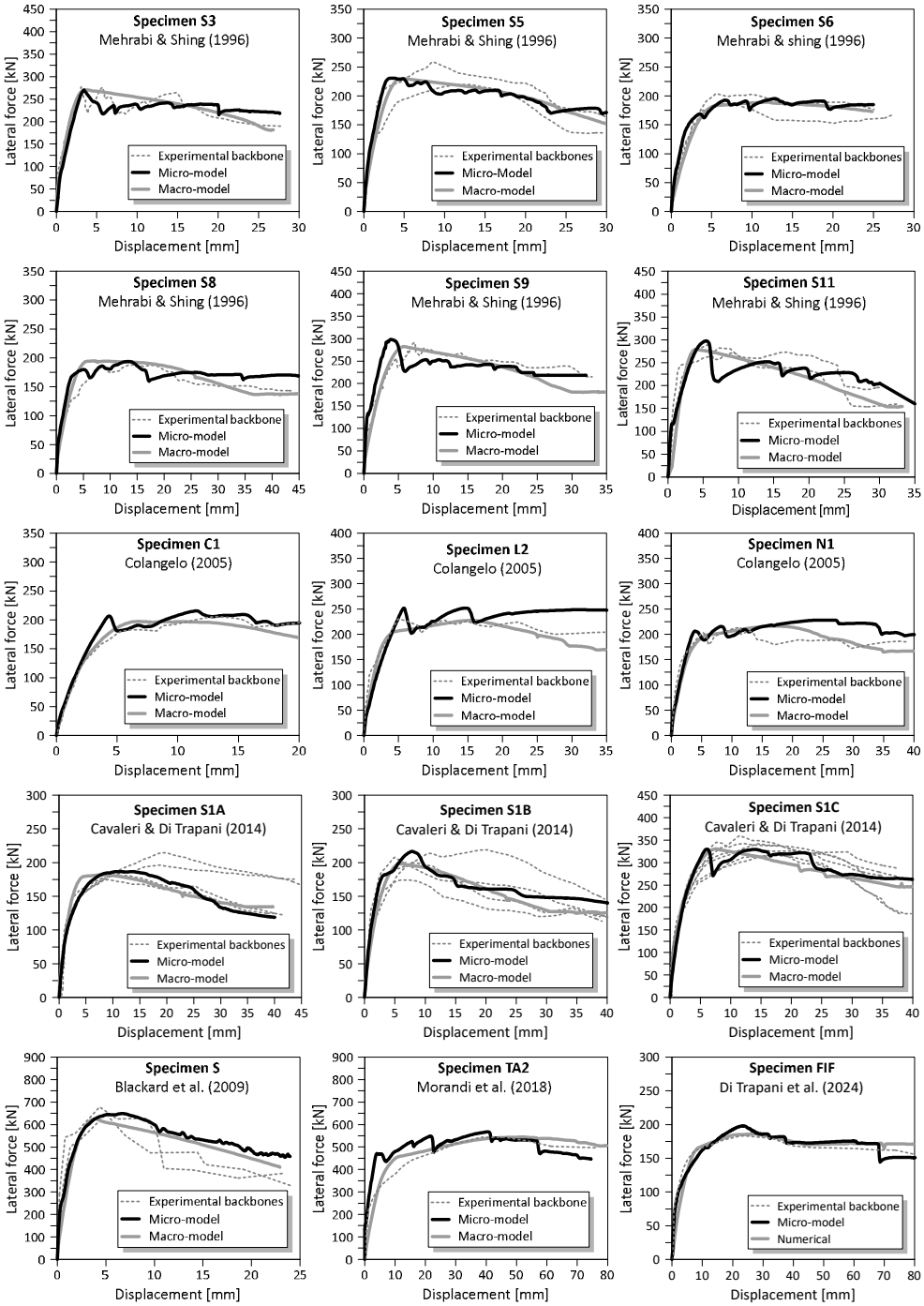

Figure 5.6: Micro and Macro-model validation: comparison between experimental and numerical overall responses for the training dataset's specimens.

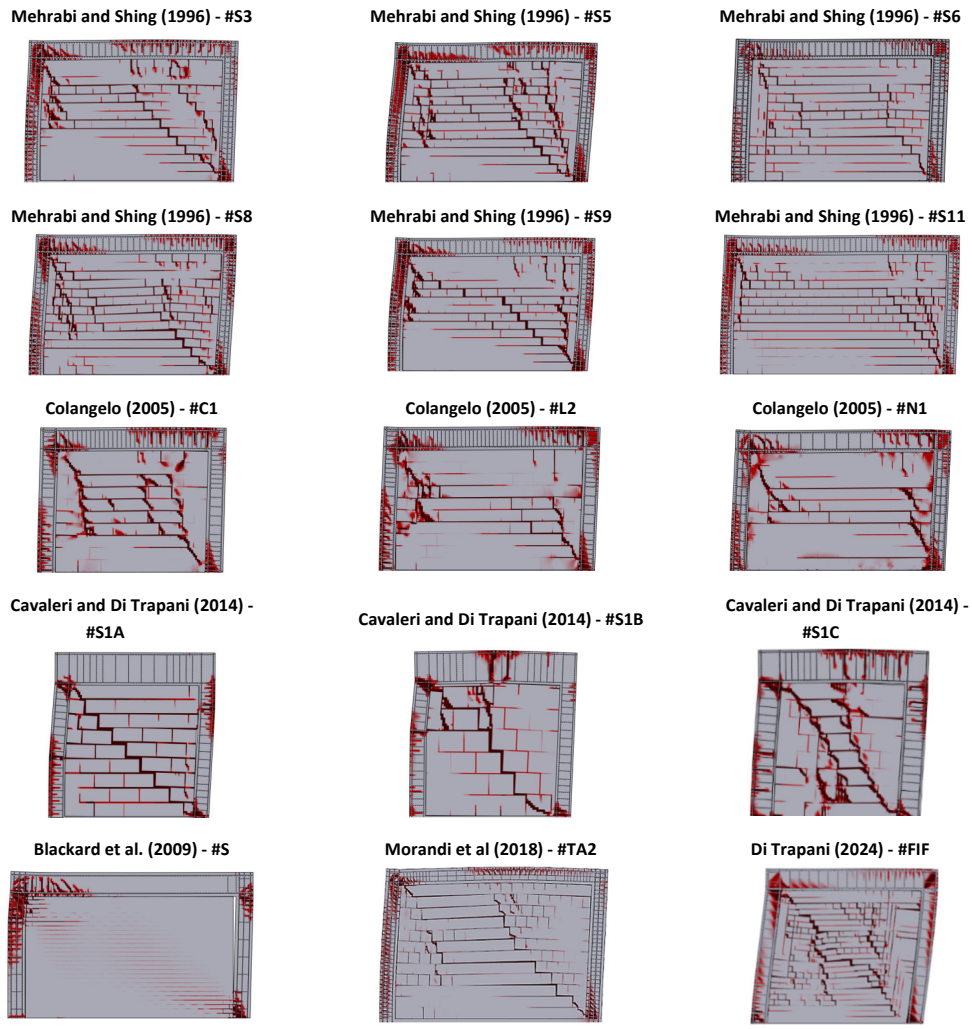

Figure 5.7: Numerical crack patterns from micro-models of the training dataset specimens at the end of the tests.

5.5 Shear demand extraction from micro- and macro-models and validation of the shear decomposition strategy

5.5.1 Extrapolation of $V_{d,\mathrm{tot}}$ and $V_{d,frame}$

The total shear demand ($V_{d,tot}$) and the drift-related shear ($V_{d,frame}$) histories were obtained from the calibrated micro- and macro-models, respectively. The extraction of the $V_{d,tot}$ history was carried out using the STKO post-processing module in combination with a Python script, as described in Chapter 3. This procedure allows the definition of section cuts, which collects the nodal force

components in the local reference system of the cut. By integrating these nodal forces across the section cut, the resulting quantities represent internal forces, enabling the construction of internal force diagrams for structural elements modelled with 2D or 3D finite elements. In this study, the method was applied to extrapolate the total shear demand by acting on the frame members of the infilled frames at each analysis step. Specifically, the shear demand histories were extracted at the windward column top-end and the leeward column bottom-end cross-sections, where the interaction with the infill produces maximum shear values (Figure 5.8). In these regions, the shear distribution exhibits a sharp increase near the ends. For this reason, the average shear demand across three cross-sections within a critical region defined by the column height (h_c) was adopted as the reference value. The three cross-sections considered are: the column end (section 1), at a distance of $0.5 \cdot h_c$ (section 2), and at a distance of h_c (section 3) (Figure 5.8). The drift-related shear demand ($V_{d,frame}$) was instead evaluated from the macro-model. Owing to the imposed loading conditions, this demand remains constant along the column height. Figure 5.8 presents the combined histories of $V_{d,tot}$ and $V_{d,frame}$ for a representative cross-section.

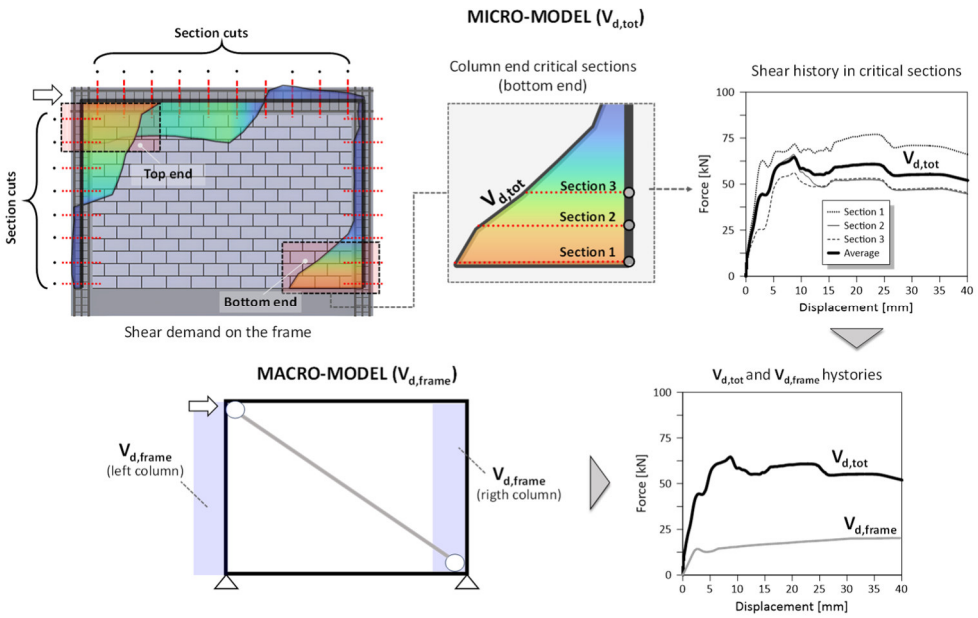

Figure 5.8: Total shear demand extraction ($V_{d,tot}$) and drift-related shear demand ($V_{d,frame}$) from micro- and the macro-models.

5.5.2 Validation of the shear decomposition model proposed in Eq. (66).

The validation of Eq. (66) for approximating the total shear demand was performed by applying the condition defined in Eq. (72) to evaluate the α coefficients. These coefficients were distinguished for the equivalent contact lengths at the top ($\alpha_{TOP}l$) and bottom ($\alpha_{BOT}l$) infill-frame interfaces (Figure 5.9a). The calibration procedure produced the representative results illustrated in Figure 5.9b, where the total shear demand is expressed through Eq. (66). In this formulation, the demand is decomposed into two contributions: $V_{d,frame}$, obtained from the structural analysis of the equivalent strut macro-model, and the additional shear demand $V_{d,inf}$, computed using Eq. (65) as a function of the equivalent contact lengths and the axial force N acting on the strut.

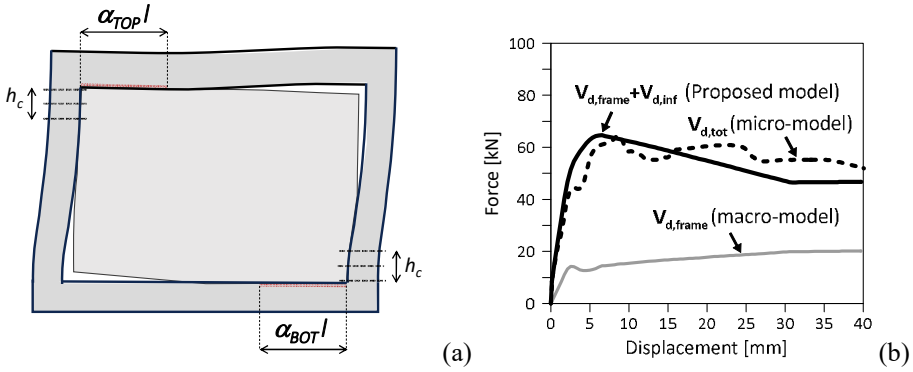

Figure 5.9: Total shear demand at column-end cross sections: (a) schematic representation of critical sections and equivalent contact lengths; (b) estimation of the total shear demand according to Eq. (66).

Figure 5.10 and Figure 5.11 present the outcomes of applying the shear decomposition model defined by Eq. (66) to estimate the total shear demand at the critical top and bottom column sections. These results are obtained using the calibrated α coefficients for each specimen. The comparison between the model predictions and the shear demands extracted from the numerical analyses demonstrates that, once the α values are properly calibrated, the decomposition rule is capable of accurately reproducing the total shear transmitted to the columns at all stages. It is noteworthy that the calibration procedure primarily targets the peak shear demand, since this constitutes the most critical condition for the seismic assessment. Nevertheless, the model retains a satisfactory capability to follow the

entire evolution of the shear response, offering a coherent approximation of the global trend and capturing the key transitions associated with stiffness degradation, contact-length evolution, and infill-frame interaction mechanisms. The full set of calibrated α coefficients for all specimens is reported in Table 18, which summarises the effective contact-length parameters for all analysed specimens.

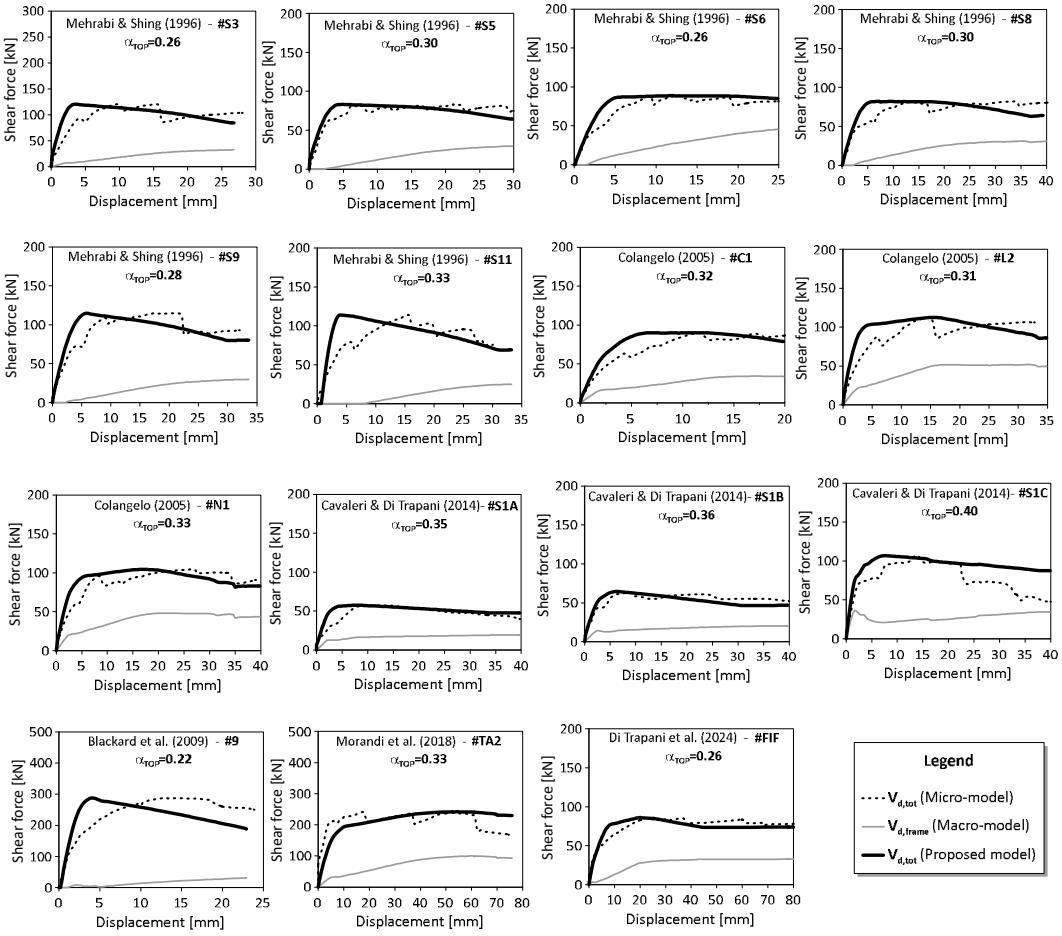

Figure 5.10: Validation of the shear decomposition model using calibrated α_{TOP} coefficients. Comparison with micro- and macro-model predictions.

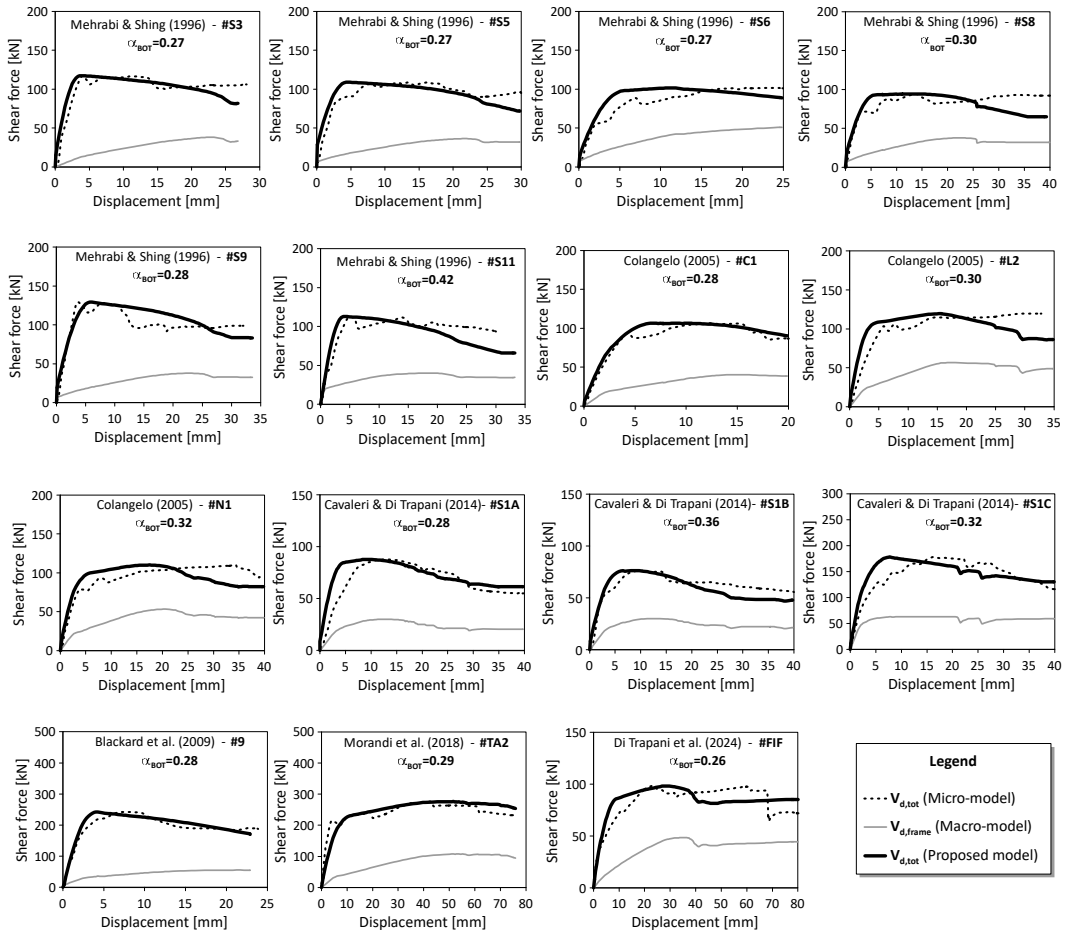

Figure 5.11: Validation of the shear decomposition model using calibrated α_{BOT} coefficients. Comparison with micro- and macro-model predictions.

Table 18: Calibrated α_{TOP} and α_{BOT} coefficients for defining the effective contact lengths at the top and bottom columns-end sections.

Spec.ID	S3	S5	S6	S8	S9	S11	C1	L2	N1	S1A	S1B	S1C	S	TA2	FIF
α_{TOP} (-)	0.26	0.30	0.26	0.30	0.28	0.33	0.32	0.31	0.33	0.35	0.36	0.40	0.22	0.33	0.26
α_{BOT} (-)	0.27	0.27	0.27	0.30	0.28	0.42	0.28	0.30	0.32	0.28	0.36	0.32	0.28	0.29	0.26

5.6 Semi-Empirical formulation for predicting α_{TOP} and α_{BOT} coefficients

5.6.1 Model definition

Recognising that the available training dataset is not sufficiently extensive to derive a fully empirical formulation for the α coefficients, a practical semi-empirical model is here proposed for the prediction of the α_{TOP} and α_{BOT} coefficients. The dataset available for this study is limited. This is mainly due to the scarcity, in the literature, of experimental campaigns that provide full material characterisation together with all the information needed for a consistent calibration of both micro- and macro-models. Relying on a limited dataset would lead to an empirical law with poor generalisability outside the specific configurations included in the training set. To overcome this limitation, the formulation builds upon a geometrically based estimation of the effective contact lengths at the top and bottom interfaces. It is assumed that these contact lengths can be related to the reference length l'_w, defined in Eq. (73) as the portion of the beam intercepted by the horizontal projection of the equivalent strut width (Figure 5.12).

$$l'_w = \frac{w}{2\sin\theta} \tag{73}$$

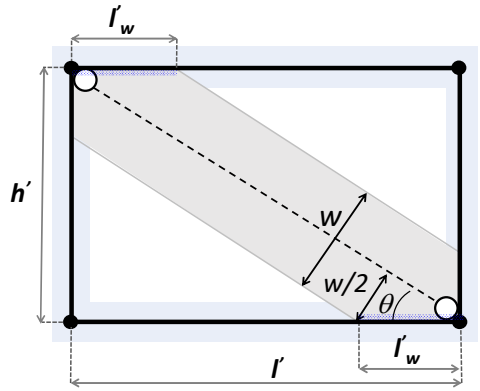

Figure 5.12: Geometric definition of l'_w.

This provides a first-order mechanical approximation. However, such a purely geometric prediction does not fully capture the variability observed in the

numerical-experimental dataset, which shows deviations (Figure 5.13a and b) linked to second-order effects like uncertainties related to the macro-modelling approach (e.g. the definition of the equivalent strut width *w* and the definition of the non-linear strut response).

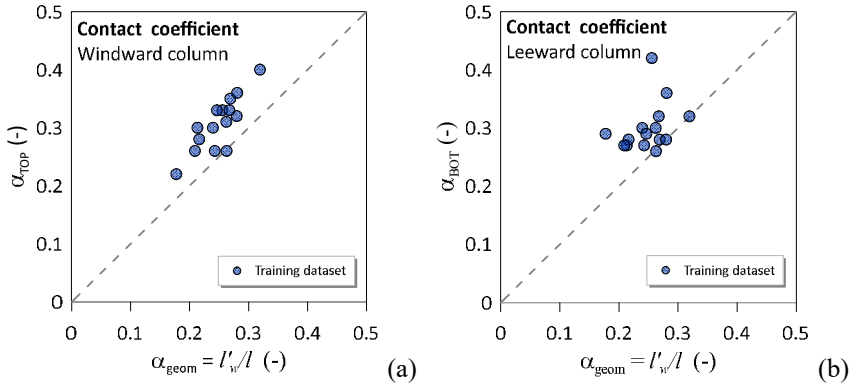

Figure 5.13: Calibrated α coefficients against geometric estimation of α based on l'_w: (a) Windward column; (b) Leeward column.

For this reason, two empirical correction factors, ξ_{TOP} and ξ_{BOT}, are introduced to scale the reference length l'_w and obtain the corresponding effective contact lengths:

$$\begin{aligned} \alpha_{TOP} l &= \xi_{TOP} \cdot l'_w \\ \alpha_{BOT} l &= \xi_{BOT} \cdot l'_w \end{aligned} \tag{74}$$

These coefficients are subsequently calibrated against the dataset, enabling the semi-empirical model to retain a clear physical basis, while incorporating data-driven corrections that enhance its predictive capability. After a sensitivity analysis of the parameters, the empirical coefficients ξ_{TOP} and ξ_{BOT} were determined by assuming that their magnitude varies as a function of the infill aspect ratio *l/h*. Their evolution was represented through a linear function, defined as:

$$\begin{aligned} \xi_{TOP} &= c_1 \left(\frac{l}{h} \right) + c_2 \\ \xi_{BOT} &= c_3 \left(\frac{l}{h} \right) + c_4 \end{aligned} \tag{75}$$

The empirical coefficients c_1, c_2, c_3, and c_4 were identified by linear least-squares regression. Specifically, the best-fit linear relationships in Eq. (75) were obtained by minimising the sum of the squared residuals (vertical distances) between the calibrated correction factors, ξ_{TOP} and ξ_{BOT}, and the corresponding regression lines. The resulting coefficients are reported in Table 19.

Table 19: Coefficients for the empirical model of ξ_{TOP} and ξ_{BOT}.

c_1	c_2	c_3	c_4
0	1.28	0.58	0.45

By replacing the identified coefficient values into Eq. (75), a constant expression is obtained for ξ_{TOP} ($\xi_{TOP}=1.28$), while ξ_{BOT} ($\xi_{BOT}=0.58(l/h)+0.45$) results in a linear function of the infill aspect ratio l/h. Subsequently, substituting the ξ_{TOP} and ξ_{BOT} formulas into Eq. (74) and isolating α_{TOP} and α_{BOT} the following semi-empirical expressions are derived:

$$\alpha_{TOP}=1.28\cdot\frac{w}{2l\sin\theta}$$
$$\alpha_{BOT}=\frac{w}{2l\sin\theta}\cdot\left(0.58\frac{l}{h}+0.45\right) \tag{76}$$

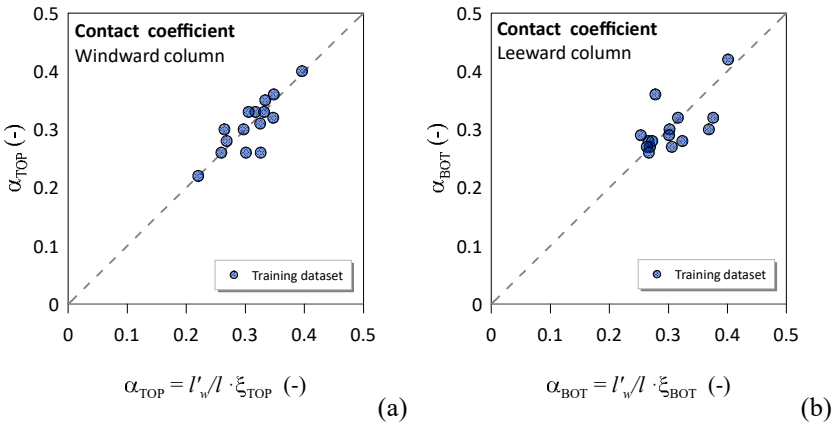

Figure 5.14: Calibrated α coefficients against the proposed semi-empirical model for α_{TOP} and α_{BOT} based on l'_w and empirical coefficients ξ_{TOP} and ξ_{BOT}, respectively: (a) Windward column; (b) Leeward column.

From the final formulations derived for α_{TOP} and α_{BOT}, it is evident that both coefficients exhibit a strong dependence on the geometrical aspect ratio, expressed either through l/h or θ. Additionally, their dependence on the equivalent strut width (w), assessed through the empirical formulation proposed by **Asteris et al. (2016)**, effectively condenses into a single parameter the combined influence of the relative infill-frame stiffness and the applied vertical load. When the coefficients α_{TOP} and α_{BOT} derived from Eq. (76) are used into Eq. (65) or (66), they enable the calculation of both the additional shear demand and the total shear demand at the windward and leeward column ends. This formulation allows for step-by-step verification of the shear capacity-demand ratios throughout the analyses, while also providing estimates of the maximum expected shear demands by replacing the current axial force with the equivalent expected strut resistance in Eqs. (65) or (66).

5.6.2 Empirical model validation and comparative analysis with existing predictive approaches

The validation of the proposed methodology was carried out by recomputing the maximum total shear demands via the shear-decomposition procedure (Eq. (66)), using the final expressions of α_{TOP} and α_{BOT} derived in Eq. (76). The predictive capability of the model was then examined through a dedicated validation dataset, consisting of five additional specimens not included in the calibration phase, together with those used for training. A first verification step focused on the estimation of the maximum total shear demand at the end of the column.

Figure 5.15 reports the comparison between the model predictions and the corresponding shear values extracted from the refined numerical simulations, taken as reference benchmarks, for both the windward and leeward columns. As shown, the agreement is generally satisfactory: the model reproduces well the peak shear demands and retains adequate robustness even when applied to the independent validation specimens.

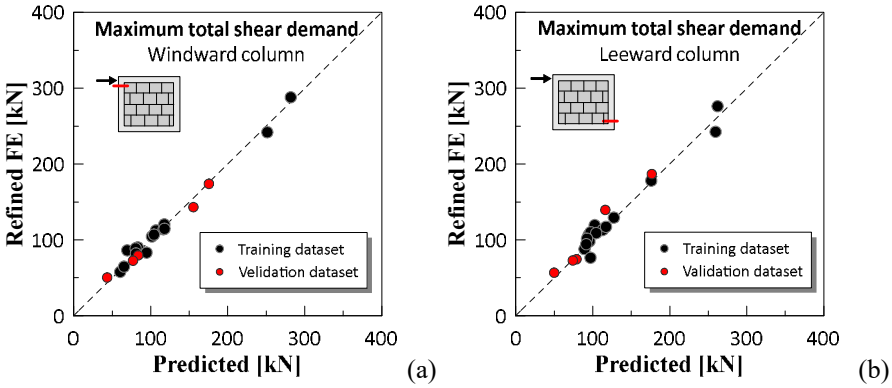

Figure 5.15: Validation of the proposed model in predicting the maximum total shear demand: (a) Windward column ends; (b) Leeward column ends.

A further step of the study involved comparing the proposed analytical formulation against the principal predictive models available in the literature. The evaluation was carried out over the entire experimental database, considering the formulations adopted in **FEMA 356 (2000)**, **Eurocode 8 (CEN, 2004a)**, and the model developed by **Di Trapani et al. (2018)**. The comparison was performed with reference to two indicators: the maximum total shear demand at the column ends and the evolution of the current shear demand throughout the analysis. The first represents the key parameter for design, assessment, and retrofit of infilled frame members, while the latter assesses how closely the predicted shear-drift response follows the reference experimental backbone curves. The comparative outcomes are presented in Figure 5.16 and Figure 5.17, with Table 20 and Table 21 listing both the benchmark (R) and predicted (P) maximum shear values together with the respective P/R ratios. The results reveal that the code-based predictive expressions (FEMA 356 and EC8) tend to be markedly conservative, on average doubling the actual shear demand, in line with observations from earlier studies (e.g., **Moretti, 2015**). Although **Eurocode 8 (CEN, 2004a)** performs slightly better than **FEMA 356 (2000)**, it still exhibits considerable dispersion. In contrast, the formulation by **Di Trapani et al. (2018)** and the model proposed here show significantly improved predictive accuracy. The first generally overestimates the shear demand by approximately +3% to +6%, with coefficients of variation (COV) between 15% and 25%. The proposed model provides an even closer agreement with the benchmark results, with a small average underestimation (-1% to -3%) and a notably lower scatter, with coefficients of variation reduced to 8% - 9%.

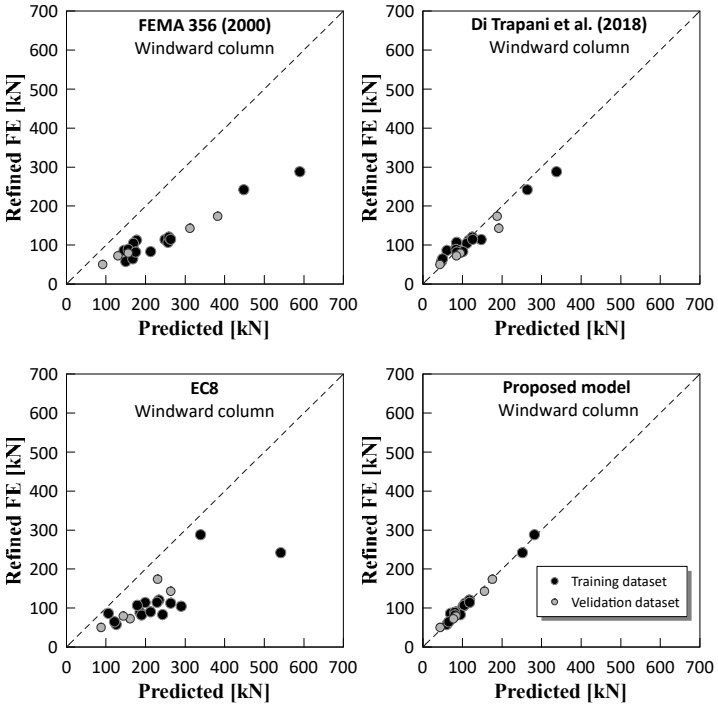

Figure 5.16: Comparison of predicted maximum total shear demand at the windward column: proposed vs. existing models.

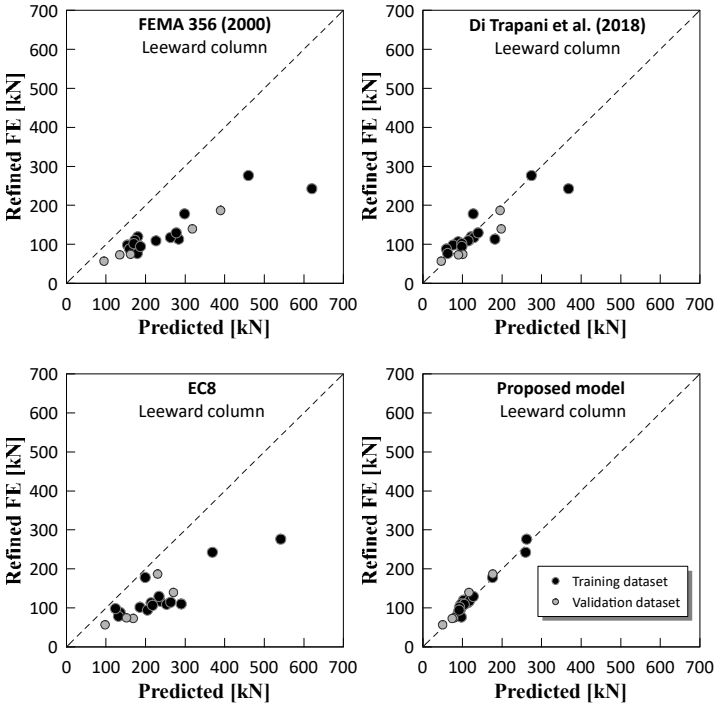

Figure 5.17: Comparison of predicted maximum total shear demand at the leeward column: proposed vs. existing models.

Table 20: Maximum total shear demand at the windward column ends: comparative assessment of the predictive performance of existing and proposed models.

Specimen ID		FEMA 356		Eurocode 8		Di Trapani et al. (2018)		Proposed model	
	Ref. FE (R) (kN)	Pred. (P) (kN)	P/R (-)	Pred. (P) (kN)	P/R (-)	Pred. (P) (kN)	P/R (-)	Pred. (P) (kN)	P/R (-)
S3	120.47	259.06	2.15	233.77	1.94	124.91	1.04	117.62	0.98
S5	83.14	212.75	2.56	243.00	2.92	100.72	1.21	94.62	1.14
S6	88.81	155.97	1.76	185.76	2.09	83.29	0.94	80.48	0.91
S8	82.07	174.82	2.13	189.85	2.31	85.57	1.04	80.86	0.99
S9	114.63	263.43	2.30	228.94	2.00	125.42	1.09	117.91	1.03
S11	113.97	248.98	2.18	198.92	1.75	147.30	1.29	116.70	1.02
C1	90.08	169.22	1.88	212.48	2.36	82.14	0.91	83.29	0.92
N1	104.43	177.05	1.70	290.12	2.78	116.47	1.12	106.86	1.02
L2	112.5	169.10	1.50	263.44	2.34	110.88	0.99	101.49	0.90
S1A	57.74	149.92	2.60	125.88	2.18	46.81	0.81	60.35	1.05
S1B	64.64	167.66	2.59	121.46	1.88	49.72	0.77	65.36	1.01
S1C	106.89	256.64	2.40	179.20	1.68	85.03	0.80	104.24	0.98
S	288.07	589.86	2.05	338.89	1.18	337.57	1.17	281.83	0.98
TA2	241.9	448.16	1.85	541.60	2.24	263.71	1.09	251.42	1.04
FIF	86.12	145.28	1.69	105.94	1.23	60.56	0.70	69.51	0.81
S7	173.88	382.198	2.20	230.36	1.32	187.527	1.08	175.55	1.01
S12	143.10	312.056	2.18	263.50	1.84	191.659	1.34	155.42	1.09
V21	72.52	129.993	1.79	160.80	2.22	84.698	1.17	76.93	1.06
R1	50.28	91.610	1.82	87.60	1.74	42.960	0.85	43.46	0.86
FT2	79.55	156.160	1.96	143.72	1.81	94.427	1.19	83.69	1.05
		μ	**2.06**		**μ**	**1.99**	**μ**	**1.03**	**μ**	**0.99**
		COV	**0.16**		**COV**	**0.23**	**COV**	**0.17**	**COV**	**0.08**

Table 21: Maximum total shear demand at the leeward column ends: comparative assessment of the predictive performance of existing and proposed models.

Specimen ID		FEMA 356		Eurocode 8		Di Trapani et al. (2018)		Proposed model	
	Ref. FE (R) (kN)	Pred. (P) (kN)	P/R (-)	Pred. (P) (kN)	P/R (-)	Pred. (P) (kN)	P/R (-)	Pred. (P) (kN)	P/R (-)
S3	117.19	262.82	2.24	236.77	2.02	128.83	1.10	117.19	1.00
S5	108.89	226.22	2.08	253.00	2.32	114.19	1.05	104.42	0.96
S6	101.6	170.31	1.68	185.76	1.83	98.12	0.97	92.44	0.91
S8	94.24	187.18	1.99	204.85	2.17	98.31	1.04	91.49	0.97
S9	129.3	277.45	2.15	233.94	1.81	139.44	1.08	127.38	0.99
S11	113.02	283.61	2.51	213.92	1.89	181.93	1.61	112.94	1.00
C1	106.42	175.23	1.65	217.48	2.04	89.01	0.84	94.59	0.89
N1	110.03	180.22	1.64	290.12	2.64	122.04	1.11	102.49	0.93
L2	114.43	172.68	1.51	263.44	2.30	116.17	1.02	97.13	0.85
S1A	87.82	159.35	1.81	135.88	1.55	59.26	0.67	89.18	1.02
S1B	78.38	179.02	2.28	131.46	1.68	62.55	0.80	97.00	1.24
S1C	178.03	298.45	1.68	199.20	1.12	127.08	0.71	175.95	0.99
S	242.51	620.25	2.56	368.89	1.52	367.96	1.52	259.52	1.07
TA2	276.2	459.92	1.67	541.60	1.96	274.32	0.99	262.05	0.95
FIF	98.12	154.27	1.57	123.94	1.26	76.12	0.78	95.74	0.98
S7	186.80	389.54	2.09	230.36	1.23	194.96	1.04	176.58	0.95
S12	139.47	318.24	2.28	270.50	1.94	197.84	1.42	116.25	0.83
V21	72.84	134.70	1.85	168.80	2.32	89.81	1.23	74.08	1.02
R1	56.66	94.88	1.67	97.60	1.72	46.33	0.82	49.81	0.88
FT2	74.37	162.10	2.18	151.72	2.04	100.62	1.35	78.84	1.06
		μ	**1.95**		**μ**	**1.87**	**μ**	**1.06**	**μ**	**0.97**
		COV	**0.17**		**COV**	**0.21**	**COV**	**0.25**	**COV**	**0.09**

The significant overestimation observed for FEMA 356 and EC8 can be attributed to the fact that both formulations ignore the reduction of the additional

shear demand arising from the tangential friction forces activated with the increasing drift level at the base of the infill. This mechanism is instead explicitly captured in the formulations of **Di Trapani et al. (2018)** and in the present model. Moreover, the improved predictive accuracy of the proposed approach is due to the introduction of dedicated expressions for the equivalent contact lengths, which reflect the geometrical and mechanical characteristics of the infilled frame and differentiate between the windward-top and leeward-bottom column sections.

Figure 5.18 and Figure 5.19 illustrate the ability of the various models to reproduce the evolution of the total shear demand over increasing displacement levels. EC8 is omitted from this comparison because its formulation enables the prediction of maximum shear only. As shown in the figures, **FEMA 356 (2000)** consistently overpredicts the total shear demand by a factor of approximately two at all drift levels. The model by **Di Trapani et al. (2018)** generally provides a closer match to the reference trend; however, its accuracy is not uniform across all cases, since it applies tangential forces to a fixed contact length equal to the equivalent strut width (w). This simplification is reasonably accurate for the leeward top beam-infill interface (Figure 5.18), but it fails to fully account for the variability of the beam-column contact regions at the windward bottom ends (Figure 5.19). On the other hand, the proposed model gives the most reliable estimates of the current total shear demand, owing to the adoption of two empirical expressions for the effective contact lengths. The trends in Figure 5.18 and Figure 5.19 clearly demonstrate the enhanced predictive performance, which remains stable for both the windward top and leeward bottom column ends.

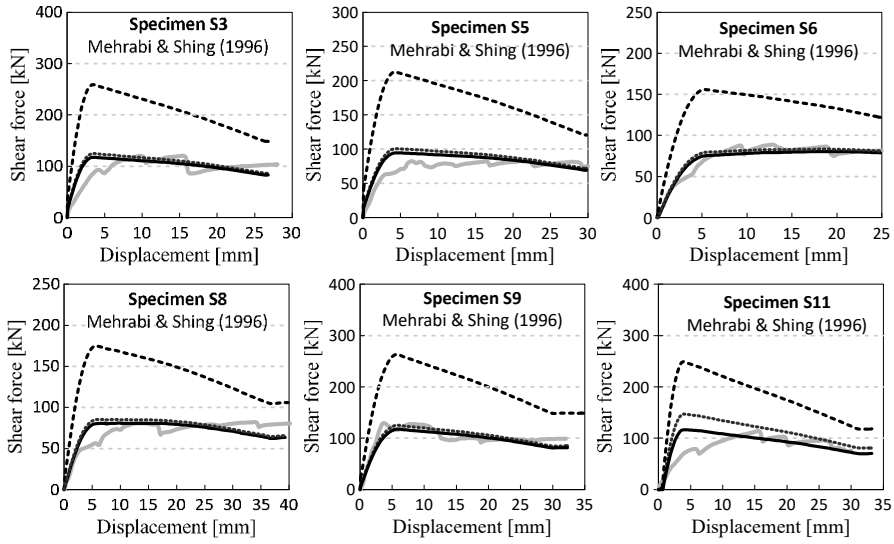

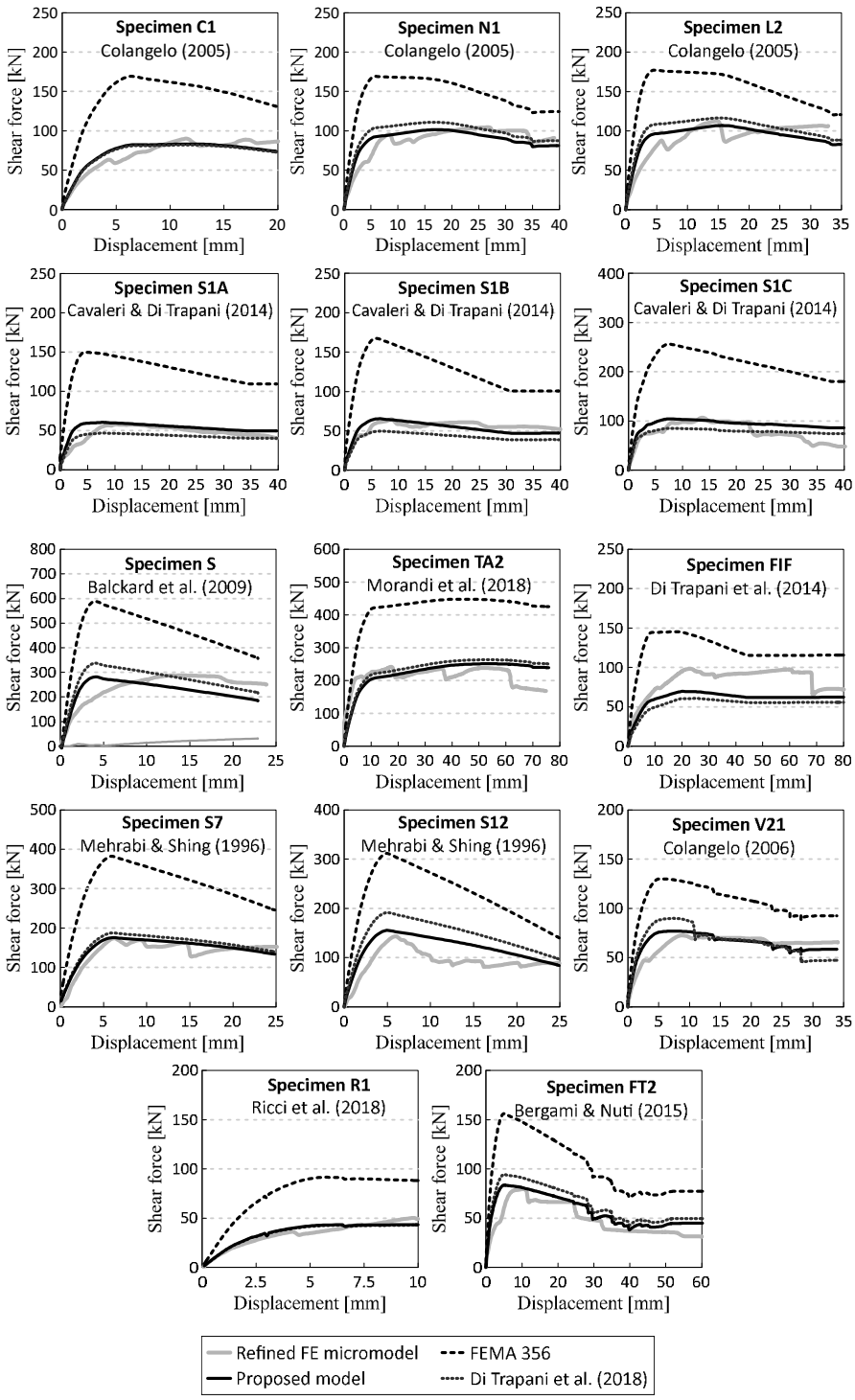

Figure 5.18: Predictive performance of the proposed and existing models in estimating the total shear demand at the windward column top ends.

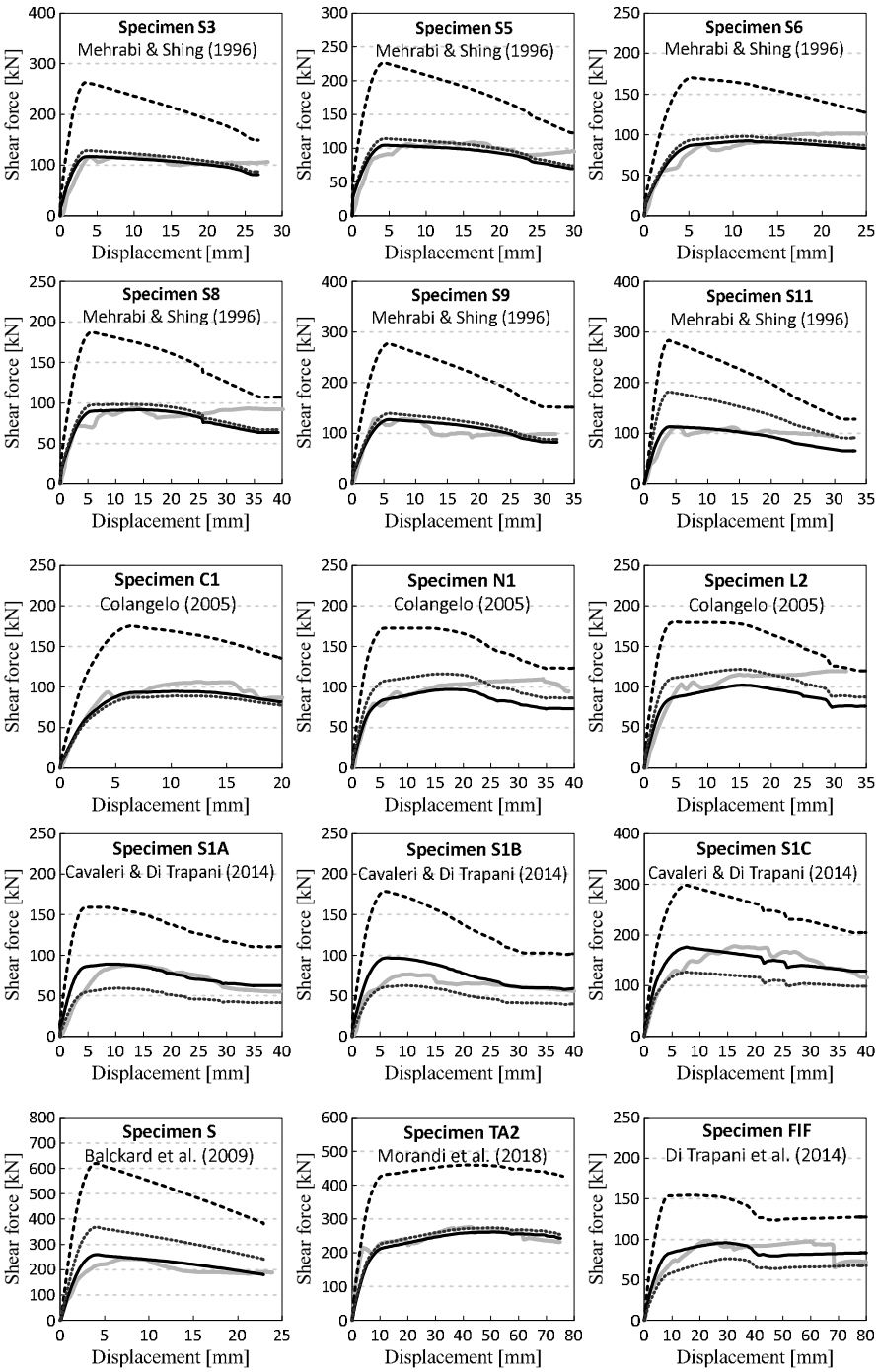
Specimen S3
Mehrabi & Shing (1996)
Specimen S5
Mehrabi & Shing (1996)
Specimen S6
Mehrabi & Shing (1996)
Specimen S8
Mehrabi & Shing (1996)
Specimen S9
Mehrabi & Shing (1996)
Specimen S11
Mehrabi & Shing (1996)
Specimen C1
Colangelo (2005)
Specimen N1
Colangelo (2005)
Specimen L2
Colangelo (2005)
Specimen S1A
Cavaleri & Di Trapani (2014)
Specimen S1B
Cavaleri & Di Trapani (2014)
Specimen S1C
Cavaleri & Di Trapani (2014)
Specimen S
Balckard et al. (2009)
Specimen TA2
Morandi et al. (2018)
Specimen FIF
Di Trapani et al. (2014)
Shear force [kN]
Displacement [mm]

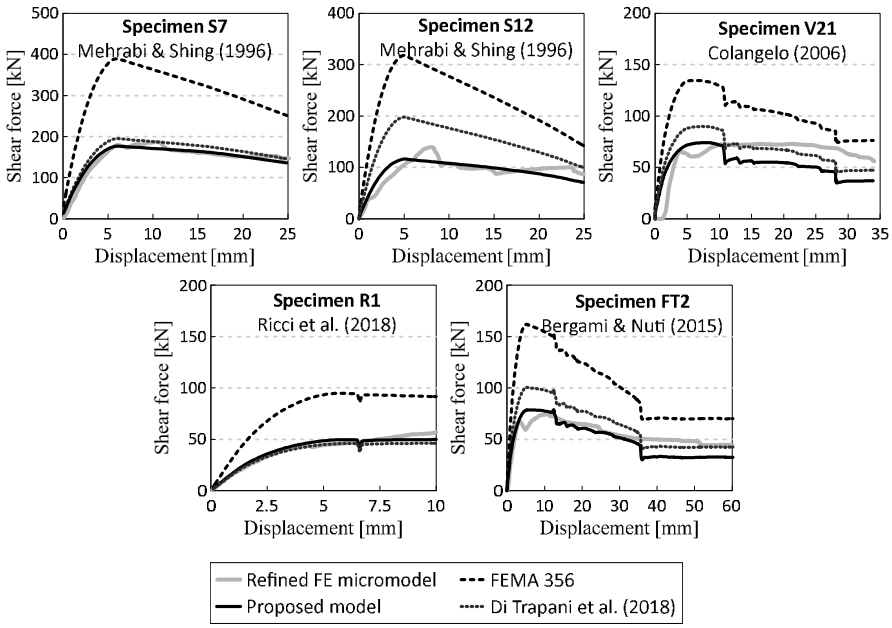

Figure 5.19: Predictive performance of the proposed and existing models in estimating the total shear demand at the leeward column bottom ends.

5.6 Uncertainty quantification of the proposed model and the available predictive formulations

The robustness of the proposed formulation was further examined by analysing its drift-dependent predictive error and comparing it with that of the other models considered. For each specimen and predictive model, the ratio between the predicted and reference total shear demand (P/R) was computed at the windward-top and leeward-bottom column sections. The analysis was carried out over a drift range spanning from 0.04% to 1.6%, discretised into 80 drift levels, corresponding to increments of approximately 0.019%. The drift values at which the P/R ratios were evaluated are schematically represented in Figure 5.20. A minimum drift of 0.04% was imposed to avoid distortions arising from very small shear values near the origin of the shear-drift curve, where numerical fluctuations may dominate. The upper limit of 1.6% corresponds to the maximum drift level attained by at least 80% of the specimens, ensuring a consistent and statistically meaningful comparison across the dataset.

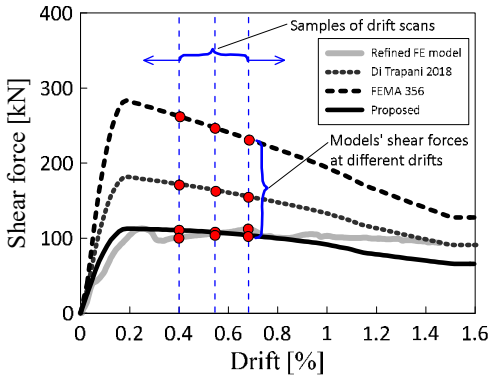

Figure 5.20: Scheme of the drift levels used to scan the shear force predictions and evaluate the P/R ratios for the windward and leeward column sections.

The P/R statistics were computed at each drift level, and the overall trends are summarised in Figure 5.21, which illustrates how the mean values and associated dispersion evolve for the different predictive models. For clarity, only a subset of the full P/R distributions per drift is shown in the figure, whereas the 95.4% percentile bounds are computed using the complete dataset. A common feature across all models is the pronounced overestimation and large variability observed at the smallest drift values. This behaviour mainly reflects the lower initial stiffness of the refined numerical model, whose response is influenced by the delayed engagement of the contact interfaces. For the **FEMA 356 (2000)** formulation, the mean P/R value at the earliest drifts is approximately 2.85, progressively decreasing to around 2.0 at 1% drift and reaching values close to 1.8 beyond this level. The models proposed by **Di Trapani et al. (2018)** and in this study display approximately comparable mean trends. However, a key distinction lies in the significantly reduced scatter achieved by the proposed model for both windward and leeward columns, as highlighted by the 95.4% percentile bounds. Moreover, once the initial drift range is exceeded, the mean predictions of the proposed model align more closely with the reference values, with overestimations remaining below 1.4. The lower variability, relative to the model of **Di Trapani et al. (2018)**, is due to the new semi-empirical expressions introduced for estimating the equivalent contact lengths, which allow the model to adapt to the specific geometric and mechanical characteristics of each case.

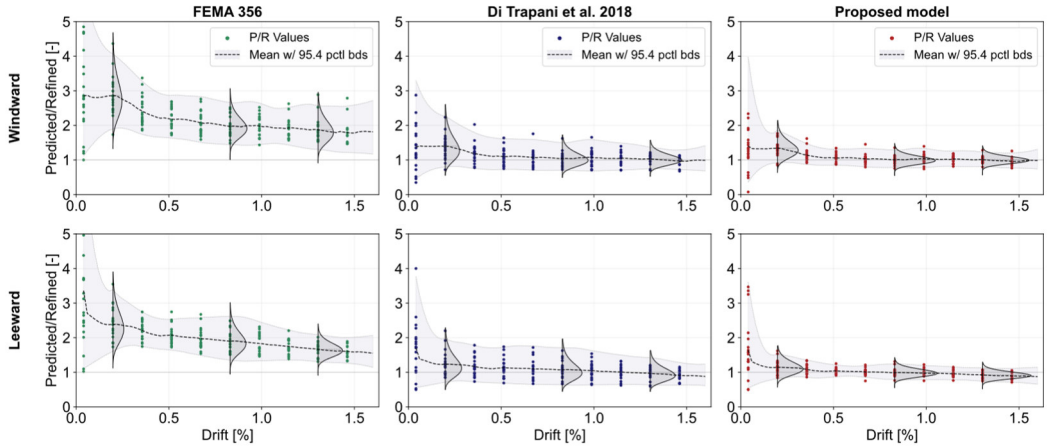

Figure 5.21: Comparison of drift-related P/R statistics for windward and leeward column predictions across the models.

A final, comprehensive evaluation was performed by consolidating the outcomes of the previous analyses and deriving global statistical indicators for each predictive model. The frequency distributions of the computed P/R ratios are shown in Figure 5.22, together with their corresponding lognormal fits. The 95.4% percentile bounds are also plotted. These distributions distinctly highlight the varying predictive capabilities of the examined models over the full drift range and for both windward-top and leeward-bottom column ends. For **FEMA 356 (2000)**, the P/R ratios exhibit a mean value of 2.076 with a coefficient of variation (COV) of 23.3%, confirming the pronounced tendency of this model to substantially overestimate the shear demand. The formulations by **Di Trapani et al. (2018)** and the current proposed model display very similar mean predictions, with P/R averages equal to 1.105 and 1.052, respectively, indicating a modest overall overestimation in both cases. However, despite the acceptable mean, the **Di Trapani et al. (2018)** model shows a higher dispersion (COV = 25.8%). The proposed model, in contrast, achieves a noticeably reduced variability, with a COV of 18.4%. The full statistical parameters, including means, standard deviations, and coefficients of variation, are summarised in Table 22.

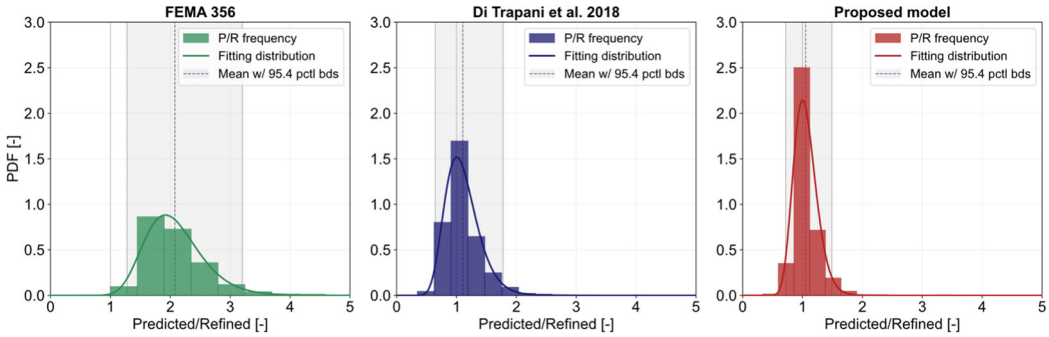

Figure 5.22: Overall P/R ratio distributions and corresponding lognormal fits for all specimens.

Table 22: Summary statistics of overall P/R ratios across the predictive models.

	FEMA 356	Di Trapani et al. (2018)	Proposed Model
Mean [-]	2.076	1.105	1.052
Std. Dev. [-]	0.483	0.285	0.194
COV [%]	23.3	25.8	18.4
μ_{ln} [-]	0.704	0.068	0.034
σ_{ln} [-]	0.229	0.253	0.182

5.7 Application of the proposed model to a full-scale structure

This section illustrates an example application of the proposed methodology to a three-story, two-bay frame structure fully infilled with masonry panels. The shear-correction model, used in conjunction with the equivalent strut approach, is also validated against the response obtained from a refined micro-model of the same structure. The geometric configuration of the prototype is reported in Figure 5.23 and Table 23. The mechanical properties of concrete, steel, masonry units, and mortar are assumed to coincide with those of specimen S1B tested by **Cavaleri and Di Trapani (2014)** and are summarised in Table 14 -Table 18.

The structural system is subjected to a uniformly distributed load of 20 kN/m applied along the beams, as well as concentrated vertical loads of 23 kN and 7.5 kN acting on the external and internal columns, respectively. The equivalent-strut representation of the frame is developed following the procedure by **Di Trapani et al. (2018)**, previously outlined in this chapter and described in detail in Chapter 2. The geometric characteristics and constitutive parameters assigned to the struts are

listed in Table 24, while Figure 5.23b provides a schematic representation of the resulting macro-model.

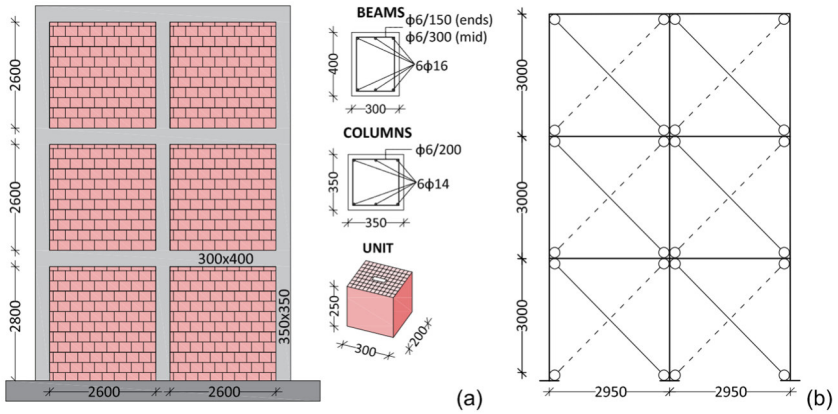

Figure 5.23: (a) Geometric layout of the full-scale reference structure; (b) Corresponding equivalent strut model (dimensions in mm).

Table 23: Geometric details of the prototype infilled-frame structure.

Type of masonry	l (mm)	h (mm)	l' (mm)	h' (mm)	t (mm)	b_c (mm)	h_c (mm)	b_b (mm)	h_b (mm)
Hollow clay units	2600	2600	2950	3000	200	350	350	300	400

Table 24: Equivalent strut model: geometric and constitutive parameters

Storey	w (mm)	t (mm)	f_{md0} (MPa)	f_{mdu} (MPa)	ε_{md0} (-)	ε_{mdu} (-)
1	1053.64	200	1.800	0.904	0.00131	0.00740
2	1049.10	200	1.800	0.899	0.00131	0.00740
3	1044.56	200	1.800	0.894	0.00130	0.00740

For the refined micro-model, the calibration of the material parameters follows the values reported in Table 14 – Table 17.

Both structural models were analysed using a modal pushover procedure. The resulting monotonic force-displacement curves are compared in Figure 5.24 to verify the consistency between the two modelling approaches. Figure 5.24b also illustrates the damage pattern obtained from the micro-model.

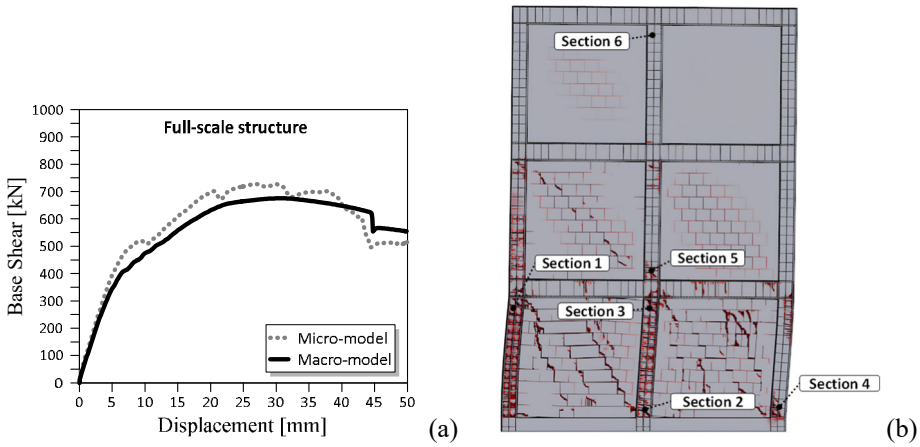

Figure 5.24: (a) Micro- vs. macro-model monotonic response comparison; (b) Micro-model damage distribution and location of monitoring sections.

Six column-end cross-sections were arbitrarily selected to monitor the evolution of the total shear demand (Figure 5.24b). The proposed formulation is applied to the equivalent strut model through the following procedure:

1. Record the history of $V_{d,frame}$ at each monitored section;
2. Record the axial force history N of all struts converging to the corresponding monitored cross-section;
3. Compute the coefficients α_{TOP} and α_{BOT} (Eq. (76)) for the windward and leeward columns associated with the monitored sections;
4. Evaluate the total shear demand $V_{d,tot}$ at each section by applying Eq. (66) over the entire displacement history.

The calculation procedure for the α_{TOP} and α_{BOT} coefficients is described in the following:

Windward columns

Sections 1 and 3

$$\alpha_{TOP} = 1.28 \cdot \frac{w}{2l \sin\theta} = 1.28 \times \frac{1053.64}{2 \times 2600 \times \sin(45.5°)} = 0.364 \quad (77)$$

Section 6

$$\alpha_{TOP} = 1.28 \cdot \frac{w}{2l \sin\theta} = 1.28 \times \frac{1044.56}{2 \times 2600 \times \sin(45.5°)} = 0.361 \tag{78}$$

Leeward columns

Sections 2 and 4

$$\alpha_{BOT} = \frac{w}{2l \sin\theta} \cdot \left(0.58 \frac{l}{h} + 0.45 \right) = \frac{1053.64}{2 \times 2600 \times \sin(45.5°)} \times (0.58 + 0.45) = 0.293 \tag{79}$$

Section 5

$$\alpha_{BOT} = \frac{w}{2l \sin\theta} \cdot \left(0.58 \frac{l}{h} + 0.45 \right) = \frac{1049.1}{2 \times 2600 \times \sin(45.5°)} \times (0.58 + 0.45) = 0.291 \tag{80}$$

The results obtained by applying the proposed model to estimate the total shear demand at the monitored sections are presented in

Figure 5.25. For comparison, the corresponding shear demands extracted from the refined micro-model of the structure are plotted in the same diagrams.

Figure 5.25 also reports the shear forces computed from the basic equivalent strut model ($V_{d,frame}$), without introducing the proposed correction, to highlight the improvements achieved by the enhanced formulation.

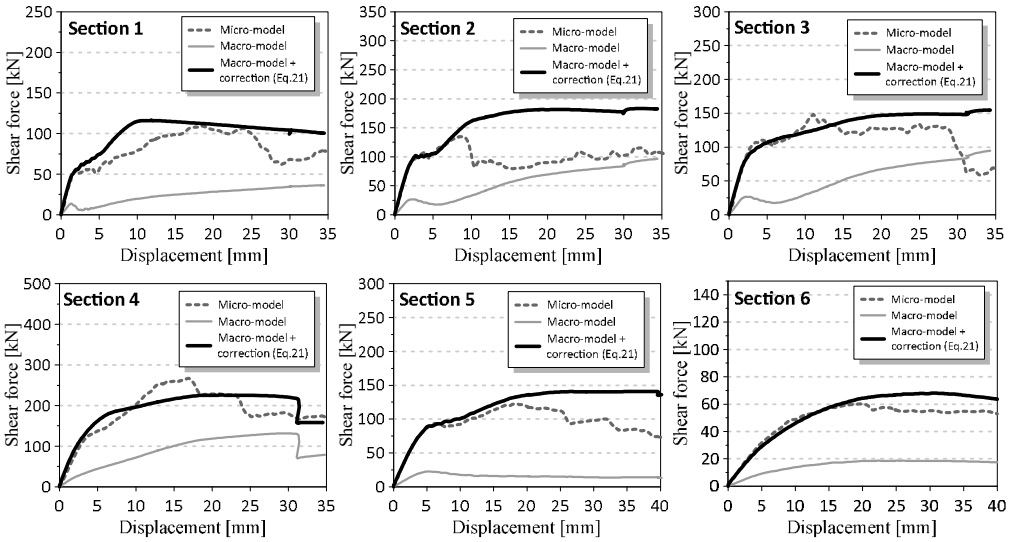

Figure 5.25: Shear demand assessment at the selected monitoring sections.

5.8 Conclusions

This Chapter has presented a practice-oriented analytical formulation for estimating the total shear demand at column ends in masonry-infilled RC frames. The proposed approach preserves the simplicity and practicality of the widely adopted concentric equivalent strut model, while enhancing its capability to capture the actual shear forces transmitted to the columns. The total shear demand is decomposed into two contributions: (i) the shear force obtained directly from the structural analysis of the frame equipped with concentric struts, and (ii) an additional component, derived analytically as a function of the current axial load in the strut and of the geometric characteristics of the infilled frame. The formulation was developed by enforcing static equivalence between the equivalent strut model and a high-fidelity finite element micro-model used as a benchmark. In the refined model, the actual shear distribution was obtained through numerical integration of nodal forces at predefined section cuts. The additional shear component was finally expressed through a semi-empirical model calibrated on numerical replicas of experimental tests. Based on the results of the study, the following conclusions can be drawn:

- The additional shear transmitted to the columns by the infill depends strongly on the tangential friction forces developing along the contact interfaces, particularly at the top and bottom beam-infill interface, in addition to the mechanical properties of the infilled frame.

- Major design codes (**EC8, FEMA 356, ASCE/SEI 41-37**) and several available predictive models do not account for these frictional actions, leading to a substantial overestimation of the infill-induced shear.

- The proposed method evaluates both the additional and total shear demand through case-specific equivalent contact lengths, representing the regions where friction forces are activated at the windward-top and leeward-bottom interfaces, using a simple semi-empirical expression.

- Compared with existing formulations, the proposed model shows markedly improved accuracy. The mean error in predicting the maximum total shear demand is -2%, whereas EC8 and FEMA 356 overestimate the demand by +93% and +100.5%, respectively. The model by **Di Trapani et al. (2018)** achieves a reduced mean error (+4.5%) but exhibits significant scatter, as it

accounts for friction forces without adapting the effective contact lengths to each configuration.

- Uncertainty quantification across different drift levels confirms similar trends, with all models exhibiting heightened variability at very small drifts; nevertheless, the proposed model maintains consistently lower dispersion.

- Beyond its improved accuracy, the proposed formulation retains the advantages of the traditional equivalent strut approach, particularly its easy implementation in nonlinear analyses, while enabling step-by-step analytical correction of column shear demand. It also allows the estimation of the maximum expected shear demand for design purposes by relating it to the peak axial resistance of the equivalent strut.

Chapter 6

A novel multi-struts macro-model for the estimation of global and local effects under IP loading

As highlighted in the previous chapters, simplified modelling strategies commonly adopted for masonry-infilled RC frames are generally unable to capture the local effects associated with infill-frame interaction, like shear demand amplification at column ends. In Chapter 5, this aspect was addressed through the development of an analytical correction model formulated within a single equivalent strut macro-model, which represents a practical and efficient solution for safety checks and seismic assessment of existing structures. This approach is especially suitable for practice-oriented applications, where simplicity and limited computational cost are essential. In parallel, several multi-strut macro-models have been proposed in the literature as an extension of the equivalent single-strut macro-model (**Chrysostomou et al., 2002; El-Dakhakhni et al., 2003; Crisafulli and Carr, 2007; Fiore et al., 2012; Jeon et al., 2015; Pashaie and Mohammadi, 2019**). However, these models have typically been calibrated and validated with reference to the global response of infilled frames, while a systematic calibration against local response, such as shear demand at column ends, still lack. In this context, the present chapter explores a multi-strut macro-modelling strategy considered as a research-oriented tool to use in computationally demanding analyses improving the representation of local interaction effects with appropriate strut positioning without the need of refined micro-models. The emphasis is therefore placed on the simultaneous reproduction of both global and local response by using a multi-strut macro-model. This chapter presents the formulation and preliminary calibration of an eccentric three-strut macro-model for masonry-infilled RC frames subjected to in-plane loading. The model is implemented within the OpenSees platform and tested with monotonic nonlinear static analyses. The

calibration is performed on a selected subset of ten experimental specimens, previously introduced in Chapter 5, by adopting the corresponding refined finite-element micro-models as reference solutions for the evaluation of local shear demand. For each specimen, the width partition coefficients and the eccentric positioning of the equivalent struts are calibrated in order to achieve a consistent agreement with the reference solutions in terms of both global force-displacement response and local shear demand at column ends. To this purpose, an optimisation procedure based on a Genetic Algorithm (GA) is adopted to explore the strut configuration space and identify the optimal set of parameters for each specimen. Once the optimal configurations are obtained, the resulting calibrated parameters are collected and post-processed through Genetic Programming (GP), with the aim of deriving formulations that capture the observed trends and provide a compact, physically interpretable description of the strut configuration. However, given the limited size of the reference dataset, this chapter should be regarded as a preliminary investigation, primarily intended to assess the feasibility of the proposed framework.

6.1 Formulation of the proposed multi-strut macro-model

The multi-strut macro-model developed in this study is implemented within the OpenSeesPy platform. All analyses are performed in a two-dimensional in-plane configuration. Boundary conditions are defined consistently with the reference experimental tests: the base nodes of the reinforced concrete frame are fully restrained, while the struts connected to the foundation beam are allowed to rotate, reproducing pinned connections. The reinforced concrete frame is modelled using 1D force-based beam-column elements, which allow an accurate representation of distributed plasticity without the need for excessive element discretisation. Fibre sections are adopted for beams and columns, enabling the explicit modelling of confined and unconfined concrete regions as well as reinforcing steel. The constitutive behaviour of concrete is modelled using the *Concrete02* material, with confined concrete accounted for with **Mander et al. (1988)**'s formulations, while reinforcing steel is described through the *Steel02* uniaxial material model. The masonry infill is represented through equivalent struts modelled as truss elements subjected exclusively to axial forces. Each strut is defined as a compression-only, pinned element characterised by a concrete-like uniaxial stress-strain relationship implemented through the *Concrete02* material. The constitutive parameters of the struts, such as the peak and ultimate strength-strain values f_{md0}, ε_{md0}, f_{mdu}, and ε_{mdu},

are derived from the empirical correlations proposed by **Di Trapani et al. (2018)**, ensuring consistency with the equivalent single-strut formulation adopted in the previous chapter.

A rectangular cross-section is assigned to all struts, with thickness equal to that of the infill wall. The total effective width of the infill panel is evaluated according to the formulation proposed by **Asteris et al. (2016)** and distributed among the three struts through weighting coefficients p_i, which control the relative contribution of each strut (w_i). The multi-strut configuration consists of three equivalent struts arranged within the frame bay: one main diagonal strut and two additional eccentric struts connected to the frame members at different vertical (d_1, d_2) and horizontal (b_1, b_2) positions. The adopted multi-strut configuration is schematically illustrated in Figure 6.1.

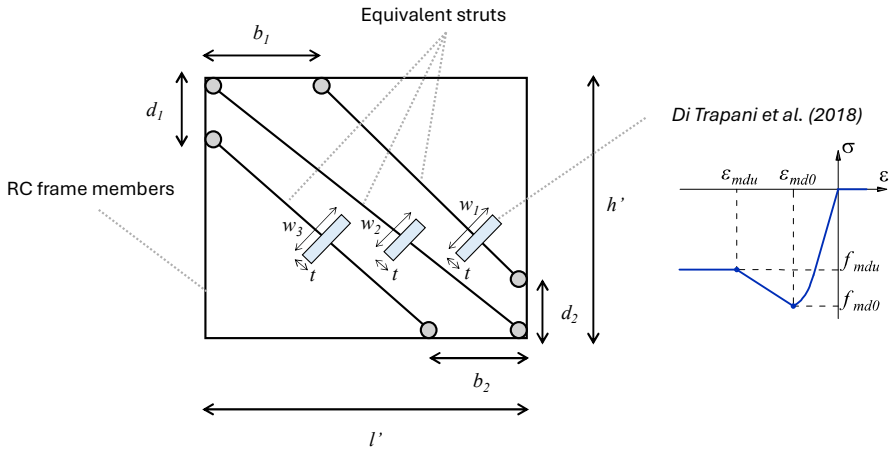

Figure 6.1: Schematic representation of the adopted multi-strut macro-model.

While the mechanical properties of the struts are kept fixed, their contribution to the structural response is governed by their effective width and spatial arrangement. In particular, the eccentric positioning of the additional struts introduces an eccentric force, which directly affects the lever arm of the axial forces transmitted by the infill and, consequently, the magnitude of the shear demand induced at column ends. The geometric parameters defining the position and the width of the eccentric struts are therefore key modelling variables of the proposed formulation, as they control the interaction between global response and local force redistribution. Their role is investigated in the following sections through a GA-based calibration framework.

6.2 General framework for the identification of the multi-strut macro-model configuration

The general framework adopted in this chapter is conceived to systematically integrate experimental evidence, refined numerical modelling, and optimisation-based parameter identification in order to support the definition of a simplified yet mechanically consistent multi-strut macro-model for masonry-infilled RC frames. The rationale of the framework is to employ high-fidelity information and to transfer it into a macro-modelling strategy capable of capturing both global and local response quantities associated with infill-frame interaction.

A dataset of experimental tests on masonry-infilled RC frames provides the reference global structural response of the systems, expressed in terms of force-displacement response. For the same structural configurations, refined finite-element micro-models developed in the STKO/OpenSees environment and calibrated against the experimental results are employed to reproduce the experimental behaviour while enabling the investigation of local interaction mechanisms that cannot be directly measured during testing. In particular, the refined numerical models are used to quantify the amplification of shear demand at column ends induced by the interaction between the masonry infill and the surrounding reinforced concrete frame.

The experimental global response and the numerical local shear demand extracted from the refined micro-models define the reference targets for the identification of the multi-strut macro-model parameters. On this basis, a parametric three-strut macro-model is formulated and analysed within a genetic algorithm-based optimisation framework, which is applied independently to each specimen included in the reference dataset. The framework is designed to identify, for each case study, a strut configuration that achieves a consistent reproduction of both the benchmark global force-displacement response and the corresponding local shear demand at critical column sections.

The application of the optimisation procedure results in a collection of specimen-specific strut configurations, expressed in terms of strut positions and width-partition coefficients defining their relative contribution. The optimal parameter sets are subsequently analysed through genetic programming symbolic regression analyses, with the aim of extracting data-driven relationships linking the

strut configuration to selected geometric and mechanical properties of the infilled frames.

The overall logic of the proposed framework is schematically illustrated in Figure 6.2.

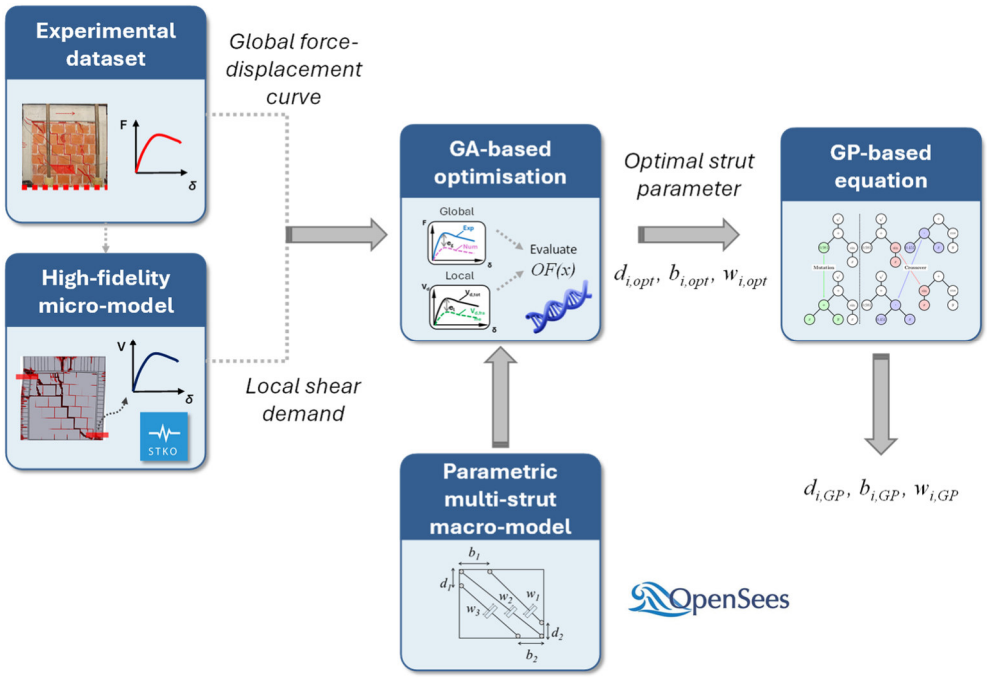

Figure 6.2: General framework for the identification of the multi-strut macro-model configuration based on experimental and numerical benchmarks, GA-based optimisation, and GP-based formulation of strut parameters.

6.2.1 Genetic Algorithm framework for the optimisation of the struts' arrangement

The identification of the proposed multi-strut macro-model configuration is formulated as a nonlinear optimisation problem, in which a genetic algorithm (GA) is adopted as the search strategy to identify a strut arrangement capable of reproducing both the global structural response of masonry-infilled RC frames and the local peak shear demand at column ends induced by infill-frame interaction. The optimisation problem is characterised by the coexistence of two response targets of different nature: the global force-displacement response and the local shear demand at critical column sections, which must be simultaneously matched within the optimisation framework.

The choice of a genetic algorithm is motivated by the intrinsic characteristics of the problem. The evaluation of the objective function requires the execution of nonlinear pushover analyses, making the optimisation process computationally expensive. Genetic algorithms belong to the class of soft-computing optimisation techniques and are particularly well suited for problems characterised by high computational burden, strong nonlinearity, complex interactions between parameters, and the presence of multiple local minima.

Within the adopted framework, the GA operates on a population of candidate solutions, each representing a mechanically admissible configuration of the multi-strut macro-model. A candidate solution is fully defined by a set of design variables and their constraint controlling the position and relative contribution of the equivalent struts. For each individual in the population a nonlinear static (pushover) analyses is performed. From these analyses, the global force-displacement response of the infilled frame and the local shear demand at column ends are extracted and compared with the corresponding reference targets.

The agreement between the macro-model predictions and the benchmark responses is quantified through a predefined objective function, which provides a scalar fitness measure for each candidate solution. This fitness value represents the basis for the evolutionary process and directly governs the selection of individuals for reproduction. At each generation, candidate solutions are evaluated based on their fitness and used to update the population through standard genetic operators, such as parent selection, crossover and mutation.

A schematic representation of the GA-based optimisation framework and its interaction with the numerical models is provided in Figure 6.3.

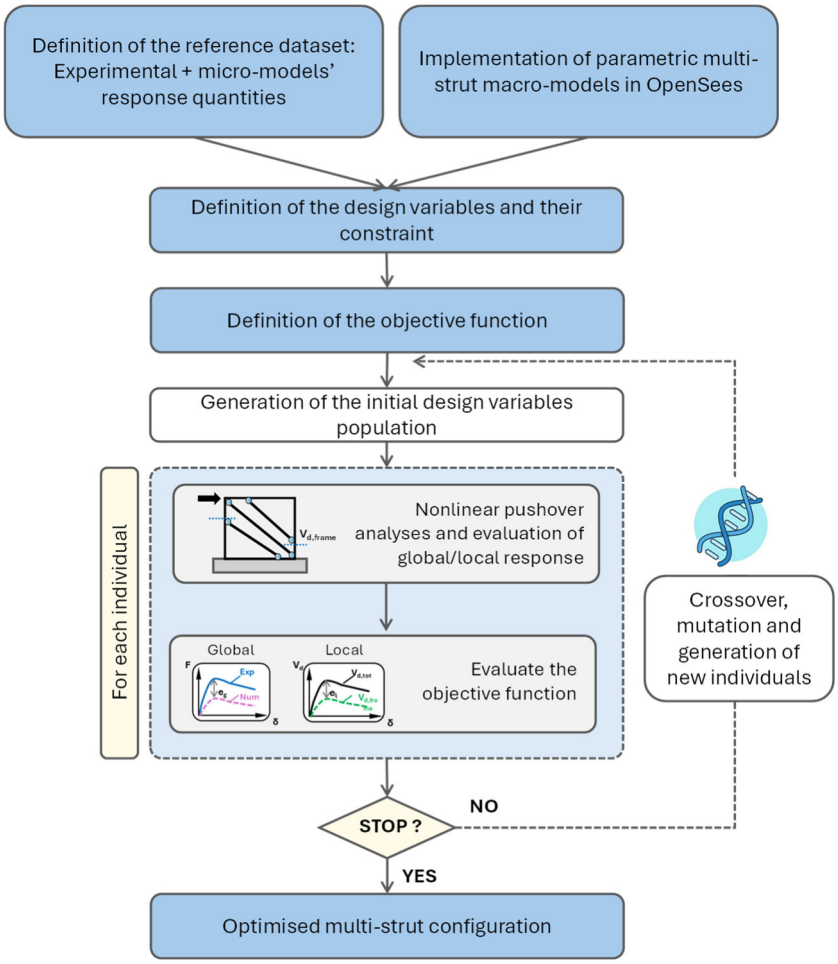

Figure 6.3: GA-based optimisation framework for the calibration of the proposed multi-strut macro-model.

6.2.2 Design variables and their constraints

The design variables are defined as the parameters governing the geometry and the relative contribution of each equivalent strut within the macro-model. In the present formulation, the mechanical properties of the equivalent struts are kept fixed and are defined according to the constitutive assumptions of **Di Trapani et al. (2018)** discussed in Chapters 2 and 5; the optimisation therefore focuses on the configuration of the strut layout rather than on material calibration. For each strut i, three continuous variables are introduced: (i) d_i, controlling the vertical position of the strut along the column height; (ii) b_i, controlling the horizontal location along the beam span; (iii) p_i, a positive weighting coefficient defining the portion of the total effective width assigned to the strut ($w_i = p_i \cdot w$).

The design vector collecting the optimisation variables can therefore be expressed as follows:

$$\boldsymbol{\theta} = \begin{bmatrix} \mathbf{d} \\ \mathbf{b} \\ \mathbf{p} \end{bmatrix} \tag{81}$$

where **d**, **b**, and **p** vectors are defined as follows:

$$\begin{aligned} \mathbf{d} &= \begin{bmatrix} d_1, & ..., & d_{n-1} \end{bmatrix} \\ \mathbf{b} &= \begin{bmatrix} b_1, & ..., & b_{n-1} \end{bmatrix} \\ \mathbf{p} &= \begin{bmatrix} p_1, & ..., & p_n \end{bmatrix} \end{aligned} \tag{82}$$

being n the number of the struts. Although the multi-strut macro-model consists of n equivalent struts, the position of the central diagonal strut is uniquely defined by the frame geometry and is therefore fixed. As a result, only the off-diagonal struts require explicit definition of their position.

The design variables are constrained to ensure geometric admissibility and physical consistency: the position parameters are bounded within the member dimensions (i.e., $d_i \in [b_c, 0.5 \cdot h]$, $b_i \in [b_c, 0.5 \cdot l]$), being b_c the column width, h the column height, and l the beam span. The width-partition coefficients p_i are required to satisfy positivity and unity-sum constraints, i.e. $p_i > 0.2$ and $\sum p_i = 1$. As a consequence, only *n-1* weight coefficients are independent. Due to these constraints, the design vector of the weighting coefficients can therefore be expressed as:

$$\mathbf{p} = \begin{bmatrix} p_1, & ..., & p_{n-1} \end{bmatrix} \tag{83}$$

6.2.3 Definition of the objective function

The GA-based optimisation framework is formulated to simultaneously account for the global structural response of the infilled frame and the local shear demand at column ends induced by infill-frame interaction. These two response components are characterised by different physical meanings and are therefore treated through different error measures within the objective function.

The discrepancy in the global response is quantified by means of the root-mean-square error (RMSE) between the experimental force-displacement envelope and the corresponding numerical response predicted by the multi-strut macro-model over the imposed displacement history, defined as:

$$RMSE_G(\boldsymbol{\theta}) = \sqrt{\frac{1}{m}\sum_{k=1}^{m}\left(F_k^{\exp} - F_k^{num}(\boldsymbol{\theta})\right)^2} \tag{84}$$

where $\boldsymbol{\theta}$ is the design vector defined in Equation (94), m denotes the number of prescribed displacement increments used to discretise the pushover response, obtained by interpolating the force-displacement curves over a set of m predefined displacement values, and $F_k^{\exp}$ and F_k^{num} are the experimental and numerical force values, respectively, evaluated at the k-th displacement increment. The RMSE is computed over the entire displacement history in order to ensure that the optimisation accounts for the overall global behaviour of the infilled frame, including stiffness, strength, and post-peak softening branch. This choice reflects the need to capture the global response in terms of both lateral capacity and ductility of the system.

The local discrepancy is expressed in terms of the absolute error in the peak shear demand at the windward and leeward column ends, denoted as $\Delta V_{WC}(\boldsymbol{\theta})$ and $\Delta V_{LC}(\boldsymbol{\theta})$, respectively. These quantities are computed as the difference between the maximum shear demand predicted by the multi-strut macro-model and the corresponding peak values extracted from the refined finite-element micro-model replicas described in Chapter 5. Accordingly, the absolute shear demand errors at the windward and leeward column ends are defined as follows:

$$\Delta V_{WC}(\boldsymbol{\theta}) = \max\left\{V_{WC,micro}\right\} - \max\left\{V_{WC,macro}(\boldsymbol{\theta})\right\}$$
$$\Delta V_{LC}(\boldsymbol{\theta}) = \max\left\{V_{LC,micro}\right\} - \max\left\{V_{LC,macro}(\boldsymbol{\theta})\right\} \quad (85)$$

In contrast to the global response, the local shear demand error metric is evaluated only at the maximum shear value, as this quantity represents the governing demand parameter for shear verification and therefore corresponds to the most critical condition.

Although the problem could be naturally formulated as a multi-objective optimisation, a single-objective formulation is adopted through linear scalarisation in order to simplify the optimisation process. The resulting objective function is defined as:

$$OF(\boldsymbol{\theta}) = RMSE_G(\boldsymbol{\theta}) + \alpha[\Delta V_{WC}(\boldsymbol{\theta}) + \Delta V_{LC}(\boldsymbol{\theta})] \quad (86)$$

where α is a weighting coefficient controlling the relative contribution of the local response with respect to the global one. The value of α is selected through a parametric analyses of the two components across the reference specimens. In the present study, the adopted value of α has been set equal to 6 for the reference database.

A schematic illustration of the computation of the global RMSE over the force-displacement curves and of the local peak shear demand absolute error at column ends is provided in Figure 6.4.

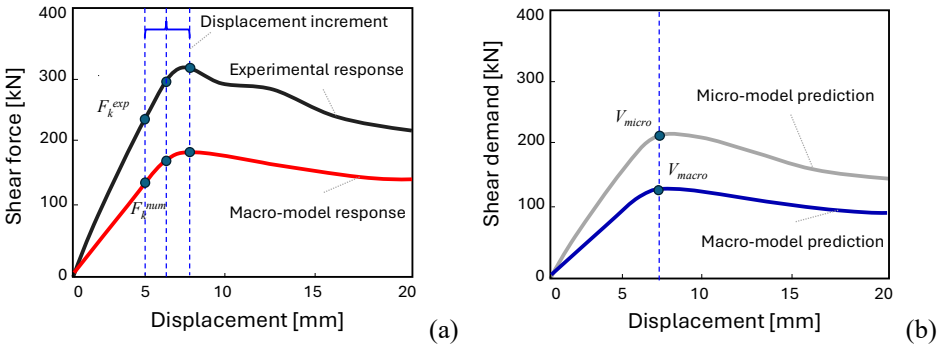

Figure 6.4: Schematisation of the computation of the two-error metrics used in the objective function: (a) Computation of the RMSE over the global force-displacement curves; (b) Computation of the absolute error in peak shear demand at column ends.

6.2.4 Main genetic operators

In the present study, the GA is used as a calibration tool implemented in Python using the PyGAD library (**Gad, 2021**), coupled with nonlinear pushover analyses in OpenSees. The effectiveness of a GA depends on a limited set of controlling parameters that govern exploration capabilities, convergence behaviour, and computational cost. Accordingly, the adopted settings were selected to ensure stable convergence while maintaining the number of structural analyses within a manageable computational effort. The optimisation was carried out using a population size of 500 individuals evolved over 50 generations. Feasibility was enforced throughout the optimisation process to ensure that all candidate solutions correspond to mechanically admissible strut configurations, consistently with the constraints defined in Section 6.2.2. The initial population was randomly generated by sampling the design variables within their admissible ranges. At each generation, parent solutions are selected using a *roulette* selection strategy. New candidate solutions are generated through a one-point crossover operator, which combines the genetic information of the parent solutions, and through mutation, implemented as a random perturbation applied to a single gene with a probability of 25%. This approach promotes exploration of the design space, reduces the risk of premature convergence to local minima, and supports the exploitation phase of the evolutionary search. *Elitism* is introduced by preserving the best two individuals in terms of fitness across successive generations, thus improving the stability of convergence. The optimisation process is terminated after reaching the maximum number of generations.

6.2.5 Genetic Programming framework for the identification of strut arrangements formulations

In order to obtain a preliminary, dataset-informed generalisation of the GA-identified strut configurations, a genetic programming (GP) procedure is adopted to perform symbolic regression of the optimal strut parameters through HeuristicLab framework (**Elyasaf et al. 2014**). In this context, GP searches for explicit expressions that link a set of selected input descriptors of the infilled frame to the target configuration parameters. Each candidate solution in the GP is therefore not a numerical vector, but a mathematical expression, represented as an expression tree and evaluated directly against the available data. The GP process starts from the construction of a training dataset, assembled by pairing, for each

specimen, an input vector $\mathbf{x}$ collecting the selected geometric and mechanical descriptors and the corresponding GA-optimal strut-configuration parameters $\boldsymbol{\theta}_{\mathbf{opt}}$. This dataset defines the reference information on which the symbolic regression is performed. An initial population of candidate expressions is then generated. Candidate models are randomly created by combining elements from a predefined terminal set (input variables and constants) and a restricted function set (mathematical operators). For each individual expression, the fitness function is evaluated. Subsequently, offsprings are generated through parent selection and through genetic operators acting directly on the expression trees. In particular, crossover recombines subtrees of two parent expressions to create offspring with mixed structural components, while mutation introduces local modifications to the expression structure (e.g., replacing an operator, altering a subtree, or perturbing constants). The evolutionary loop (fitness evaluation → selection → genetic operators) is repeated until a stopping criterion is met, such as reaching a maximum number of generations or observing no further improvement in fitness. The final outcome of the GP is the expression (or set of expressions) that maximise the fitness function, providing the best compromise between predictive accuracy and formulation compactness. A scheme of the GP-framework is shown in Figure 6.5.

The GP algorithm is implemented with a population of 1000 individuals evolved over 50 generations. Parent selection is performed using a tournament selection strategy (tournament size = 4), while elitism is ensured by preserving the best individual at each generation. Crossover is performed through random subtree swapping, enabling the exchange of functional structures between individuals. Mutation includes both random operator mutation and random perturbation of variables, with an overall mutation probability of 15%. These operators allow exploration of the functional space while maintaining diversity within the population. To ensure physically meaningful results and mitigate overfitting, the search space is constrained by imposing bounds on the identified parameters, as done for the GA framework. In addition, relatively simple functional forms are favoured during the evolutionary process to avoid overly complex expressions not supported by the available data.

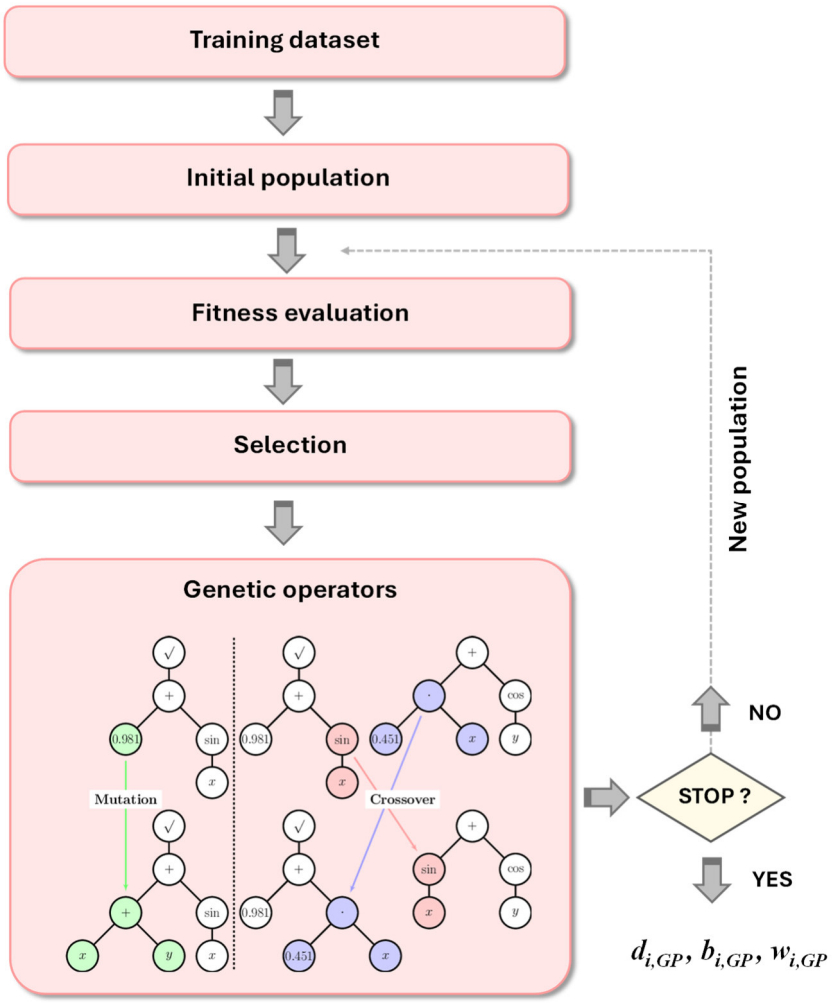

Figure 6.5: GP-framework for the identification of struts arrangement formulations.

6.3 Reference dataset

The calibration of the proposed multi-strut macro-model relies on experimental specimens and high-fidelity micro-models already presented in Chapter 5. In order to avoid unnecessary repetition, this section focuses on defining the reference dataset, while detailed descriptions of the experimental tests and micro-modelling strategies are intentionally omitted and referred to Chapter 5.

6.3.1 Reference experimental tests

The reference experimental single-storey, single-bay infilled RC frame specimens are selected from the experimental database already investigated in Chapter 5, for which corresponding refined micro-models were developed. In the present chapter, a selected subset of ten experimental specimens is considered. The reduced number of specimens considered reflects a limitation of the present study, as the calibration was conducted before the full experimental database presented in Chapter 5 became available. Future extensions will address the application of the proposed framework to a larger number of case studies. The selected specimens were chosen based on the representativeness of different infill typologies and geometric configurations. These specimens were selected from the experimental campaigns conducted by **Mehrabi et al. (1996)**, **Colangelo (2005)**, **Cavaleri and Di Trapani (2014)**, **Morandi et al. (2018)**, and **Di Trapani et al. (2024)**. For the reader convenience, the selected specimens, together with their main geometric and mechanical properties, are summarised in Table 25. A detailed description of the experimental setup, material properties, loading protocols, and observed response is provided in Chapter 5.

Table 25: Reference dataset: Typological, geometric, and mechanical details of the specimens.

Reference	Spec. ID	Type of masonry	l (mm)	h (mm)	t (mm)	b_c (mm)	h_c (mm)	b_b (mm)	h_b (mm)	f_{vm} (MPa)	f_{m1} (MPa)	f_{m2} (MPa)
Mehrabi et al. (**1996**)	S5	Solid concrete	2108	1422	92	178	178	152	228.6	1.15	13.84	13.84
	S6	Hollow concrete	2108	1422	92	203	203	152	228.6	0.70	5.30	10.10
	S11	Solid concrete	2948	1422	92	178	178	152	228.6	1.03	11.44	11.44
Colangelo (**2005**)	C1	Hollow clay	1700	1300	120	200	200	200	250	0.87	3.39	5.10
	L2	Hollow clay	2300	1300	120	200	200	200	250	0.87	3.39	5.10
	N1	Hollow clay	2300	1300	160	200	200	200	250	0.58	2.74	3.90
Cavaleri and Di Trapani (**2014**)	S1A	Solid calcarenite	1600	1600	200	200	200	200	400	0.73	3.08	2.67
	S1B	Hollow clay	1600	1600	150	200	200	200	400	1.07	4.18	8.70
Morandi et al. (**2018**)	TA2	Hollow clay	4220	2950	350	350	350	350	350	0.36	1.08	4.64
Di Trapani et al. (**2024c**)	FIF	Hollow clay	2200	2100	230	250	250	250	350	0.36	2.52	3.36

6.3.2 Reference micro-models

For each selected experimental specimen, the corresponding refined finite element micro-model developed and discussed in Chapter 5 is adopted as the reference solution for local response calibration. The micro-model replicas of the experimental tests are assumed to provide a reliable representation of both the global response and the local interaction mechanisms between the masonry infill and the surrounding RC frame. The main output extracted from the micro-models is the local shear demand at critical column sections. To estimate the local shear demand at each critical section, three section cuts were introduced at the column ends at distances equal to $0 \cdot h_c$, $0.5 \cdot h_c$, and h_c from the column end, with h_c representing the column depth. The shear demand was defined as the mean value of the shear forces extracted at the three section cuts, as defined and evaluated in Chapter 5. These quantities form the basis for the calibration of the proposed macro-model. Further details on the formulation of the refined micro-models, the adopted material parameters, and the numerical results, including the procedure used to extract the local shear demand at critical sections, are provided in Chapter 5.

6.3.3 Macro-models of the reference dataset

For each specimen included in the reference dataset, a corresponding three-strut macro-model was developed in OpenSeesPy by reproducing the specimen geometry and boundary conditions adopted in the experimental tests and consistently implemented in the refined micro-model replicas. The infilled RC frames were modelled using the approach introduced in Section 6.1. The mechanical material properties, including the constitutive law adopted for the equivalent struts and the total effective infill width w are defined in Chapter 5 and are not reported here for the sake of brevity.

6.4 Results of the optimisation-based calibration

This section presents the results of the optimisation-based calibration of the proposed eccentric three-strut macro-model. The output of the calibration consists of a set of optimised parameters defining the geometry and the relative contribution of the three struts. In particular, the optimisation determines the eccentric positions of the two additional struts (through the location parameters d_1, d_2, b_1, b_2), and the distribution of the total effective infill width among the three struts (through the weighting coefficients p_i, so that $w_i = p_i \cdot w$).

The parameters resulted from the optimisation for the specimens analysed are summarised in Table 26.

Table 26: Optimal parameters for the reference dataset.

Specimen ID	w_1 (mm)	w_2 (mm)	w_3 (mm)	d_1 (mm)	d_2 (mm)	b_1 (mm)	b_2 (mm)
S5	276.2	110.5	198.3	351	291	280	187
S6	314.4	125.7	220.0	325	281	193	145
S11	370.7	111.2	333.7	350	580	550	240
C1	302.4	120.9	211.7	210	290	209	153
L2	307.0	92.1	245.6	290	413	280	172
N1	312.8	93.8	250.2	235	405	250	173
S1A	286.3	159.1	222.7	482	330	205	396
S1B	298.8	166.0	232.4	332	498	390	208
TA2	606.1	242.4	424.2	229	465	356	152
FIF	372.5	207.0	289.8	261	235	171	140

The results for the global and local response are presented specimen-by-specimen in the following subsections, allowing a direct comparison between the calibrated macro-model predictions and the corresponding reference responses for each case study.

6.4.1 Global response

The global response of the calibrated multi-strut macro-model is evaluated by comparing the numerical pushover curve obtained with the GA-optimised strut configuration against the corresponding experimental force-displacement response for each of the reference specimens. Since the experimental campaigns were generally conducted under cyclic loading protocols, the experimental benchmark is expressed in terms of a monotonic backbone/envelope curve, derived from the cyclic response in order to ensure consistency with the monotonic nonlinear static analyses adopted in this chapter. Figure 6.6 shows the specimen-by-specimen overall global response comparison. Across the full dataset, the optimised configurations provide a good agreement with the experimental global behaviour. In particular, the optimised configurations well capture the initial stiffness, peak lateral resistance, and softening behaviour after peak.

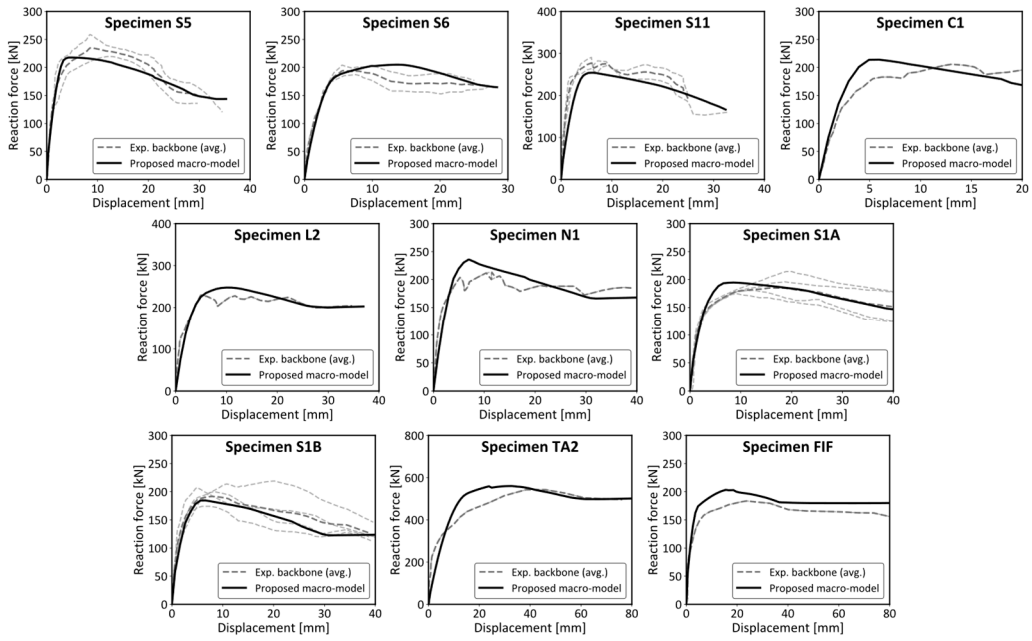

Figure 6.6: Comparison between experimental and optimised macro-model overall responses for the reference dataset's specimens.

A quantitative measure of the global fit is provided through the RMSE, expressed in terms of lateral force (kN) and computed over the entire displacement range of the pushover curve. Results are summarised in Table 36.

Table 27: RMSE values of the global force-displacement curve for the reference specimens after the optimisation.

Specimen ID	**S5**	**S6**	**S11**	**C1**	**L2**	**N1**	**S1A**	**S1B**	**TA2**	**FIF**
RMSE (kN)	232.5	295.8	390.7	293.3	292.2	369.8	191.4	271.3	1400.7	520.9

Although the optimisation is designed to simultaneously fit global and local targets, the global response remains adequately reproduced for all infill arrangements considered (solid/hollow units, different aspect ratios, different frame member sections). This outcome indicates that introducing eccentric struts and calibrating their arrangement does not compromise the ability of the macro-model to represent the overall global behaviour. Instead, the GA identifies configurations that preserve global stiffness and strength while enabling additional degrees of freedom to match the actual local shear demand, discussed in the following subsection.

6.4.2 Local shear demand

The local response of the calibrated multi-strut macro-model is assessed in terms of shear demand at the windward and leeward columns, evaluated as the average of the shear forces extracted at the three defined section cuts, consistently with the procedure adopted in Chapter 5. Figure 6.7 presents the specimen-by-specimen comparison between the shear demand predicted by the GA-calibrated multi-strut macro-model and the corresponding reference values obtained from the micro-models, for both windward and leeward columns. The results indicate that, in most cases, the calibrated multi-strut macro-model is able to reproduce not only the peak shear demand, which was the objective of the optimisation process, but also the evolution of shear demand at different drift levels with satisfactory accuracy across the reference dataset.

In addition, Table 37 summarises the comparison in terms of peak shear demand (V_{max}) at column ends, reporting the GA-optimised macro-model predictions and the corresponding refined micro-model values together with the GA-to-micro-model prediction ratio ($V_{max,GA}$ / $V_{max,micro}$). Overall, considering both windward and leeward column ends, the ratios exhibit a mean value of 1.015 with a coefficient of variation (COV) of 2.43%.

Table 28: Comparison between macro-model and micro-model peak shear demand V_{max} at windward and leeward column ends.

	Windward column			**Leeward column**		
Spec ID	$V_{max,GA}$ **(kN)**	$V_{max,micro}$ **(kN)**	$V_{max,GA}$ / $V_{max,micro}$ **(-)**	$V_{max,GA}$ **(kN)**	$V_{max,micro}$ **(kN)**	$V_{max,GA}$ / $V_{max,micro}$ **(-)**
S5	83.14	84.85	0.98	108.89	104.58	1.04
S6	88.81	87.77	1.01	101.60	99.74	1.02
S11	113.97	114.51	0.99	113.02	110.64	1.02
C1	90.08	85.63	1.05	106.42	105.03	1.01
L2	112.50	110.82	1.01	119.43	118.48	1.01
N1	104.43	100.81	1.04	110.03	110.12	0.99
S1A	60.47	60.59	0.99	92.59	92.29	1.00
S1B	64.64	65.43	0.99	75.60	78.09	0.97
TA2	241.90	234.27	1.03	276.20	275.48	1.00
FIF	86.12	81.17	1.06	98.12	93.52	1.05
		μ_w	1.02		μ_l	1.01
		COV	0.03		**COV**	0.02

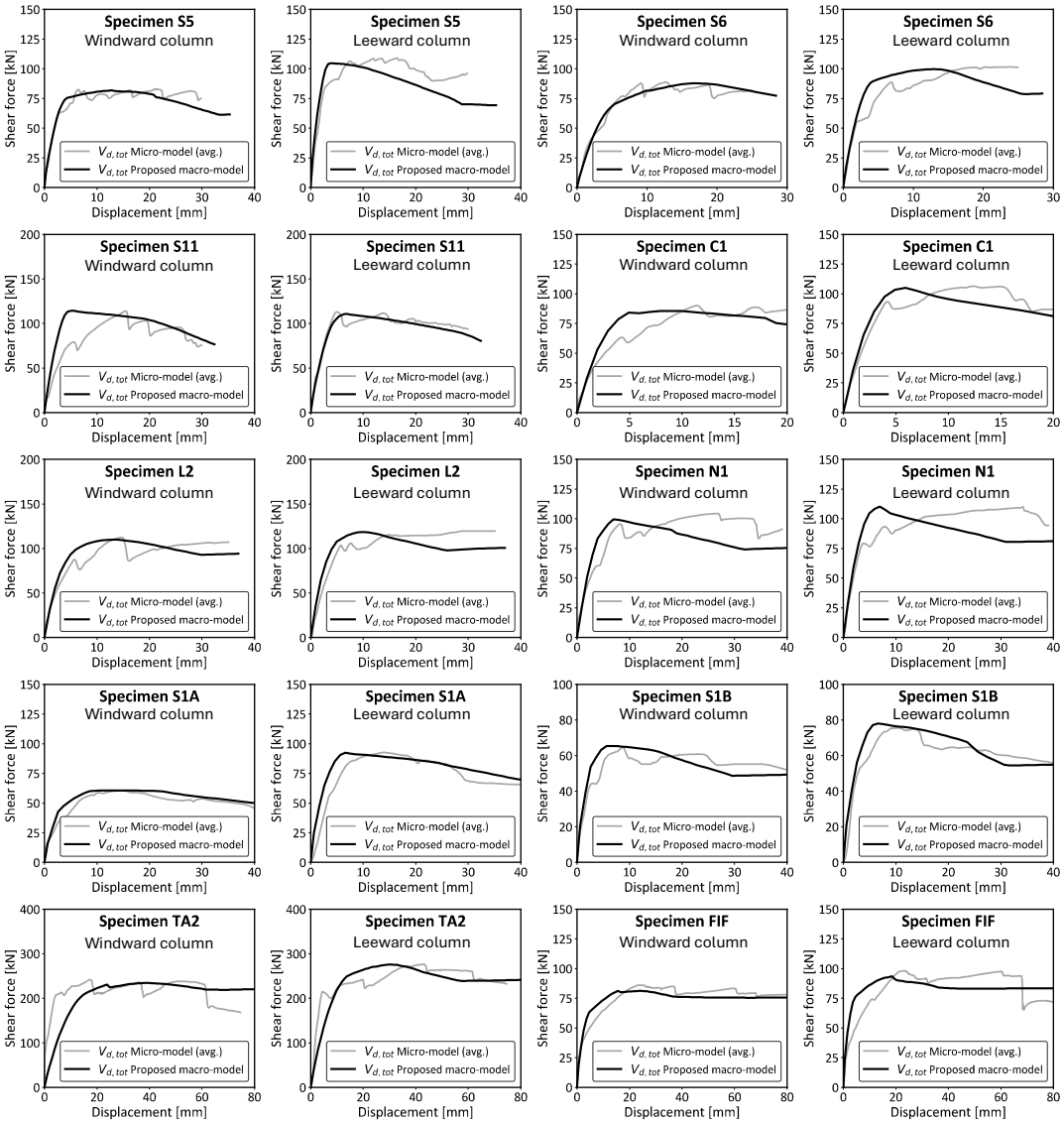

Figure 6.7: Comparison between micro-model and optimised macro-model shear demand at both windward and leeward column ends for the reference dataset's specimens.

6.5 Identification of data-driven strut arrangement formulations

Although the limited size of the reference dataset, this section aims to preliminary generalise the collected optimal parameter solutions by deriving predictive relationships for the key parameters governing the three-strut configuration. Specifically, data-driven expressions are proposed to estimate the width partition coefficients, and the geometric location of the diagonal struts. The

purpose is to replace case-by-case optimisation with formulations that can be directly applied once the geometry and mechanical properties of the infilled RC frame are known.

6.5.1 Data-driven formulations proposed for the estimation of the struts' configuration

The data-driven relationships were derived by post-processing the set of reference dataset optimal configurations obtained from the GA calibration, discussed in Section 6.4. For each reference specimen, the GA provides an optimal parameter vector (**p**, **d**, **b**) describing the three-strut layout, including the width partition coefficients and the geometric coordinates defining the diagonal struts position. By collecting these optimal solutions across the dataset, an input-output database was assembled, in which the GA-optimal parameters represent the target variables to be predicted. A wide set of potential physically and mechanically meaningful predictors was initially considered (e.g., infill geometry, stiffness ratios, masonry strengths, infill thickness, etc.). The selection of the predictor variables was guided by their physical and mechanical relevance and by their influence on the GA-optimal solutions. Accordingly, Table 29 reports, for each specimen, the subset of predictors effectively adopted in the final relationships, specifically the infill aspect ratio l'/h', the dimensionless infill-frame stiffness parameter λ^*(**Papia et al., 2003**), and the unit-to-mortar compressive strength ratio f_b/f_m.

Table 29: Selected predictors adopted for the empirical formulation of the strut-configuration parameters for the reference specimens.

Specimen ID	l'/h' (-)	f_b/f_m (-)	λ^* (-)
S5	1.41	0.89	2.24
S6	1.41	1.37	0.47
S11	1.91	1.20	1.66
C1	1.17	0.41	0.37
L2	1.54	0.41	0.27
N1	1.54	0.58	0.25
S1A	0.91	2.31	2.95
S1B	0.91	0.96	2.16
TA2	1.46	0.72	0.46
FIF	0.97	1.99	2.32

First, the width-partition relationships are introduced, which define the coefficients p_i governing how the total effective infill width is distributed among the three equivalent struts. Post-processing of the GA-optimal solutions shows that, within the considered dataset, the optimal weight coefficients exhibit clear and stable trends primarily governed by the infill aspect ratio *l'/h'*. This behaviour is mechanically consistent, since *l'/h'* directly controls the inclination of the compression diagonal and the extent of the contact regions along beams and columns. As a result, the variation of p_i across specimens can be described through simple relationships in terms of *l'/h'*, defined consistently with the constraint adopted in the optimisation framework ($p_i > 0.2$ and $\sum p_i = 1$), so that the effective width assigned to each strut can be directly computed as $w_i = p_i \cdot w$, where w is the total effective infill width. The corresponding expressions are provided below.

$$\tilde{p}_1 = \begin{cases} 0.45 & if \quad l'/h' \le 1 \\ 0.50 & if \quad l'/h' > 1 \end{cases} \tag{87}$$

$$\tilde{p}_2 = -0.11\left(\frac{l'}{h'}\right) + 0.35 \tag{88}$$

$$\tilde{p}_3 = \begin{cases} 0.45 & if \quad l'/h' \le 1.5 \\ 0.184\left(\frac{l'}{h'}\right) + 0.1 & if \quad l'/h' > 1.5 \end{cases} \tag{89}$$

Figure 6.8 compares the resulting strut effective widths w_i predicted by the proposed weight relationships with the corresponding GA-optimal values for the reference specimens. Some data points overlap due to similar values.

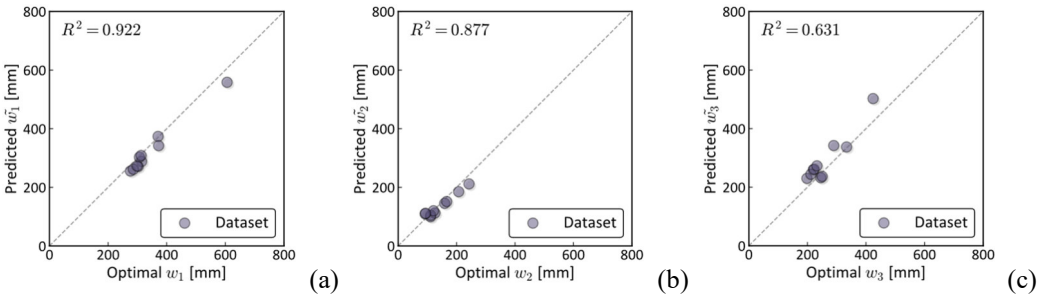

Figure 6.8: Predicted vs. GA-optimal effective width w_i for the reference specimens: (a) Strut 1 (w_1); (b) Strut 2 (w_2); (c) Strut 3 (w_3).

Subsequently, data-informed formulations are introduced for the positioning of the two eccentric struts, defining their vertical coordinates d_i along the columns and the corresponding horizontal coordinates b_i along the beam span. Unlike the width weights, these parameters reflect a more complex relationship between infill geometry and the relative stiffness and strength of the infill-frame system. Accordingly, the location parameters were expressed as functions of the selected predictors l'/h', λ^*, and f_b/f_m. Given this, the formulations of the struts' location were derived through symbolic regression based on genetic programming, implemented in the HeuristicLab platform (**Elyasaf et al. 2014**), as discussed in Section 6.2.4. Given the relatively limited size of the available dataset, particular attention was paid to mitigating the risk of overfitting. For the parameters d_i identified through Genetic Programming (GP), the dataset was split into training and validation subsets, with approximately 80% of the data used for training and the remaining portion used to verify the generalization capability of the obtained expressions. In addition, the GP formulation was constrained to relatively simple functional forms to avoid overly complex and non-physical relationships. For the parameters b_i, a linear regression approach was adopted using the full dataset. Given the simplicity of the model, the risk of overfitting is inherently limited, as no higher-order terms or nonlinear combinations were introduced. Therefore, the obtained relationships are considered robust within the limited range of the analysed data.

The resulting GP-equations adopted for d_1 and d_2 together with the corresponding expressions for b_1 and b_2, are reported below.

$$\tilde{d}_1 = \frac{1}{0.017 - 0.0048 \cdot \lambda^*} + \frac{1}{0.063 - 0.039 \cdot \left(f_b / f_m\right)} + 153.59 \tag{90}$$

$$\tilde{d}_2 = 49.39\left(\frac{l'}{h'}\right)^3 + \frac{1}{0.39 \cdot \left(f_b / f_m\right) - 0.37} + 227.18 \tag{91}$$

$$\tilde{b}_1 = 0.96 \cdot \tilde{d}_2 - 74.04 \tag{92}$$

$$\tilde{b}_2 = 0.82 \cdot \tilde{d}_1 - 55.80 \tag{93}$$

Figure 6.9 compares the predicted and GA-optimal values of the diagonal strut location parameters for the reference specimens. Some data points overlap due to similar values.

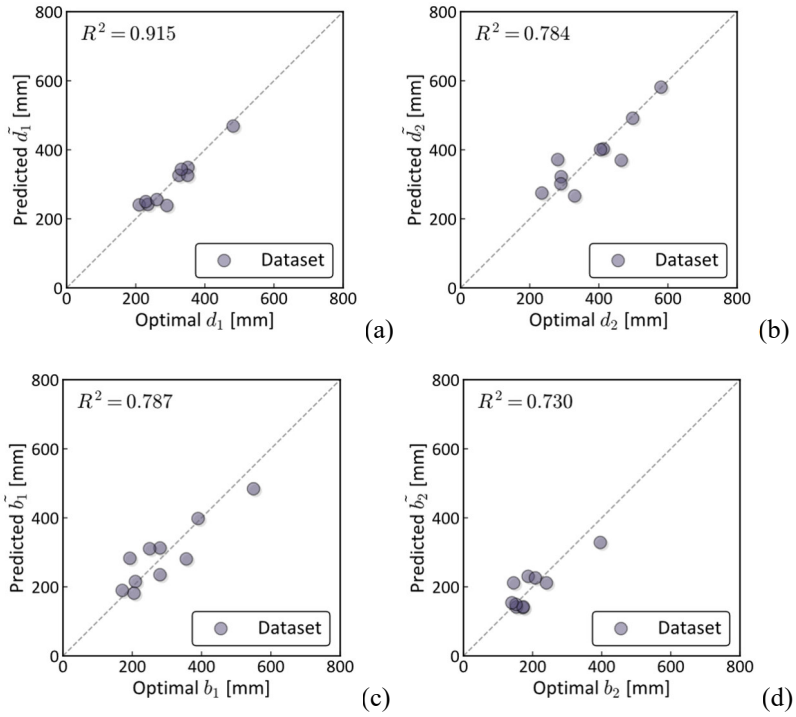

Figure 6.9: Predicted vs. GA-optimal struts positions for the reference specimens: (a) Vertical position d_1; (b) Vertical position d_2; (c) Horizontal position b_1; (d) Horizontal position b_2.

For completeness, the values obtained from the proposed empirical formulations are also reported in Table 30.

Table 30: Updated strut width and diagonal strut positions evaluated by Eqs. (87)-(93).

Spec ID	w_1 (mm)	w_2 (mm)	w_3 (mm)	d_1 (mm)	d_2 (mm)	b_1 (mm)	b_2 (mm)
S5	255.5	99.6	229.9	349.0	322.0	235.0	230.4
S6	288.3	112.4	259.5	325.9	371.7	282.8	211.4
S11	373.7	104.6	337.4	326.0	581.5	484.2	211.5
C1	271.1	120.0	244.0	240.5	301.5	215.4	141.4
L2	303.0	109.4	232.3	238.5	402.8	312.7	139.8
N1	308.7	111.5	236.7	241.6	400.6	310.5	142.3
S1A	261.5	145.2	261.5	468.8	266.3	181.6	328.6
S1B	272.8	151.5	272.8	343.5	491.7	398.0	225.9
TA2	558.5	211.6	502.6	249.8	369.7	280.9	149.1
FIF	342.2	185.0	342.2	255.7	274.7	189.7	153.9

6.5.2 Performance assessment of the data-driven formulations

This subsection assesses the structural response obtained when the three-strut macro-model is defined directly through the data-driven relationships introduced in Section 6.5.1. Due to the limited number of available reference specimens, the formulations are evaluated on the same dataset used for their derivation; accordingly, the aim is not to provide a validation of the expressions, but rather to quantify how these affect the predicted global and local response.

6.5.2.1 Global response

The effect of the data-driven formulations on the global behaviour is assessed by comparing the pushover response obtained with the GP-based macro-model against the experimental force-displacement backbone for each reference specimen. Figure 6.10 presents the specimen-by-specimen comparison of the global response.

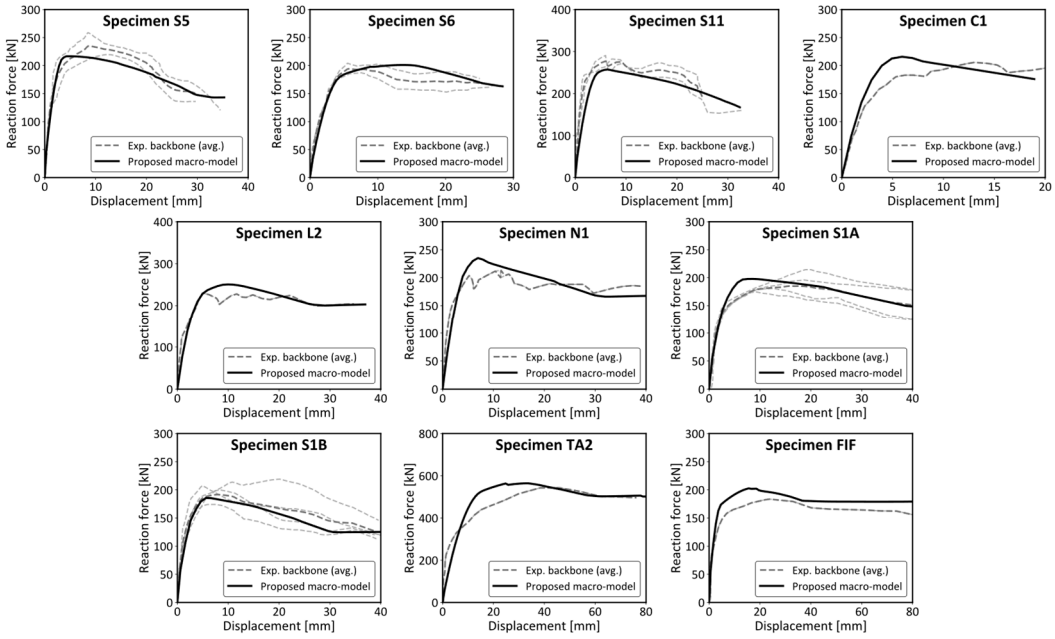

Figure 6.10: Comparison between experimental and data-driven macro-model overall responses for the reference dataset's specimens.

Overall, the results show that the macro-model implemented through the proposed expressions preserves the main accuracy of the global response across the reference dataset, particularly the initial stiffness, peak strength, and post-peak evolution. This suggests that adopting the GP-derived strut configuration does not significantly affect the predicted global behaviour. To support this observation,

Table 31 reports the RMSE values computed over the full displacement history, highlighting the precision and the accuracy with respect to the GA-optimised configurations discussed in Section 6.4. Additionally, Figure 6.11 summarises the distribution of the global response error ratio between the GP-based and the GA-optimised macro-model ($RMSE_{GP}/RMSE_{GA}$) across the reference specimens, providing a concise measure of the discrepancy introduced by replacing the optimised configuration with the empirical one. Overall, the ratios cluster around unity (μ = 1.01), indicating that the empirical formulations generally preserve the global accuracy achieved by the GA, with a limited dispersion (COV = 9.1%).

Table 31: RMSE comparison between the GA-optimised and the data-driven configuration.

Specimen ID	**$RMSE_{GA}$ (kN)**	**$RMSE_{GP}$ (kN)**	**$RMSE_{GP}/RMSE_{GA}$ (-)**
S5	232.50	248.96	1.07
S6	295.81	253.24	0.86
S11	390.68	411.83	1.05
C1	293.32	289.01	0.99
L2	292.19	326.93	1.12
N1	369.75	382.37	1.03
S1A	191.43	221.19	1.16
S1B	271.33	248.94	0.92
TA2	1400.74	1345.73	0.96
FIF	520.89	502.58	0.96
		μ	1.01
		COV	0.09

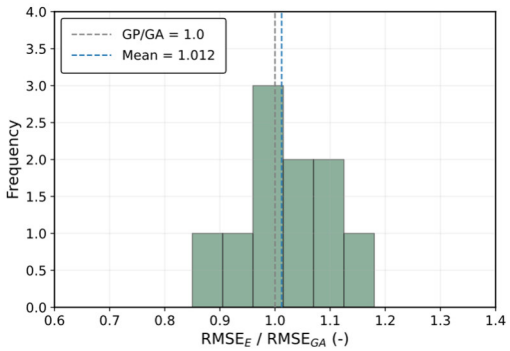

Figure 6.11: Overall RMSE (E)/RMSE (GA) ratio distributions for the reference specimens.

6.5.2.2 Local shear demand

The impact of the data-driven strut configuration on the local response is assessed in terms of column-end shear demand at the windward and leeward

columns. Figure 6.12 presents, specimen-by-specimen, the comparison between the shear demand throughout the displacement history predicted by the GP-based three-strut macro-model and the corresponding reference results obtained from the refined micro-models, for both windward and leeward columns.

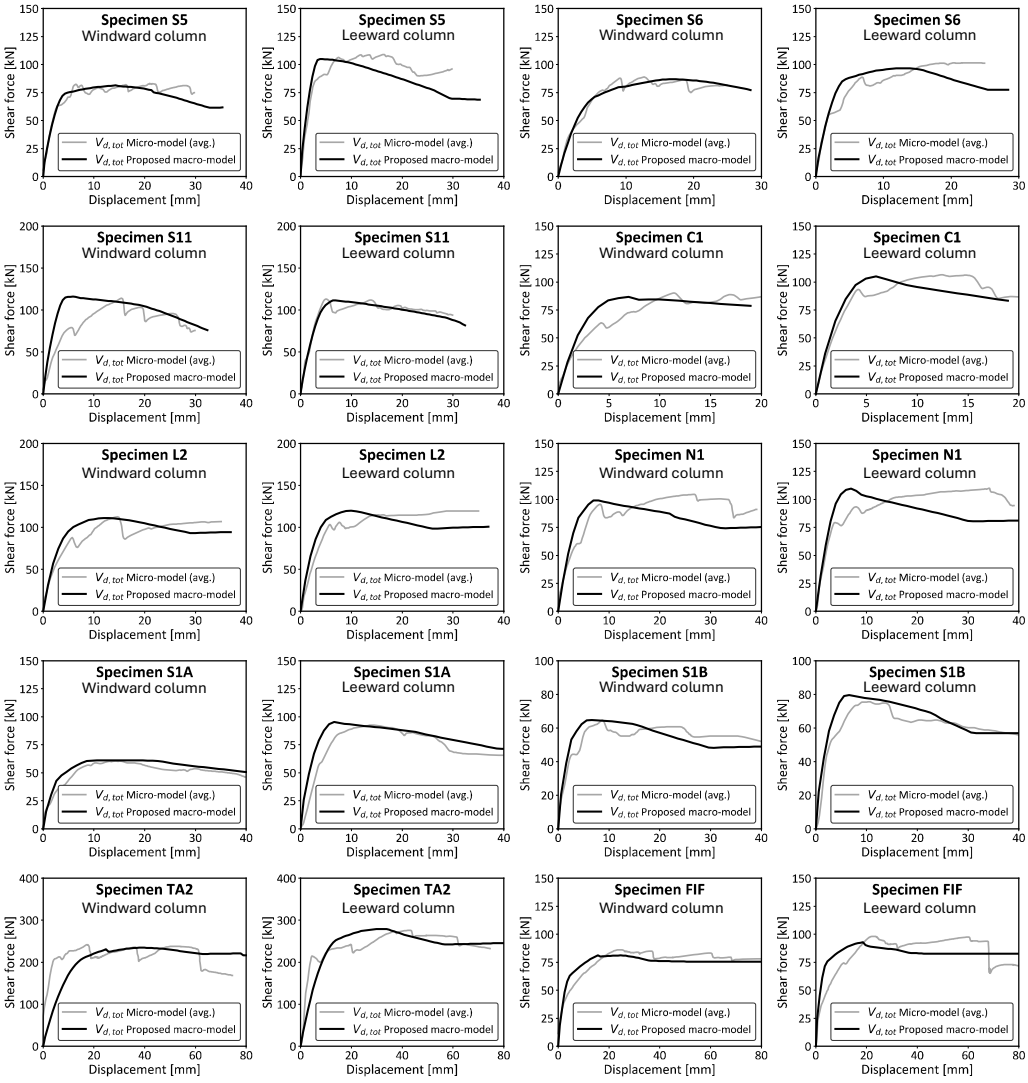

Figure 6.12: Comparison between micro-model and data-driven macro-model shear demand at both windward and leeward column ends for the reference dataset's specimens.

The results show that adopting the GP formulations, shear-drift responses remain close to the GA-optimised predictions, not only in terms of peak shear demand (V_{max}) but also over the full displacement history. To complement these outcomes, Table 32 reports the peak shear demands predicted by the GA-optimised

($V_{max,GA}$) and GP-based ($V_{max,GP}$) configurations, together with their ratio, providing a quantitative measure of the deviation from the GA-optimal response.

Table 32: Peak shear demand comparison between the GA-optimised and the data-driven configuration.

	Windward column			Leeward column		
Specimen ID	**$V_{max,GA}$ (kN)**	**$V_{max,GP}$ (kN)**	**$V_{max,GP}$ / $V_{max,GA}$ (-)**	**$V_{max,GA}$ (kN)**	**$V_{max,GP}$ (kN)**	**$V_{max,GP}$ / $V_{max,GA}$ (-)**
S1A	81.85	81.33	0.99	104.58	104.81	1.00
S1B	87.77	86.88	0.99	99.74	96.72	0.97
FIF	114.51	115.95	1.01	110.64	111.57	1.01
C1	85.63	86.62	1.01	105.03	104.93	1.00
S5	110.82	111.03	1.00	118.48	119.76	1.01
S6	100.81	99.14	0.98	110.12	109.70	1.00
TA2	60.59	61.19	1.01	92.29	95.41	1.03
L2	65.43	64.68	0.99	78.09	79.55	1.02
N1	234.27	234.60	1.00	275.48	279.05	1.01
S11	81.17	81.08	1.00	93.52	92.83	0.99
		μ	0.99		**μ**	1.00
		COV	0.01		**COV**	0.02

Additionally, Figure 6.13a and b summarise the distribution of the peak shear ratio between the GP-based and the GA-optimised macro-model configurations, expressed as $V_{max,GP}$ / $V_{max,GA}$, for the windward and leeward column ends, respectively. In both cases, the ratios cluster around unity, indicating that the GP-based formulations generally preserve the local peak shear demand achieved by the GA-optimised configurations. In particular, the windward ratios show a mean value μ = 0.99 with COV = 1.03%, whereas the leeward ratios yield μ = 1.00 with COV = 1.64%.

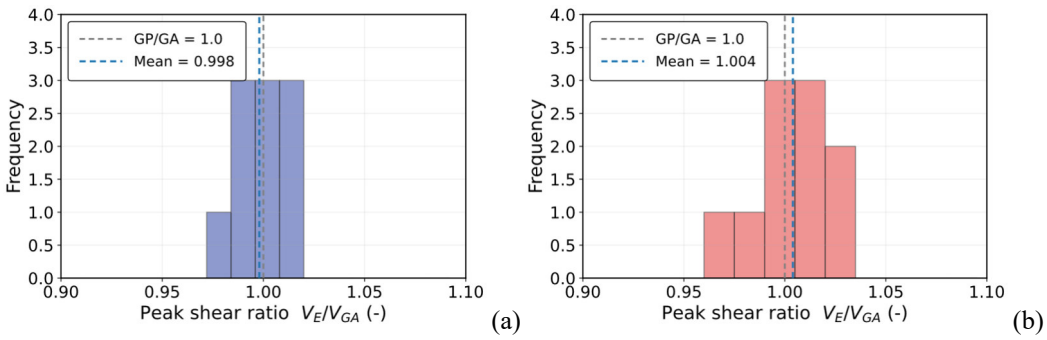

Figure 6.13: $V_{max,GP}$ / $V_{max,GA}$ ratio distributions for the reference specimens: (a) Windward column ends; (b) Leeward column ends.

6.6 Conclusions

This chapter presented a three-strut macro-modelling strategy aimed at reproducing not only the global response of masonry-infilled RC frames under in-plane loading, but also the local shear demand amplification at column ends induced by infill-frame interaction. The model was implemented in OpenSees and calibrated against a reference set of experimental specimens by using experimental and refined finite element micro-models results as response benchmarks. A GA-based optimisation framework was adopted to identify, for each specimen, mechanically admissible strut configurations in terms of width partition and eccentric strut positioning. The collected optimal configurations were subsequently post-processed through genetic programming to derive data-driven correlations that allow the strut layout to be defined.

Based on the results of the study, the following conclusions can be drawn:

- The proposed multi-strut formulation is able to reproduce the main features of the global force-displacement response across the reference dataset, while simultaneously capturing the amount of forces transferred to windward and leeward column ends.

- The GA-based calibration framework demonstrated satisfactory results, exploring different configurations and identifying strut layouts that achieve a balanced agreement with benchmark responses in terms of both global behaviour and peak shear demand.

- The preliminary data-driven formulations derived from the GA-optimal data offer a practical means to evaluate strut widths and locations along the RC frame while keeping a high level of accuracy with respect to the GA-optimised configurations. In particular, the global error ratio ($RMSE_{GP}/RMSE_{GA}$) and the peak shear demand ratios ($V_{max,GP}$ / $V_{max,GA}$) between the GP-based and GA-optimised models at the windward and leeward column ends show mean values close to 1.0 with very low dispersion. Overall, these results indicate that, for the considered dataset, the preliminary data-driven expression has a negligible impact on the estimated global response and local peak shear demand at column ends with respect to the GA-optimised model.

- Additionally, the strategies presented in this chapter and in Chapter 5 provides two parallel solutions for addressing infill-induced shear amplification in RC frames. The model approach in Chapter 5 retains the simplicity of the conventional single-strut approach by introducing an analytical correction to estimate column-end shear demand for practice-oriented seismic assessments. Building on the same physical motivation, the present chapter proposes a calibrated eccentric multi-strut macro-model that explicitly reproduces the actual shear demand at column ends, offering a computationally efficient alternative to refined micro-modelling when both global response and local shear demand need to be captured.

However, despite these outcomes, it should be emphasised that the results presented here are primarily intended to illustrate the potential of the proposed framework and to provide an initial, preliminary contribution to the study of multi-strut configurations. Accordingly, the following limitations should be acknowledged:

- The GP-based formulations are derived and assessed on a limited number of specimens; expanding the reference dataset is necessary to support robust generalisation of these formulations and to validate the proposed macro-model.

- The present study adopts a specific constitutive law for the equivalent struts. However, several alternative constitutive models are available in the literature and no universally accepted standard exists. Future work should therefore investigate the sensitivity of the identified trends to different constitutive assumptions and, if necessary, derive formulations that remain valid across different strut material models.

- The calibration was performed under monotonic quasi-static loading conditions. Future studies may be essential to verify the performance of the GP-based macro-model under nonlinear dynamic analyses.

Chapter 7

Nonlinear dynamic validation of a simplified local shear demand-oriented macro-model

The influence of masonry infills on the seismic behaviour of RC frames has been widely recognised throughout this thesis, both in terms of their contribution to global response and, more importantly, in the development of additional forces due to local interaction. Chapters 3 has shown that the interaction mechanisms at the frame-infill interface may lead to substantial increases in the shear demand at column ends, and that conventional single-strut representations are unable to capture these effects. High-fidelity numerical models, such as the refined micro-modelling strategies adopted in Chapter 3, can capture the full complexity of the infill-frame interaction, including the progressive evolution of contact lengths, damage localisation, and the resulting redistribution of internal forces. However, their high computational cost and modelling effort limit their applicability in common practice. Simplified approaches based on equivalent strut macro-models offer a more practical alternative, however classical single-strut representations are unable to reproduce local interaction effects due to the concentric positioning of the strut. Although multi-strut macro-models may overcome this limitation, most of the formulations currently available in the literature are primarily calibrated to reproduce the global response of infilled frames, and their validation has been almost exclusively limited to global performances with no validation for the local response.

As discussed in Chapter 2, several analytical formulations have been proposed to correct the shear demand at critical sections while retaining a simplified macro-modelling approaches. Within this context, the present thesis has introduced two complementary strategies aimed at bridging the gap between high-fidelity

numerical models and simplified macro-models. The first strategy consists of an analytical correction of the shear demand, in which the additional shear induced by the frame-infill interaction is expressed as a function of the horizontal component of the axial force in the equivalent strut and of the frictional force developing along a specific contact length between the infill and the beam. The second strategy involves the development of a novel three-strut macro-model, calibrated to reproduce both global and local response features by defining strut positioning rules derived from the analysed dataset. While both approaches provide a potentially effective means of estimating the additional shear demand induced by infills using simplified modelling strategies, their calibration and validation have been limited to IP monotonic loading.

What remains unsolved is whether these simplified formulations maintain their predictive capability when applied to nonlinear dynamic scenarios representative of real earthquake excitation. This gap motivates the study presented in this chapter, which aims at providing a comprehensive dynamic validation of a shear demand-oriented macro-modelling strategy, assessing whether it can reliably capture the local response observed in experimental full-scale shake table tests. The chapter builds directly upon the framework introduced earlier in the thesis. A high-fidelity numerical model of a full-scale infilled RC frame structure (**Rebecchi et al., 2023**) tested at the EUCENTRE shake-table laboratory was first developed using the STKO/OpenSees software platform. The model was employed as an experiment-informed digital replica, obtained through a rigorous calibration framework, to accurately reproduce the experimental behaviour and to evaluate response parameters that cannot be directly measured during the tests, such as the evolution of the internal forces. The calibration procedure involved sensitivity analyses and genetic algorithm-based optimisation of the vibration frequencies, accounting for both the elastic and the non-linear response. The calibrated model therefore provides a benchmark solution against which simplified modelling approaches can be assessed. Subsequently, one of the two simplified strategies proposed in this thesis is introduced, such as the analytical formulation for the correction of the local shear demand for single-strut macro-model, and its performance is evaluated under nonlinear dynamic conditions. The second approach, based on the development of a multi-strut macro-model, is not yet subjected to dynamic validation, as it is considered at a more preliminary stage of development. For this reason, the nonlinear dynamic validation presented in this chapter is intentionally focused on the single-strut macro-model adjusted by the proposed analytical shear-demand

formulation. This study thus contributes to bridging the gap between high-fidelity numerical models of infilled frames and the need for computationally efficient, simplified tools capable of capturing additional internal forces under seismic excitation.

The experimental data used in this chapter were kindly provided by ISAAC Antisismica and Kerakoll S.p.A., which are gratefully acknowledged.

7.1 Reference full-scale experimental campaign

The nonlinear dynamic validation presented in this chapter is based on a reference full-scale experimental campaign carried out at the EUCENTRE shake-table laboratory (**Rebecchi et al., 2023**). The programme involved two identical reinforced concrete buildings tested under sequential incremental dynamic tests. The two structures were considered as twin specimens, one equipped with an active control system and the other uncontrolled. For the purposes of the present study, only the experimental results related to the uncontrolled building are considered, providing a benchmark for investigating the interaction between RC frames and masonry infills on a typical infilled RC frame building.

7.1.1 Specimen details and material properties

The reference structure, referred to as *East building*, is a three-storey single-bay RC frame infilled with masonry panels. The building design details, including, storey heights, masonry typology, columns' cross-sections, and slab thicknesses, were representative of typical existing RC buildings. The structural system consisted of moment-resisting frames in the longitudinal direction, regular in elevation and plan. The building footprint measures 5.0 × 2.1 m, with an inter-story height of 2.5 m. The RC frame is characterised by cast-in-place reinforced concrete slabs with a thickness of 40 cm and RC columns with square cross-sections measuring 20 × 20 cm. The columns were reinforced with four 16 mm diameter longitudinal steel bars and 8 mm diameter transverse reinforcement, spaced at 10 cm and reduced to 5 cm at the column ends of the first storey. The masonry infills consist of hollow clay blocks with nominal dimensions of 8 × 25 × 25 cm, connected with mortar layers, representative of a typical infill typology adopted in existing infilled RC frame structures. Figure 7.1 illustrates the overall building configuration together with the main structural details.

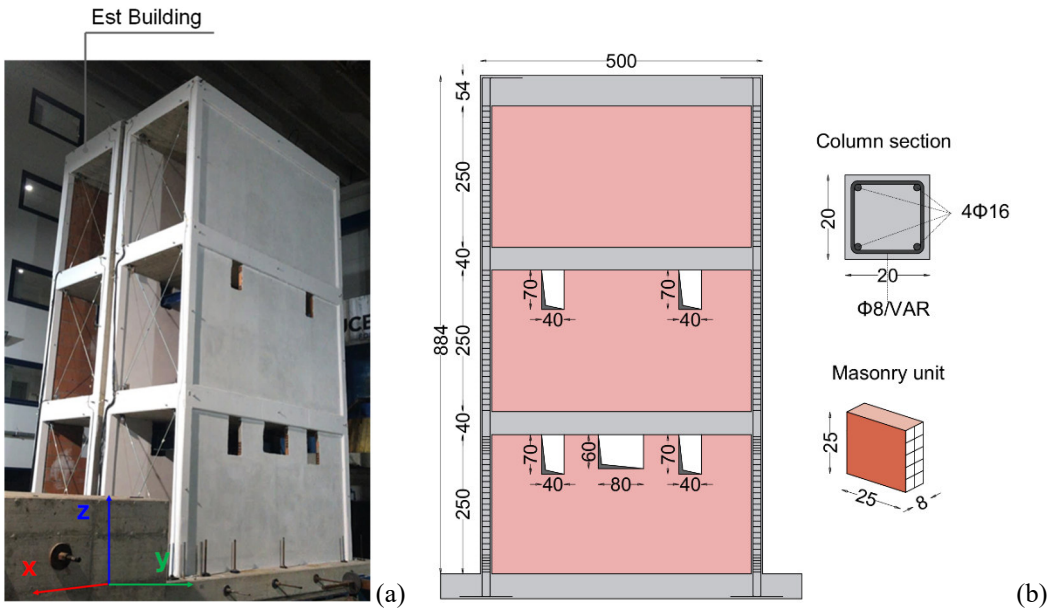

Figure 7.1: Details of the reference structure: (a) Full-scale twin buildings tested in the experimental campaign (**Rebecchi et al., 2023**); (b) Geometry, column reinforcement, and masonry typology (dimensions in cm).

Material properties of concrete, reinforcing steel and masonry panels were characterised through dedicated experimental tests performed within the experimental campaign. The experimentally identified mechanical properties, including elastic moduli and strength parameters, were adopted as reference values for the numerical simulations presented later in this chapter. The key mechanical properties are summarised in Table 33.

Table 33: Mechanical parameters of concrete frame and masonry panels.

Concrete compressive strength f_c (MPa)	41.59
Masonry compressive strength perpendicular to the holes f_{mv} (MPa)	2.25
Masonry compressive strength parallel to the holes f_{mh} (MPa)	1.93
Masonry elastic modulus perpendicular to the holes E_{mv} (MPa)	4004
Masonry elastic modulus parallel to the holes E_{mh} (MPa)	4535
Masonry shear modulus G (MPa)	855

7.1.2 Input motion, test protocol and instrumentation

The seismic input adopted for the shake-table tests was derived from the Irpinia 1980 earthquake record (peak ground acceleration PGA=0.32g), applied along the longitudinal direction (*x-axis*), as shown in Figure 7.2. The experimental program

consisted of a sequence of incremental dynamic tests in which the input ground motion was progressively scaled, with PGA ranging from 0.10g to 0.43g. A total of 19 tests were performed (Table 34), allowing the progressive development of damage in the non-structural elements and the onset of cracking in the structural members.

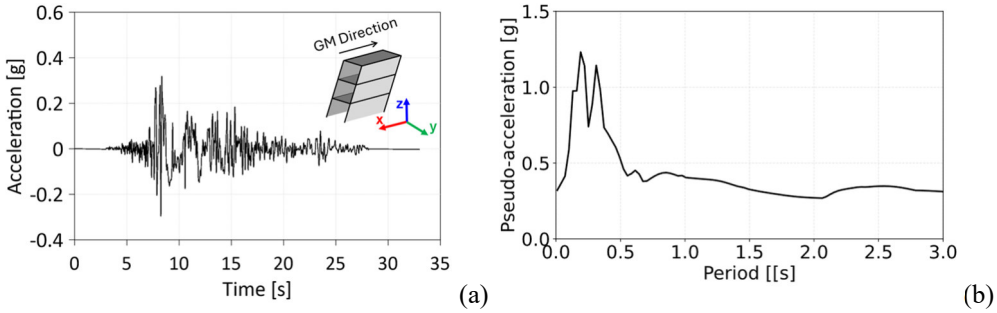

Figure 7.2: Ground motion input: (a) Reference ground motion record from the Irpinia 1980 earthquake; (b) Pseudo-acceleration spectrum with 5% damping.

Table 34: Experimental loading protocol.

Test ID	PGA scale (%)
01	10.0
02	17.5
03	25.0
04	32.5
05	40.0
06	45.0
07	50.0
08	60.0
09	61.7
10	63.3
11	65.0
12	66.7
13	68.3
14	70.0
15	10.0
16	30.0
17	50.0
18	70.0
19	137.0

The structure was instrumented with an extensive monitoring system comprising 11 accelerometers (1 on the shake-table, 1 on the foundation, 3 per each

floor of the building) and 11 displacement transducers, providing experimental data for the assessment of the dynamic response during the shake-table tests. For the purposes of the present study, the acceleration records collected during the experimental campaign were available and constituted the primary experimental output used for the validation of the numerical model.

Prior to the execution of the seismic tests, an Experimental Modal Analysis (EMA) was carried out on the undamaged structure by the authors (**Rebecchi et al., 2023**) using a sine wave excitation generated by a 1.5 kg vibrodyn installed on the top floor of the buildings. Experimental Modal Analysis, originally developed in the field of structural dynamics in the 1960s and 1970s, is a well-established technique for the identification of modal parameters from measured dynamic response data under a given input. During the experimental campaign, the fundamental natural frequencies, mode shapes and equivalent damping ratios were identified. However, at the time of the current study, the information available from the experimental modal identification was limited to the identified modal frequencies only, while no access was provided to the remaining modal data, such as input/output signals used for EMA, mode shapes, and damping ratios. Table 35 reports the identified modal frequencies corresponding to the torsional mode (Mode 1) and to the first two flexural modes in the x-direction (Modes 2 and 3), which corresponds to the direction of the applied ground motion. Although the seismic input was unidirectional, the torsional mode was also considered in this study in case of accidental eccentricities, which may induce torsion.

Table 35: Identified modal frequencies from the experimental campaign.

Mode 1, f_1 (Hz)	6.68
Mode 2, f_2 (Hz)	8.39
Mode 3, f_3 (Hz)	29.91

The experimentally identified modal frequencies represent a starting point for the modal parameters' identification, which serves as a benchmark for the numerical calibration procedures described in Section 7.2.

7.2 High-fidelity numerical replica of the infilled RC frame full-scale structure

7.2.1. General features and model assembly

The refined 3D finite element model of the reference specimen was developed using the STKO/OpenSees software platform (**Petracca et al., 2017a**), reproducing the nonlinear dynamic response of the full-scale infilled RC building described in Section 7.1. The adopted modelling strategy was assumed to achieve a balanced compromise between accuracy and computational efficiency, while preserving the capability to capture the local interaction mechanisms governing force transfer between the RC frame and the masonry infills.

To this end, a homogenised continuum representation was adopted for the masonry infill panels, alternatively to the refined micro-modelling approach employed in previous chapters. In the current case study, this simplification was considered acceptable with reference to the damage mechanisms observed during the experimental campaign (**Rebecchi et al., 2023**), where no sliding phenomena were detected and the infill response was dominated by diagonal shear cracking with damage concentration at the panel corners. Based on these observations, the homogenised approach was considered sufficient to represent the in-plane nonlinear behaviour of the infills while significantly reducing the computational efforts associated with micro-modelling. The masonry infill panels were modelled using orthotropic, homogenised layered *ASDShellQ4* elements, with nonlinear constitutive *ASDConcrete3D* material model (**Petracca et al., 2023**). The orthotropic material wrapper was employed to define direction-dependent mechanical properties with respect to the local reference system of the shell element, allowing different elastic parameters, such as Young's moduli (E_x, E_y, E_z) and shear moduli (G_{xy}, G_{xz}, G_{yz}), as well as strength parameters along the principal material directions. This formulation enables a realistic representation of the anisotropic behaviour of masonry, while using a homogenised continuum model. The adopted modelling strategy allows the simulation of tensile cracking, compressive crushing, and stiffness degradation under cyclic loading. A detailed description of the constitutive model and its governing parameters is provided in Chapter 3.

The RC frame members were modelled using the same layered *ASDShellQ4* formulation combined with the *ASDConcrete3D* constitutive model. Reinforcing bars were explicitly modelled using 1D displacement *beam-column* elements with fiber-section, adopting the actual bar diameters and embedding them within the concrete frame thickness using *ASDEmbedding* node-elements. Floor slabs were modelled using *ASDShellQ4* elements with an elastic membrane-plate section, limiting additional nonlinear complexity as no damage is expected.

A key aspect of the modelling strategy is the explicit representation of the frame-infill interaction. Rather than adopting a frictional contact formulation, which may lead to numerical convergence issues in full nonlinear dynamic analyses, a continuum contact layer was introduced between the infill panels and the surrounding RC frame. The interface behaviour was governed by a compression-only constitutive law implemented via a user-defined *ASDConcrete3D* material. This approach preserves the force transfer under compression while preventing tensile interaction, ensuring numerical robustness and a stable simulation of the contact response throughout the dynamic analyses. An overview of the adopted modelling assumptions and the element assembly is provided in Figure 7.3.

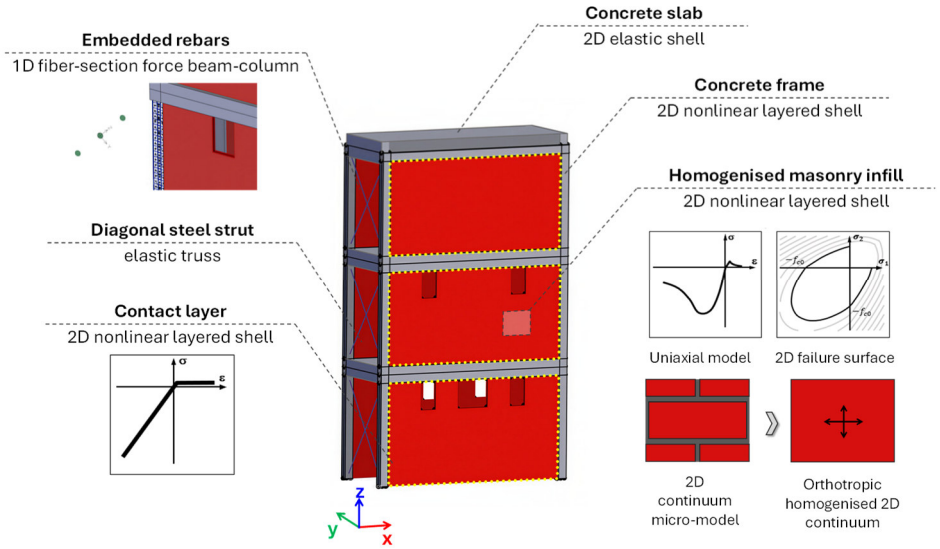

Figure 7.3: Modelling approach and assembly of the full-scale infilled RC frame specimen.

The finite element structured mesh was generated with an average element size of approximately 200 mm. Local mesh refinement was introduced in critical regions where increased shear demand is expected due to frame-infill interaction,

particularly in proximity to column ends and infill corners. The selected mesh was therefore considered adequate to ensure a reliable representation of the nonlinear response while maintaining reasonable computational burden using OpenSeesMP and partitioning the model into 10 subdivisions, as already discussed in Chapter 3.

Boundary conditions were defined to closely replicate the experimental setup adopted during the shake-table tests. The base of the RC frame was fully restrained, enforcing fixed translational and rotational degrees of freedom to represent the rigid connection to the shake-table. The steel diagonal trusses were constrained to the concrete frame by using an *EqualDOF* condition ensuring the constraint of the displacements along the three global axis. In-plane seismic excitation was applied through imposed ground motion acceleration, reproducing the unidirectional input motion adopted in the experimental campaign. A schematic representation of the finite element mesh and the adopted boundary conditions is provided in Figure 7.4.

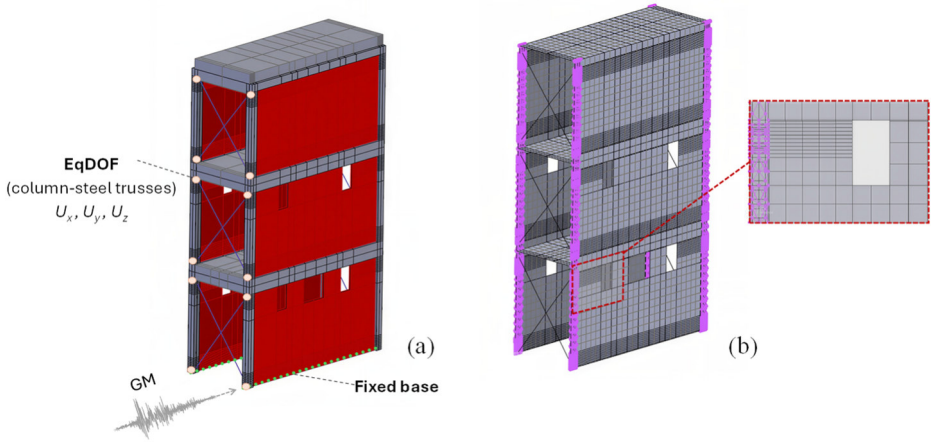

Figure 7.4: Model configuration: (a) Boundary conditions; (b) Mesh architecture.

The numerical analyses were conducted following a stage analysis procedure. At the first stage, self-weights were applied to the structure to establish the initial stress state under gravity loads. The latter was followed by a nonlinear dynamic analysis stage, in which the seismic response of the structure was simulated through time-history analyses. The ground motion was applied incrementally according to the same scaling factor adopted in the experimental program. Nonlinear dynamic analyses were performed using the Newmark time integration scheme with parameters $\gamma = 0.5$ and $\beta = 0.25$, corresponding to the constant-average-acceleration method. This implicit integration scheme is unconditionally stable for linear systems and is widely adopted in nonlinear structural dynamics due to its robustness

and accuracy in capturing inertia effects under seismic excitation. Damping was introduced through a Rayleigh formulation, in which the viscous damping matrix is expressed as a linear combination of the mass and stiffness matrices. The Rayleigh coefficients were calibrated by targeting a constant damping ratio equal to 2% within the range of the two identified flexural modal frequencies along the ground motion direction (*x-axis*). The time step adopted in the numerical analyses was set equal to the sampling time of the experimental acquisition system. Other details regarding the analysis settings, not mentioned here, can be found in Chapter 3.

7.2.2 Calibration framework

The calibration of the refined numerical model was performed through a structured and objective framework aimed at reproducing both the elastic dynamic properties and the nonlinear response observed during the experimental campaign. The procedure consists of two consecutive stages, starting with the calibration of the elastic response via modal analysis and subsequently extending to the nonlinear dynamic phase. This strategy allows the influence of key material parameters to be isolated and assessed separately, first with respect to the elastic dynamic behaviour and subsequently with respect to the nonlinear dynamic response. The calibration process combined sensitivity analyses and optimisation techniques, where necessary, focusing on parameters primarily governing the modal frequencies in the elastic range and on those controlling the vibration frequency decay associated with peak floor accelerations and damage evolution in the nonlinear regime. This approach ensures a consistent and physically meaningful calibration of the model across different response levels. An overview of the adopted calibration framework is provided in Figure 7.5.

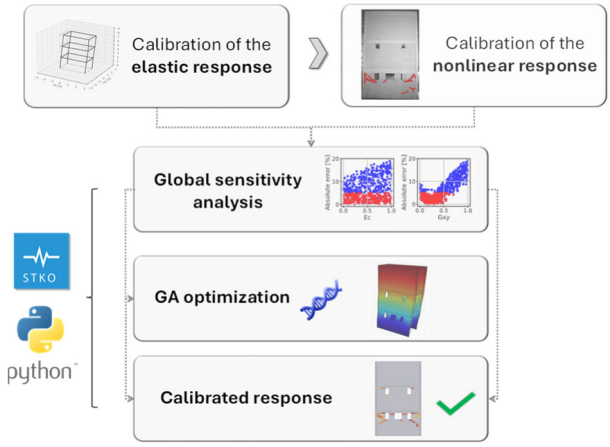

Figure 7.5: Calibration framework for the elastic and nonlinear dynamic response.

7.2.2.1 Elastic response calibration via modal analysis

The first stage of the calibration framework focused on the elastic dynamic response of the structure, characterised by its modal properties. Calibrating the numerical model at the elastic level is essential to ensure a correct representation of the global stiffness distribution and mass participation before introducing material nonlinearity and damage effects. An accurate reproduction of the elastic modal characteristics is essential to provide a reliable basis for subsequent nonlinear dynamic analyses.

Initial ranges for material elastic parameters were defined based on the experimental characterisation tests, complemented by common literature formulations. Particular attention was given to the elastic properties of both masonry infills and reinforced concrete frame, as their stiffness contributions were identified as the most influential factors governing the fundamental vibration frequencies of the system. The selected parameters and their acceptable ranges are formally introduced and quantified in the sensitivity analysis discussed in Section 7.2.2.1.2.

7.2.2.1.1 Data processing and Experimental Modal Analysis (EMA)

In order to establish reliable benchmark modal parameters for the elastic calibration of the numerical model, a modal identification was performed using the acceleration acquisitions collected during the initial phase of the shake-table testing. As discussed in Section 7.1, the information available from the experimental modal analysis carried out prior to the seismic campaign was limited to the identified natural frequencies, with no access to the complete set of modal identification data. For this reason, an independent modal identification was conducted using the experimental data recorded during the first low-intensity seismic test. The modal identification was based on the input/output acceleration acquisitions during the first 6 seconds of the initial record, corresponding to a PGA of 0.032 g, equal to 10% of the reference Irpinia 1980 reference ground motion, as shown in Figure 7.6. At this excitation level, the structure exhibited no damage, and both the RC frame and the masonry infills can be reasonably assumed in their elastic range. This assumption allows the extracted modal properties to be interpreted as representative of the undamaged structural configuration, providing a consistent benchmark for the elastic calibration.

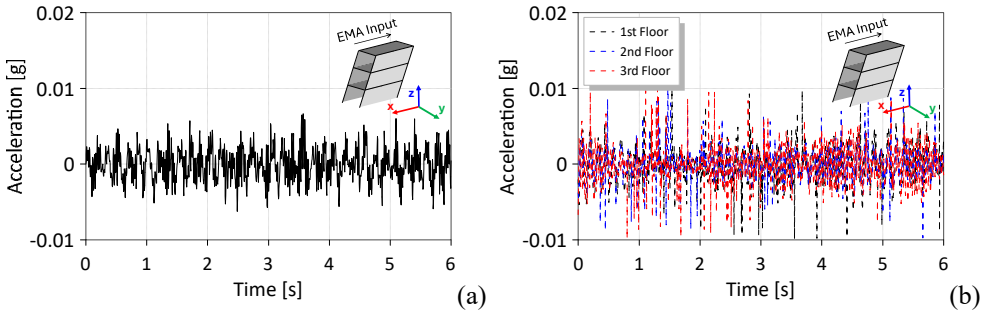

Figure 7.6: Input/output acceleration acquisitions for EMA: (a) EMA input; (b) Measured acceleration data at the three floor levels along the input direction.

Prior to modal identification, signal processing is required to ensure the robustness and reliability of the identified modal parameters. If signals are not properly pre-processed, or if inappropriate sampling rates and filtering strategies are adopted, the amplitude, phase, and frequency content of the signals may be significantly altered, leading to biased or inaccurate results **(Karanikoloudis et al., 2021**). All acceleration records were acquired during the reference experimental campaign with a sampling frequency of 256 Hz. Subsequently, a zero-phase fourth-order digital Butterworth band-pass filter was applied, with cutoff frequencies set between 0.2 Hz and 50 Hz (**Mitra, 2001**).

As a preliminary investigation, the frequency content of the measured signals was explored by evaluating the power spectral density (PSD) of the acceleration data recorded at the three floor levels. In addition, PSDs in terms of displacement were evaluated by converting the acceleration spectra into displacement spectra through division by the square of the circular frequency. Figure 7.7 reports the PSD estimates of the acceleration measurements at the first, second, and third floors, and the corresponding PSDs in terms of displacements, showing the presence of two dominant frequency peaks next to 8 and 27 Hz consistently observed across all measurement levels. While direct inspection of the PSDs allows for a preliminary identification of the dominant response frequencies, a formal experimental modal analysis combining frequency response functions and stabilisation diagrams provides an objective modal parameter identification.

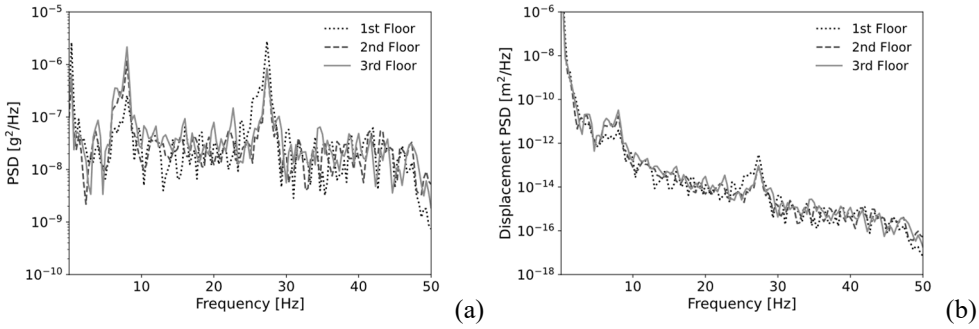

Figure 7.7: Power spectral density plots of the acceleration and displacement acquisitions at the first, second, and third floors during the initial sequence (6s) of the lowest seismic intensity test (PGA=0.032g): (a) PSD plots in terms of acceleration [g^2/Hz]; (b) PSD plots in terms of displacement [m^2/Hz].

An Experimental Modal Analysis based on frequency response function was adopted by using SdyPy library (**Zaletelj et al., 2019**). Given the availability of both cut-base acceleration (first 6 seconds of the 10% PGA of the Irpinia ground motion) and floor measurements, the identification was performed using an input/output formulation based on acceleration transmissibility functions. For each response channel, the frequency response function (FRF) was estimated using the classical $H(f) = H_1$ estimator:

$$H(f) = \frac{S_{xy}(f)}{S_{xx}(f)} \tag{94}$$

where $S_{xy}(f)$ is the cross-power spectral density between input and output, and $S_{xx}(f)$ is the auto-power spectral density of the input. The resulting FRFs were assembled into a FRF matrix collecting multiple output channels for a single input, thus defining a SIMO (Single Input / Multi-Output) approach. Based on the FRF matrix a stabilisation diagram was built to distinguish physical from non-physical modes. The Least-Squares Complex Frequency Domain method (LSCF), also known as PolyMAX, was adopted. The approach is based on a common-denominator representation of the FRF matrix, from which the system poles are identified as the roots of a complex polynomial. For each assumed model order, a set of candidate complex-valued poles is obtained, where the imaginary part is related to the modal natural frequency and the real part governs the associated modal damping ratio. By progressively increasing the model order, physical structural modes are expected to appear as poles that remain approximately

invariant in frequency and damping across consecutive model orders. To isolate physically meaningful modes, a set of stability and physical acceptable criteria was applied to the identified poles. First, poles were required to satisfy frequency and damping stability conditions between consecutive model orders, defined through relative thresholds on the variations of natural frequency and damping ratio. Additional physical filters were introduced by restricting the damping ratio to the range $0.05\% \leq \zeta \leq 20\%$. To facilitate the identification of dominant modes, the distribution of the stabilised pole frequencies was assessed using a Kernel Density Estimation (KDE) probability function. The latter highlights clusters associated with dominant modes, and only peaks exceeding the 95th percentile of the KDE function were selected. The resulting stabilisation diagram, together with the mean FRF amplitude, and KDE distribution is illustrated in Figure 7.8. A comparison between the flexural modal frequencies identified in the current study and those reported in the previous experimental campaign highlights a generally good level of agreement. The first frequency identified herein, equal to 8.04 Hz, is very close to the value previously reported (8.39 Hz). The second frequency is identified at a lower value, equal to 27.33 Hz, compared to the corresponding frequency reported in the previous study (29.91 Hz). The consistent stabilisation of the identified poles supports the reliability of the frequency value of 27.33 Hz, which is therefore adopted as representative of the second flexural mode in the present study.

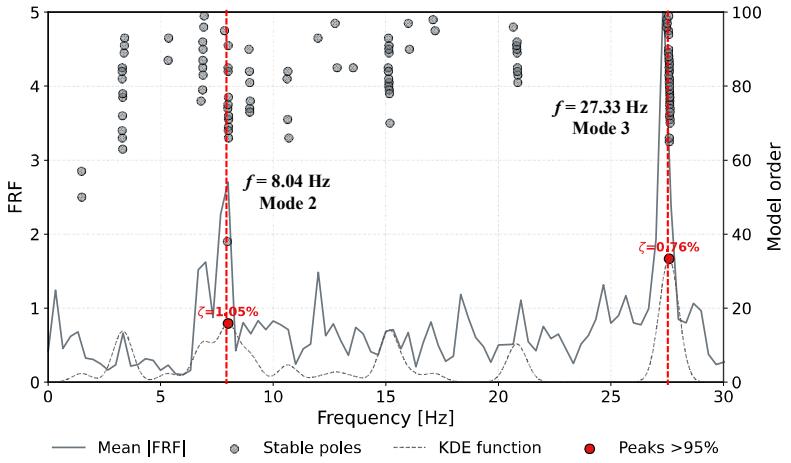

Figure 7.8: Stabilisation diagram and modal identification based on FRF matrix.

The mode shapes associated with the identified flexural frequencies were derived from the FRF-based identification. The resulting mode shapes are reported in Figure 7.9.

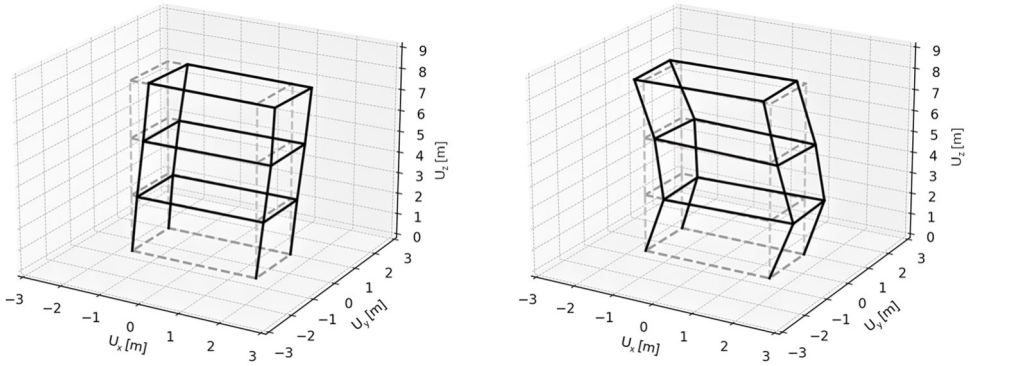

Figure 7.9: Mode shapes extracted from the FRF-based experimental modal identification: (a) First flexural mode; (b) Second flexural mode.

Given the unidirectional nature of the EMA input, only the flexural modes aligned with the direction of the applied ground motion were undoubtedly identified (Mode 2 and 3, respectively). The available data therefore do not allow the estimation of a pure torsional response (Mode 1) and its associated mode shape. However, the torsional natural frequency reported in the previous experimental campaign (6.68 Hz) is adopted as a reference value, with the understanding that no further validation of the torsional mode shape can be performed. The identified flexural modal frequencies and the previous identified torsional frequency were finally adopted as benchmark quantities for the elastic calibration of the numerical model. These frequencies are employed in the sensitivity analysis and optimisation stages described in Sections 7.2.2.1.2 and 7.2.2.1.3.

7.2.2.1.2 Sensitivity analysis

A global sensitivity analysis (GSA) was performed to quantify the influence of elastic material parameters (input) on the modal properties (output) of the specimen and to support the calibration of the refined numerical model against the experimental identified elastic response. A Regional Sensitivity Analysis (RSA) formulation was employed, which is well suited for models characterised by nonlinear responses and moderate computational cost, and allows sensitivity assessment through both quantitative metrics and visual analysis. The analysis was conducted following the framework proposed by **Pianosi et al. (2015)**, as implemented in the SAFE (Sensitivity Analysis For Everybody) toolbox. In the adopted approach the output variability is explored over the entire feasible space of the input parameters rather than around a single variable, varying the input parameters all-at-time (AAT). The input space was explored through Latin

Hypercube Sampling (LHS), which ensures an efficient representation of the parameter domain. The total number of samples was set equal to 100·N, where N is the number of input parameters, in line with recommended practices for RSA applications and with the computational cost of the refined numerical model. All input parameters were modelled as independent random variables and assigned uniform probability distributions with a coefficient of variation (COV) of ± 30% around their reference mean values (μ). Given the relatively limited variability range and the uncertainty related to possible relationship between different material parameters, the assumption of independence was considered appropriate and consistent with common practice in global sensitivity studies. The overall workflow of the global sensitivity analysis adopted in this study is schematically illustrated in Figure 7.10.

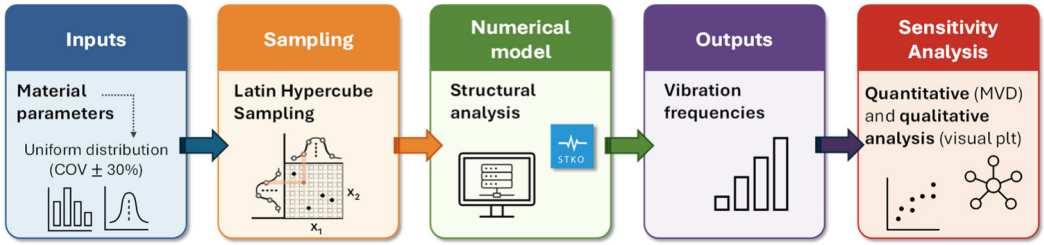

Figure 7.10: Schematic workflow of the global sensitivity analysis adopted in this study.

The set of input parameters includes the elastic properties of both masonry infills and reinforced concrete frame, which are expected to govern the elastic dynamic response of the structure. For masonry, an orthotropic elastic behaviour is assumed and described through the Young's moduli E_x, E_y, and E_z, together with the shear moduli G_{xy}, G_{xz}, G_{yz}, all defined in the local coordinate system of the infill elements. In addition, the Young's modulus of concrete E_c is considered to account for the contribution of the reinforced concrete frame stiffness. For masonry, the reference parameters E_x, E_y, G_{xy}, G_{xz}, were directly assigned based on experimental material tests (see Table 33). The remaining elastic parameters were estimated based on the abaci proposed by **Zhou et al. (2022)**. In particular, the out-of-plane Young's E_z was derived as a fraction of the elastic modulus of the masonry unit, assuming $E_z = 0.95 \cdot E_b$, where E_b is the experimentally measured elastic modulus of the unit, equal to 2180 MPa. The shear modulus G_{yz} was instead obtained as $G_{yz} = 0.9 \cdot G_b$, with G_b computed from E_b using the classical relationship between Young's and shear modulus, assuming a Poisson's ratio $\nu = 0.2$. For concrete, in the absence of experimentally measured elastic properties, the Young's modulus was estimated

as a function of the measured concrete compressive strength f_c, in accordance with the expression provided by **NTC 2018** (Section 4.1.12.1.1), assuming $E_c=22000\cdot(f_c/10)^{0.3}$. Table 36 summarises the reference values of the elastic input parameters adopted in the numerical model.

Table 36: Reference elastic input parameters adopted as mean values.

Concrete elastic modulus E_c (MPa)	33738
Masonry elastic modulus E_x (MPa)	4535
Masonry elastic modulus E_y (MPa)	4004
Masonry elastic modulus E_z (MPa)	2071
Masonry shear modulus G_{xy} (MPa)	855
Masonry shear modulus G_{xz} (MPa)	855
Masonry shear modulus G_{yz} (MPa)	863

For each sampled parameter set ($100\cdot N$ = 700), a linear modal analysis was performed, and the resulting natural frequencies were extracted. The outputs of the sensitivity analysis were defined as the frequencies of the three vibration modes of interest that are the torsional mode (Mode 1), the first flexural mode along the x-axis (Mode 2), and the second flexural mode along the x-axis (Mode 3).

The influence of each input parameter on the modal frequencies was assessed through a set of complementary visualisation tools, as recommended by (Pianosi et al., 2015). These include scatter plots, parallel coordinate plots, and tornado plots which allow a qualitative and quantitative analysis. A preliminary mode-by-mode sensitivity analysis was initially performed to explore the influence of the input parameters on individual vibration modes; for the sake of brevity, these results are reported in Appendix A, while the following discussion focuses on the global sensitivity analysis accounting for all modes simultaneously, which is directly relevant to the subsequent calibration strategy. In the global assessment, behavioural simulations were defined as those satisfying the acceptance criterion for all three vibration modes. The model response was therefore evaluated in terms of the root mean square error (RMSE) between the numerical modal frequencies and the experimentally identified ones. Simulations with RMSE values lower than 0.5 Hz were classified as behavioural. This criterion enables the identification of material parameters that consistently control the overall modal response of the structure. Figure 7.11 summarises the results of the global sensitivity analysis through scatter plots of RMSE versus the normalised elastic input parameters. The results clearly indicate that the in-plane masonry shear modulus G_{xy} is the most

influential parameter governing the modal response, followed by a secondary influence of the concrete Young's modulus E_c. The remaining masonry elastic parameters exhibit a weak correlation with the RMSE and do not significantly affect the global dynamic behaviour within the explored variability ranges. Figure 7.12 further illustrates the global sensitivity results by means of parallel coordinate plots and MVD-based tornado diagrams. The parallel coordinate plots show a pronounced clustering of the behavioural simulations around the mean values of G_{xy}, while a less clear concentration is observed for E_c, indicating a wider admissible range for the latter. The tornado diagrams quantify this behaviour through the Maximum Vertical Distance (MVD), defined as the maximum distance between the empirical cumulative distribution functions (ECDFs) of all simulations and of the behavioural simulations. The resulting MVD values consistently identifies G_{xy} as the dominant parameter, followed by E_c, whereas all other elastic parameters exhibit significantly lower values.

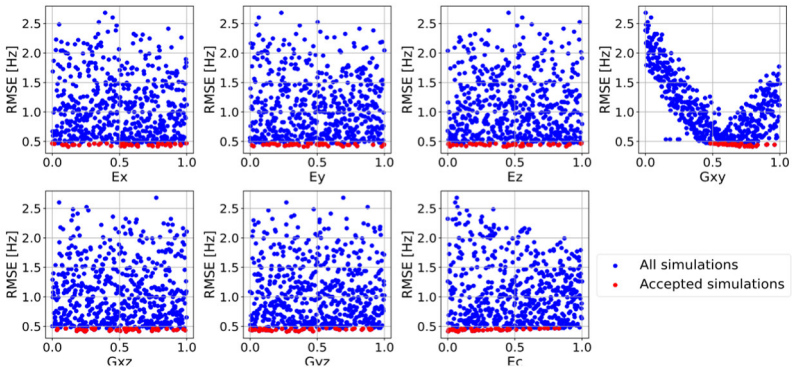

Figure 7.11: Scatter plots of the RMSE between numerical (refined model) and identified experimental frequencies versus normalised elastic input parameters for the three vibration modes. Blue and red markers indicate all and behavioural simulations (RMSE<0.5 Hz), respectively.

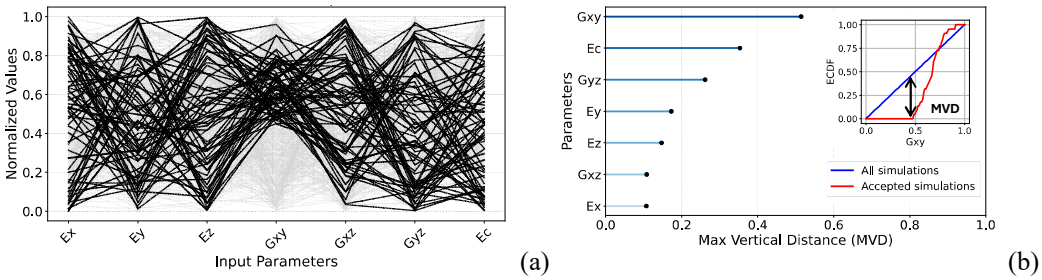

Figure 7.12: Parallel coordinate plots of behavioural simulations and MVD-based tornado diagrams for all modes sensitivity analysis (refined model).

Overall, the global sensitivity analysis confirms that the elastic dynamic response of the infilled RC frame is primarily governed by the interaction between the in-plane shear behaviour of the masonry infill and the stiffness of the reinforced concrete frame. These findings provide a robust basis for the subsequent calibration phase and justify focusing the parameter identification on a reduced set of physically meaningful and influential elastic properties, motivating the adoption of further optimisation strategies to minimise the global RMSE.

7.2.2.1.3 Calibrated response

To refine the elastic response of the reference infilled frame model, a GA-based optimisation was performed. The GA was implemented in Python using the DEAP library (**Fortin et al., 2012**) and was coupled with modal analyses in STKO/OpenSees. The optimisation problem was formulated by defining the design vector:

$$\boldsymbol{\theta} = \left[G_{xy}, E_c \right] \tag{95}$$

collecting the parameters governing the elastic stiffness contribution of the masonry infill and the surrounding RC frame. Consistently with the outcomes of the sensitivity analysis, reported in the previous paragraph, the optimisation was intentionally restricted to these two parameters, while all remaining elastic parameters were kept fixed assuming their mean values. Each candidate solution was constrained within physically admissible bounds defined by assuming a coefficient of variation equal to 30% around the reference mean values derived from experimental and literature data. The initial population of 100 individuals was randomly generated. At each generation, 100 offspring was created, which one coming from parents selected through a *tournament selection* with tournament size equal to 3. A uniform crossover operator, with a probability equal to 0.7, was used with a gene selection probability equal to 0.5. Then, with a probability of 0.3, a uniform mutation was applied, with a gene mutation probability of 0.2. The fitness of each individual was evaluated by running an eigenvalue analysis in OpenSees and computing the discrepancy between numerical and experimental frequencies for the three target modes. The objective function was defined as the root mean square error (RMSE) of numerical and experimental frequencies, as follows:

$$OF(\boldsymbol{\theta}) = \sqrt{\sum_{i=1}^{n} \frac{\left(f_{num,i}(\boldsymbol{\theta}) - f_{\exp,i}\right)^2}{n}} \tag{96}$$

where n is the number of the considered modes, $f_{num,\mathrm{i}}$ and $f_{exp,\mathrm{i}}$ denote the numerical and experimentally identified natural frequencies of the i-mode, respectively. To limit computational burden, the stopping criterion on the number of generations has been coupled with an early-stopping of a stall over 10 generations with a tolerance of 10^{-4}. The optimisation converged towards an optimal solution corresponding to E_c = 28583 MPa and G_{xy} = 950 MPa. These values fall within the assumed parameter ranges and represent moderate adjustments with respect to the reference (mean) configuration, thus preserving the physical consistency of the updated elastic properties. Using the mean parameter values, the numerical model exhibited a global discrepancy with respect to the experimental modal frequencies, quantified by an RMSE equal to 0.56 Hz. After optimisation, the updated parameter set led to an improvement in the modal frequency matching, with the RMSE reducing to 0.39 Hz, corresponding to an overall error reduction of approximately 30%. The experimental frequencies, together with the numerical predictions obtained using the mean and the GA-optimised parameter values, are reported in Table 37.

Table 37: Comparison between experimental and numerical natural frequencies of the three target modes for the mean and GA-optimised parameter sets, together with the corresponding RMSE values.

	Experimental	**Mean Values**	**Optimised Values**
Mode 1, f_1 (Hz)	6.68	6.88	6.90
Mode 2, f_2 (Hz)	8.04	8.51	8.62
Mode 3, f_3 (Hz)	27.33	26.51	27.05
	RMSE	0.56	0.39

Although the optimisation objective function was intentionally formulated exclusively in terms of modal frequencies, the reliability of the optimal solution was further assessed through a posteriori validation of the mode shapes by means of the Modal Assurance Criterion (MAC). Since experimental mode shapes were available only for the second and third modes, as already explained in the previous sections, the MAC matrix was computed solely on these modes. Figure 7.13 shows the comparison between the numerical and the experimental mode shapes for the

two considered flexural modes, together with the corresponding natural frequencies.

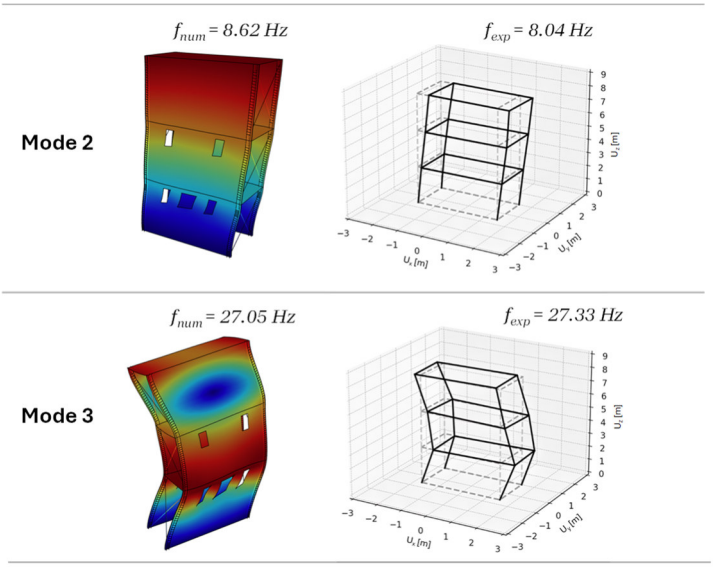

Figure 7.13: Numerical (refined model) and experimental mode shapes of the two flexural modes considered for MAC validation, with corresponding natural frequencies.

The MAC between the experimental mode shape $\boldsymbol{\phi}_{exp}$ and the numerical one $\boldsymbol{\phi}_{num}$ was computed as:

$$MAC - i = \frac{\left|\boldsymbol{\phi}_{\exp,i}^{T} - \boldsymbol{\phi}_{num,i}\right|^{2}}{\left(\boldsymbol{\phi}_{\exp,i}^{T}\boldsymbol{\phi}_{\exp,i}\right)\left(\boldsymbol{\phi}_{num,i}^{T}\boldsymbol{\phi}_{num,i}\right)} \tag{97}$$

with values near the unit indicating highly correlated mode shapes. The resulting MAC values, equal to 0.986 for Mode 2 and 0.901 for Mode 3, with negligible off-diagonal terms, confirm an excellent agreement between numerical and experimental modal vectors (Figure 7.14). This demonstrates that the improved frequency correspondence obtained through the GA optimisation was consistent not only in terms of modal frequencies but also in terms of mode shapes.

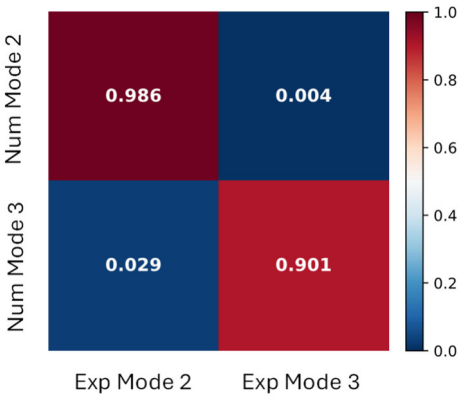

Figure 7.14: MAC matrix between numerical (refined model) and experimental mode shapes of the two flexural modes considered for model validation.

7.2.2.2 Non-linear dynamic response calibration via incremental time-history analyses

Following the calibration of the elastic response through modal analysis, the nonlinear dynamic behaviour of the numerical model was investigated with incremental nonlinear time-history analyses. This phase aims to assess the capability of the model to reproduce the experimentally observed response under increasing PGA levels, with particular attention to the global dynamic behaviour and the development of damage mechanisms induced by infill-frame interaction. Within the sequence of the first ten experimental shaking-table tests, the evolution of the dynamic response was first examined in order to identify the onset of structural damage and stiffness degradation. In particular, the experimental modal analysis highlighted the first test at which a clear decay of the natural vibration frequencies occurs, marking the transition from an elastic response to the damage initiation. Based on this observation, two reference intensity levels were selected for the nonlinear dynamic calibration: the last test preceding any measurable frequency decay, representative of the undamaged or quasi-elastic state, and the first test associated with a reduction of the natural frequencies, indicative of the onset of stiffness degradation. To guide the calibration and selection of the nonlinear model parameters, the response of each numerical simulation was evaluated using a global error metric, combining information from both the frequency domain and the time domain. Specifically, the metric accounts for the discrepancy between numerical and experimental vibration frequencies and the error associated with the peak floor accelerations. This strategy allows the key

mechanisms governing the transition from elastic to damaged behaviour to be captured while limiting the computational cost of the nonlinear analyses.

7.2.2.2.1 Modal frequency decay associated with damage initiation

The identification of the first test associated with damage initiation was supported by the experimental modal analysis (EMA) outputs, built on the same hypothesis presented in Section 7.2.2.1.1. Figure 7.15 illustrates the frequency response function (FRF) together with the stabilisation diagram obtained from the EMA for the first shaking-table test in which a modification of the frequency content is observed, corresponding to Test 04.

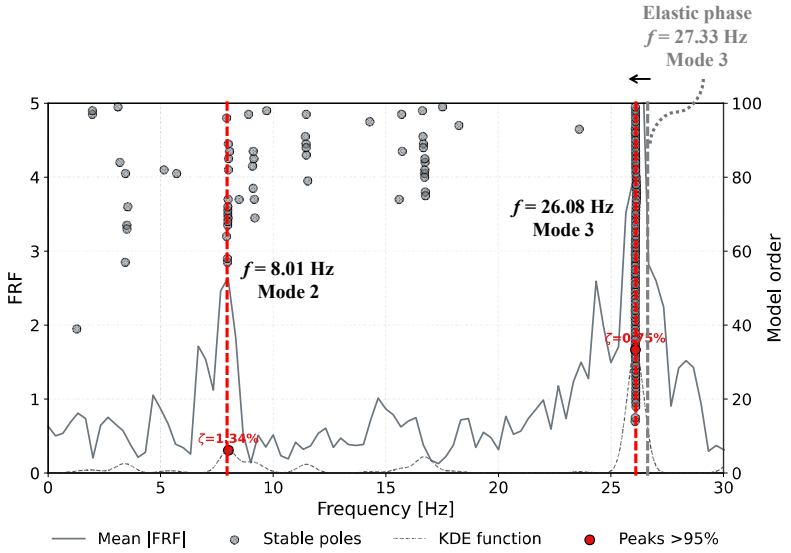

Figure 7.15: Stabilisation diagram and modal identification based on the FRF matrix for Test 04, showing the first detectable variation in the natural vibration frequencies.

From the experimental results, the frequency content does not exhibit a significant variation in the first flexural mode, whose frequency slightly decreases from 8.04 Hz, identified under elastic conditions, to 8.01 Hz at Test 04. Conversely, a more pronounced variation is observed for the second flexural mode, whose frequency decreases from 27.33 Hz in the elastic regime to 26.08 Hz at Test 04. This reduction represents a clear deviation from the previously stable trend and indicates the initiation of stiffness degradation. Based on this, Test 03, yet representative of the undamaged state, and Test 04, corresponding to the first variation of the modal frequencies, were selected as reference tests for the nonlinear sensitivity analysis of the refined model.

7.2.2.2.2 Sensitivity analysis

The sensitivity analysis was performed consistently with the assumptions and framework previously described in Section 7.2.2.1.2. The analysis focused on the mechanical properties of masonry infills, which play a crucial role in governing infill-frame interaction mechanisms and the associated modification of damage mechanisms. In particular, the selected input variables were the tensile strength of masonry f_t, controlling crack initiation, the tensile fracture energy G_t, governing post-cracking softening in tension, and the parameter $A_{\sigma xyxy}$ defined as the ratio between tensile and shear strength, used to calibrate the shear resistance of masonry. The compressive fracture energy G_c was not treated as an independent variable but was consistently derived from the selected value of G_t, in accordance with the adopted formulations discussed in Chapter 3. For each input parameter, a reference mean value was defined based on experimental evidence and literature data and reported in Table 38.

Table 38: Reference nonlinear input parameters adopted as mean values.

Masonry tensile strength	f_t (MPa)	0.19
Masonry tensile fracture energy	G_t (N/mm)	0.08
Masonry tensile-to-shear strength ratio	$A_{\sigma xyxy}$ (-)	1

As described in the elastic calibration framework, the uncertainty associated with the masonry mechanical properties was explicitly accounted for by assigning a uniform probability distribution to each parameter. The input parameters were varied independently within physically admissible lower and upper bounds with a COV ± 40%. These limits ensure that the sensitivity analysis investigates an extended yet physically meaningful parameter space. Differently from the elastic calibration phase, the nonlinear sensitivity analysis was not based on a single response indicator. Instead, the model response was evaluated through a global normalised error metric, defined as a weighted combination of frequency-based and time-domain indicators:

$$\mathrm{NRMSE}_{\mathrm{glob}} = w_i \cdot \mathrm{NRMSE}_{\mathrm{freq}} + w_j \cdot \mathrm{NRMSE}_{\mathrm{acc,peak}} \tag{98}$$

where $\mathrm{NRMSE}_{\mathrm{freq}}$ represents the normalised root mean square error between the experimentally identified and numerically predicted flexural vibration frequencies, and $\mathrm{NRMSE}_{\mathrm{acc,peak}}$ denotes the normalised error associated with the peak floor

accelerations. Both terms were normalised with respect to the corresponding maximum experimental values, allowing the two contributions to be combined. The weighting coefficients w_i and w_j were selected to balance the relative importance of the two error components. Particularly, after a preliminary investigation, they were chosen to assign greater importance on the peak acceleration response, since the frequency-based error shows limited variability and remains low across the analysed simulations ($NRMSE_{freq}$ range between 0.059 and 0.065). Accordingly, the weights were set $w_i = 0.3$ for the frequency contribution and $w_j = 0.7$ for the peak acceleration contribution.

The results are summarised in Figure 7.16 and Figure 7.17. Behavioural simulations were defined as those characterised by a sufficiently low value of the global normalised error ($NRMSE_{glob} < 0.15$). This threshold was adopted to preserve a subset of simulations for interpretation.

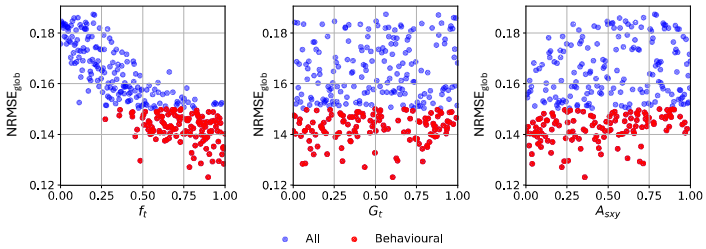

Figure 7.16: Scatter plots of the global normalised error $NRMSE_{glob}$ as a function of the nonlinear masonry parameters for the refined model (behavioural simulations $NRMSE_{glob}<0.15$).

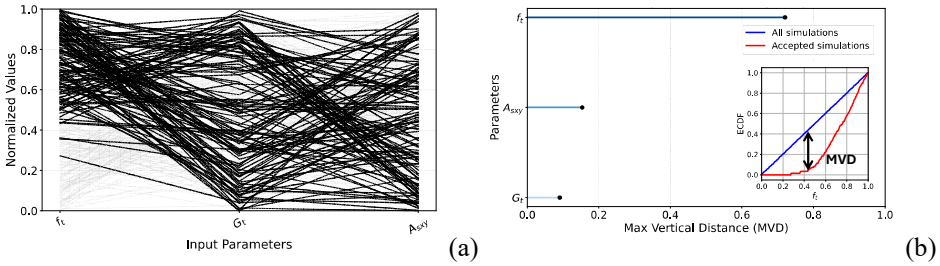

Figure 7.17: Parallel coordinate plots of behavioural simulations and MVD-based tornado diagrams for nonlinear response sensitivity analysis (refined model).

Considering the global error $NRMSE_{glob}$, the simulations clearly indicate that the most influential parameter is the masonry tensile strength f_t. This trend is evident from the scatter plots reported in Figure 7.16 and is further confirmed by the MVD-based tornado diagram in Figure 7.17b, which quantifies the sensitivity in terms of

the maximum vertical distance between the empirical cumulative distribution functions of the behavioural simulations and of the full set of simulations. Additional insight is provided by the parallel coordinate plot in Figure 7.17a. The behavioural simulations are observed to cluster around higher values of f_t, whereas a larger variability is associated with the remaining parameters. In particular, acceptable model responses are obtained both for combinations characterised by lower values of G_t and higher values of $A_{\sigma xyxy}$, as well as for higher G_t coupled with lower $A_{\sigma xyxy}$, suggesting that these two parameters compensate for each other's effects.

7.2.2.2.3 Calibrated response

Based on the outcomes of the sensitivity analysis presented in the previous section, the calibration of the nonlinear response of the refined model was addressed through a guided selection of material parameters. Although a formal optimisation based on a Genetic Algorithm could be adopted, the limited variability observed in the global error ($NRMSE_{glob}$) and the high computational burden associated with nonlinear dynamic analyses of the refined model, makes this approach unnecessarily demanding for the scope of this study.

For this reason, the calibration was based on a limited investigation within the subset of behavioural simulations identified in the sensitivity analysis. These simulations are characterised by sufficiently low values of the global normalised error, $NRMSE_{glob}<0.15$, and therefore already provide a satisfactory representation of the experimental response. It is worth noting that, within this subset, the minimum value of $NRMSE_{glob}$ is not exclusively representative, as all behavioural simulations exhibit comparably low error levels. Consequently, the selection was not solely driven by the global error. Instead, a reduced set of ten candidate parameter configurations was identified among those minimising $NRMSE_{glob}$, while at the same time covering a sufficiently wide range of values of the most dispersed parameters, like the tensile fracture energy G_t and the tensile-to-shear strength ratio $A_{\sigma xyxy}$. The candidate configurations were then further evaluated by analysing the expected damage evolution under the sequence of the first ten shaking-table tests. In this way, the final selection was based not only on the ability to reproduce modal frequencies and peak floor accelerations, but also on the capability of the model to consistently capture the experimentally observed damage mechanisms.

Among the subset of simulations, the selected parameter set corresponds to f_t = 0.25 MPa, G_t = 0.05 N/mm, and $A_{\sigma xyxy}$ = 1.25. This configuration ensures an acceptable agreement in terms of vibration frequencies and peak floor accelerations (NRMSEglob = 0.14), while also providing sufficient accuracy in the crack pattern between the experiment and the numerical replica. The comparison of numerical and experimental PSDs, illustrated in Figure 7.18 and Figure 7.19, is given for the first four shaking-table tests (PGA= 0.032g – 0.104g), where the experimental acquisitions allow a reliable spectral interpretation. The results indicate that the refined model accurately captures the dominant spectral peaks, showing good agreement with the experimental response in terms of both amplitude and frequency. A slight discrepancy is observed for the first vibration mode, with a numerical frequency of 8.61 Hz compared to the experimental value of 8.01 Hz, whereas the second vibration mode remains well reproduced. Minor discrepancies are observed in the remaining frequency ranges.

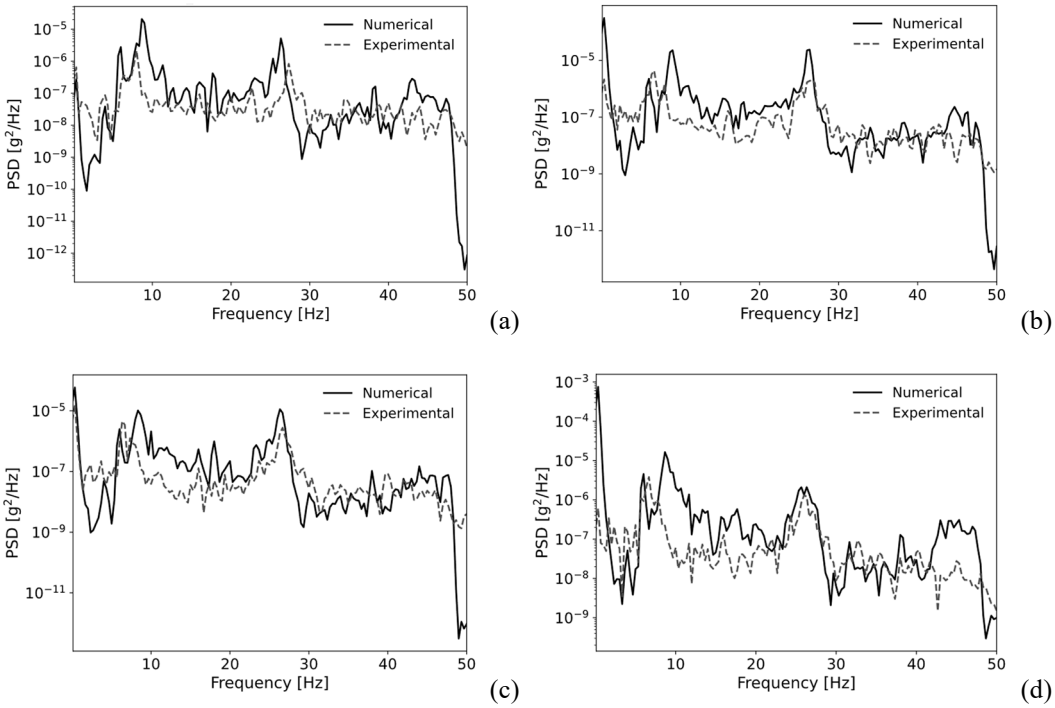

Figure 7.18: Experimental vs. Numerical power spectral density plots in terms of accelerations at the third floor, for the first four shake-table tests: (a) Test 01 (PGA=0.032g); (b) Test 02 (PGA=0.056g)); (c) Test 03 (PGA=0.08g); (d) Test 04 (PGA=0.104g).

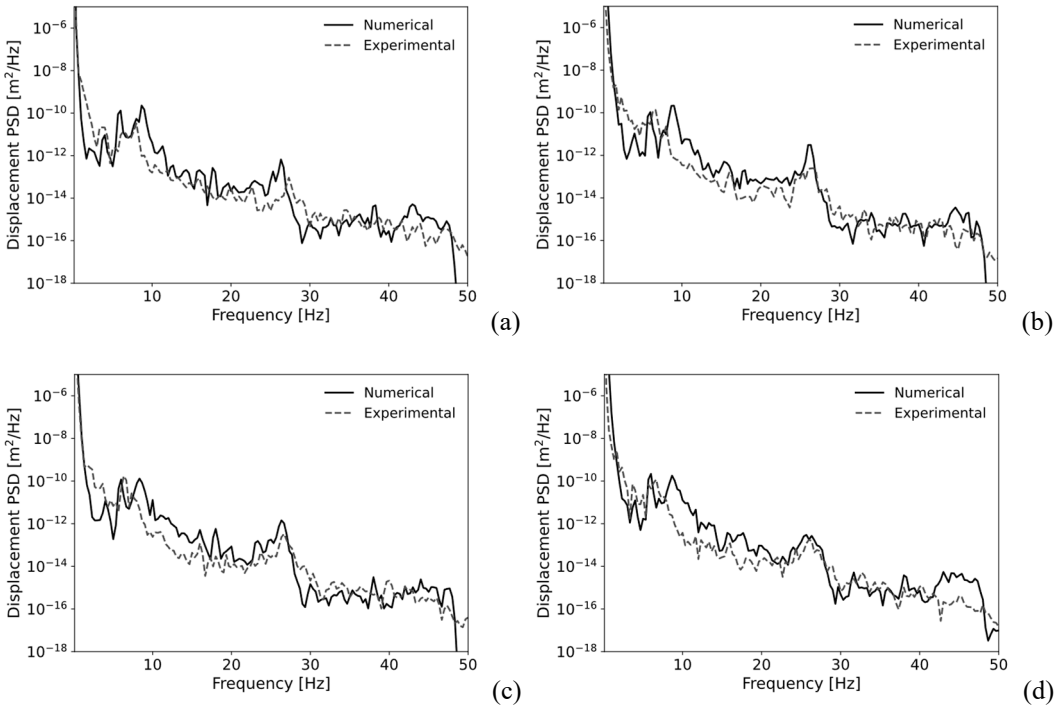

Figure 7.19: Experimental vs. Numerical power spectral density plots in terms of displacements at the third floor, for the first four shake-table tests: (a) Test 01 (PGA=0.032g); (b) Test 02 (PGA=0.056g)); (c) Test 03 (PGA=0.08g); (d) Test 04 (PGA=0.104g).

Finally, the calibrated model was employed to simulate the first ten shaking-table tests, up to the stage at which significant damage developed. Figure 7.20 compares the experimentally observed crack pattern with the numerical prediction at the end of the loading sequence (Test 10, PGA= 0.2g). The numerical model is able to capture the dominant damage mechanisms, including the localisation of damage at the infill-frame interfaces and the onset of diagonal shear cracking at the masonry panel corners between the ground and first storey, corresponding to the most heavily loaded infills.

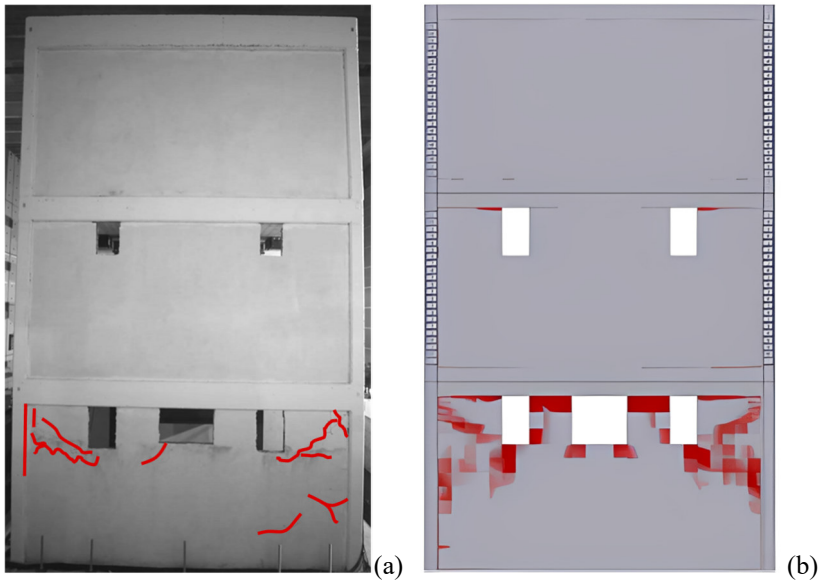

Figure 7.20: Experimental vs. Numerical damage pattern at the end of the dynamic sequence (Test 10, PGA=0.2g): (a) Experimental cracks; (b) Numerical cracks.

Overall, the nonlinear calibration of the refined model highlights that the combined use of frequency-based error with peak floor accelerations error, and damage observations provides a guided selection of physically consistent parameter set, reproducing both the global dynamic behaviour and damage mechanism.

7.2.3 Local shear demand assessment at critical sections

After calibration, the numerical model was considered a reliable numerical replica of the reference case-study building. So that the refined model was further employed to extract local response quantities not directly measurable during the experiments, such as the local shear demand. As discussed in Chapter 5, the local shear demand was evaluated by introducing a set of section cuts at the column ends, identified as critical sections. For each critical section, three distinct section cuts were defined in order to obtain a representative approximation of the shear force. The three cuts are located at distances equal to $0 \cdot h_c$, $0.5 \cdot h_c$, and h_c from the column end, where h_c is the column depth. The local shear demand associated with each critical section was then computed as the average value of the shear forces extracted at the three section cuts, consistently with the procedure described in Chapter 5. The definition of the adopted section cuts and their spatial distribution along the structure is shown in Figure 7.21. Among the identified critical sections, only the

columns at the first storey (C1 - C4) are considered, as they experienced the highest shear demand during the sequential incremental dynamic tests.

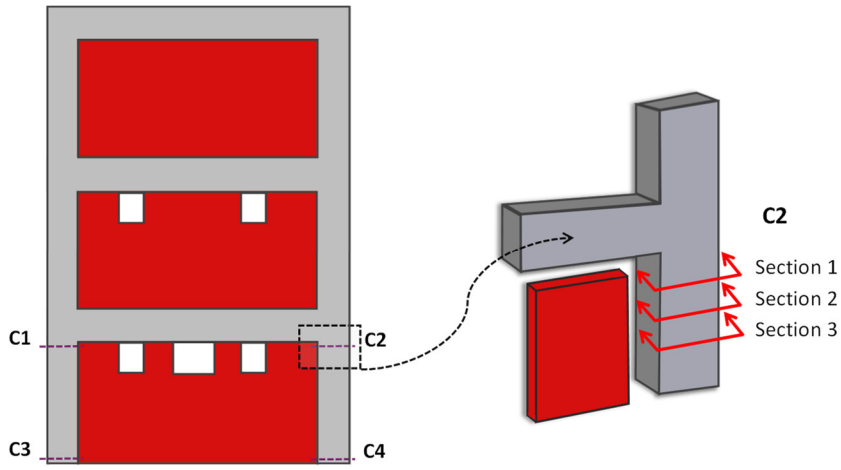

Figure 7.21: Location of critical sections (C1 - C12) and definition of section cuts (Section 1, 2, 3) for each section.

At each section cut, the shear force was evaluated through numerical integration of the nodal forces, as described in detail in Chapter 5. The numerical extraction was performed at each time step of the nonlinear dynamic analyses, allowing the reconstruction of the full cyclic evolution of the shear force at the selected critical sections. This procedure enables the actual shear demand to be consistently evaluated by means of a validated refined model, overcoming the lack of direct experimental measurements of local internal forces. The resulting cyclic shear force histories at critical sections (C1 - C4) are reported in Figure 7.22 for the last test of the loading sequence (Test 10, PGA=0.2g). These results represent a fundamental outcome of the refined numerical model, as they form the benchmark for the validation of the analytical correction model for single-strut macro-model discussed in the following sections.

At a PGA level of 0.2 g (Test 10), the cyclic shear demand in the first-storey columns remains relatively low, reflecting a response that is predominantly elastic and characterised by limited interstorey drift. At this stage, the infill panels are still largely effective, contributing to the lateral stiffness of the system and reducing the shear demand transferred to the columns.

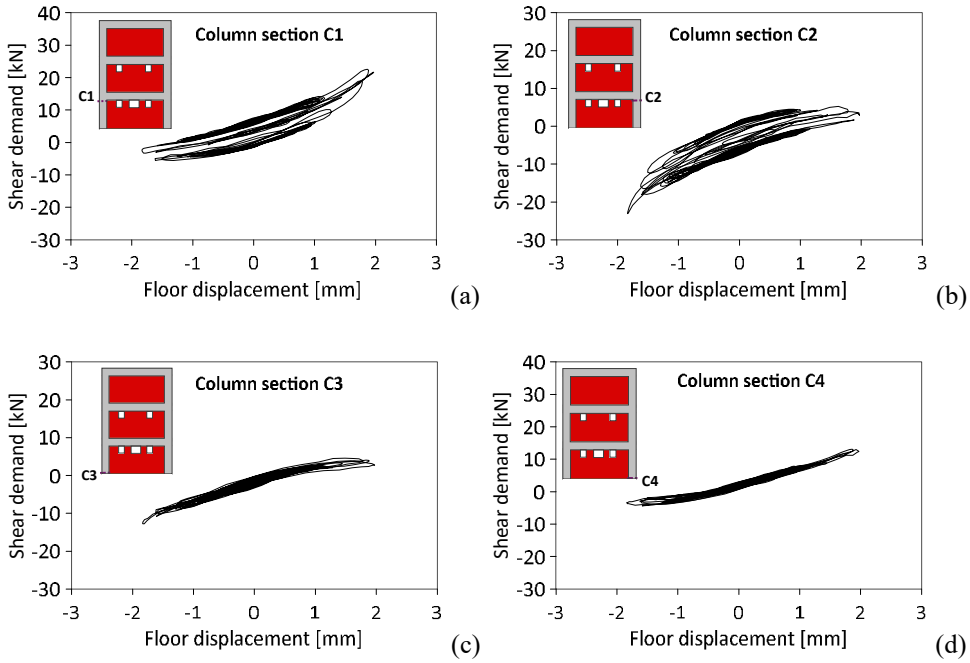

Figure 7.22: Cyclic shear force histories at first-storey columns (Test 10, PGA=0.2g): (a) Top column end C1; (b) Top column end C2; (c) Bottom column end C3; (d) Bottom column end C4.

7.3 Dynamic validation of the analytical correction model for single-struts using the digital replica of the reference building

7.3.1 Equivalent single-strut macro-model of the reference building

The seismic response of the reference infilled RC building was also simulated using an equivalent single-strut macro-modelling approach, aimed at reproducing the global in-plane contribution of the masonry infills with reduced computational cost. Within this approach, each masonry infill panel is replaced by a diagonal compression-only strut, modelled as a pinned, no-tension element with a nonlinear behaviour. The latter was modelled following the formulations proposed by **Di Trapani et al. (2018)**. The constitutive response of the equivalent strut is defined through a small set of parameters governing peak strength, peak deformation, ultimate residual strength, and ultimate deformation capacity in compression, which are evaluated via empirical correlations (**Di Trapani et al., 2018**). The stress-strain backbone is implemented in OpenSees using the *Concrete02* uniaxial material model. The geometric definition of the equivalent strut is governed by its

effective width w, which controls both stiffness and strength contributions. In the present study, the full equivalent width w is initially evaluated following the formulation proposed by **Asteris et al. (2016)**. A detailed discussion of the equivalent strut width and the constitutive strut parameters is provided in Chapter 2 and Chapter 5.

The effect of openings is subsequently introduced through the empirical reduction model proposed by **Decanini et al. (2014)**. This formulation is adopted because it was calibrated on a broad experimental database including infilled RC frames with different opening sizes and positions providing a robust representation of the geometric weakening effects induced by openings. According to **Decanini et al. (2014)**, the stiffness reduction factor ρ is expressed as a function of two geometric ratios, namely the opening-to-panel area ratio α_a and the opening-to-panel length ratio α_l:

$$\alpha_a = \frac{A_{openings}}{A_{panel}} \cdot 100 \;\; ; \; \alpha_l = \frac{l_0}{l} \cdot 100 \tag{99}$$

Where $A_{openings} = l_0 \cdot h_0$ is the area of the opening. For unreinforced masonry infills, the reduction factor is given by:

$$\rho = 0.55 \cdot e^{-0.035\alpha_a} + 0.44 \cdot e^{-0.025\alpha_l} \tag{100}$$

In the adopted approach the reduction factor affects only the effective resisting area of the equivalent strut, according to:

$$A_{strut,red} = \rho \cdot t \cdot w \tag{101}$$

where t is the infill thickness. Conversely, the constitutive parameters of the stress-strain law are evaluated using the full width w, ensuring that it remains representative of the material behaviour calibrated on solid panels, whereas the mechanical effect of openings is reflected in a proportional decrease of stiffness and strength at the element level. The resulting values of the equivalent strut width w, together with the corresponding reduced widths w_{red} accounting for the presence of openings, are summarised in Table 39.

Table 39: Full and reduced equivalent strut widths adopted for the macro-model of the masonry infill panels.

Storey	w (mm)	w_{red} (mm)
1	947.61	547.20
2	943.05	707.44
3	939.18	939.18

The resulting modelling approach can be summarised as follows:
- the full equivalent width w is computed following **Asteris et al. (2016)** with r = 1;
- the reduction factor ρ is evaluated according to **Decanini et al. (2014)** and used to define the reduced strut width $w_{red} = \rho \cdot w$;
- the constitutive parameters governing the nonlinear stress-strain law of the strut are derived using the un-reduced width w using **Di Trapani et al. (2018)** model, avoiding double-counting of the opening effect.

The frame elements are modelled with 1D force-based *beam-column* elements with the nonlinear uniaxial *ASDConcrete1D* material model, which includes automatic fracture energy regularization features.

The following sections focus on the calibration of the dynamic response of the equivalent single-strut macro-model, adopting the same framework introduced for the refined numerical model. The calibration of the macro-model is essential to follow the fundamental assumption of the formulation proposed in Chapter 5 and here validate for dynamic loading scenarios. In particular the refined and macro models must exhibit a consistent global behaviour. Only once global response is calibrated, local response predicted by the two modelling strategies can be compared.

7.3.1.1 Elastic response calibration via modal analysis

The elastic response of the equivalent single-strut macro-model was calibrated by means of modal analysis, following the same framework adopted for the refined numerical model and described in Section 7.2.2. The calibration was performed by comparing the numerical modal frequencies of the equivalent single-strut macro-model with the experimentally identified ones discussed in Section 7.2.2.1. As for the refined model, the calibration focused on the three vibration modes of interest. The influence of the macro-model parameters on the modal frequencies was therefore investigated through sensitivity analyses, followed by a calibration stage

aimed at minimising the global discrepancy between numerical and experimental frequencies. The following sections present the results of the sensitivity analysis and the optimised elastic response of the equivalent single-strut macro-model.

7.3.1.1.1 Sensitivity analysis

The analysis was conducted following the same global sensitivity framework adopted for the refined numerical model (Section 7.2.2.1.2). In the current case, the sensitivity analysis was initially aimed at investigating the influence of the full set of constitutive parameters defining the stress-strain law proposed by **Di Trapani et al. (2018)** on the elastic response, specifically the peak elastic strength (f_{md0}), the corresponding strain (ε_{md0}), the residual strength (f_{mdu}), and the corresponding strain (ε_{md0}). Conversely, the elastic properties of the reinforced concrete frame were not included among the uncertain input parameters, as they had already been calibrated during the elastic optimisation of the refined numerical model. The same calibrated concrete elastic properties were therefore adopted in the macro-model, ensuring consistency between the two models and allowing the effects of modelling simplifications to be isolated. The reference constitutive parameters of the equivalent strut, derived from the model by **Di Trapani et al. (2018)**, are reported in Table 40. A uniform distribution was assigned to all input variables with a COV ± 30%.

Table 40: Reference constitutive parameters of the equivalent strut derived from **Di Trapani et al. (2018)**.

Input parameter	**Reference value**
Peak compressive strength f_{md0} (MPa)	1.61
Residual strength f_{mdu} (MPa)	0.15
Peak strain ε_{md0} (-)	0.00047
Ultimate strain ε_{mdu} (-)	0.00933

The output quantities were defined as the natural frequencies of the three vibration modes of interest (Modes 1, 2, and 3), and the global model response was evaluated in terms of the root mean square error (RMSE) between numerical and experimentally identified frequencies. The behavioural simulations are those with a RMSE lower than 0.5 Hz.

The results of the sensitivity analysis, illustrated in Figure 7.23 and Figure 7.24, indicate that the elastic dynamic response of the macro-model is predominantly governed by the parameters defining the initial stiffness of the equivalent strut

constitutive law (f_{md0}, ε_{md0}). This outcomes, clearly highlighted by the parallel coordinate plots in Figure 7.24, provides a rational basis for restricting the subsequent calibration stage to a reduced set of parameters of the equivalent strut, while keeping the strut geometry fixed.

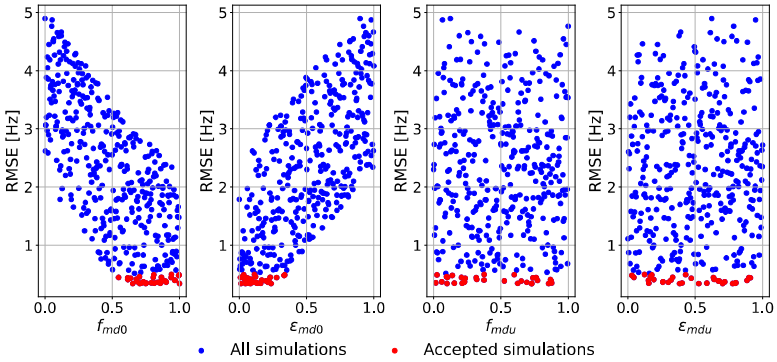

Figure 7.23: Scatter plots of the RMSE between numerical (macro-model) and identified experimental frequencies versus normalised elastic input parameters for the three vibration modes. Blue and red markers indicate all and behavioural simulations (RMSE<0.5 Hz), respectively.

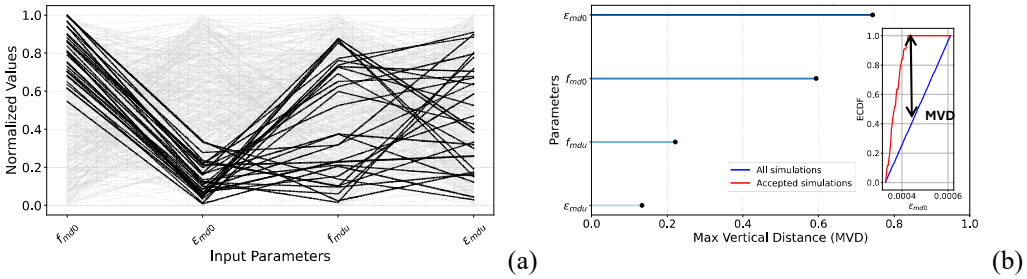

Figure 7.24: Parallel coordinate plots of behavioural simulations and MVD-based tornado diagrams for all modes sensitivity analysis (macro-model).

7.3.1.1.2 Calibrated response

The sensitivity results clearly indicate that the modal frequencies are predominantly controlled by the peak compressive strength f_{md0} and the corresponding strain ε_{md0}. In particular, the parallel coordinate plot reported in Figure 7.24a shows a clear clustering of the simulations associated with lower RMSE values towards higher values of f_{md0} and lower values of ε_{md0}, corresponding to an increase in the initial tangent stiffness of the equivalent strut. This trend is consistently observed across the three vibration modes considered (Appendix A) and provides direct evidence of the parameter combination leading to an improved agreement with the experimentally identified modal frequencies. Given the clear

monotonic trends emerging from the sensitivity analysis, a formal optimisation procedure based on a genetic algorithm was not necessary in this case. Accordingly, the simulation exhibiting the minimum RMSE among the sensitivity analysis samples ($100N$ = 400) was selected. The corresponding constitutive parameters governing the elastic stiffness of the equivalent strut were therefore selected, specifically f_{md0} = 1.92 MPa and $\varepsilon_{md0} = 3.224 \cdot 10^{-4}$, thus defining the elastic modulus with the tangent stiffness $K_{el} = f_{md0} / \varepsilon_{md0}$ = 5955.3 MPa.

Using the reference (mean) values of the constitutive parameters directly obtained from the formulation proposed by **Di Trapani et al. (2018)**, the macro-model predicts modal frequencies associated with a global error quantified by an RMSE equal to 2.21 Hz. After updating the constitutive parameters to the selected optimal values, the numerical modal frequencies exhibit a significantly improved agreement with the experimental ones, with the RMSE reducing to 0.34 Hz. This corresponds to an overall error reduction of approximately 85%. The experimental frequencies, together with the numerical predictions obtained using the mean and the optimised parameter values, are reported in Table 41.

Table 41: Comparison between experimental and numerical natural frequencies of the three target modes for the mean and optimised parameter sets, together with the corresponding RMSE values.

	Experimental	**Mean Values**	**Optimised Values**
Mode 1, f_1 (Hz)	6.68	5.72	6.39
Mode 2, f_2 (Hz)	8.04	7.44	8.55
Mode 3, f_3 (Hz)	27.33	23.68	27.21
	RMSE	2.21	0.34

The updated macro-model was further assessed through a posteriori comparison of the numerical and experimental mode shapes by evaluating MAC. As for the refined numerical model, the MAC analysis was limited to the two flexural modes (Modes 2 and 3), for which experimental mode shapes are available. Figure 7.25 shows the comparison between the numerical and experimental mode shapes, while the corresponding MAC matrix is reported in Figure 7.26.

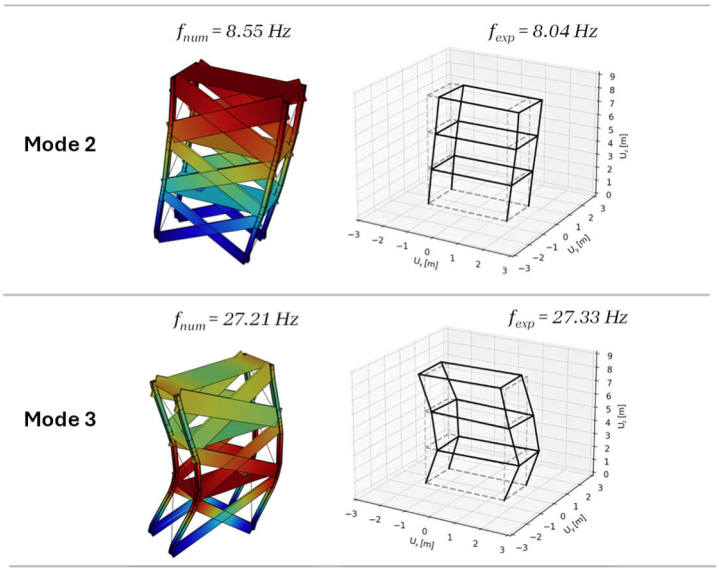

Figure 7.25: Numerical (macro-model) and experimental mode shapes of the two flexural modes considered for MAC validation, with corresponding natural frequencies.

The resulting MAC values, equal to 0.986 for Mode 2 and 0.906 for Mode 3, with quasi-zero off-diagonal terms, indicate a high correlation between the numerical and experimental eigen vectors.

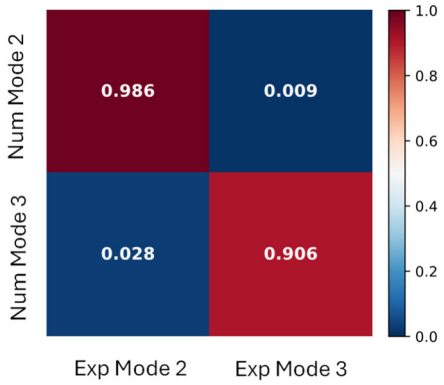

Figure 7.26: MAC matrix between numerical (macro-model) and experimental mode shapes of the two flexural modes considered for model validation.

7.3.1.2 Non-linear dynamic response calibration via incremental time-history analyses

Following the calibration of the elastic response, the nonlinear dynamic behaviour of the macro-model was investigated by incremental nonlinear time-history analyses. The objective is to assess the capability of the simplified

equivalent strut formulation to reproduce the experimentally observed global dynamic response under increasing PGA levels, while maintaining a computationally efficient modelling framework. The investigation follows the same strategy adopted for the refined model reported in Section 7.2.2.2.

7.3.1.2.1 Sensitivity analysis

The sensitivity analysis was performed to investigate the influence of the nonlinear constitutive parameters governing the cyclic behaviour of the macro-model. A preliminary sensitivity study on the elastic response highlighted the existence of two ideal values of the peak elastic strength f_{md0}^{*} and the corresponding strain ε_{md0}^{*}. These two parameters defines the elastic stiffness of the equivalent strut, $K_{el} = f_{md0}^{*} / \varepsilon_{md0}^{*}$. While the elastic stiffness K_{el} was kept fixed in order to preserve the optimised elastic response, the values of f_{md0} and ε_{md0} are not defined a priori. Moreover, variations of f_{md0} may influence the nonlinear response of the macro-model. For this reason, f_{md0} was treated as an independent input parameter, while the corresponding strain ε_{md0} was derived accordingly through the identified elastic stiffness K_{el}. Therefore, the sensitivity analysis was focused on the parameters controlling the post-elastic and cyclic behaviour of the equivalent strut, such as the peak compressive strength (f_{md0}), the residual compressive strength (f_{mdu}), the corresponding deformation capacity (ε_{mdu}), and the loading-unloading coefficient (λ). For each input parameter, a reference mean value was defined based on **Di Trapani et al. (2018)**'s formulations and reported in Table 42. A uniform distribution was assigned to all input variables with a COV ± 40%.

Table 42: Reference input parameters of the equivalent strut derived from **Di Trapani et al. (2018)**.

Input parameter	**Reference value**
Compressive strength* f_{md0}	1.92
Residual strength f_{mdu} (MPa)	0.15
Ultimate strain ε_{mdu} (-)	0.00933
Loading-unloading coefficient λ (-)	0.08

* optimal value obtained from the calibration of the elastic phase.

The model response was evaluated in terms of the global error $NRMSE_{glob}$, which considers the error related to the natural frequencies and the error related to the peak floor accelerations, as reported in Section 7.2.2.2.2. For the macro-model, the sensitivity analysis highlights a markedly different behaviour compared to the refined model. In particular, a larger variability is observed both in the frequency-based error and in the peak floor acceleration error. This confirms the higher

modelling uncertainty associated with the simplified macro-modelling approach due to a higher degree of freedom of the model. As a consequence, neither of the two response indicators can be considered dominant in driving the overall model performance. For this reason, the global normalised error was defined by assigning equal weights to the two contributions, adopting $w_i = w_j = 0.5$ for both the frequency-related and the peak acceleration-related error component. Behavioural simulations were identified as those characterised by a sufficiently low global error, e.g. $NRMSE_{glob} < 0.15$. This threshold was adopted to preserve a subset of simulations for interpretation. The results of the sensitivity analysis are summarised in Figure 7.27 and Figure 7.28. The scatter plots reported in Figure 7.27 show that, the most influential parameter is the compressive strength of the equivalent strut (f_{md0}). This is further confirmed by the MVD-based tornado plot (Figure 7.28b), where the larger maximum vertical distance indicates f_{md0} as the dominant parameter among the other investigated. Additional insight is provided by the parallel coordinate plot in Figure 7.28a. Behavioural simulations exhibit a large dispersion across all input parameters whit the exception for f_{md0}, which clusters within a range that goes from 1.8 MPa to 2.69 MPa.

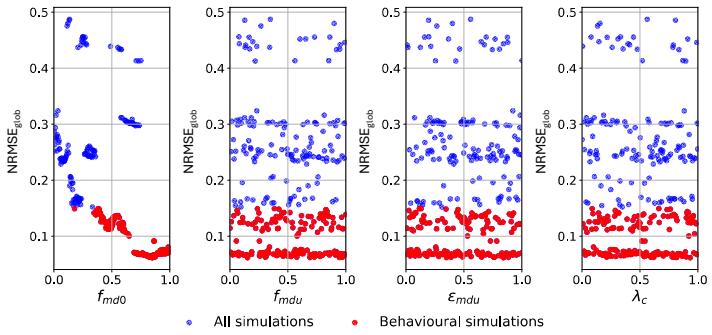

Figure 7.27: Scatter plots of the global normalised error $NRMSE_{glob}$ as a function of the nonlinear masonry parameters for the macro-model (behavioural simulations $NRMSE_{glob}$<0.15).

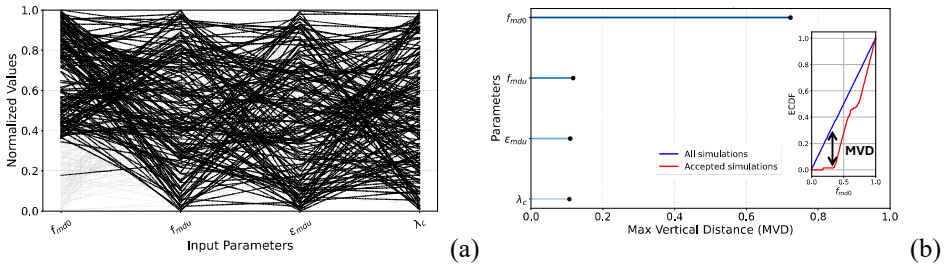

Figure 7.28: Parallel coordinate plots of behavioural simulations and MVD-based tornado diagrams for nonlinear response sensitivity analysis (macro-model).

Overall, more pronounced than in the refined model, the sensitivity analysis highlights the intrinsic limitations of frequency-based metrics for the calibration of hysteretic parameters in simplified macro-models and motivates the adoption of additional response-based criteria for the selection of the final parameter set, as the peak floor accelerations.

7.3.1.2.2 Calibrated response

For the macro-model, the calibration of the nonlinear response rely exclusively on the structural response in the time and frequency domains. In this context, the calibration is driven by the ability of the model to reproduce the experimentally observed vibration characteristics and peak floor accelerations, as quantified through the global normalised error $NRMSE_{glob}$. Accordingly, the calibrated parameter set was selected among the behavioural simulations by identifying the configuration that minimises $NRMSE_{glob}$ while remaining consistent with the sensitivity trends previously discussed. The selected parameter set corresponds to a compressive strength of the equivalent strut $f_{md0} = 2.68$ MPa, a residual compressive strength $f_{mdu} = 0.15$ MPa, with a corresponding deformation capacity $\varepsilon_{mdu} = 0.0119$, and a cyclic loading-unloading coefficient $\lambda = 0.065$. This configuration gives a global error $NRMSE_{glob} = 0.07$.

The predictive capability of the calibrated macro-model was further assessed by comparing numerical and experimental PSDs of both acceleration and displacement responses (Figure 7.29 and Figure 7.30). The comparison is reported for the first four shaking-table tests, for which the experimental records provide reliable spectral information. The results indicate that the macro-model satisfactorily reproduces the dominant spectral peaks, showing good agreement with the experimental data in terms of both frequency content and amplitude. A slight discrepancy is observed for the first modal frequency, with the numerical value equal to 8.5 Hz compared to the experimental frequency of 8.01 Hz, while other minor differences are found in the amplitude at higher frequency ranges. Overall, the spectral comparison confirms the adequacy of the selected parameter set in capturing the global dynamic behaviour of the structure during the initial stages of response, characterised by moderate nonlinearity.

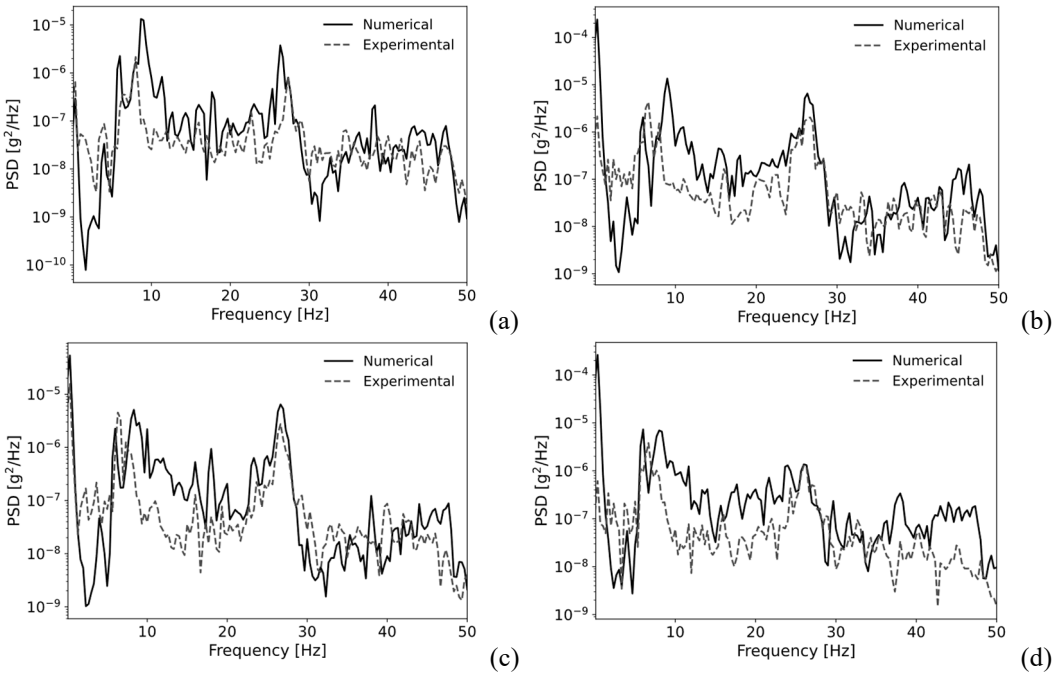

Figure 7.29: Experimental vs. Numerical power spectral density plots in terms of accelerations at the third floor, for the first four shake-table tests: (a) Test 01 (PGA=0.032g); (b) Test 02 (PGA=0.056g)); (c) Test 03 (PGA=0.08g); (d) Test 04 (PGA=0.104g).

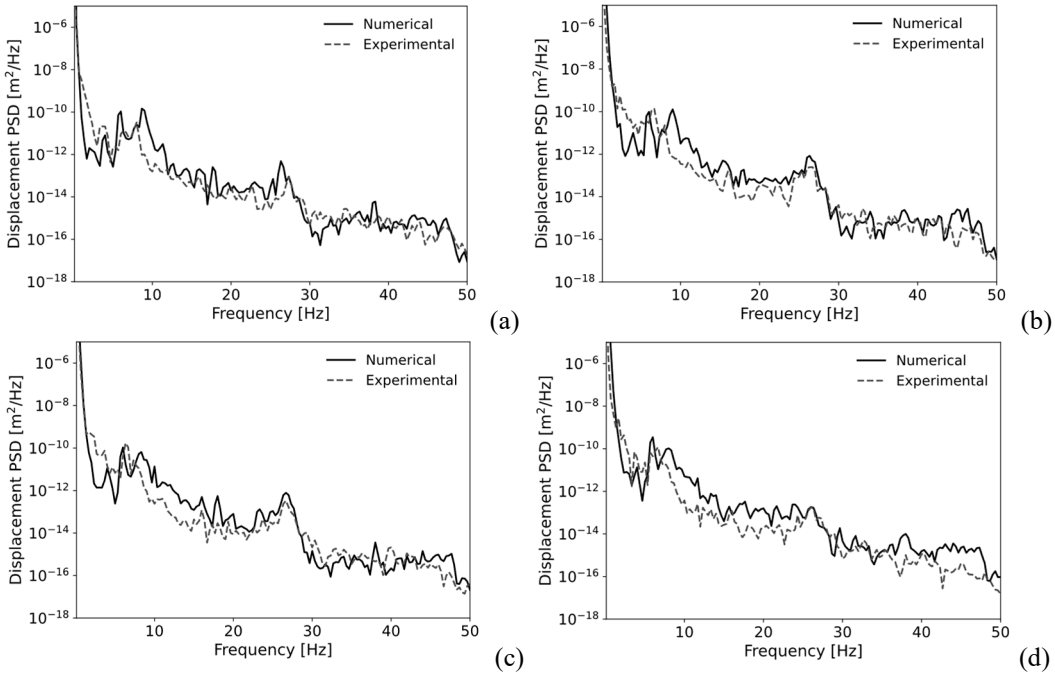

Figure 7.30: Experimental vs. Numerical power spectral density plots in terms of displacements at the third floor, for the first four shake-table tests: (a) Test 01 (PGA=0.032g); (b) Test 02 (PGA=0.056g)); (c) Test 03 (PGA=0.08g); (d) Test 04 (PGA=0.104g).

The calibrated macro-model was subsequently employed to simulate the full sequence of the first ten shaking-table tests characterised by increasing PGA levels. This procedure allows the extraction, from a global calibrated model, of the drift-related shear demand and the axial force in the equivalent strut. These quantities are required for the application and validation of the analytical shear correction model for single-strut representations, which is presented and assessed in the following section.

7.3.2 Nonlinear dynamic validation: Refined vs. Proposed analytical model

The nonlinear dynamic validation aims at assessing the capability of the proposed analytical correction model for the single strut macro-model to reproduce the local response observed under dynamic loading in terms of shear demand at critical sections. The comparison is performed against the refined numerical model, which is treated as the benchmark reference, being explicitly calibrated on the experimental response and able to capture local infill-frame interaction mechanisms.

The validation is carried out by considering a subset of the reference experimental shaking-table tests characterised by progressively increasing intensity levels, corresponding to the first ten tests of the experimental campaign. The selected ground motion records and the associated peak ground acceleration (PGA) levels are consistent with those previously adopted for the calibration phase (from 0.032 g to 0.20 g).

In addition to the experimental loading protocol, further numerical simulations were performed on the calibrated models to investigate the structural response at higher seismic intensity levels.

7.3.2.1 Proposed analytical model

The proposed analytical correction model for single-strut macro-model, illustrated in detail in Chapter 5, is based on the shear decomposition rule originally introduced by **Saneinejad and Hobbs (1995)**, according to which the total shear demand at the end of a column in a masonry-infilled RC frame can be expressed as the sum of two contributions: the shear associated with the global lateral drift of the frame and an additional component induced by the infill-frame interaction. Accordingly, the total shear demand at a column end is expressed as:

$$V_{d,tot} = V_{d,frame} + V_{d,inf} \tag{102}$$

where $V_{d,\text{frame}}$ is the shear demand obtained from the structural analysis of the equivalent strut macro-model, and $V_{d,\text{inf}}$ represents the additional shear transferred to the column through the infill-frame contact mechanisms. By enforcing global static equivalence between the equivalent strut representation and the actual infilled frame system, the additional shear contribution can be analytically expressed as a function of the axial force acting in the equivalent strut. The final formulation adopted in this study is:

$$V_{d,tot} = V_{d,frame} + N\left(\cos\theta - \frac{\mu \cdot \sin\theta \cdot \alpha l}{w}\right) \tag{103}$$

where N is the axial force in the equivalent strut, w is the strut width, t is the infill thickness, θ is the inclination angle of the equivalent strut, μ is the friction coefficient at the infill-frame interface (assumed equal to 0.7 in the study presented in Chapter 5), and α defines the effective contact coefficient between the infill and the surrounding frame, expressed as a portion of the panel length. For further information the reader could refer to Chapter 5.

7.3.2.2 Local shear demand: Refined vs Proposed analytical correction model

The validation of the proposed analytical formulation is carried out through a direct comparison between the local shear demand extracted from the refined numerical model and the shear demand estimated by the analytical correction model (Equation (103)). The refined model is adopted as an experiment-informed reference, as it was calibrated against the global shaking-table response and is able to explicitly capture the force transfer mechanisms developing at the infill-frame interfaces. The comparison focuses on the column ends at the first storey (C1-C4), which were identified as the most loaded. For each column, the total shear force predicted by the refined model is compared with the shear demand estimated by the analytical formulation. In this first stage, the analytical model is applied in its original form (Equation (103)), adopting a constant friction coefficient μ=0.7, employed to calibrate the analytical model on the maximum shear demand observed under pushover analyses, as illustrated in Chapter 5. The results of the comparison

at the end of the reference experimental loading sequence (Test 10, PGA = 0.20 g) are reported in Figure 7.33.

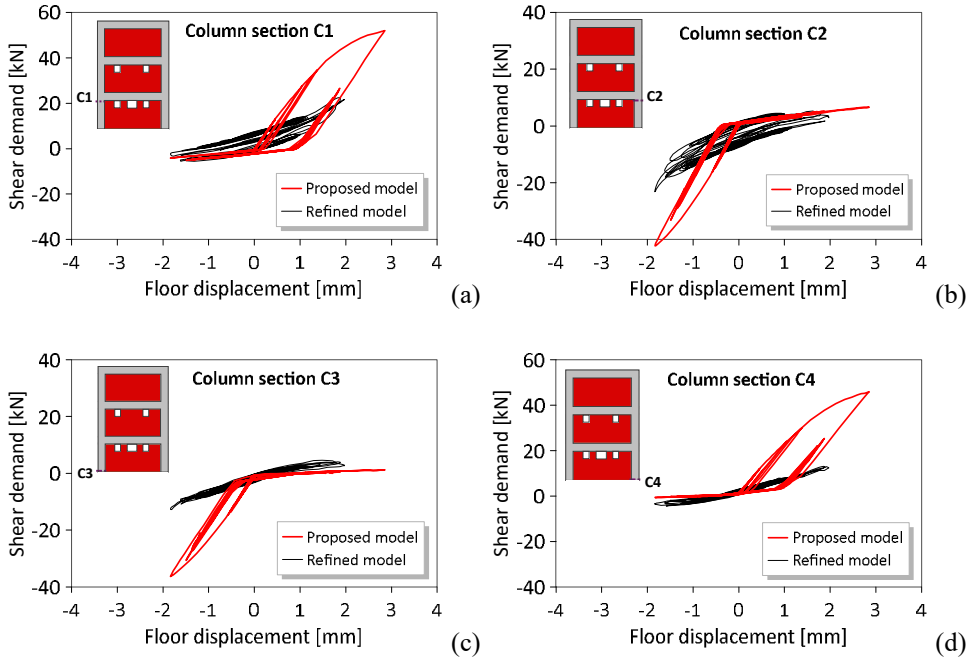

Figure 7.31: Local shear demand prediction (μ = 0.7) comparison at first-storey column ends (C1 - C4) at the end of the experimental loading sequence (Test 10, PGA = 0.20 g) : (a) C1; (b) C2; (c) C3; (d) C4.

The comparison highlights an overestimation of the local shear demand when the analytical formulation is applied with a constant friction coefficient (μ=0.7). This overestimation is more pronounced at low to moderate drift levels, where the shear demand predicted by the refined model remains significantly lower than the value estimated by the analytical correction. This discrepancy can be attributed to two main factors. First, the analytical formulation was calibrated on the maximum shear demand attained under monotonic loading, which corresponds to advanced damage states due to higher drift level, and to a full mobilisation of the infill-frame interaction mechanisms. When applied to nonlinear dynamic analyses, especially at low drift levels, this calibration leads to conservative estimates of the shear demand. Second, as already discussed in Chapter 5, the dispersion of the shear demand prediction is higher at low drift levels, where the interaction mechanisms are only partially activated and the contribution of the masonry infills is highly sensitive to small variations in the contact conditions. As a result, the use of a formulation calibrated on peak quantities under monotonic loading, becomes less representative of the actual dynamic force transfer at early response stages. In addition, the original

formulation assumes a constant friction coefficient at the infill-frame interface. However, the frictional behaviour of the interface is intrinsically state-dependent, as it is governed by the evolution of normal contact forces and by the progressive degradation of the contact surfaces. Under dynamic loading, cyclic opening and closing of the interface and the accumulation of damage lead to a reduction of the effective frictional resistance, which cannot be captured by a constant parameter.

To address this limitation, the friction coefficient μ is herein reinterpreted as an equivalent, state-dependent parameter that reflects the current damage level at the infill-frame interface (μ_{eq}), so that:

$$\mu_{eq} = \beta\mu \tag{104}$$

Specifically, the coefficient β is expressed as a function of the peak interstorey drift ratio, as follows:

$$\beta(IDR_{\max}) \rightarrow IDR_{\max} = \max_{t}\left(\frac{\Delta_i(t)}{h_{sc}}\right) \tag{105}$$

where $\Delta_i(t)$ is the horizontal displacement of the storey and h_{sc} is the squat column height.

For each seismic input, the value of IDR_{max} obtained from the refined model is used to identify the equivalent friction coefficient μ_{eq} that allows the analytical formulation to better reproduce the local shear demand predicted by the refined numerical replica. This yields an equivalent friction coefficient (μ_{eq}) associated with each intensity level, directly linking the analytical correction to a physically meaningful damage-related response quantity. Substituting the latter into Equation (103) the following formulation is obtained:

$$V_{d,tot} = V_{d,frame} + N\left(\cos\theta - \frac{\beta\mu\cdot\sin\theta\cdot\alpha l}{w}\right) \tag{106}$$

Figure 7.33 summarises the values of the calibrated state-dependent corrective coefficient β for different analysed seismic inputs as a function of the corresponding peak interstorey drift ratio. For the selected dynamic tests within the incremental dynamic loading sequence, it is shown a decreasing trend of β, and therefore of μ_{eq},

with increasing drift demand, reflecting the progressive degradation of the infill-frame contact conditions and the reduction of effective frictional resistance as damage accumulates.

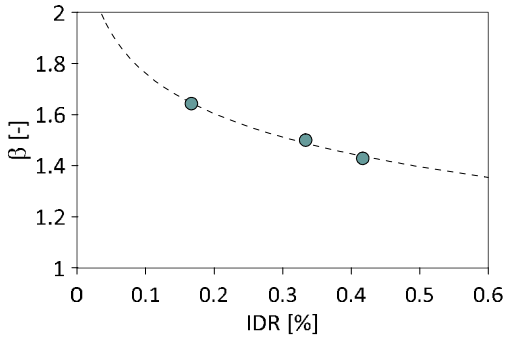

Figure 7.32: Variation of the corrective coefficient β with respect to the maximum drift reached at selected tests throughout the loading sequence.

Thus, leading to the following equation:

$$\beta = -0.227 \ln\left(IDR_{\max}\right) + 1.2385 \tag{107}$$

Therefore, the comparison is herein extended to the refined numerical model and the analytical formulation corrected as a function of the peak interstorey drift ratio. The results are presented for two selected input tests, representative of different intensity and drift demand levels. Figure 7.33 and Figure 7.34 reports the comparison between the local shear demand predicted by the refined model and that obtained through the proposed analytical correction using the drift-dependent coefficient β for selected seismic inputs (PGA: 0.1g and 0.2g). The comparison confirms that, once the state-dependent correction is adopted, the analytical formulation is able to reproduce the local shear demand with significantly improved accuracy over a wide range of seismic intensities. At low drift levels, the proposed correction mitigates the overestimation observed when a constant friction coefficient is employed, leading to a closer agreement with the refined numerical results.

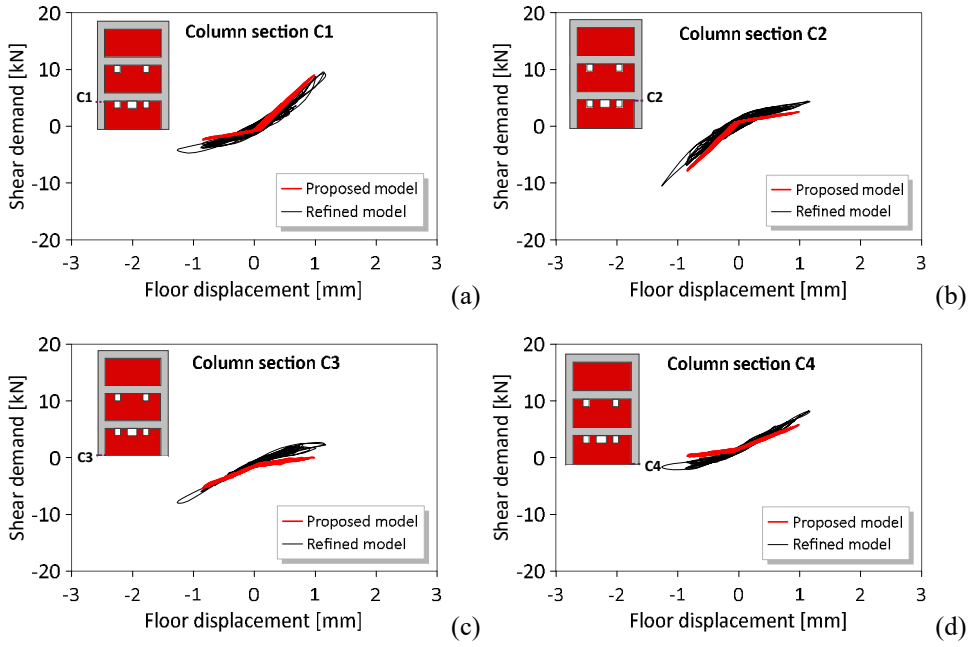

Figure 7.33: Corrected local shear demand prediction comparison at first-storey column ends (C1 - C4) at the end of the Test 5 (PGA = 0.10 g) : (a) C1; (b) C2; (c) C3; (d) C4.

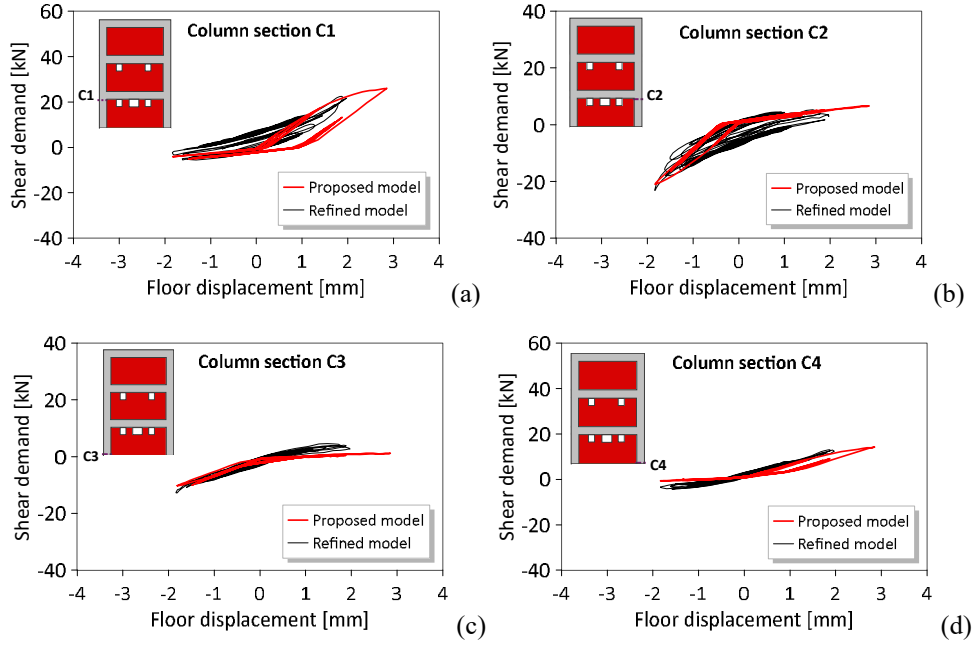

Figure 7.34: Corrected local shear demand prediction comparison at first-storey column ends (C1 - C4) at the end of the Test 10 (PGA = 0.20 g) : (a) C1; (b) C2; (c) C3; (d) C4.

Furthermore, additional numerical investigations were carried out. The objective is to assess whether the proposed correction model, incorporating the estimated β coefficient formulation, retains its effectiveness when subjected to higher levels of seismic intensity. The first numerical analysis was executed by using the no-scaled reference Irpinia earthquake as ground motion (PGA = 0.32g) and applying it as a single-event excitation to the calibrated numerical models. The results are reported in terms of shear cyclic demand in Figure 7.35. At this intensity level, the refined model exhibits a modest increase in local shear demand at the first-storey column ends, associated with the mobilisation of the masonry infills and the concentration of contact forces at the infill-frame interfaces. The shear demand estimated through the proposed β correction formulation is in good agreement with the numerical results, confirming that the correction model is able to consistently capture the onset and evolution of infill-induced shear demand under moderate seismic excitation.

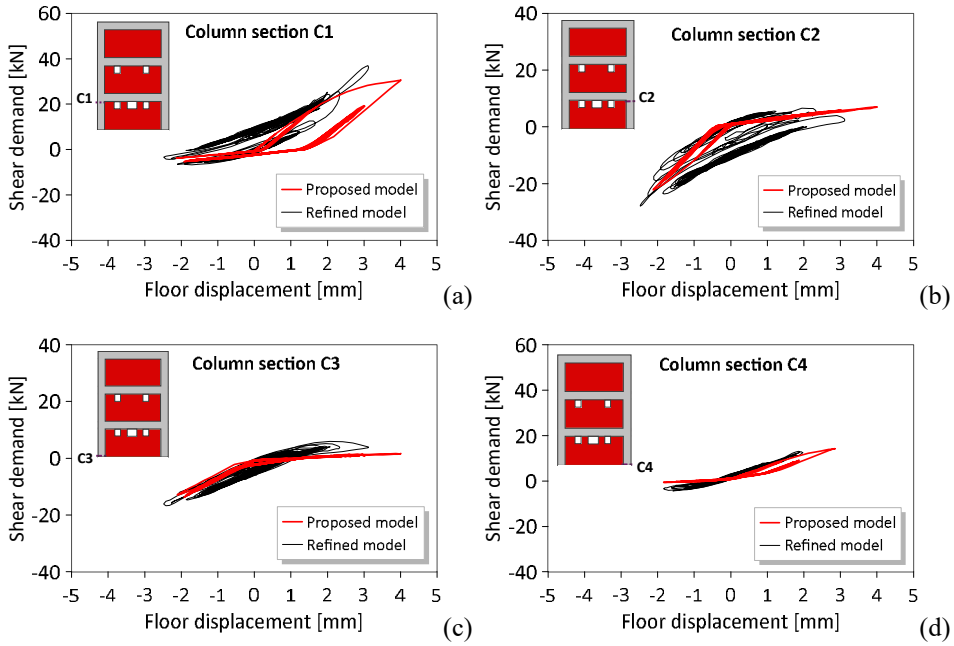

Figure 7.35: Corrected local shear demand prediction comparison at first-storey column ends (C1 - C2) at a higher seismic intensity level (Numerical test 1, PGA = 0.32 g): (a) C1; (b) C2; (c) C3; (d) C4.

The second numerical investigation involved scaling the reference ground motion to a PGA of 0.64 g and applying it as a single-event excitation, with the aim of assessing whether higher seismic intensity leads to an increase in shear demand associated with infill-frame interaction. In this case, an increase in the shear demand

at the most loaded column end (Section C1) is observed, with peak values reaching approximately 60 kN. At this intensity level, the proposed shear demand model, corrected with the state-dependent β coefficient, remains effective in accurately capturing the maximum shear demand. Conversely, the macro-model exhibits significantly higher displacement demands with respect to the refined model, which can be attributed to its higher deformability under marked nonlinear response. However, it is important to emphasise that the model presented in Chapter 5, and subsequently corrected herein, is conceived as a shear demand-oriented formulation. Accordingly, for its intended purpose, the prediction remains reliable, as confirmed by the comparison between the maximum shear attained in the most highly loaded column (C1) and the envelope of the shear demand estimated through the proposed correction formula (Figure 7.36). Furthermore, the results indicate that, emerging higher nonlinearities and infill-frame mobilisation, the equivalent friction coefficient converges towards the value adopted in the original analytical model calibrated through pushover analysis (μ = 0.7) and presented in Chapter 5. This behaviour suggests that the corrected analytical formulation preserves its predictive capability even under higher seismic intensity levels.

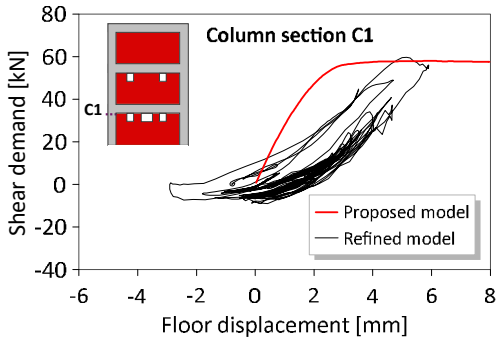

Figure 7.36: Corrected local shear demand prediction comparison at first-storey column ends (C1 - C2) at a higher seismic intensity level (Numerical test 2, PGA = 0.32 g) for the most loaded column end (Section C1).

Overall, these comparisons confirm that the proposed analytical correction enables the macro-modelling approach to potentially bridge the gap between simplified macro-models and refined numerical models (micro-/meso-), allowing a reliable estimation of local shear demand under nonlinear dynamic loading without the need for computationally expensive modelling strategies.

7.4 Conclusions

This chapter addressed the problem of estimating the local shear demand induced by masonry infills in reinforced concrete frames under nonlinear dynamic loading, with particular emphasis on the limitations of conventional simplified macro-modelling approaches. While equivalent strut models are widely adopted for their computational efficiency, their inability to capture infill-frame interaction mechanisms leads to significant inaccuracies in the prediction of column-end shear forces, especially under dynamic loading conditions. To overcome this limitation, the chapter investigated the applicability of a shear-demand-oriented analytical correction, validated against experimental shake-table data through a refined numerical benchmark.

Based on the outcomes presented, the following conclusions can be drawn:

- A full-scale masonry-infilled RC frame tested on a shake table was adopted as a reference case study to assess the nonlinear dynamic response and to compare modelling strategies with different levels of refinement. A high-fidelity numerical model was used as an experiment-informed benchmark, while a simplified equivalent strut macro-modelling approach was enhanced through the proposed analytical shear-demand formulation.

- A general and objective calibration framework for the global response was employed, consisting of two consecutive stages: the calibration of the elastic response through modal analysis, followed by the calibration of the nonlinear dynamic response through incremental time-history analyses supported by sensitivity analyses and optimisation procedures. This framework allows the global response to be objectively guided in both the elastic and nonlinear phases.

- The elastic calibration phase, based on the experimental identification of modal frequencies through EMA and on global sensitivity analyses, enabled a consistent calibration of the global stiffness, providing a reliable elastic baseline for the subsequent nonlinear dynamic analyses.

- The nonlinear calibration demonstrated that frequency-based error indicators alone are insufficient to guide the calibration process under dynamic loading. The combined use of frequency-based metrics, peak floor accelerations, and damage observations (where available) proved necessary to identify physically consistent parameter sets.

- The application of the original analytical shear-demand formulation, calibrated under pushover analyses, highlighted inaccuracies when extended to nonlinear dynamic analyses, particularly at low drift levels. In this regime, the analytical model tends to overestimate the local shear demand, reflecting the fact that the formulation is calibrated on peak shear demand associated with advanced damage states and full mobilisation of infill-frame interaction mechanisms.

- To address this limitation, the analytical formulation was extended by introducing a state-dependent correction in which the friction coefficient is expressed as a function of the peak interstorey drift ratio. This modification allows the analytical model to account for the progressive activation and degradation of the infill-frame interface under dynamic loading.

- The drift-dependent analytical correction significantly improves the estimation of local shear demand across a wide range of seismic intensity levels, enabling the simplified model to reproduce both the magnitude and the evolution of the shear demand envelopes observed in the refined numerical benchmark. At moderate drift levels, the corrected formulation naturally converges towards the original calibration, confirming the internal consistency of the proposed approach.

- The effectiveness of the corrected analytical formulation was confirmed not only within the experimentally investigated intensity range but also under a higher numerical seismic demand (PGA: 0.32g and 0.64 g), indicating that the proposed correction preserves its predictive capability under more severe loading conditions.

- Overall, the proposed drift-dependent analytical correction provides a computationally efficient enhancement of simplified macro-modelling strategies, allowing a more reliable estimation of local shear demand in masonry-infilled RC frames under nonlinear dynamic loading while preserving the practical advantages of equivalent strut models.

- It should be emphasised that the conclusions drawn in this chapter are inherently linked to the characteristics of the analysed reference structure, including its geometry, mass distribution, infill configuration, and masonry typology. While the proposed correction is physically grounded and supported by experimental evidence, the present study should be regarded as a preliminary investigation. With the purpose of a generalisation, further validation is required through the application of the proposed methodology to a broader range of structural

configurations, including systems with higher participating mass, irregular or eccentric layouts, different RC member cross-sections, and alternative masonry typologies and mechanical properties.

Conclusions

This thesis has addressed the complex seismic behaviour of masonry-infilled RC frames through multiscale modelling strategies, with the specific aim of bridging the gap between high-fidelity numerical modelling and practice-oriented assessment tools. Although masonry infills were traditionally classified as non-structural components, the results presented herein clearly demonstrate that their interaction with RC frames plays a crucial role in both global and local seismic response.

A comprehensive review of the literature has shown that, despite more than six decades of research, no consensus has yet emerged on a universally accepted modelling strategy for infilled RC frames. Micro- and meso-modelling approaches provide the closest representation of the actual mechanics of infill-frame interaction, allowing the explicit simulation of stress transfer, contact conditions, and damage evolution. However, their high computational cost limits their applicability to research-oriented studies. Conversely, simplified macro-models, most notably equivalent strut formulations, remain the most employed option in engineering practice and large-scale assessments, despite their intrinsic limitations in capturing local interaction effects.

Within this context, a major contribution of this thesis lies in the critical and systematic use of refined micro-modelling strategies to investigate infill-frame interaction effects. These models were shown to accurately reproduce the global structural response observed in experimental tests under monotonic, cyclic, and nonlinear dynamic loading conditions, thus constituting reliable digital replicas of the physical specimens. On this basis, the refined models enabled the consistent extraction of response quantities that cannot be directly measured experimentally, such as the actual internal force distribution within the RC frame members. Their role within this research was not to propose a practical alternative for engineering applications, but to provide a physically grounded benchmark against which simplified modelling strategies can be assessed, calibrated, and extended beyond their traditional scope.

Building upon this reference framework, the thesis has focused on one of the most critical yet insufficiently addressed aspects of infill-frame interaction: the amplification of shear demand at column ends and beam-column joints. The numerical and experimental evidence confirms that the presence of masonry infills

can induce substantial additional shear forces, potentially leading to brittle local failures. These mechanisms are not captured by conventional single-strut macro-models and are only partially addressed by multi-strut formulations, whose definition remains strongly model-dependent and often validated against global response metrics alone.

To overcome this limitation, an analytical and practice-oriented shear demand correction model was developed and validated. The proposed formulation links the additional shear demand to the axial force acting in the equivalent strut and to the geometrical and mechanical properties of the infilled frame system. A key outcome of this work is the demonstration that, when combined with a standard equivalent strut macro-model, the proposed correction allows for a reliable estimation of local shear demand without the need of refined numerical simulations. Notably, the validity of this approach was confirmed not only under static conditions, but also within a nonlinear dynamic context through comparison with full-scale shake-table test results.

The extension of the investigation to nonlinear dynamic analyses represents a further advancement with respect to existing studies. The refined numerical models were calibrated through a structured framework combining sensitivity analyses and optimisation procedures, allowing the most influential parameters to be systematically identified and selected on the basis of experimental evidence. The calibrated models successfully reproduced the experimental modal properties, global response, and damage evolution observed during shake-table testing, thereby constituting reliable digital replicas of the reference experiment from which local force demands could be extrapolated. The close agreement observed between refined numerical outcomes and simplified analytical predictions under dynamic loading conditions provides strong evidence of the robustness and practical applicability of the proposed methodology for seismic assessment purposes.

In parallel with the analytical shear-demand correction strategy, this thesis has also contributed through the development of a calibrated multi-strut macro-modelling approach. By introducing off-diagonal struts, the proposed three-strut formulation overcomes the intrinsic limitations of conventional single-strut models in capturing infill-induced shear amplification at column ends, while preserving an accurate representation of the global in-plane response. The formulation was first calibrated against experimental evidence and refined micro-modelling benchmarks using a genetic-algorithm-based optimisation framework, which enabled the systematic identification of mechanically admissible strut arrangements. These

GA-optimal configurations were subsequently employed as training data for genetic-programming-based formulations, from which analytical expressions governing strut positioning were derived. The resulting GP-defined configurations were shown to reproduce both global response and peak local shear demand with accuracy comparable to GA-optimised solutions, providing a computationally efficient alternative to refined models when local interaction effects need to be explicitly represented.

Overall, the findings of this thesis highlight that neglecting infill-frame interaction, or considering masonry infills solely in terms of global stiffness and strength contributions, may lead to unconservative seismic assessments of existing RC buildings. In particular, the amplification of local shear demand emerges as a governing mechanism for seismic vulnerability, especially in older structures designed without modern capacity design principles. Within this context, the work presented in this thesis provides a coherent and experimentally validated basis for improving the seismic assessment of masonry-infilled RC frames, offering a rational compromise between accuracy and computational efficiency and enabling engineers to explicitly account for both global response and critical local effects within standard analysis procedures.

References

Al-Chaar, G., Mehrabi, A. B., & Manzouri, T. (2008). *Finite element interface modeling and experimental verification of masonry-infilled R/C frames*. Masonry Society Longmont, CO.

Anić, F., Penava, D., Sarhosis, V., & Abrahamczyk, L. (2021). Development and Calibration of a 3D Micromodel for Evaluation of Masonry Infilled RC Frame Structural Vulnerability to Earthquakes. *Geosciences*, *11*(11), 468. https://doi.org/10.3390/geosciences11110468

Asteris, P. G., Cavaleri, L., Di Trapani, F., & Sarhosis, V. (2016). A macro-modelling approach for the analysis of infilled frame structures considering the effects of openings and vertical loads. *Structure and Infrastructure Engineering*, *12*(5), 551–566.

Basha, S. H., & Kaushik, H. B. (2019). A novel macromodel for prediction of shear failure in columns of masonry infilled RC frames under earthquake loading. *Bulletin of Earthquake Engineering*, *17*(4), 2219–2244. https://doi.org/10.1007/s10518-018-00537-5

Bažant, Z. P., & Oh, B. H. (1983). Crack band theory for fracture of concrete. *Matériaux et Constructions*, *16*(3), 155–177. https://doi.org/10.1007/BF02486267

Bergami, A. V., & Nuti, C. (2015). Experimental tests and global modeling of masonry infilled frames. *Earthq. Struct*, *9*(2), 281–303.

Bertoldi, S. H., Decanini, L. D., & Gavarini, C. (1993). Telai tamponati soggetti ad azioni sismiche, un modello semplificato: Confronto sperimentale e numerico. *Atti Del 6 Convegno Nazionale*, 815–824.

Blackard, B., Willam, K., & Mettupalayam, S. (2009). Experimental observations of masonry infilled reinforced concrete frames with openings. *Special Publication*, *265*, 199–122.

Blasi, G., De Luca, F., & Aiello, M. A. (2018). Brittle failure in RC masonry infilled frames: The role of infill overstrength. *Engineering Structures*, *177*, 506–518. https://doi.org/10.1016/j.engstruct.2018.09.079

Blasi, G., De Luca, F., Perrone, D., Greco, A., & Antonietta Aiello, M. (2021). Mid 1.1: Database for characterization of the lateral behavior of infilled frames. *Journal of Structural Engineering*, *147*(10), 04721007.

Buonopane, S. G., & White, R. N. (1999). Pseudodynamic Testing of Masonry Infilled Reinforced Concrete Frame. *Journal of Structural Engineering*, *125*(6), 578–589. https://doi.org/10.1061/(ASCE)0733-9445(1999)125:6(578)

Campione, G., Cavaleri, L., Macaluso, G., Amato, G., & Di Trapani, F. (2015). Evaluation of infilled frames: An updated in-plane-stiffness macro-model considering the effects of vertical loads. *Bulletin of Earthquake Engineering*, *13*(8), 2265–2281. https://doi.org/10.1007/s10518-014-9714-x

Cavaleri, L., & Di Trapani, F. (2014). Cyclic response of masonry infilled RC frames: Experimental results and simplified modeling. *Soil Dynamics and Earthquake Engineering*, *65*, 224–242. https://doi.org/10.1016/j.soildyn.2014.06.016

Cavaleri, L., & Di Trapani, F. (2015). Prediction of the additional shear action on frame members due to infills. *Bulletin of Earthquake Engineering*, *13*(5), 1425–1454. https://doi.org/10.1007/s10518-014-9668-z

Cavaleri, L., Di Trapani, F., Asteris, P. G., & Sarhosis, V. (2017). Influence of column shear failure on pushover based assessment of masonry infilled reinforced concrete framed structures: A case study. *Soil Dynamics and Earthquake Engineering*, *100*, 98–112. https://doi.org/10.1016/j.soildyn.2017.05.032

Celano, F., Cimmino, M., Coppola, O., Magliulo, G., & Salzano, P. (2016). *Report dei danni registrati a seguito del terremoto del Centro Italia del 24 agosto 2016 (Release 1)*.

Celarec, D., & Dolšek, M. (2013). The impact of modelling uncertainties on the seismic performance assessment of reinforced concrete frame buildings. *Engineering Structures*, *52*, 340–354. https://doi.org/10.1016/j.engstruct.2013.02.036

Çelebi, M., Bazzurro, P., Chiaraluce, L., Clemente, P., Decanini, L., DeSortis, A., Ellsworth, W., Gorini, A., Kalkan, E., Marcucci, S., Milana, G., Mollaioli, F., Olivieri, M., Paolucci, R., Rinaldis, D., Rovelli, A., Sabetta, F., & Stephens, C. (2010). Recorded Motions of the 6 April 2009 Mw 6.3 L'Aquila, Italy, Earthquake and Implications for Building Structural Damage: Overview. *Earthquake Spectra*, *26*(3), 651–684. https://doi.org/10.1193/1.3450317

CEN. (2004a). *Eurocode 8—Design of structures for earthquake resistance, part 1: General rules, seismic actions and rules for building.*

Chrysostomou, C. Z., Gergely, P., & Abel, J. F. (2002). A SIX-STRUT MODEL FOR NONLINEAR DYNAMIC ANALYSIS OF STEEL INFILLED FRAMEs. *International Journal of Structural Stability and Dynamics*, *02*(03), 335–353. https://doi.org/10.1142/S0219455402000567

Colangelo, F. (2005). Pseudo-dynamic seismic response of reinforced concrete frames infilled with non-structural brick masonry. *Earthquake Engineering & Structural Dynamics*, *34*(10), 1219–1241.

Crisafulli, F. J., & Carr, A. J. (2007). Proposed macro-model for the analysis of infilled frame structures. *Bulletin of the New Zealand Society for Earthquake Engineering*, *40*(2), 69–77. https://doi.org/10.5459/bnzsee.40.2.69-77

D'Ayala, D., Worth, J., & Riddle, O. (2009). Realistic shear capacity assessment of infill frames: Comparison of two numerical procedures. *Engineering Structures*, *31*(8), 1745–1761. https://doi.org/10.1016/j.engstruct.2009.02.044

De Luca, F., Verderame, G. M., Gómez-Martínez, F., & Pérez-García, A. (2014). The structural role played by masonry infills on RC building performances after the 2011 Lorca, Spain, earthquake. *Bulletin of Earthquake Engineering*, *12*(5), 1999–2026. https://doi.org/10.1007/s10518-013-9500-1

De Luca, F., Woods, G. E. D., Galasso, C., & D'Ayala, D. (2018). RC infilled building performance against the evidence of the 2016 EEFIT Central Italy post-earthquake reconnaissance mission: Empirical fragilities and comparison with the FAST method. *Bulletin of Earthquake Engineering*, *16*(7), 2943–2969. https://doi.org/10.1007/s10518-017-0289-1

De Risi, M., Del Gaudio, C., & Verderame, G. (2019). Evaluation of Repair Costs for Masonry Infills in RC Buildings from Observed Damage Data: The Case-

Study of the 2009 L'Aquila Earthquake. *Buildings*, *9*(5), 122. https://doi.org/10.3390/buildings9050122

De Risi, M. T., Del Gaudio, C., Ricci, P., & Verderame, G. M. (2018). In-plane behaviour and damage assessment of masonry infills with hollow clay bricks in RC frames. *Engineering Structures*, *168*, 257–275. https://doi.org/10.1016/j.engstruct.2018.04.065

De Risi, M. T., Ricci, P., & Verderame, G. M. (2017). Modelling exterior unreinforced beam-column joints in seismic analysis of non-ductile RC frames. *Earthquake Engineering & Structural Dynamics*, *46*(6), 899–923.

Decanini, L. D., Liberatore, L., & Mollaioli, F. (2014). Strength and stiffness reduction factors for infilled frames with openings. *Earthquake Engineering and Engineering Vibration*, *13*(3), 437–454.

Del Vecchio, C., Di Ludovico, M., Pampanin, S., & Prota, A. (2018). Repair Costs of Existing RC Buildings Damaged by the L'Aquila Earthquake and Comparison with FEMA P-58 Predictions. *Earthquake Spectra*, *34*(1), 237–263. https://doi.org/10.1193/122916EQS257M

Di Trapani, F., Bertagnoli, G., Ferrotto, M. F., & Gino, D. (2018). Empirical Equations for the Direct Definition of Stress–Strain Laws for Fiber-Section-Based Macromodeling of Infilled Frames. *Journal of Engineering Mechanics*, *144*(11), 04018101. https://doi.org/10.1061/(ASCE)EM.1943-7889.0001532

Di Trapani, F., Di Benedetto, M., Petracca, M., & Camata, G. (2024). Local infill-frame interaction under seismic loads: Investigation through refined micro-modeling. *Engineering Structures*, *315*, 118088. https://doi.org/10.1016/j.engstruct.2024.118088

Di Trapani, F., Khan, N. A., Zhou, L., Demartino, C., & Monti, G. (2024). Cyclic response of infilled RC frames with window and door openings: Experimental results and damage interpretation. *Earthquake Engineering & Structural Dynamics*, *53*(1), 43–67.

Di Trapani, F., Vizzino, A., Tomaselli, G., Sberna, A. P., & Bertagnoli, G. (2022). A new empirical formulation for the out-of-plane resistance of masonry infills in reinforced concrete frames. *Engineering Structures*, *266*, 114422. https://doi.org/10.1016/j.engstruct.2022.114422

Dolšek, M., & Fajfar, P. (2008). The effect of masonry infills on the seismic response of a four-storey reinforced concrete frame—A deterministic assessment. *Engineering Structures*, *30*(7), 1991–2001. https://doi.org/10.1016/j.engstruct.2008.01.001

Doudoumis, I. N. (2007). Finite element modelling and investigation of the behaviour of elastic infilled frames under monotonic loading. *Engineering Structures*, *29*(6), 1004–1024. https://doi.org/10.1016/j.engstruct.2006.07.011

El-Dakhakhni, W. W., Elgaaly, M., & Hamid, A. A. (2003). Three-Strut Model for Concrete Masonry-Infilled Steel Frames. *Journal of Structural Engineering*, *129*(2), 177–185. https://doi.org/10.1061/(ASCE)0733-9445(2003)129:2(177)

Elyasaf, A., Sipper, M. Software review: the HeuristicLab framework. Genet Program Evolvable Mach 15, 215–218 (2014). https://doi.org/10.1007/s10710-014-9214-4

Eurocode 2: Design of concrete structures : part 1-1: general rules and rules for buildings. (2004). British Standards Institution.

Fardis, M. N., & Panagiotakos, T. B. (1997). Seismic design and response of bare and masonry-infilled reinforced concrete buildings part II: infilled structures. *Journal of Earthquake Engineering*, *1*(03), 475–503.

FEMA 356. (2000). *Prestandard and commentary for the seismic rehabilitation of buildings. Report FEMA-356.*

Fiore, A., Netti, A., & Monaco, P. (2012). The influence of masonry infill on the seismic behaviour of RC frame buildings. *Engineering Structures*, *44*, 133–145. https://doi.org/10.1016/j.engstruct.2012.05.023

Fortin, F.-A., De Rainville, F.-M., Gardner, M.-A. G., Parizeau, M., & Gagné, C. (2012). DEAP: Evolutionary algorithms made easy. *The Journal of Machine Learning Research*, *13*(1), 2171–2175.

Furtado, A., Rodrigues, H., Arêde, A., & Varum, H. (2021). A Review of the Performance of Infilled RC Structures in Recent Earthquakes. *Applied Sciences*, *11*(13), 5889. https://doi.org/10.3390/app11135889

Gad, A. F. (2021). *PyGAD: An Intuitive Genetic Algorithm Python Library* (Version 1). arXiv. https://doi.org/10.48550/ARXIV.2106.06158

Hak, S., Morandi, P., & Magenes, G. (2013). *Local effects in the seismic design of RC frame structures with masonry infills*. 4th ECCOMAS thematic conference on computational methods in structural dynamics and earthquake engineering.

Hermanns, L., Fraile, A., Alarcón, E., & Álvarez, R. (2014). Performance of buildings with masonry infill walls during the 2011 Lorca earthquake. *Bulletin of Earthquake Engineering*, *12*(5), 1977–1997. https://doi.org/10.1007/s10518-013-9499-3

Holmes, M. (1961). Steel frames with brickwork and concrete infilling. *Proceedings of the Institution of Civil Engineers*, *19*(4), 473–478. https://doi.org/10.1680/iicep.1961.11305

Huang, H., & Burton, H. V. (2019). Classification of in-plane failure modes for reinforced concrete frames with infills using machine learning. *Journal of Building Engineering*, *25*, 100767. https://doi.org/10.1016/j.jobe.2019.100767

Jeon, J., Park, J., & DesRoches, R. (2015). Seismic fragility of lightly reinforced concrete frames with masonry infills. *Earthquake Engineering & Structural Dynamics*, *44*(11), 1783–1803. https://doi.org/10.1002/eqe.2555

Karanikoloudis, G., Lourenco, P. B., Mendes, N., Serra, J. B., & Boroschek, R. (2021). Monitoring of induced groundborne vibrations in cultural heritage buildings: Miscellaneous errors and aliasing through integration and filtering. *International Journal of Architectural Heritage*, *15*(1), 205–228.

Karavelić, E., Nikolić, M., Ibrahimbegovic, A., & Kurtović, A. (2019). Concrete meso-scale model with full set of 3D failure modes with random distribution of aggregate and cement phase. Part I: Formulation and numerical implementation. *Computer Methods in Applied Mechanics and Engineering*, *344*, 1051–1072.

Kaushik, H. B., Rai, D. C., & Jain, S. K. (2006). Code Approaches to Seismic Design of Masonry-Infilled Reinforced ConcreteFrames: A State-of-the-Art Review. *Earthquake Spectra*, *22*(4), 961–983. https://doi.org/10.1193/1.2360907

Koutromanos, I., Stavridis, A., Shing, P. B., & Willam, K. (2011). Numerical modeling of masonry-infilled RC frames subjected to seismic loads. *Computers & Structures*, *89*(11–12), 1026–1037. https://doi.org/10.1016/j.compstruc.2011.01.006

Liberatore, L., Noto, F., Mollaioli, F., & Franchin, P. (2018). In-plane response of masonry infill walls: Comprehensive experimentally-based equivalent strut model for deterministic and probabilistic analysis. *Engineering Structures*, *167*, 533–548. https://doi.org/10.1016/j.engstruct.2018.04.057

Lotfi, H. R., & Shing, P. B. (1991). An appraisal of smeared crack models for masonry shear wall analysis. *Computers & Structures*, *41*(3), 413–425. https://doi.org/10.1016/0045-7949(91)90134-8

Lotfi, H. R., & Shing, P. B. (1994). Interface Model Applied to Fracture of Masonry Structures. *Journal of Structural Engineering*, *120*(1), 63–80. https://doi.org/10.1061/(ASCE)0733-9445(1994)120:1(63)

Lu, Xinzheng, Xie, L., Guan, H., Huang, Y., & Lu, Xiao. (2015). A shear wall element for nonlinear seismic analysis of super-tall buildings using OpenSees. *Finite Elements in Analysis and Design*, *98*, 14–25.

Lubliner, J., Oliver, J., Oller, S., & Oñate, E. (1989). A plastic-damage model for concrete. *International Journal of Solids and Structures*, *25*(3), 299–326. https://doi.org/10.1016/0020-7683(89)90050-4

Mainstone, R. (1971). On the stiffness and strengths of infilled frames. *Proceedings of the Institution of Civil Engineers*, *49*(2), 230. https://doi.org/10.1680/iicep.1971.6267

Mallick, D. V., & Severn, R. T. (1967). THE BEHAVIOUR OF INFILLED FRAMES UNDER STATIC LOADING. *Proceedings of the Institution of Civil Engineers*, *38*(4), 639–656. https://doi.org/10.1680/iicep.1967.8192

Mander, J. B., Priestley, M. J. N., & Park, R. (1988). Observed Stress-Strain Behavior of Confined Concrete. *Journal of Structural Engineering*, *114*(8), 1827–1849. https://doi.org/10.1061/(ASCE)0733-9445(1988)114:8(1827)

Mazza, F., & Donnici, A. (2021). In-plane and out-of-plane seismic damage of masonry infills in existing r.c. structures: The case study of De Gasperi-Battaglia school in Norcia. *Bulletin of Earthquake Engineering*, *19*(1), 345–376. https://doi.org/10.1007/s10518-020-00981-2

McKenna, F., Fenves, G. L., & Scott, M. H. (2000). *Open system for earthquake engineering simulation* [Computer software]. University of California.

Mehrabi, A. B., Benson Shing, P., Schuller, M. P., & Noland, J. L. (1996). Experimental Evaluation of Masonry-Infilled RC Frames. *Journal of Structural Engineering*, *122*(3), 228–237. https://doi.org/10.1061/(ASCE)0733-9445(1996)122:3(228)

Mehrabi, A. B., & Shing, P. B. (1997). Finite element modeling of masonry-infilled RC frames. *Journal of Structural Engineering*, *123*(5), 604–613.

Milanesi, R. R., Morandi, P., & Magenes, G. (2018). Local effects on RC frames induced by AAC masonry infills through FEM simulation of in-plane tests. *Bulletin of Earthquake Engineering*, *16*(9), 4053–4080. https://doi.org/10.1007/s10518-018-0353-5

Mitra, S. K. (2001). *Digital signal processing: A computer-based approach*. McGraw-Hill Higher Education.

Model Code 2010. 1. (2012). International Federation for Structural Concrete (fib).

Morandi, P., Hak, S., & Magenes, G. (2018). Performance-based interpretation of in-plane cyclic tests on RC frames with strong masonry infills. *Engineering Structures*, *156*, 503–521.

Morandi, P., Kurukulasuriya, M., Milanesi, R., Bolognini, D., Grottoli, L., Dacarro, F., & Magenes, G. (2025). Dynamic shaking table out-of-plane tests on weak masonry infills with and without previous in-plane loading. *Journal of Building Engineering*, *100*, 111670.

Moretti, M. L. (2015). Seismic design of masonry and reinforced concrete infilled frames: A comprehensive overview. *American Journal of Engineering and Applied Sciences*, *8*(4), 748.

Nafeh, A. M. B., & O'Reilly, G. J. (2024). Fragility functions for non-ductile infilled reinforced concrete buildings using next-generation intensity measures based on analytical models and empirical data from past earthquakes. *Bulletin of Earthquake Engineering*, *22*(10), 4983–5021. https://doi.org/10.1007/s10518-024-01955-4

Nakamura, H. (2001). Compressive fracture energy and fracture zone length of concrete. *Modeling of Inelastic Behavior of RC Structures under Seismic Loads*, 471–487.

Nasiri, E., & Liu, Y. (2017). Development of a detailed 3D FE model for analysis of the in-plane behaviour of masonry infilled concrete frames. *Engineering Structures*, *143*, 603–616. https://doi.org/10.1016/j.engstruct.2017.04.049

NTC 2018. (2018). *Norme Tecniche per le Costruzioni, Decreto Ministeriale del 17 Gennaio 2018*.

Oliver, J. (1989). A consistent characteristic length for smeared cracking models. *International Journal for Numerical Methods in Engineering*, *28*(2), 461–474. https://doi.org/10.1002/nme.1620280214

Oliver, J., Huespe, A. E., & Cante, J. C. (2008). An implicit/explicit integration scheme to increase computability of non-linear material and contact/friction problems. *Computer Methods in Applied Mechanics and Engineering*, *197*(21–24), 1865–1889. https://doi.org/10.1016/j.cma.2007.11.027

Papia, M. (1988). Analysis of infilled frames using A coupled finite element and boundary element solution scheme. *International Journal for Numerical Methods in Engineering*, *26*(3), 731–742. https://doi.org/10.1002/nme.1620260315

Papia, M., Cavaleri, L., & Fossetti, M. (2003). Infilled frames: Developments in the evaluation of the stiffening effect of infills. *Structural Engineering and Mechanics*, *16*(6), 675–694.

Pashaie, M. R., & Mohammadi, M. (2019). Estimating the local and global effects of infills on steel frames by an improved macro-model. *Engineering Structures*, *187*, 120–132. https://doi.org/10.1016/j.engstruct.2019.02.064

Paulay, T., & Priestley, M. J. N. (1992). *Seismic design of reinforced concrete and masonry buildings*. Wiley. https://doi.org/10.1002/9780470172841

Penava, D., Sigmund, V., & Kožar, I. (2016). Validation of a simplified micromodel for analysis of infilled RC frames exposed to cyclic lateral loads. *Bulletin of Earthquake Engineering*, *14*(10), 2779–2804. https://doi.org/10.1007/s10518-016-9929-0

Petracca, M., Camata, G., Spacone, E., & Pelà, L. (2023). Efficient Constitutive Model for Continuous Micro-Modeling of Masonry Structures. *International Journal of Architectural Heritage*, *17*(1), 134–146. https://doi.org/10.1080/15583058.2022.2124133

Petracca, M., Candeloro, F., & Camata, G. (2017a). *STKO user manual* [Computer software]. ASDEA Software Technology.

Petracca, M., Pelà, L., Rossi, R., Zaghi, S., Camata, G., & Spacone, E. (2017b). Micro-scale continuous and discrete numerical models for nonlinear analysis of masonry shear walls. *Construction and Building Materials*, *149*, 296–314. https://doi.org/10.1016/j.conbuildmat.2017.05.130

Pianosi, F., Sarrazin, F., & Wagener, T. (2015). A Matlab toolbox for global sensitivity analysis. *Environmental Modelling & Software*, *70*, 80–85.

Polyakov, S. V. (1960). On the interaction between masonry filler walls and enclosing frame when loaded in the plane of the wall. *Translations in Earthquake Engineering*, *2*(3), 36–42.

Rebecchi, G., Calvi, P. M., Bussini, A., Dacarro, F., Bolognini, D., Grottoli, L., Rosti, M., Ripamonti, F., & Cii, S. (2023). Full-scale shake table tests of a reinforced concrete building equipped with a novel servo-hydraulic active mass damper. *Journal of Earthquake Engineering*, *27*(10), 2702–2725.

Ricci, P., Di Domenico, M., & Verderame, G. M. (2018). Experimental assessment of the in-plane/out-of-plane interaction in unreinforced masonry infill walls. *Engineering Structures*, *173*, 960–978.

Rodrigues, H., Varum, H., & Costa, A. (2010). Simplified Macro-Model for Infill Masonry Panels. *Journal of Earthquake Engineering*, *14*(3), 390–416. https://doi.org/10.1080/13632460903086044

Roosta, S., & Liu, Y. (2022). Development of a Macro-Model for concrete masonry infilled frames. *Engineering Structures*, *257*, 114075. https://doi.org/10.1016/j.engstruct.2022.114075

Saneinejad, A., & Hobbs, B. (1995). Inelastic Design of Infilled Frames. *Journal of Structural Engineering*, *121*(4), 634–650. https://doi.org/10.1061/(ASCE)0733-9445(1995)121:4(634)

Sezen, H., Elwood, K. J., Whittaker, A. S., Mosalam, K. M., Wallace, J. W., & Stanton, J. F. (2000). *Pacific Earthquake Engineering Research Center*.

Sezen, H., & Moehle, J. P. (2004). Shear Strength Model for Lightly Reinforced Concrete Columns. *Journal of Structural Engineering*, *130*(11), 1692–1703. https://doi.org/10.1061/(ASCE)0733-9445(2004)130:11(1692)

Sinaie, S., Ngo, T. D., & Nguyen, V. P. (2018). A discrete element model of concrete for cyclic loading. *Computers & Structures*, *196*, 173–185.

Smith, B. S. (1966). Behavior of Square Infilled Frames. *Journal of the Structural Division*, *92*(1), 381–404. https://doi.org/10.1061/JSDEAG.0001387

Spacone, E., Filippou, F. C., & Taucer, F. F. (1996). Fibre beam-column model for non-linear analysis of RC frames: Part I. Formulation. *Earthquake Engineering & Structural Dynamics*, *25*(7), 711–725. https://doi.org/10.1002/(SICI)1096-9845(199607)25:7%253C711::AID-EQE576%253E3.0.CO;2-9

Stafford Smith, B., & Carter, C. (1969). A method of analysis for infilled frames. *Proceedings of the Institution of Civil Engineers*, *44*(1), 31–48. https://doi.org/10.1680/iicep.1969.7290

Stavridis, A., Koutromanos, I., & Shing, P. B. (2012). Shake-table tests of a three-story reinforced concrete frame with masonry infill walls. *Earthquake Engineering & Structural Dynamics*, *41*(6), 1089–1108. https://doi.org/10.1002/eqe.1174

Stavridis, A., & Shing, P. B. (2010). Finite-Element Modeling of Nonlinear Behavior of Masonry-Infilled RC Frames. *Journal of Structural Engineering*, *136*(3), 285–296. https://doi.org/10.1061/(ASCE)ST.1943-541X.116

Structural Engineering Institute & American Society of Civil Engineers (Eds). (2014). *ASCE standard ASCE/SEI 41-13: American Society of Civil Engineers: seismic evaluation and retrofit of existing buildings*. American Society of Civil Engineers.

Uva, G., Porco, F., & Fiore, A. (2012). Appraisal of masonry infill walls effect in the seismic response of RC framed buildings: A case study. *Engineering Structures*, *34*, 514–526. https://doi.org/10.1016/j.engstruct.2011.08.043

Vamvatsikos, D., & Fragiadakis, M. (2010). Incremental dynamic analysis for estimating seismic performance sensitivity and uncertainty. *Earthquake Engineering & Structural Dynamics*, *39*(2), 141–163.

Wali, O., Islam, Z. U., Rahman, F. U., Ullah, F., Jamil, I., & Azab, M. (2026). Simulation and validation of masonry infill wall behavior: A Micro modelling approach in Abaqus. *Journal of Building Pathology and Rehabilitation*, *11*(1), 5. https://doi.org/10.1007/s41024-025-00673-x

Wararuksajja, W., Srechai, J., & Leelataviwat, S. (2020). Seismic design of RC moment-resisting frames with concrete block infill walls considering local infill-frame interactions. *Bulletin of Earthquake Engineering*, *18*(14), 6445–6474. https://doi.org/10.1007/s10518-020-00942-9

Zhou, Y., Sluys, L. J., & Esposito, R. (2022). An improved mean-field homogenization model for the three-dimensional elastic properties of masonry. *European Journal of Mechanics-A/Solids*, *96*, 104721.

Appendix A: Preliminary mode-by-mode sensitivity analysis for the elastic response

A preliminary sensitivity analysis was conducted on a mode-by-mode basis to investigate the influence of the elastic material parameters on individual vibration modes. For each mode i, the numerical response was evaluated in terms of absolute error (%) between the computed modal frequency $f_{num,\mathrm{i}}$ and the experimentally identified value $f_{exp,\mathrm{i}}$. Behavioural simulations were defined as those satisfying an absolute error within ± 5% for the considered mode.

A.1. Refined model

Figure A.1 reports the scatter plots of the absolute error versus the normalised input parameters for the three vibration modes. Figure A.2 presents the corresponding parallel coordinate plots and MVD-based tornado diagrams. The results show that the in-plane masonry shear modulus G_{xy}, consistently emerges as the most influential parameter across all modes, followed by a secondary influence of the concrete Young's modulus E_c. The remaining elastic parameters exhibit a limited impact on the modal response and remain largely distributed over their variability ranges.

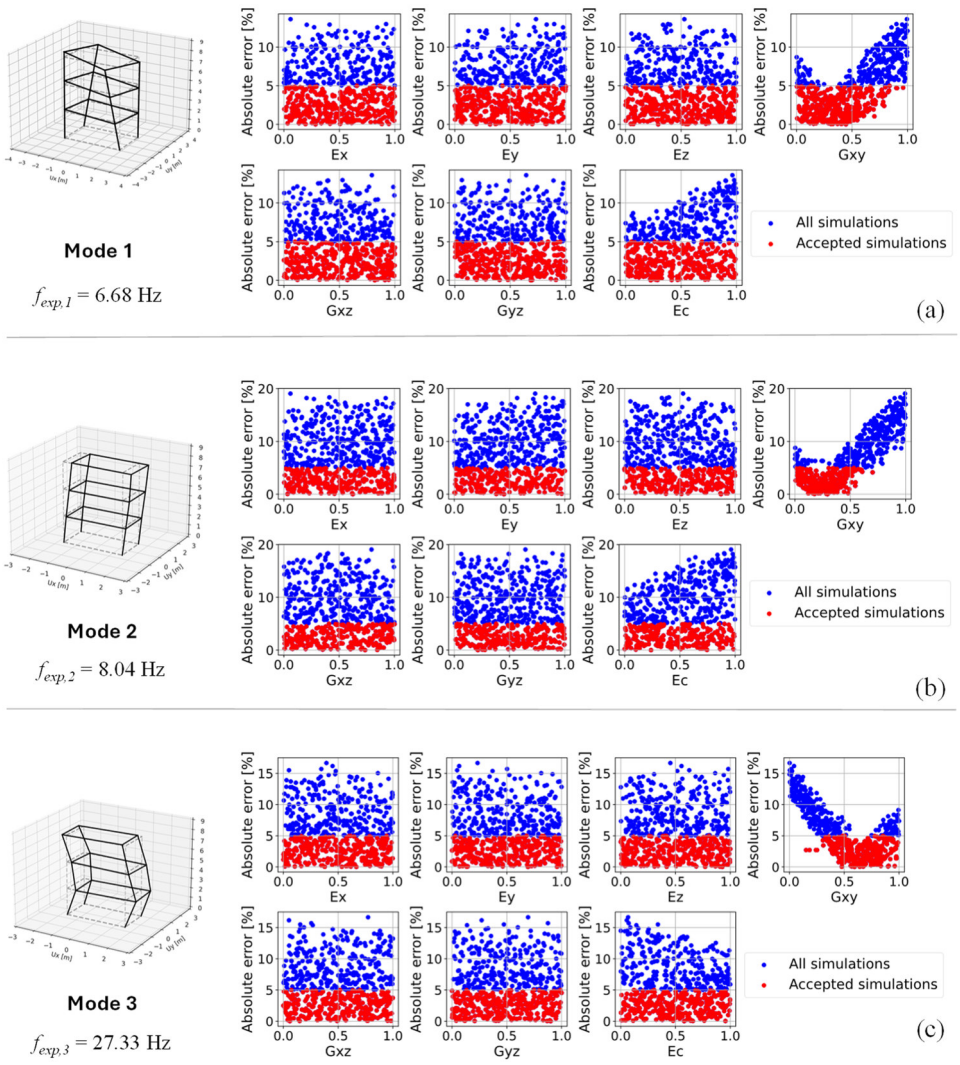

Figure A.1: Scatter plots mode-by-mode for the refined model: (a) Mode 1; (b) Mode 2; (c) Mode 3. Blue and red markers indicate all and behavioural simulations (± 5% error), respectively.

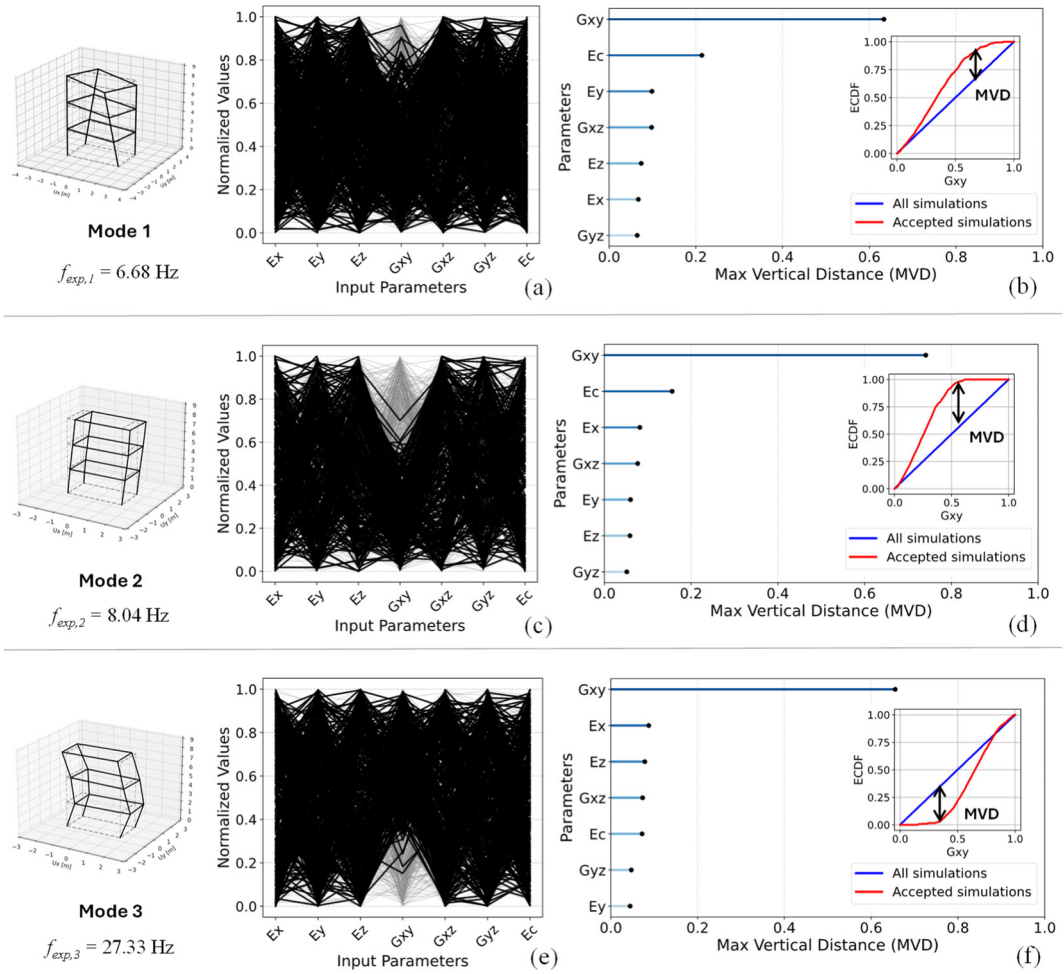

Figure A.2: Parallel coordinate plots of behavioural simulations and MVD-based tornado diagrams for the mode-by-mode sensitivity analysis (refined model).

A.2. Single strut macro-model

Figure A.3 reports the scatter plots of the absolute error between numerical and experimental modal frequencies versus the normalised constitutive parameters of the equivalent strut for the three vibration modes considered. Figure A.4 presents the corresponding parallel coordinate plots and the MVD-based tornado diagrams. The results indicate that the elastic dynamic response of the macro-model is predominantly governed by the parameters controlling the initial stiffness of the strut constitutive law, as expected, the peak compressive strength f_{md0} and the corresponding strain ε_{md0}. Conversely, the post-peak parameters (f_{mdu}, ε_{mdu}) exhibit a negligible influence on the modal frequencies within the explored variability ranges and remain largely distributed across their domains.

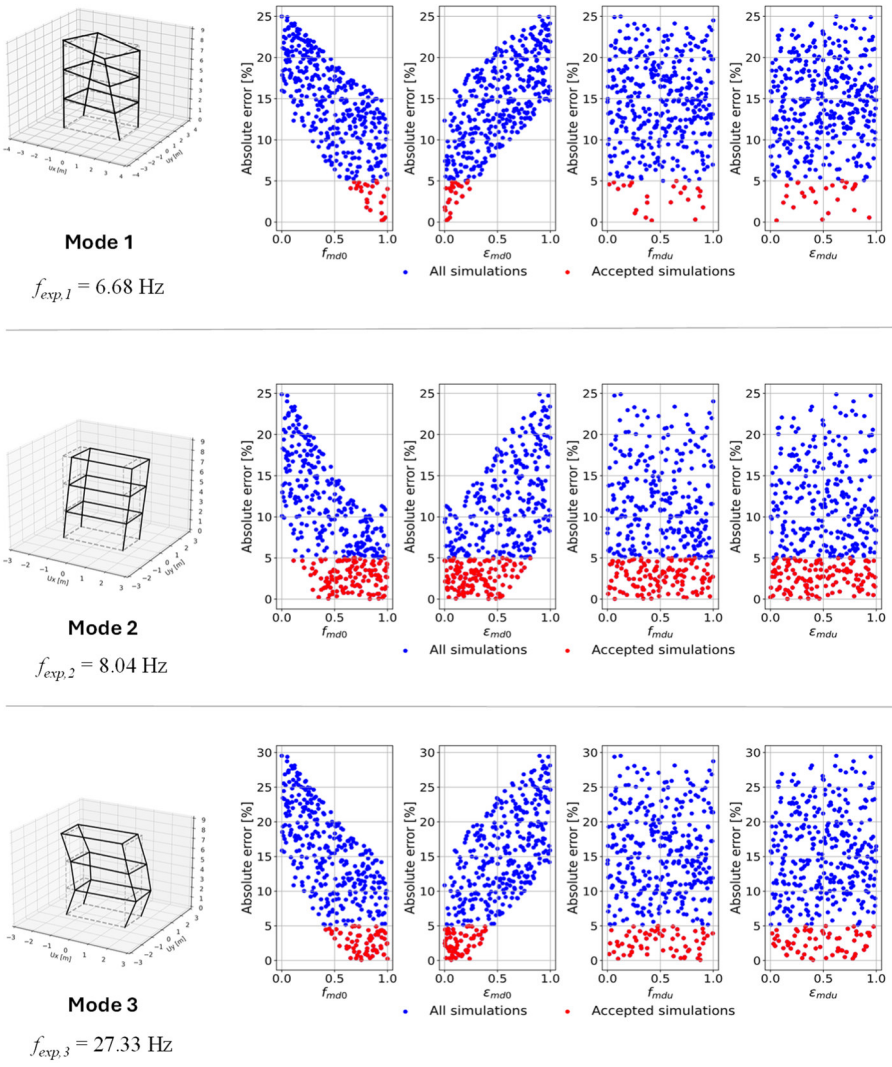

Figure A.3: Scatter plots mode-by-mode for the macro-model: (a) Mode 1; (b) Mode 2; (c) Mode 3. Blue and red markers indicate all and behavioural simulations (± 5% error), respectively.

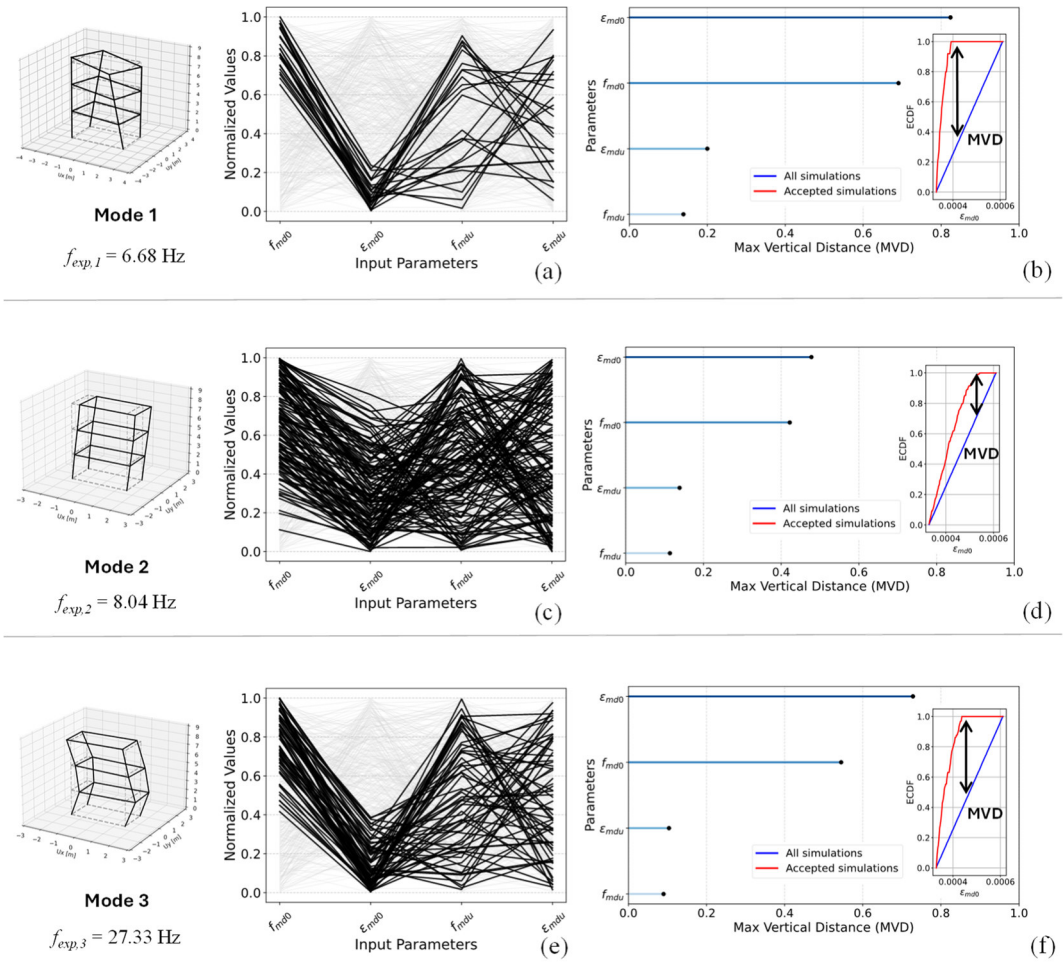

Figure A.4: Parallel coordinate plots of behavioural simulations and MVD-based tornado diagrams for the mode-by-mode sensitivity analysis (macro-model).